Investigating working memory impairment after traumatic brain injury

Ms. Amy Jolly

Imperial college London

The computational, cognitive and clinical neuroimaging laboratory (C^3NL)

Department of Brain Sciences,

This thesis is submitted for the degree of Doctor of Philosophy

ABSTRACT

Working memory impairment after traumatic brain injury (TBI) is common and can lead to long-term disability. Predicting which patients are likely to develop impairments and providing effective treatments is currently challenging. This is in part due to the heterogeneity in damage acquired across the population.

Diffusion tensor imaging (DTI) provides a means to quantify white matter damage associated with working memory impairment after TBI. I therefore investigated whether the development of a diagnostic pipeline using DTI could sensitively detect axonal injury in individual patients and provide insight into the impairments observed. Next, I applied a graph theoretical approach to determine whether distinct patterns of white matter damage were associated with working memory impairment and whether these measures could predict impairment in subacute TBI. Finally, I examined whether the application of machine learning to neuroimaging data could predict the effect of methylphenidate on working memory in patients and whether multimodal imaging improved prediction models.

I found that almost a third of patients with no visible MRI damage had evidence of axonal injury when using my diagnostic pipeline and that patients diagnosed with impairment had significantly poorer cognitive and functional outcomes. I found that patterns of white matter damage associated with alterations to the structural topology of the working memory network were related to working memory impairments after TBI and that network measures could accurately predict working memory outcomes in a novel, subacute TBI population. Finally, I demonstrated that the prediction of treatment effects on working memory performance could be achieved, but only when multimodal imaging was used.

These findings provide mechanistic insights into the development of working memory impairment after TBI and a diagnostic pipeline that can account for heterogeneity in the population. This work also identifies clinically useful prognostic markers, and provides evidence to support the development of more tailored treatments after TBI.

Table of Contents

CHAPTER 1 ..... *23*

INTRODUCTION *23*

1.1 Aims and objectives *24*

1.2 Hypothesis *24*

1.3 Chapter summary *25*

1.4 Traumatic brain injury (TBI) *26*

1.4.1 Definition of TBI 26

1.4.2 TBI severity and the MAYO classification system 26

1.4.3 The Economic, health and social burden of TBI 28

1.5 Pathophysiology of TBI *29*

1.5.1 dynamic processes of pathophysiology after TBI 29

1.5.2 Grey matter contusions and atrophy 30

1.5.3 White matter damage via Diffuse axonal injury (DAI) 30

1.5.4 Dopaminergic abnormalities after TBI 32

1.6 Working memory *34*

1.6.1 Incidence of working memory impairment after TBI 34

1.6.2 Definition of working memory and theoretical models 35

1.6.4 Moving beyond classical models of working memory 38

1.7 The neural basis of working memory impairment after TBI *41*

1.7.1 Grey matter lesions and working memory impairment 41

1.7.2 TAI and working memory impairment 42

1.7.3 Dopamine abnormalities and their association to working memory impairment 43

1.8 Current limitations in the prediction and treatment of working memory impairment after TBI *44*

1.8.1 The need for better diagnostics within the clinical setting 44

1.8.2 The need to account for individual differences to improve prognosis 44
1.8.3 The need for multimodal imaging to tailor treatments for working memory impairment 45
Chapter 2 ..... *47*
Materials and Methods *47*
2.1 Assessing cognition in TBI *48*
2.1.1 Classical neuropsychology testing 48
2.1.1.1 WTAR 48
2.1.1.2 Matrix reasoning 48
2.1.1.3 The Peoples Test (from the Peoples and Doors Test) 49
2.1.1.4 Logical Memory test 49
2.1.1.5 Colour-Word Interference Test (DKEFS) 50
2.1.1.6 The Trail Making Test 52
2.1.2 Computerised cognitive testing 53
2.1.2.1 MKL 54
2.1.2.2 PAL 54
2.1.2.3 SOS 55
2.1.2.4 FTM 56
2.1.2.5 OOO 57
2.1.2.6 HTT 58
2.1.3 Modified Paired associates learning task 59
2.2 Imaging structural and functional changes in the brain after TBI *60*
2.2.1 Principles of MRI 60
2.2.2 Diffusion tensor imaging (DTI) and fractional anisotropy 63
2.2.3 ^{123}I-Ioflupane SPECT 67
2.2.4 Resting state functional connectivity 69
2.2.5 Lesion segmentation 71
2.3 Structural MRI and SPECT acquisition parameters *71*
2.3.1 Structural MRI acquisition 71
2.3.2 SPECT acquisition 71
2.4 Structural MRI and SPECT pre-processing *72*

2.4.1 DTI 72
2.4.2 T1-MPRAGE 72
2.4.3 ^{123}I-Ioflupane SPECT 72
2.5 Quantifying structural network topology from diffusion tensor imaging 73
2.5.1 Graph theory 73
2.5.2 Defining the structural connectome to assess network topology 74
2.5.3 Small-world topology 76
2.5.3.1 Global efficiency 77
2.5.3.2 Local Efficiency 77
2.5.3.3 Degree centrality 79
2.5.3.4 Clustering coefficient 80
2.6 Multivariate statistical analysis 82
2.6.1 Canonical correlation analysis method 82
2.7 Machine learning 83
2.7.1 Classification and regression-based machine learning 83
2.7.2 Validating machine learning models: Cross-validation 85
2.7.2.1 K-fold cross-validation 86
2.7.3 Hyperparameter optimisation and nested cross-validation 87
2.7.4 Evaluating model performance in machine learning 88
2.7.4.1 Evaluating classification models 88
2.7.4.2 Evaluating regression models 89
2.7.4.3 Permutation testing 90
2.7.5 The Pattern recognition for neuroimaging toolbox (PRoNTo) 90
Chapter 3 93
Detecting axonal injury in individual traumatic brain injury patients 93
3.1 Abstract 94
3.2 Introduction 95
3.3 Methods 97
3.3.1 Participants 97
3.3.2 Neuropsychological and functional outcomes assessment 103

3.3.3 Structural MRI acquisition 103
3.3.4 Delineation of focal lesion location 104
3.4 Statistical analysis 104
3.4.1 Diffusion tensor imaging group-level analysis 104
3.4.2 Pipeline for the diagnosis of axonal injury in individual patients 105
3.4.3 Selection of white matter tract ROI's for use in diagnostic tool 107
3.4.4 Testing the effect of age on diagnosis 109
3.4.5 Testing the impact of control sample size on diagnosis 110
3.4.6 Testing the specificity of the diagnostic pipeline 111
3.4.7 Neuropsychological assessment and functional outcomes 111
3.4.8 Testing the effect of time since injury on diagnosis 112
3.5 Results 113
3.5.1 Tract selection 113
3.5.2 TBI patients demonstrate significant group-level reductions in FA 116
3.5.3 An individual test of white matter damage 117
3.5.4 Diffusion abnormalities in relation to other imaging measure of TBI 119
3.5.5 Susceptibility weighted imaging and diffusion MRI provide distinct information 119
3.5.6 Controlling for the presence of focal lesions 119
3.5.7 Individual case studies 121
3.5.8 Controlling for age in diffusion measurements 124
3.5.9 Control sample size influences specificity of diagnosis 129
3.5.10 High specificity for identifying abnormalities in traumatic brain injury patients compared to healthy controls 132
3.5.11 Functional and cognitive impairments are greater in patients with evidence of axonal injury 132
3.5.12 Functional and cognitive impairments do not differ between patients when categorised on the basis of visible damage on MRI 136

3.5.13 Greater intervals between injury and MRI are observed in patients diagnosed with axonal injury using the pipeline 137
3.5.14 Diagnosis of axonal injury in subacute TBI patients is reliable but longitudinal assessments are recommended 137
3.6 Discussion 141
Chapter 4 147
Dissociable structural sub-networks underlie working memory and reasoning deficits after traumatic brain injury 147
4.1 Abstract 148
4.2 Introduction 149
4.3 Materials and Methods 152
4.3.1 Participants 152
4.3.2 Structural MRI acquisition 157
4.3.3 Neuropsychological assessment 157
4.3.3.1 Computerised cognitive assessment 157
4.3.3.2 Standard neuropsychological assessment 159
4.3.4 Diffusion tensor imaging 159
4.3.5 Behavioural data 159
4.3.6 Graph theory analysis 160
4.3.7 Connectivity matrix pre-processing and extraction of reasoning and working memory networks for graph theory analysis 162
4.3.8 Graph theory measures 162
4.3.9 Multivariate correlational analysis of reasoning/working memory performance and structural networks 163
4.3.10 Cross-sectional and correlational analysis of graph theory measures 164
4.4 Results 164
4.4.1 TBI patients perform significantly less well on cognitive tasks and have widespread diffuse axonal injury 164
4.4.2 Computerised tasks load onto two distinct cognitive components 167

4.4.3 Reasoning and working memory tasks correlate to standard clinical neuropsychological tests 169
4.4.4 Abnormal working memory and reasoning structural networks after TBI 170
4.4.5 Patients demonstrate alterations in local/nodal network properties 172
4.4.6 Canonical Correlation Analysis confirms dissociable relationships between working memory/reasoning and structural networks 174
4.4.7 Correlation of global network properties with cognitive performance in patients 178
4.4.8 Local/nodal level network properties correlate to cognitive performance in patients differentially 178
4.5 Discussion 185
Chapter 5 191
Longitudinal changes in structural 191
5.1 Abstract 192
5.2 Introduction 193
5.3 Materials and Methods 195
5.3.1 Participants 195
5.3.2 Structural MRI acquisition 197
5.3.3 Cognitive assessment 197
5.3.3.1 Standard Neuropsychological testing 197
5.3.3.2 Computerised working memory task 200
5.3.4 Image pre-processing 200
5.3.4.1 Diffusion tensor imaging 200
5.3.4.2 Delineation of focal lesions 201
5.3.5 Statistical analysis 201
5.3.5.1 Cognitive assessment 201
5.3.5.2 Longitudinal cognitive assessment 202
5.3.5.3 Cross-sectional comparison of FA and assessment of longitudinal changes within patients 202
5.3.5.4 Quantification of graph theory metrics 203
5.3.6 Cross-sectional analysis of working memory network topology 203

5.3.7 Association between network measures at subacute and chronic timepoints to working memory performance 204

5.3.8 Calculation of longitudinal network changes and association to working memory performance 204

5.3.9. Quantification of lesion load within the working memory network 205

5.3.10 Using machine learning to predict working memory performance at the chronic phase of injury using subacute network measures 206

5.4 Results 207

5.4.1 TBI patients demonstrate evidence of cognitive impairment 207

5.4.2 TBI patients demonstrate evidence of axonal injury at subacute and chronic timepoints 207

5.4.3 TBI patients demonstrate evidence of focal lesions in regions associated with the working memory network 209

5.4.4 Abnormal graph theory measures in the working memory network are present at the subacute and chronic phases of injury 209

5.4.5 Average network measures of modularity are related to working memory performance at the chronic phase of injury 212

5.4.6 Longitudinal increases in local efficiency are associated with higher working memory scores in the chronic phase of injury 213

5.4.7 Machine learning approaches using nodal measures of degree centrality sub-acutely predict working memory performance at the chronic phase of injury 214

5.5 Discussion 217

Chapter 6 221

Predicting the treatment effect of methylphenidate in working memory using multimodal imaging 221

6.1 Abstract 222

6.2 Introduction 223

6.3 Materials & Methods 225

6.3.1 Participants 225

6.3.2 Study design 229

6.3.3 Study procedures 230
6.3.4 MRI 230
6.3.5 ^{123}I-Ioflupance SPECT 231
6.3.6 Cognitive testing 231
6.3.7 Structural MRI 231
6.3.8 Resting-state fMRI 231
6.3.9 Statistical analysis of neuroimaging data 232
6.3.10 Statistical analysis of cognitive data 233
6.3.11 Application of Machine learning to neuroimaging data 234
6.3.12 Classification of patients and controls using machine learning 236
6.3.12.1 Single imaging classification models 236
6.3.12.2 Multimodal classification models 237
6.3.12.3 Validation and assessment of classification models 237
6.3.13 Prediction of response to Methylphenidate treatment using regression-based machine learning 238
6.3.13.1 Single imaging regression models 238
6.3.13.2 Multimodal regression models 238
6.3.13.3 Validation and assessment of regression-based models 239
6.3.14 Assessment of single and multimodal model performance using a model comparison approach 239
6.4 Results 240
6.4.1 TBI patients demonstrate significantly poorer performance on working memory tasks 240
6.4.2 Patients demonstrate abnormalities in brain structure and function 241
6.4.3 Classification of patients and controls can be made using single imaging modalities 242
6.4.4 Multimodal imaging can improve classification accuracy 243
6.4.5 The impact of methylphenidate on working memory performance is variable 246
6.4.6 Multimodal imaging can predict treatment effect of methylphenidate on working memory performance where single modality models cannot 248

6.5 Discussion *252*

Chapter 7 ..... *257*

Discussion *257*

7.1 Summary of findings *258*

7.1.1 Chapter 3 258

7.1.2 Chapter 4 259

7.1.3. Chapter 5 260

7.1.4 Chapter 6 261

7.2 Interpretation *262*

7.2.1 Heterogeneity in working memory impairments after TBI is associated with the distribution of damage across the structural networks that underpin it 262

7.2.2 Identifying the structural connectome of working memory can aid prognosis of impairments 263

7.2.3 Network neuroscience provides insights into the potential mechanisms of working memory impairment 264

7.2.4 Broad heuristics in the clinical setting are useful but quantifying white matter damage at the individual level is valuable 265

7.2.5 Working memory impairment is not limited to white matter damage: the case for multimodal imaging and machine learning 265

7.3 Future research *267*

7.3.1 Prediction of working memory impairment using structural network measures 267

7.3.2 Targeted modulation of the working memory network and its associated structural connectivity 267

7.3.3 The use of methylphenidate to treat working memory 268

7.3.4 Investigating the multiple dimensions of working memory after TBI 268

Appendix *293*

List of figures

Figure 1: Figure from Sharp, D. J. et al. (2014) detailing primary and secondary processes of axonal injury and consequences for structural network disconnection relating to functional network disruption.

Figure 2: Figure from Jenkins et al., 2018 illustrating subdivisions of the striatum and striatal binding ratio (SBR) calculated from SPECT scans in TBI patients and controls.

Figure 3: Percentage of objective and subjective impairments observed in 222 patients attending TBI outpatient clinic at St Mary's hospital.

Figure 4: Figure illustrating the classical model of working memory as proposed by Baddeley. & Hitch (1974).

Fig 5: The multicomponent model of working memory as defined by Baddeley, 2000.

Figure 6: Overlapping voxels derived from meta-analysis of working memory task activation maps across 189 fMRI studies of healthy individuals (Rottschy et al., 2011).

Figure 7: Figure from. Soreq et al., 2019 demonstrating multivariate connectivity patterns across working memory tasks and processes.

Figure 8: Overall thesis themes and their role in improving the treatment of working memory impairment after TBI.

Figure 9: Example trial from the Matrix Reasoning subtest from the WAIS-III (Weschler., 1945).

Figure 10: Example of the four trials included within the colour-interference test from the Delis-Kaplan executive function battery (DKEFS).

Figure 11: Example of Trail Making Tests Part A and B.

Figure 12: Example of computerised Monkey Ladder (MKL) task and graphics presented on Ipad.

Figure 13: Example of Paired Associates Learning (PAL) task and graphics presented on Ipad.

Figure 14: Self Ordered Search (SOS) task and graphics presented on the Ipad.

Figure 15: Feature Match (FTM) task and graphics presented on the Ipad.

Figure. 16: Odd One Out (OOO) task and graphics as presented on the Ipad.

Figure 17: Hampshire Tree Task (HTT) and graphics as presented on the Ipad.

Figure 18: Modified PAL task graphics.

Figure 19: Example of hydrogen nuclei alignment to external magnetic field and precession properties.

Figure 20: Example of gradient fields and impact on hydrogen nuclei precession.

Figure 21: Example images of B0 diffusion image and several diffusion weighted images across different directions.

Figure 22: Example of 3x3 diffusion array.

Figure 23: Example of diffusion tensor and diffusion array for isotropic and anisotropic water movement.

Figure 24: Example of diffusion tensor and equation for the calculation of FA.

Figure 25: ^{123}I-Ioflupance SPECT scans of TBI patients and healthy controls.

Figure 26: Example of directed vs undirected graphs used in graph theory.

Figure 27: Figure from Imms et al., 2019 Demonstrating impact of edge connectivity on small-world network topology.

Figure 28: Example of Local Efficiency at different scales.

Figure 29: Example of impact of axonal injury on local efficiency measures of a given node

Figure 30: Example of degree centrality.

Figure. 31: Example of Clustering coefficient.

Figure 32: Example of alterations to clustering coefficient due to axonal injury

Figure 33: Example of CCA structure and input data.

Figure 34: Example of classification problem with hyperplane.

Figure 35: Example of regression using machine learning.

Figure 36: Example of 5-fold cross-validation.

Figure 37: Example of hyperparameter optimisation during k-fold cross validation.

Figure 38: Schematic of hierarchical nature of MKL algorithm for machine learning.

Figure 39: DTI diagnostic pipeline processing steps.

Fig 40: Data-driven tract selection

Figure 41: Tracts selected for use in diagnostic pipeline.

Figure 42: Diagnostic results using the DTI diagnostic pipeline for each individual TBI patient.

Figure 43: Diagnostic results when including or excluding areas of lesion.

Figure 44: Individual case studies.

Figure 45: Tract mean FA for healthy control cohort, grouped by age.

Fig 46: Diagnostic results for each tract when controlling for age.

Figure 47: Reliability and accuracy measures using smaller control group sample sizes to identify DTI abnormalities in individual TBI patients.

Figure 48: Cognitive and functional outcomes in patients diagnosed with and without axonal injury.

Figure 49: Longitudinal diagnostic results of subacute TBI cohort.

Figure 50: Intraclass correlation coefficient (ICC) of diagnostic results (z-scores and FDR corrected p values) between subacute and chronic timepoints in TBI patients.

Figure 51: Illustration of extraction of structural connectomes from task-activation maps produced by Hampshire *et al*., 2012.

Figure 52: Schematic of the six computerised cognitive tasks used to assess TBI patients and controls.

Fig 53: Overview of graph theory analysis methods.

Figure 54. Cross-sectional analysis of TBI patients and controls for cognitive performance and whole-brain fractional anisotropy.

Figure 55: Principal component analysis of patient cognitive data.

Figure 56: Association between working memory/reasoning performance derived from computerised tasks and classical neuropsychological test performance in patients.

Figure 57: Cross-sectional analysis of local/nodal properties in TBI patients and controls.

Figure 58: Sub-sampling canonical correlation analysis results to assess model genralisability and overfit.

Figure 59: Back projection of canonical variates to task and node data from Canonical correlation analysis.

Fig 60: Local graph theory network measures and correlation to cognitive performance.

Figure 61: Correlation coefficients of local/nodal working memory network measures across the ten connectome threshold iterations.

Figure 62: Correlation coefficients of local/nodal reasoning network measures across all ten connectome threshold iterations.

Figure 63: Cognitive and neuroimaging results

Figure 64: Local/nodal network measures in acute and sub-acute phases of injury in TBI patients compared to controls.

Figure 65: Association between local efficiency network changes between acute and sub-acute timepoints and working memory performance in patients.

Figure 66: Regression-based machine learning results using acute local/nodal degree centrality measures to predict working memory performance at six months.

Figure 67: Study design for patients and controls.

Figure 68: Schematic of machine learning research strands.

Figure 69: Associations between baseline working memory task performance in TBI patients and controls and PCA cognitive component loadings.

Figure 70: Cross sectional comparison of brain structure and function in TBI patients compared to healthy controls.

Fig 71: Uni- and multimodal classification results for TBI patient and control neuroimaging data.

Figure 72: Treatment effect of methylphenidate on working memory performance in patients.

Figure 73: Results of multimodal regression-based model for the prediction of methylphenidate treatment effect of working memory performance in patients.

List of Tables

Table 1: Mayo classification severity system categories and criteria.

Table 2: TBI patient demographics.

Table 3: Patient demographics of additional longitudinal subacute TBI patient cohort (n=25).

Table 4: List of candidate tracts considered for use in the diagnostic pipeline.

Table 5: Diagnostic results for individual patients with and without accounting for age.

Table 6: Demographics of TBI patients.

Table 7: Standard neuropsychological test battery performance for patients and controls.

Table 8: List of nodes for working memory and reasoning networks.

Table 9: TBI patient demographics and time since injury at subacute and chronic assessments.

Table 10: List and description of sub-tests included within the RBANS.

Table 11: TBI patient demographics.

Table 12: Multimodal classification model results using MKL.

Table 13: Multimodal regression model results using MKL.

ACKNOWLEDGEMENTS

I would first like to thank Professor David Sharp for his limitless support, knowledge and guidance throughout my PhD and during my time at C^{3}NL. I cannot express enough the gratitude for the opportunities and trust in my abilities provided to me as a member of the team.

I would also like to thank Dr Adam Hampshire for his patience, endless support and knowledge which has allowed me to develop as a scientist. Our conversations are always enlightening and as the years have gone by, less intimidating, which suggests I have learnt a thing or two along the way.

I am grateful to every member of C^{3}NL for providing a fantastic research environment and helping me throughout the years. I hope to support others the way this team has supported me.

I would like to thank every individual who volunteered to take part in research, particularly patients. I have enjoyed all of the conversations shared with them.

I would like to thank my wonderful Mum, Kathy and Dad, Chris, who have given me unwavering love and support throughout my life and helped nurture my love of science. There are not enough words to thank them and I hope I have made them proud.

I want to thank my amazing partner Andy, for his patience and support. He has put up with me where I'm sure others would not throughout this PhD. Thank you for everything.

Finally, I would like to dedicate this thesis to my late brother Matthew, who's bravery fighting brain cancer never left my memory and inspired me to study the brain.

STATEMENT OF PUBLICATIONS

The data presented in Chapter 4 has been published in Brain:

Jolly A.E., Scott G., Sharp D., Hampshire A. Distinct patterns of structural damage underlie working memory and reasoning deficits after traumatic brain injury (2020), *Brain*, 143(4), 1158–1176.

The data presented in Chapter 3 is under review after revisions at Brain.

The data presented in chapters 5 and 6 are being prepared for submission to Brain.

The data presented in chapters 3, 4 and 6 have been used for other publications that are relevant to this thesis:

Li L, Violante I, Zimmerman K, Leech R, Hampshire A, Patel M, Opitz A, McArthur D, Jolly A, Carmichael D, Sharp DJ 2019, Traumatic axonal injury influences the cognitive effect of non-invasive brain stimulation, Brain, Vol:142, ISSN:1460-2156

Jolly, A. E., Raymont, V., Cole, J. H., Whittington, A., Scott, G., De Simoni, S., . . . Sharp, D. J. (2019). Dopamine D2/D3 receptor abnormalities after traumatic brain injury and their relationship to post-traumatic depression. Neuroimage Clin, 24, 101950.

De Simoni, S., Jenkins, P. O., Bourke, N. J., Fleminger, J. J., Hellyer, P. J., Jolly, AE., Sharp, D. J. (2018). Altered caudate connectivity is associated with executive dysfunction after traumatic brain injury. Brain, 141(1), 148-164.

Jenkins, P. O., De Simoni, S., Bourke, N. J., Fleminger, J., Scott, G., Towey, D. J., . . . Sharp, D. J. (2018). Dopaminergic abnormalities following traumatic brain injury. Brain, 141(3), 797-810.

Scott, G., Zetterberg, H., Jolly, A., Cole, J. H., De Simoni, S., Jenkins, P. O., . . . Sharp, (2018). Minocycline reduces chronic microglial activation after brain trauma but increases neurodegeneration. Brain, 141(2), 459-471.

Feeney, C., Sharp, D.J., Hellyer, P.J., Jolly, A.E., Cole, J.H., Scott, G., Baxter, D., Jilka, S., Ross, E., Ham, T.E., Jenkins, P.O., Li, L.M., Gorgoraptis, N., Midwinter, M. and Goldstone, A.P. (2017), Serum insulin-like growth factor-I levels are associated with improved white matter recovery after traumatic brain injury. Ann Neurol., 82: 30-43

DECLARATION OF ORIGINALITY

The work within this thesis is my own except where otherwise referenced.

The data presented in chapters 3, 4 and 6 are a collation of data collected as part of Dr Peter Jenkins, Dr Claire Feeney and Dr Gregory Scott's PhD work which I helped to collect during my time as a research assistant within C^3NL.

The data presented in chapter 5 was collected during my PhD with a wider research team inclusive of Professor David Sharp, Dr Adam Hampshire, Dr Neil Graham, Mr Karl Zimmerman, Ms. Emma-Jane Mallas, Mr Niall Bourke, Mr. William Trender and Ms. Maria Balaet.

The SPECT imaging data and resting state functional connectivity measures included in chapter 6 were pre-processed by Dr Peter Jenkins and Dr Sara De Simoni and have previously been published (Jenkins et al., 2019; De Simoni et al., 2017). All statistical analysis with this data including cross-sectional comparisons and machine learning were conducted by myself. Figure 50 presented within chapter 6 was produced with the help of Dr Eyal Soreq.

I contributed to the manual lesion segmentation included in the thesis chapters however, these were also created by Mr Niall Bourke, Dr Neil Graham and Mr Karl Zimmerman.

COPYRIGHT DECLARATION

The copyright of this thesis rests with the author. Unless otherwise indicated, its contents are licensed under a Creative Commons Attribution-NonCommercial 4.0 International Licence (CC BY-NC).

Under this licence, you may copy and redistribute the material in any medium or format. You may also create and distribute modified versions of the work. This is on the condition that: you credit the author and do not use it, or any derivative works, for a commercial purpose.

When reusing or sharing this work, ensure you make the licence terms clear to others by naming the licence and linking to the licence text.

Where a work has been adapted, you should indicate that the work has been changed and describe those changes. Please seek permission from the copyright holder for uses of this work that are not included in this licence or permitted under UK Copyright Law.

CHAPTER 1

INTRODUCTION

In this chapter I describe the aims, objectives and hypothesis of this thesis and provide an outline of the remaining chapters. I describe the pathophysiology of TBI, the incidence of working memory deficits within this population and current understandings of the mechanisms related to its function and impairment after TBI. I describe the current limitations in the prediction and treatment of working memory impairment after injury.

1.1 Aims and objectives

The aim of this thesis was to investigate structural and functional changes in the brain after traumatic brain injury (TBI) and their association to working memory impairment. A combination of structural and functional MRI, single photon emission computed tomography (SPECT), cognitive assessments, machine learning and drug interventions were used.

The objectives of the thesis are:

1. To investigate the impact of white matter damage on working memory after TBI, using measures of fractional anisotropy (FA) and computerised cognitive assessments.

2. To identify patterns of white matter damage associated with working memory impairment from a network neuroscience perspective, incorporating graph theoretical measures of structural connectivity.

3. To stratify patients based on their cognitive and neuroimaging profiles to improve prognosis and interventions using multimodal imaging and regression-based machine learning.

1.2 Hypothesis

1. There will be specific patterns of white matter damage associated with working memory impairment after TBI

2. Identifying these patterns will help to improve prediction of working memory impairment in patients.

3. Accounting for individual variability in the TBI population will help to improve prognosis and targeted interventional treatments of working memory impairments.

1.3 Chapter summary

In chapter 2, I describe the materials and methods used across my experimental chapters.

In chapter three, I develop and test a novel pipeline to accurately quantify and diagnose axonal injury in individual patients using diffusion MRI. I examine the impact of lesions, age, sample size and time since injury on diagnostic results and investigate cognitive (inclusive of working memory) and functional impairments in patients diagnosed with or without evidence of axonal injury using the pipeline, in comparison to standard clinical markers.

In chapter four, I investigate the relationship between patterns of axonal injury as quantified using FA and working memory impairment in a chronic TBI population. I apply a graph theoretical approach to structural connectomes defined using a working memory task-fMRI activation map to determine whether alterations to network topology can provide insights into the mechanisms underlying impairment.

In chapter five, I investigate abnormalities in the working memory network topology previously defined and tested in chapter four, in a subacute TBI population. I examine whether longitudinal changes within network topology are associated with working memory performance six months post-injury and determine whether local/nodal graph theoretical measures at the subacute phase can predict working memory at the chronic phase.

In chapter six, I use a combination of cortico-striatal resting state functional connectivity, single-photon emission computed tomography (SPECT) and structural MRI to determine whether the effect of methylphenidate on working memory in

patients can be predicted using machine learning. I explore whether multi-modal imaging models outperform unimodal machine learning models.

In chapter seven, I summarise the findings of my thesis and discuss how they contribute to our understanding of working memory impairment after TBI. I conclude by describing possible directions for future research on the basis of my work.

1.4 Traumatic brain injury (TBI)

1.4.1 Definition of TBI

Traumatic brain injury (TBI) is defined as an injury to the brain caused by external forces, leading to alterations in its structure and function (Menon et al., 2010). The most common mechanisms of injury are road traffic accidents (RTA), violence and falls. Injuries can vary greatly across a TBI population and is in part related to the forces exposed to the brain at the point of injury (e.g. acceleration-deceleration vs. blunt force).

1.4.2 TBI severity and the MAYO classification system

Heterogeneity within the TBI population poses a particular challenge for the management of patients clinically. The categorisation of injury severity has therefore proved useful on the basis of its association to mortality (Roozenbeek et al., 2012; Thornhill et al., 2000), likelihood of surgical intervention (Vukic et al., 1999) and cognitive impairments both acutely and chronically (Christensen et al., 2008), to inform the management of patients.

The Mayo classification system is widely used to categorise severity (Malec et al., 2007) and comprises of three broad categories; moderate-severe (definite), mild (probable) and symptomatic (possible). Classification is made on the basis of clinical presentation and imaging (Table 1) providing a comprehensive overview that is not

hindered by incomplete medical records. This method has been well validated and is therefore used to categorise TBI patients included within this thesis.

Severity	Criteria
Moderate-severe (definite)	One or more of the following criteria Presentation: ▪ Death ▪ Loss of consciousness (LOC) > 30 minutes ▪ Post-traumatic anterograde amnesia >24 hours ▪ Glasgow coma score (GCS) <13 in the initial 24 hours Imaging: ▪ Intracerebral haemorrhage ▪ Subdural haemorrhage ▪ Epidural haemorrhage ▪ Sub-arachnoid haemorrhage ▪ Cerebral or haemorrhagic contusion ▪ Penetrating TBI (dura penetrated) ▪ Brainstem injury
Mild (probable)	Presentation: ▪ Loss of consciousness (LOC) momentarily to < 30 minutes ▪ Post-traumatic anterograde amnesia momentarily to < 2-4 hours Imaging: ▪ Depressed basilar or linear skull fracture (dura intact)

Symptomatic (possible)	Presentation: ▪ None of the moderate-severe or mild criteria ▪ One or more of the following are present; blurred vision, confusion (mental status changes), dizziness, headache, nausea or focal neurological symptoms.

Table 1: Mayo classification severity system categories and criteria.

1.4.3 The Economic, health and social burden of TBI

Traumatic brain injury is one of the leading causes of long-term disability in the world (Hyder et al., 2007). It has been estimated that up to ten million individuals will be affected by TBI each year (Humphreys et al., 2013). In the UK alone, approximately 1.4 million patients attend hospital following a head injury (Lawrence et al., 2016). Advancements in emergency medicine have ensured that survival after severe TBI has improved (Vella et al., 2017; Stein et al., 2010), however patients are often left with long-term disabilities that can persist across the lifespan. This is an important factor in the context of the wider impact of TBI on the healthcare system and economy. For example, TBI is commonly observed after falls in elderly populations, and will likely increase with an increasingly ageing population. Conversely, TBI due to road traffic accidents (RTA) are shown to be associated with a younger population where disabilities may persist across the lifespan, requiring support for many decades (Peeters et al., 2015; Maas et al., 2013).

Chronic cognitive, emotional and physical disabilities result in patients being unable to return to work or regain independence. As a result, they rely upon a myriad of social and healthcare services, increasing the burden on families and an already overwhelmed care system. In two large observational studies it was shown that more than half of severe TBI patients were moderately disabled one year after injury (Thornhill et al., 2007) whilst a large proportion had not returned to work/school after four years, and remained living with family (Jacobs et al., 1988). Although the true economic cost of TBI in the UK is hard to quantify, studies have estimated this to be

as high as £15 billion annually (Centre for mental health report, 2018; www.centreformentalhealth.co.uk), highlighting the need for improved treatment and management of TBI associated disability.

1.5 Pathophysiology of TBI

1.5.1 dynamic processes of pathophysiology after TBI

TBI is not a static insult to the brain, as demonstrated by a number of animal and human studies that highlight a cascade of processes triggered after injury (Werner & Englehard., 2007). These likely reflect the heterogeneity of outcomes seen in patients, and the incidences of cognitive decline that can occur long after the initial injury (Gorgoraptis et al., 2019). Primary injuries occur at the point of TBI, whereby focal damage such as contusions, haematomas or skull fractures can arise due to direct impacts to the head. More diffuse injuries can also occur to the axons (diffuse axonal injury, DAI) and vasculature (diffuse vascular injury, DVI) via acceleration-deceleration forces.

After the initial insult, secondary injury can arise. In the more immediate timeframe, this can result in ischaemia (Vespa., 2016) as well as increased intracranial pressure (ICP) which can lead to further damage via compression and cell death (Ordookhanian et al., 2018). Long-term secondary injury is also present in the form of extended neuroinflammation (Schimmel et al., 2017) and subsequent neurodegeneration (Graham et al., 2019), demonstrating a clear association with cognitive decline in TBI patients long after their injury. Understanding the impact of both primary and secondary injuries to the brain and time since injury is therefore important to help elucidate the mechanisms of disability in acute and chronic TBI populations.

1.5.2 Grey matter contusions and atrophy

Focal contusions to the brain are commonly observed in regions closest to the bony protrusions of the skull such as the orbito-frontal, occipital and temporal lobes (Gurdjian., 1975; Bigler et al., 2007). In patients with severe focal lesions, a high mortality rate is observed (approximately 40%) (Marshall et al., 1991). In survivors, cognitive and emotional impairments are observed, with working memory and planning impairments being noted after lesions to the dorsolateral prefrontal cortex (DLPFC) (Cicerone et al., 2006) and apathy and impaired awareness observed when lesions to subcortical and frontal grey matter regions are present (Andersson et al., 1999; Spikman et al., 2010). Nevertheless, poor correlations to cognitive and functional outcomes are observed (Bigler et al., 2007) suggesting other potential mechanisms (Gaffan et al., 2005). For example, DAI has been shown to co-occur in a large proportion (~50%) of patients presenting with focal lesions (Skansden et al., 2010).

Grey matter atrophy as a result of neurodegenerative processes is also observed from months to many years post-injury (Ross., 2011). Evidence of an association between TBI and the development of dementia has long been established (Fleminger et al., 2003; Krueger et al., 2011; Corkin et al., 1989; Graham et al., 2019) illustrating the long-term consequences of TBI. Accelerated atrophy above and beyond normal ageing has been shown to be generalised across the whole grey matter after TBI and have strong associations to episodic memory performance (Sidaros et al., 2009; Cole et al., 2015). However, atrophy is not restricted to grey matter, with greater rates observed within the white matter (Cole et al., 2015). Furthermore, alterations to white matter structure have been shown to be a strong predictor of cerebral volume loss (Ding et al., 2008; Poudel et al., 2020) suggesting the impact of white matter damage upon cognition may be greater than that of focal contusions.

1.5.3 White matter damage via Diffuse axonal injury (DAI)

Diffuse axonal injury (DAI), also referred to as traumatic axonal injury (TAI) to reflect secondary injury to white matter, is highly associated with both cognitive and functional

outcomes after TBI (Kinnunen et al., 2011; Fagerholm et al., 2015; Bazarian et al., 2009). The viscoelastic properties of white matter make this tissue structure particularly vulnerable to damage when forces are applied to the brain. Evidence of axonal injury is therefore observed across a range of injury severities inclusive of mild to moderate-severe TBI (Wilde et al., 2008; Brown et al., 2001; Rabinowitz et al., 2015). In studies of mild TBI, persistent cognitive problems have been demonstrated to be associated with alterations to the white matter microstructure where no other evidence of injury is observed, highlighting its importance in cognitive function (Lo et al., 2009; Hellstrom et al., 2017; Grossman et al., 2013). In more severe cases of TBI, prediction of long-term outcomes is founded in the extent and severity of DAI (Adams et al., 1989 ; Benson et al., 2007) with more severe axonal injury resulting in long-term disorders of consciousness or death (Bernat., 2009).

Although DAI remains one of the most clinically useful predictors of long-term outcome after TBI (Lee et al., 2012; Adams et al., 1989), recovery can vary greatly within this population (Rabinowitz et al., 2014). This may in part be due to the varied distribution of damage acquired to the white matter across patients. Long-range white matter connections such as the corpus callosum are commonly damaged after TBI (Meythaler et al., 2001; Pandit et al., 2013, Sharp et al., 2014), however the biomechanics of forces applied to the brain during injury can vary greatly between patients and lead to varied propagation of strain and subsequent damage (Cloots et al., 2008). This has been particularly highlighted with the advancement of finite element modelling of strain forces in the brain during injury (Ghajari et al., 2017) and provides a promising means to better predict location and impact of forces to white matter. Long-term demyelination of white matter projections via Wallerian degeneration have also been demonstrated to be associated with cognitive and functional impairments (Hill et al., 2016). This is likely due to the relationship between white matter damage and alterations to functional connectivity, grey matter volume and dopaminergic function (Hayes et al., 2016; Ding et al., 2008; Jenkins et al., 2016; Sharp et al., 2014) (Fig. 1).

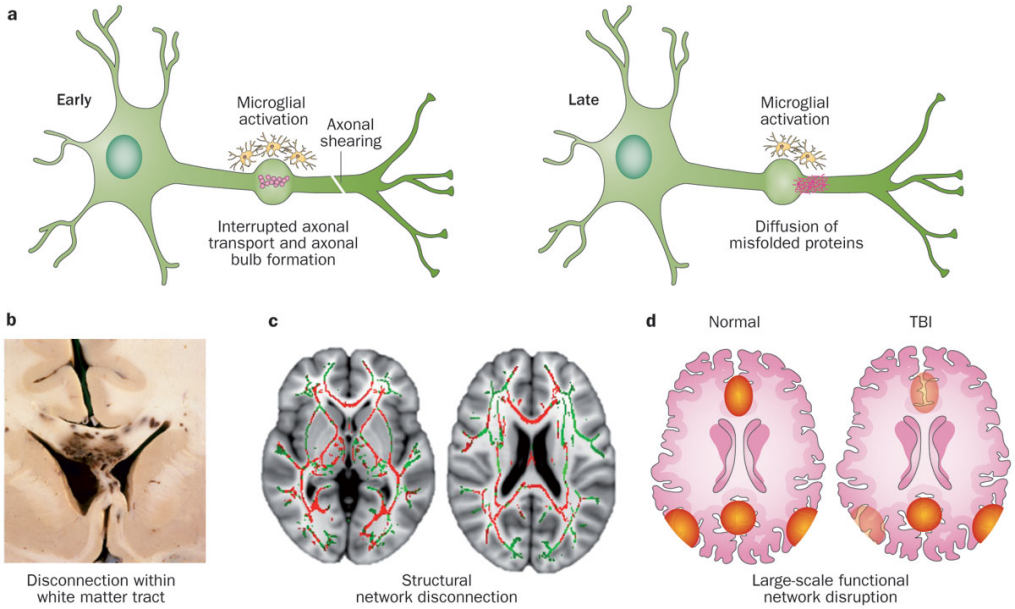


Figure 1: Figure from Sharp, D. J. et al. (2014) detailing primary and secondary processes of axonal injury and consequences for structural network disconnection relating to functional network disruption. A. Illustration of primary and secondary damage to white matter. B. Histological evidence of white matter disconnection in the corpus callosum. C. Evidence of widespread structural disconnection due to white matter damage (highlighted as reduced fractional anisotropy in red). D. Illustration of impact of structural dysconnectivity on functional networks in the brain underpinned by white matter. Permission for Figure obtained from D. P. Agamanolis, Northeast Ohio Medical University, OH, USA, Sharp, D. J. et al. (2014) Network dysfunction after traumatic brain injuryNat. Rev. Neurol. doi:10.1038/nrneurol.2014.15

1.5.4 Dopaminergic abnormalities after TBI

Dopamine (DA) is a neuro-modulatory neurotransmitter that is associated with cognitive function (Bales et al., 2009). TBI can lead to disruption to the dopaminergic system as evidenced by significant alterations in dopamine transporter (DaT) and dopamine receptor levels in the striatum (Donnemiller et al., 2000; Wagner et al., 2014). In animal models of TBI, a significant reduction in dopaminergic neurons in the substantia nigra (~25%) is observed soon after injury followed by a hypo-dopaminergic state (Wagner et al., 2005b). Reductions in DaT are therefore posited to reflect a compensatory downregulation of dopamine clearance in order to maintain levels of endogenous dopamine.

After TBI, alterations to DaT and dopaminergic D2/D3 receptors have been shown to relate to cognitive and emotional impairments in humans (Jenkins et al., 2016; Jolly et al., 2019). These findings suggest a promising therapeutic target via the use of dopaminergic interventions such as methylphenidate (Newsome et al., 2015; Manktelow et al., 2017). However, heterogeneity in the patient population has led to varied results (Jenkins et al., 2016). A recent study demonstrated that disruption to the dopamine system in chronic TBI varied greatly, with approximately 20% of patients being identified as having altered caudate DaT (Jenkins et al., 2018) (Fig. 2). Abnormalities were associated with reduced substantia nigra volume and evidence of axonal injury in the ascending dopaminergic white matter projections, providing insight into the potential mechanisms of dopamine disruption and variability within the population.

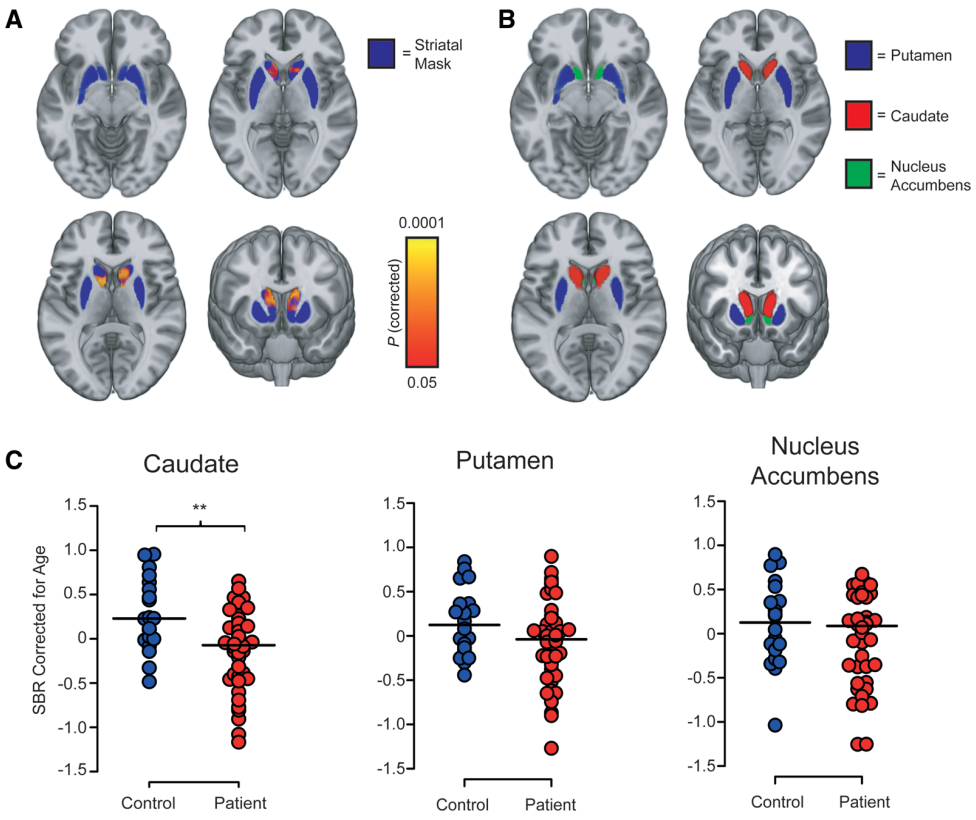


Figure 2: Figure from Jenkins et al., 2018 illustrating subdivisions of the striatum and striatal binding ratio (SBR) calculated from SPECT scans in TBI patients and controls. A. Significant voxelwise reductions in DaT observed in the caudate of TBI patients compared to controls. **B.** Striatal subdivisions **C.** Cross-sectional comparison of average DaT within striatal subdivisions between TBI patients and controls. Jenkins et al., 2018 Brain, Volume 141, Issue 3, March 2018, Pages 797–810,

1.6 Working memory

1.6.1 Incidence of working memory impairment after TBI

Working memory impairment is one of the most common deficits observed after TBI (McAllister et al., 2004). In studies of acute and chronic TBI, working memory impairments have been shown to be a core cognitive deficit in both mild and moderate-severe injuries (Mc Dowell et al., 1997; Christodoulou et al., 2001; McAllister et al., 2004). Importantly, abnormalities in working memory function have been shown to underpin deficits in other cognitive domains such as reasoning, attention and short-term memory (Leclercq et al., 2000; Park et al 1999). It is therefore unsurprising that working memory deficits can lead to long-term disability and poor functional outcomes in patients (Levin et al., 1978; McMillan et al., 1987; Cicerone et al., 2000). In an audit of a large cohort of patients attending our TBI outpatient clinic at St Mary's hospital (n=222), objective and subjective measures of working memory impairment were observed to be the most prevalent issues patients faced (Fig. 3). Impairments within working memory tasks were also found to be associated with poorer performance in executive function, reasoning and memory, reflecting similar findings to the literature.

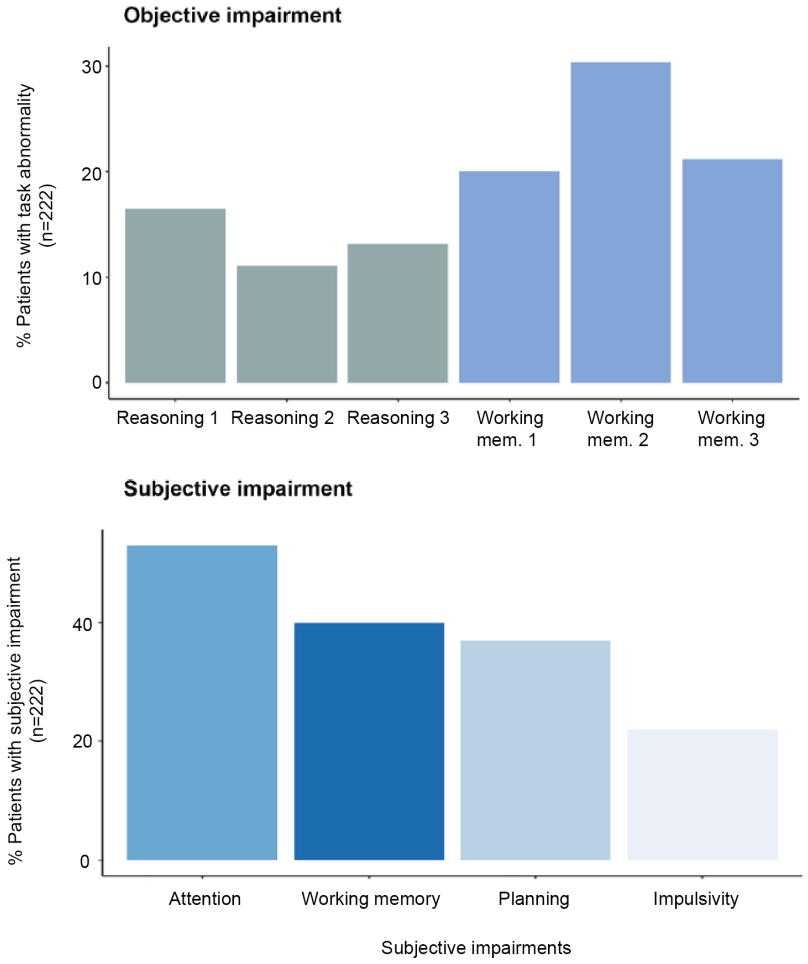


Figure 3: Percentage of objective and subjective impairments observed in 222 patients attending TBI outpatient clinic at St Mary's hospital. Objective impairment calculated as cognitive task score >-1.5 SD below healthy control cohort.

1.6.2 Definition of working memory and theoretical models

Working memory is defined as the ability to maintain and manipulate information temporarily in mind to perform complex behaviours (Miller et al., 1960; Coons et al., 1960; Atkinson & Shiffrin., 1968; Baddeley & Hitch., 1974; D'Esposito & Postle., 2015). In classical models of working memory (Fig. 4), this process was posited to be supported by a central executive system and two sub-systems known as the visuospatial sketchpad and articulatory loop (Baddeley & Hitch., 1974), whereby the visuospatial sketchpad was associated with the temporary storage of visuospatial

stimuli and the articulatory loop was involved in the temporary storage of verbal/numerical stimuli during working memory.

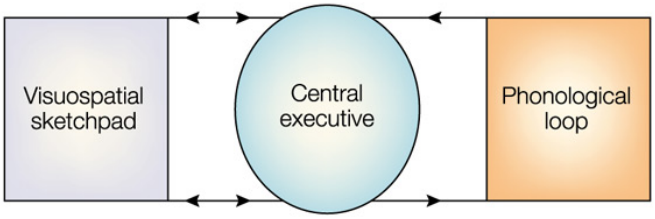


Figure 4: Figure illustrating the classical model of working memory as proposed by Baddeley. & Hitch (1974). Figure reproduced from Baddeley A. The episodic buffer: a new component of working memory?. Trends Cogn Sci. 2000;4(11):417-423

Several neuroimaging studies have supported the presence of such systems within the brain and demonstrated that visuospatial and verbal components of working memory utilise storage and active rehearsal processes to support the maintenance of information. In verbal working memory, evidence of a short-term phonological store and articulatory rehearsal system have been highlighted via the use of PET (Baddeley., 1992), whereby active rehearsal of digits or words is achieved by looping through stimuli in order to refresh the memory trace (Baddeley et a., 1992; Vallar et al., 1997, Baddeley., 2000). In visuospatial working memory, information is further divided into visual and spatial components for maintenance and rehearsal (Barton et al., 2007; Owen et al., 1996). Importantly, active rehearsal within these sub-systems has provided insights into the limited capacity nature of working memory by illustrating a balance between processing and storage within a limited resource system (Bays et al., 2008). As stimulus load increases, accuracy in working memory decreases as sub-systems struggle to rehearse before the memory trace decays (Katkov. Et al., 2014; Caplan et al., 1992; Della Sala et al., 1999; Ma et al., 2014).

Although maintenance is fundamental to working memory, the ability to manage processes and direct attention is also key. This has been suggested as a core role for what was described as the central executive system (Baddeley., 1998), as a means to plan and initiate effective cognitive strategies (e.g. rehearsal) during working memory. In dual-paradigm tasks, where increased load is applied due to the need to divide attention, reduced working memory performance is observed (McDowell et al.,

1997). Furthermore, in studies with high task rule complexity, widespread individual differences in performance are attributed to the failure of executive processes in working memory to manage and schedule the complex task rules for action (Duncan et al., 2008; Duncan et al., 2013). Deficits in working memory have therefore been suggested to be the result of impaired attentional and executive function processes. This is supported by the strong relationships observed between impaired performance on working memory and executive function tasks after TBI (De Simoni et al., 2018; McAllister et al., 2009; Caeyenberghs et al., 2014).

Although neuroimaging has provided evidence in support of the systems described in the classic Baddeley model of working memory, it has also highlighted its limitations in fully describing the broad processes implicated in working memory. Numerous studies of working memory demonstrate the utilisation of long-term memory (LTM) and synthesis of different types of information for success, resulting in newer models to be defined. For example, in visuospatial working memory tasks, the identification of an object relies upon LTM whilst the ability to correctly remember the spatial location of each object during a task relies upon the ability to combine different types of information into a single representation for response (Lewis-Peacock et al., 2008). The proposal of an additional system known as the “episodic buffer” was therefore made, whereby information from different sources could be bound together to create new representations for problem solving (Baddeley., 2000; Wheller & Treisman., 2002; D’Esposite & Postle., 2015) (Fig. 5). This multicomponent model of working memory has remained a prominent theoretical framework for many years, illustrating the fundamental role of working memory in supporting other complex behaviours such as reasoning (Hampshire et al., 2012; Petrides et al., 1993).

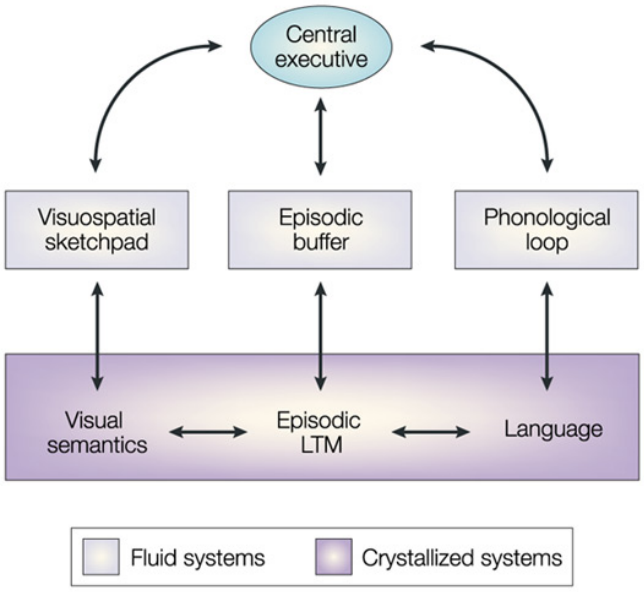


Fig 5: The multicomponent model of working memory as defined by Baddeley, 2000. Figure reproduced from Baddeley A. The episodic buffer: a new component of working memory?. *Trends Cogn Sci*. 2000;4(11):417-423.

1.6.4 Moving beyond classical models of working memory

Recently, more nuanced models of working memory that encompass the features of a multi-component framework within a more holistic perspective of brain function have been proposed (D'Esposite & Postle., 2015). Although earlier research was suggestive of distinct aspects of working memory mapping to distinct regions in the brain, the emergence of network neuroscience has challenged this view, instead supporting more state-based models of working memory. Neuroimaging studies have demonstrated that working memory is associated with vastly distributed regions in the brain both cortically and sub-cortically, inclusive of the frontal, parietal and superior temporal lobes as well as the basal ganglia (Cohen et al., 1997; Owen et al., 1999; Fletcher & Henson 2001; Cabeza et al., 2000, Rottschy et al., 2011) (Fig. 6). More recently, evidence of the role of the cerebellum in working memory has begun to emerge with increased activation associated with increased load (Chen & Desmond., 2005a,b). Modern neuroimaging studies have therefore begun to demonstrate that the multiple dimensions of working memory are in fact supported by widespread functional networks that have variable spatial patterns of activation but with common overlapping regions within the brain.

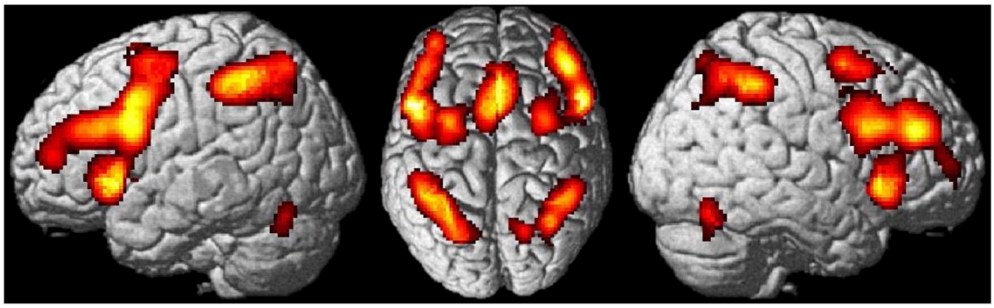


Figure 6: Overlapping voxels derived from meta-analysis of working memory task activation maps across 189 fMRI studies of healthy individuals (Rottschy et al., 2011). Figure reproduced from Rottschy C, Langner R, Dogan I, et al. Modelling neural correlates of working memory: a coordinate-based meta-analysis. *Neuroimage*. 2012;60(1):830-846.

State-based models posit that the short-term maintenance of information during working memory is supported by internal mental representations of stimulus that are controlled via focused attention. In this way, different states of dynamic brain activation across multiple regions in the brain for different types of stimulus (e.g. semantic versus perceptual) are established and brought into "conscious awareness" during working memory through selective attention. For semantic working memory tasks, state-based models propose that long-term memory is accessed in order to first recognise the stimulus (e.g. word, digit or letter). These stimulus representations are subsequently held in mind (maintained) via increased activation until no longer needed, whereby the focus of attention controlling this state shifts.

This theory is supported by a number of behavioural studies in which the reaction time of stimulus recognition during working memory is impacted by the inclusion of a cue that details which subset of stimuli will be probed after a maintenance period (Oberauer et al., 2001; Oberauer et al., 2002; Oberauer et al., 2005). In sensorimotor state-based models, it is posited that the systems involved in the perception of this type of information (e.g. colours, orientations, auditory pitches) are likely to be employed during the short-term maintenance of the same type of information. Several studies have illustrated support for this by demonstrating activation within the brain that reflect stimulus-specific states (Magnussen., 2000; Magnussen & Greenlee., 1999; Zaksas et al., 2001) such as additional activation in regions classically associated with language during verbal working memory tasks (Paulesu et al., 1993)

and activation of regions associated with spatial and visual processing during visuospatial tasks (Salmon et al., 1996).

In a recent study by Soreq et al., 2019, machine learning techniques were employed to demonstrate that different working-memory domains (e.g. stimulus type) and processes (e.g. encode, maintenance and response) could be accurately classified on the basis of multivariate connectivity patterns. They demonstrated that working memory is supported by dynamic connectivity within the brain that reflects transient brain states (often with overlapping regions) in response to the varied information and demands required across a number of working memory tasks (Fig. 7). This work provided unique insights into the neural mechanisms of working memory that support state-based models (D'Esposito & Postle., 2015) and help to consolidate the vast literature highlighting variations and commonalities in regional activation across working memory tasks.

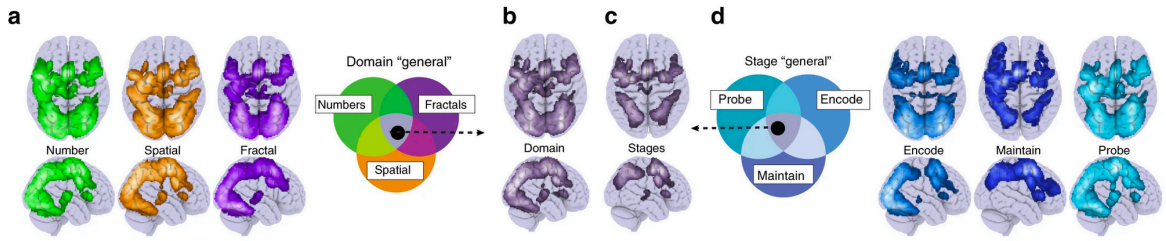


Figure 7: Figure from. Soreq et al., 2019 demonstrating multivariate connectivity patterns across working memory tasks and processes. A. Activation commonalities across stimulus type working memory tasks. **B.** Domain general activation map. **C.** Subset of voxels from within the domain general map that were activated during all stages of working memory tasks (e.g. probe, encode, maintain). **D.** Activation commonalities during the three stages of working memory tasks. Figure reproduced from Soreq, E., Leech, R. & Hampshire, A. Dynamic network coding of working-memory domains and working-memory processes. *Nat Commun* **10,** 936 (2019). https://doi.org/10.1038/s41467-019-08840-8

Although numerous theoretical models of working memory exist, there is consistency in regard to the fundamental building blocks associated with this complex behaviour. Namely that attentional and executive processes are integral to its function and hierarchical in nature, eliciting top-down control to the brain states employed for the active maintenance and manipulation of different stimulus types for different task demands. Most importantly, however, is the converging evidence that working

memory encompasses a broad range of cognitive processes integral to human intelligence (Oberauer et al., 2003; Barbey et al., 2013; Duncan et al., 2012), and that the study of its impairments can help us to understand the complex relationship to other higher-order cognitive processes to improve patient outcomes after TBI.

1.7 The neural basis of working memory impairment after TBI

1.7.1 Grey matter lesions and working memory impairment

Lesions to the dorsolateral prefrontal cortex (DLPFC) have been shown to impact upon the ability to organise and monitor information during working memory, leading to deficits (Petrides., 1995, Petrides & Milner., 1982, Barbey et al., 2013). More generally, damage to the prefrontal cortex (PFC) has been associated with impairments to executive function, selective attention and working memory, supporting the notion that such cognitive processes are not independent of one another (Duncan., 2001). Indeed, it has been demonstrated that the PFC is part of a wider multiple demand system which is employed in a range of different cognitive tasks (Duncan et al., 2010) with a particular role in eliciting top-down control for attending to and selecting the relevant information for working memory (Postle., 2006; Lara & Wallis., 2015). The PFC has therefore been implicated as a particularly important region for working memory, whereby lesions can result in severe impairments. In contrast, lesions to grey matter outside of the PFC have demonstrated weak associations to working memory impairments after TBI. From a network neuroscience perspective, this may reflect the resilience of working memory networks to lesions in brain regions (nodes) (Aerts et al., 2016), as processes are generally not reliant upon a single anatomical region (Soreq et al., 2019). However, this resilience may fail when damage to hierarchically important nodes or hubs such as the PFC occurs (D'Esposito et al., 2006; Fagerholm et al., 2015) which are central to managing the complex processes employed during working memory (Duncan et al., 2001).

1.7.2 TAI and working memory impairment

In contrast to grey matter alterations, traumatic axonal injury has been consistently related to working memory impairments (Hellstrom et al., 2013; Palacios et al., 2012). Alterations to white matter integrity as quantified using fractional anisotropy (FA) have illustrated widespread correlations to a number of visuospatial and verbal working memory task deficits (Palcios et al., 2012; D'all Acqua et a., 2017; Fagerholm et al., 2015). Previous literature has provided a patchwork of results, by demonstrating associations between numerous white matter tracts and working memory impairment after TBI. For example, damage to large white matter tracts such as the corpus callosum, superior longitudinal fasciculus, corona radiata and medial forebrain bundles are commonly implicated in working memory impairment (Palcios et al., 2011; Vestergaard et al., 2001; Owens et al., 2016). These findings may on the one hand reflect the heterogeneity of damage across patients, or on the other, represent correlational analyses that assess only one aspect of working memory (Ackerman et al., 2005) from specific regions which are in fact part of a wider structural connectome underpinning working memory (Caeyenberghs et al., 2016).

As the understanding of functional networks and their relationship to structure has progressed, studies investigating the structural connectomes that support working memory have emerged (Palacios et al., 2011). Structural dysconnectivity via TAI has been posited to result in a degradation in the efficiency of information flow across cognitive networks (Hillary et al., 2014) that in turn leads to functional abnormalities and impairment (Palacios et al., 2001; Pandit et al., 2013; Caeyenberghs et al.,2016). The recent application of graph theory has helped to support this theory by illustrating that structural dysconnectivity alters network topology, moving away from an optimal small-world architecture to a less efficient topology that hinders information processing (Sporns et al., 2006; Bassett et al., 2006; Hillary et al., 2014 ;Pandit et al., 2013). Importantly, studies of TBI using graph theory have shown variable effects of structural dysconnectivity upon higher-order cognition dependent upon the nodes it impacts (Fagerholm et al., 2015; Hillary et al., 2014). This provides a promising avenue for exploring the variability of working memory deficits within patients in the context of different patterns of network dysconnectivity.

1.7.3 Dopamine abnormalities and their association to working memory impairment

Dopaminergic abnormalities after TBI are commonly associated with working memory impairment (Bales et al., 2008; Manktelow et al., 2017; Lan et al., 2019). Animal studies have provided some insights into the potential mechanisms of impairment by highlighting the neuro-modulatory role of dopamine upon the PFC. In studies of primates, the use of dopaminergic antagonists to mimic hypodopaminergic states similar to TBI have resulted in spatial working memory deficits that are attributed to altered function in the PFC (Arnsten et al., 1998). Similarly, local depletion of dopamine within the PFC via perfusion has demonstrated spatial working memory deficits in rats (Brozoski et al., 1979). In contrast, increases to dopaminergic levels via pharmacological interventions have been shown to improve spatial working memory in older primates with dopamine depletion (Arnsten et al., 1994) and alter BOLD activity within the PFC during working memory tasks in humans (Fallon et al., 2017).

The relationship between working memory and dopamine can be understood as a result of striatal dopamine modulating function in the PFC via cortico-striatal connectivity (Fallon et al., 2017). Neuroimaging studies of the neurocircuitry of this system have illustrated that dopaminergic neurons from the midbrain project to the PFC via the meso-cortical dopamine pathway (Williams et al., 1998; Ott & Neider., 2019). Disruption to these cortico-striatal circuits by either altered endogenous dopamine or loss of dopaminergic signalling due to axonal injury would therefore impact upon working memory network function. In studies of TBI, disruption to these cortico-striatal circuits both functionally and structurally (De Simoni et al., 2018; Jenkins et al., 2018) have been observed and associated with impaired executive functioning processes and working memory (De Simoni et al., 2018; Jenkins et al., 2018). The use of methylphenidate to compensate for dopamine depletion after TBI has provided some promising results in the treatment of working memory impairments, although these are limited (Manktelow et al., 2017; Jenkins et al., 2019).

1.8 Current limitations in the prediction and treatment of working memory impairment after TBI

1.8.1 The need for better diagnostics within the clinical setting

Long-term working memory impairments in patients with otherwise normal MRI and CT imaging is not uncommon within a clinical setting. Functional disability may explain a proportion of these cases (Fann et al., 1995), however the application of DTI in TBI research suggests accurate diagnosis of axonal injury is lacking (Hellstrom et al., 2013). Evidence of microstructural white matter changes in individuals with otherwise normal imaging suggest that patients may be incorrectly diagnosed as without DAI, impacting upon the type of care they receive post-injury. By utilising DTI measures within the clinical setting, a more accurate method to diagnose axonal injury can be applied, whereby microstructural changes to white matter are quantified within individual patients to identify those at risk of developing working memory impairments. Part of this thesis therefore attempts to address this current limitation and provide a practical tool for clinicians.

1.8.2 The need to account for individual differences to improve prognosis

Prediction of working memory impairment after TBI is currently difficult and is due to the heterogeneity in damage observed across patients. The broad heuristic that the presence of DAI increases the likelihood of impairment is useful but not accurate at the individual level. Currently, there is a need to develop prognostic markers of working memory impairment that can account for individual variability in white matter damage. This can be achieved by first identifying the patterns of white matter damage that are associated with working memory impairment after TBI and assessing how well these patterns are able to predict working memory. This is particularly important at the acute phase of injury where more accurate predictions may help to inform the types of care patients receive after discharge from hospital.

1.8.3 The need for multimodal imaging to tailor treatments for working memory impairment

As described in a number of studies, abnormalities within the brain after TBI are complex and not restricted to a single system. Research has suggested that systems are not impacted uniformly at the point of injury and damage to one system within the brain (e.g. white matter) may result in a proliferation of damage to other systems within the brain (Werner., 2007; McKee & Daneshvar., 2015). Attempts to understand this complex relationship have been the focus of much research in the hopes of finding effective therapeutic targets for working memory impairments (Scott et al., 2018; Manktelow et al., 2017; Li et al., 2019; Jenkins et al., 2019). Multimodal neuroimaging has begun to provide a means to examine the impact of TBI across numerous structural and functional systems within patients in an attempt to understand their interaction with one another after injury. This holistic picture may be particularly useful in the context of predicting whether pharmacological interventions such as methylphenidate will be successful. Without the use of multimodal imaging, tailoring treatment to individual patients to increase its efficacy will remain challenging (Maas et al., 2014).

This thesis therefore attempts to explore and improve the current limitations in the prediction and treatment of working memory impairment after TBI. My research aims to tackle three key areas that currently limit the management of working memory impairments after TBI and seeks to provide practical tools for use within a clinical setting (Fig. 8).

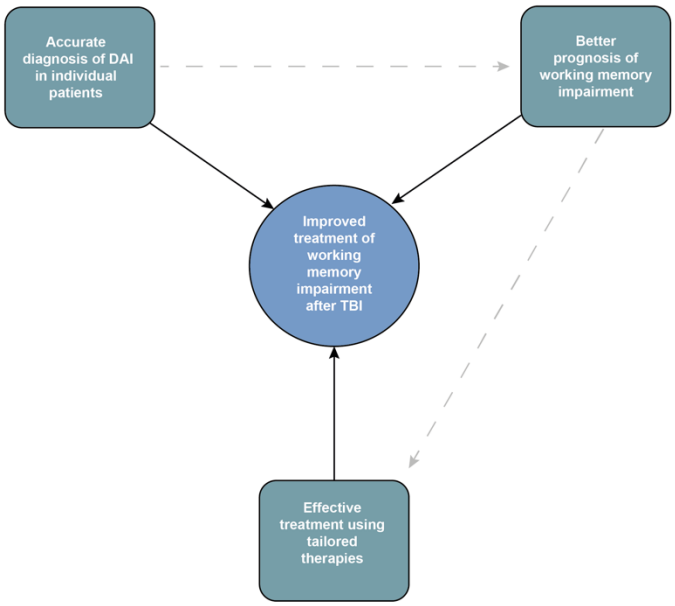


Figure 8: Overall thesis themes and their role in improving the treatment of working memory impairment after TBI. Black arrows demonstrated primary impact. Grey dashed arrows represent the secondary benefits and relationships between each theme of the thesis.

Chapter 2

Materials and Methods

In this chapter, I describe the materials and methods used within my thesis. I describe the methods used to assess cognition in TBI as well as the neuroimaging techniques implemented to quantify structural and functional changes in the brain in this population. I also detail some of the statistical methods implemented in the remaining chapters.

2.1 Assessing cognition in TBI

2.1.1 Classical neuropsychology testing

A battery of standard pen and paper neuropsychological tests were performed by TBI patients and controls to assess cognitive function across a range of domains broadly associated with intellectual function, reasoning, memory and executive function in chapters three and four. These tests have previously been used to assess cognitive function in TBI (Jilka et al., 2014; Kinnunen et al., 2011) and include:

1. The Wechsler Test of Adult Reading (WTAR) (Weschler, 1945)
2. Matrix reasoning subtest from the Weschler Adult Intelligence Scale (WAIS-III) (Weschler, 1945)
3. The peoples test (PT) from the Peoples and Door Test (Weschler., 1945)
4. The logical memory subtest of the Weschler memory scale (Weschler, 1945)
5. The colour-word interference (Stroop) test from the Delis-Kaplan executive function system (DKEFS, Delis et al., 2004)
6. The Trail-Making Test (Partington & Leiter., 1949)

2.1.1.1 WTAR

The WTAR is designed to measure premorbid levels of intellectual ability in individuals aged between 16 to 89 years. This test comprises of a list of 50 words that have atypical pronunciations in order to prevent individuals being able to employ strategies associated with standard pronunciation rules. The greater the number of words correctly pronounced by individuals, the higher the premorbid intellectual function is assumed to be. Evidence suggests that reading recognition remains relatively intact after TBI and is therefore used as a premorbid marker in patients (Weschler., 1945).

2.1.1.2 Matrix reasoning

The Matrix reasoning subtest from the WAIS-III is designed to measure abstract reasoning and problem solving. This test consists of 26 trials of increasing difficulty to

solve. Each trial consists of a 2x2 grid, where three out of the four squares contain a shape. Individuals must choose from one of five shapes presented below to complete the grid on the basis of rules inferred from the other shapes presented. An example of this task is shown below (Fig. 9). A point is awarded for each correct trial, such that the higher the score, the stronger an individual's abstract reasoning/fluid intelligence abilities are assumed to be.

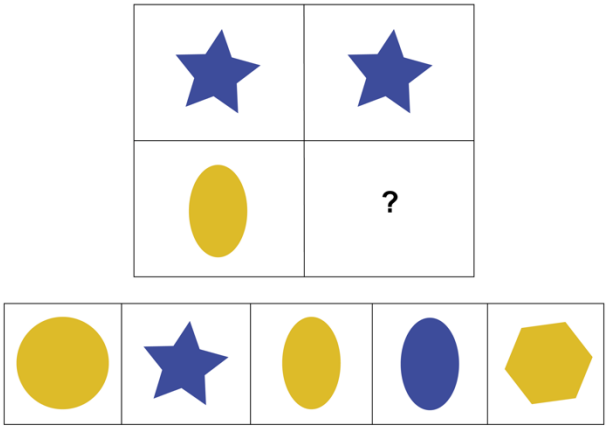


Figure 9: Example trial from the Matrix Reasoning subtest from the WAIS-III (Weschler., 1945). Top panel represents matrix to complete. Bottom panel consists of shapes that can be used to fill matrix inclusive of one correct and four foils.

2.1.1.3 The Peoples Test (from the Peoples and Doors Test)

The Peoples Test is designed to measure long-term memory with verbal recall. In this test, individuals are presented with pictures of four people and are told their profession and name. After a short delay, individuals are asked to verbally recall the name for each of the four individuals they were shown, as prompted by their profession (e.g. "What was the name of the doctor?"). This process is completed three times to allow for learning. After an extended delay period (~20 minutes) patients are asked to recall the names of each of the four people to measure forgetting.

2.1.1.4 Logical Memory test

The logical memory test is designed to measure memory encoding using verbal recall. Individuals are read a short story and asked to repeat back in as much detail as

possible both immediately and after a delay (~20 minutes). Individuals are read two different stories (logical memory subtests 1 and 2). Points are awarded for specific words recalled in the story. A forced choice recognition trial is also performed after the long delay to investigate recognition. The higher the scores the better the immediate and delayed memory performance an individual has.

2.1.1.5 Colour-Word Interference Test (DKEFS)

The Colour-Word Interference Test is a measure of executive function based on the classic Stroop effect (Stroop., 1935). This test comprises of four trials of increasing difficulty (Fig. 10). In trial 1, individuals are asked to name the colour of panels of squares (e.g. green, red, blue, red). In trial 2, individuals are asked to read words aloud that describe colours (printed in black ink). In trial 3, the Stroop paradigm is introduced whereby individuals must name the colour of the ink that the word is written in. In this trial, the word describing a colour is incongruent to the ink colour it is printed in. In trial 4, a switching rule is introduced, where individuals must perform the same rule as trial 3 (naming the ink colour of a word) except where a word is framed in a box. When a word is inside of a box, they must read the actual word, rather than name the ink colour it is printed in.

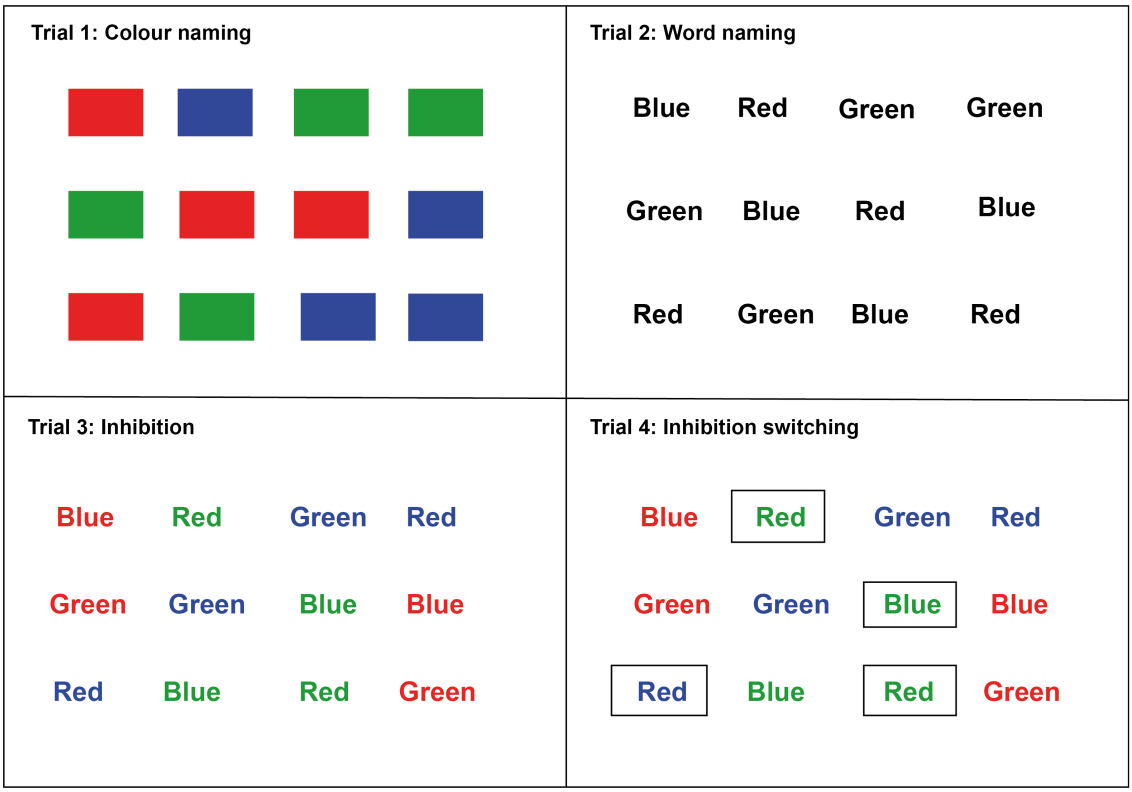


Figure 10: Example of the four trials included within the colour-interference test from the Delis-Kaplan executive function battery (DKEFS). Trials 1-2 represent baseline measurements of colour-naming and word reading. Trial 3 introduces Stroop effect testing inhibition and Trial 4 includes and additional task switching rule.

The faster the time to complete this task without errors the better executive function abilities are assumed to be. Contrasts between trial times are also made to determine the cost of inhibiting responses (the stroop effect) and task switching. These are calculated as:

$$\text{Baseline} = \frac{(\text{Colour naming} + \text{word reading})}{2}$$

$$\text{Inhibition} = \text{Inhibition (trial 3)} - \text{Baseline}$$

$$\text{Switching} = \text{Switch (trial 4)} - \text{Baseline}$$

$$\text{Inhibition Vs, Switching} = \text{Switching} - \text{Inhibtion}$$

2.1.1.6 The Trail Making Test

The Trail Making Test is designed to measure information processing and executive function abilities. This test comprises of two trials, the first using only numbers ranging from 1-25 whilst the second includes both letters and numbers (Fig. 11). On trial A, individuals must draw a line between the numbers in ascending numerical order, starting from 1-2-3 and so on until the end. On trial B, individuals must connect numbers and letters in ascending order by switching between a number to a letter until the end (e.g. 1-A-2-B-3-C). If an individual makes an error, they are guided back to the last correct point in the sequence and asked to resume from there. The faster the completion time, the greater information processing performance in trial A and executive function ability in trial B is assumed to be. To control for individual differences in information processing when examining executive function, times from trial A are subtracted from times from trial B as an additional contrast measure of executive function.

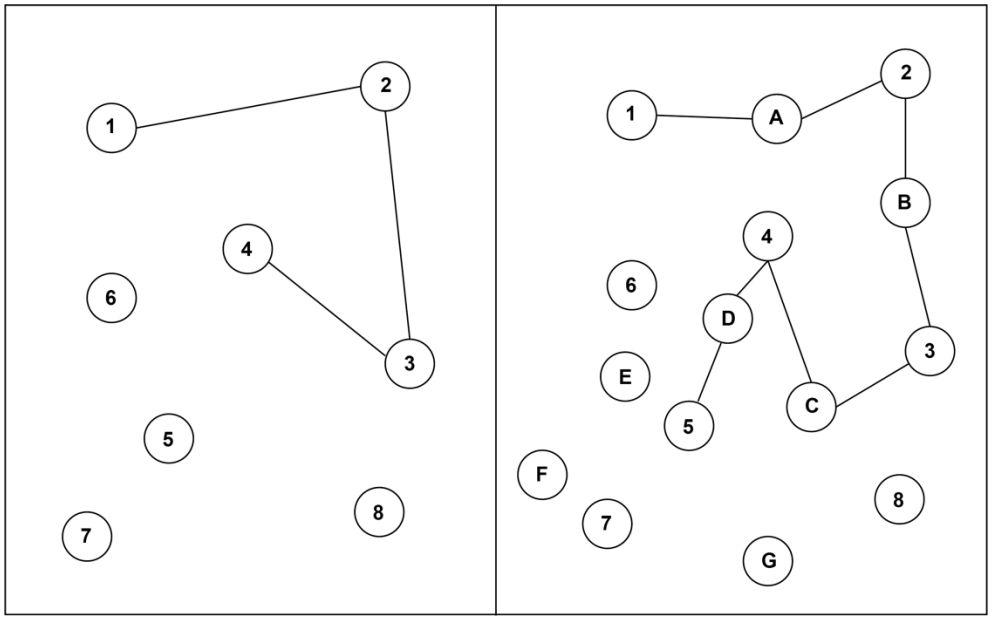


Figure 11: Example of Trail Making Tests Part A and B. Left panel represents trail making test A, connecting circles in ascending numerical order. Right panel represents trail making test part B, were circles must be connected by switching between numbers and letters in ascending order.

Although no explicit working memory tasks are included in the classical pen and paper neuropsychological tests employed, a number of executive function tasks are. Executive function has been shown to be a core cognitive process associated with

working memory in healthy individuals and TBI patients (McDowell et al., 1997; Osaka et al., 2004) and may therefore be complimentary to working memory task assessments. Furthermore, this battery was included to determine whether performance on novel computerised tasks captured the same cognitive variance as classical neuropsychological tests, aiding interpretation and assessing the potential clinical utility of computerised measures.

2.1.2 Computerised cognitive testing

Computerised cognitive testing of TBI patients and healthy controls was performed using an Ipad with a custom app developed by Dr Adam Hampshire in chapters three, four and six. The tasks included are well described in two large internet-based control cohorts of healthy individuals (Hampshire et al., 2012, Daws et al., 2017, n>44600) and have been investigated using task-fMRI (Hampshire et al., 2012). Six computerised cognitive tasks were used and included:

1. Monkey Ladder (MKL), a visuospatial working memory task based on primate research (Inoue and Matsuzawa., 2007).
2. Paired Associates Learning (PAL) an object-spatial version of the binding paradigm that has previously been used in other clinical populations (Gould *et al*., 2005) and in TBI patients with post-traumatic amnesia (PTA) (De Simoni *et al*., 2016).
3. Self-Ordered Search (SOS) a visuospatial working memory task developed from behavioural measures of strategy in searching (Collins *et al*., 1998).
4. Feature Match (FTM) based on a classical feature search task used to measure attentional processing (Treisman and Gelade., 1980).
5. Odd One Out (OOO) a deductive reasoning task based on a subset of problems from the Cattell culture fair intelligence test (Cattell., 1949).
6. Hampshire Tree Task (HTT) a spatial planning task designed by Dr Hampshire and related to the Tower of London Task (Shallice., 1982).

2.1.2.1 MKL

In the MKL, squares containing numbers are displayed on screen in random locations on an invisible 5x5 grid (Fig. 12). After a short period of time, the numbers disappear but the squares remain. Individuals are required to remember the location of the numbers and respond by pressing on the blank squares in ascending numerical order where the numbers were. If the participant answers correctly, the next trial increases the number of squares by one. If they answer incorrectly, then there is one less square. The task starts at a difficulty level of two squares. The main outcome measure is the average number of squares achieved. Mean population performance is 7.85, 1.154 S.D.

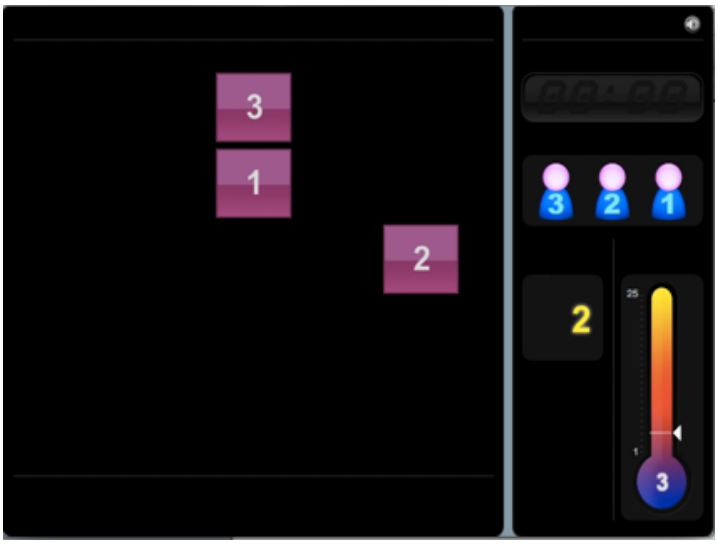


Figure 12: Example of computerised Monkey Ladder (MKL) task and graphics presented on Ipad. To the right, three lives are presented. Each error results in the loss of one of the lives. The thermometer represents the current score achieved. The left panel demonstrates the MKL task encoding phase, where numbers are presented for a short period of time before disappearing.

2.1.2.2 PAL

In the PAL task, boxes are displayed at random locations on the screen in an invisible 5x5 grid and reveal one at a time an image that is within them (Fig. 13). Once all images have been revealed and subsequently hidden, an object that matches one of the concealed objects is displayed. Individuals must select which box the matching object is hidden in. If the participant answers correctly, the next trial has one more

square. If they answer incorrectly, then there is one less square. The task starts at a difficulty level of two squares. The main outcome measure is average number of squares achieved. Mean population performance is 5.28, 1.13 S.D.

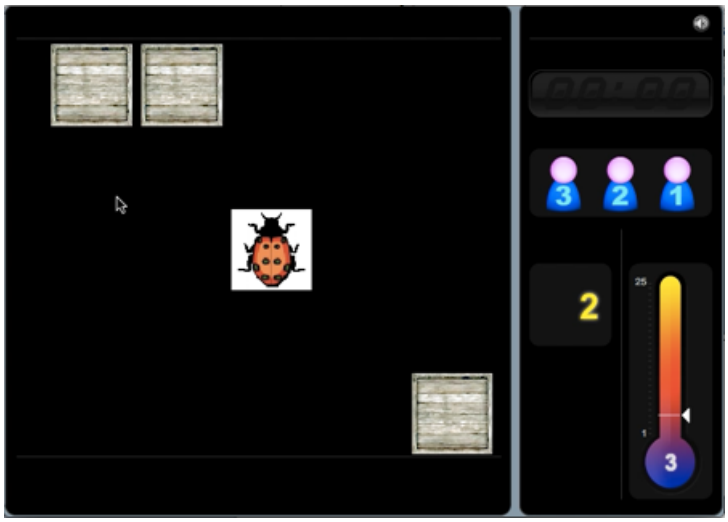


Figure 13: Example of Paired Associates Learning (PAL) task and graphics presented on Ipad. Right panel displays the number of available lives which reduce for each error made. The thermometer represents the current score achieved. The left panel represents the stimulus screen where images are presented one by one inside each of the boxes.

2.1.2.3 SOS

In the SOS task, boxes are displayed on the screen at random locations in an invisible 5x5 grid (Fig. 14). Individuals need to search through boxes by clicking on them to collect hidden tokens. A token will not appear in the same box twice on a trial and the participant must continue to search through the boxes until all tokens have been found in every box. If an individual searches a box that has previously revealed a token or searches the same empty box before finding a token, they will incur an error. If the participant answers correctly, the next trial has one more square. If they answer incorrectly, then there is one less square. The task starts at a difficulty level of four boxes (minimum task level=two boxes). The main outcome measure is the average number of boxes achieved. Mean population performance is 8.23, 2.1 S.D.

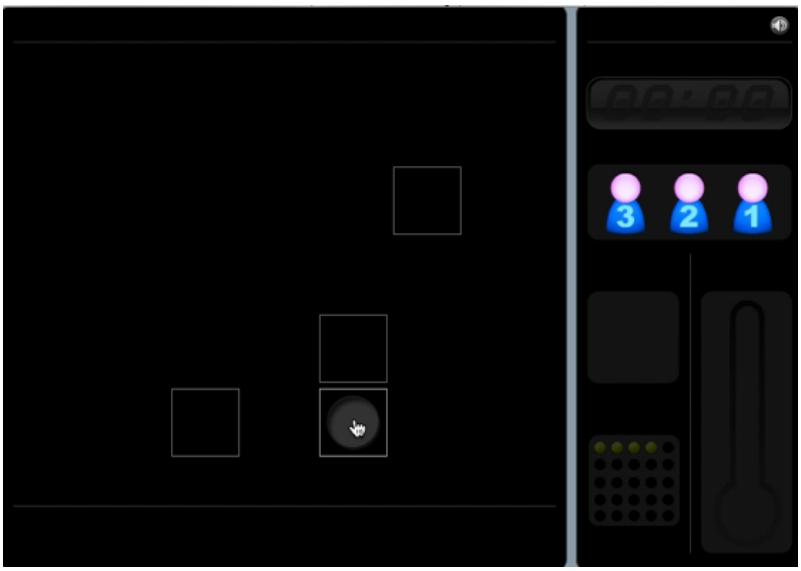


Figure 14: Self Ordered Search (SOS) task and graphics presented on the Ipad. The right panel displays the number of lives left (out of three) as well as the number of tokens already collected during the trial as highlighted by the yellow dots being highlighted for each token collected. The left panel represents the stimulus screen where clicking on each box either reveals a token (a yellow dot) or no token (a grey dot).

2.1.2.4 FTM

In FTM, two grids are displayed in parallel each containing a set of shapes. In half of the trials, the grids differ by one shape (Fig. 15). The participant must decide whether the two grids are identical or different by selecting match or mismatch response button. Participants must solve as many problems as possible in 90 seconds. If the response is correct, the total score increases by the number of shapes prese4nted in the grid and the number of shapes presented in subsequent trials increases. If a participant makes an error the total score decreases by the number of shapes in the grid and the subsequent trials have fewer shapes than the previous trial. The first trial of grids contains on two shapes each. The main outcome measure is the total score achieved after 90 seconds. Mean population performance is 131.35, 32.79 S.D.

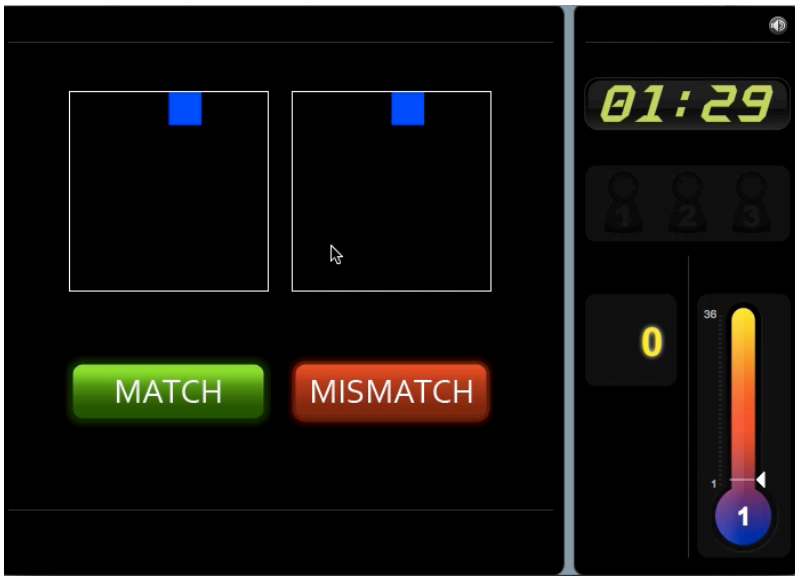


Figure 15: Feature Match (FTM) task and graphics presented on the Ipad. The right panel represents the amount of time left to complete the task, whilst the thermometer displays the current score achieved. The left panel represents the stimulus and response screen where individuals much either press Match or Mismatch depending on whether they believe the two shapes presented above are identical or not.

2.1.2.5 OOO

In OOO, a 3x3 grid of objects is displayed. The objects displayed contain a variable number of copies of a coloured shape. (Fig. 16). The features that make up the object in each cell of the grid (colour, shape, number of copies) are related to each other based on a set of rules. The participant must identify the rules that relate the object features and select the one cell whose contents do not correspond to those rules. The participant must solve as many problems as possible in 180 seconds. If the response is correct, the total score increases by one point and the next problem is more complex. If the response is incorrect, the total score decreases by one point. The outcome measure is the total score achieved in 180 seconds. Population mean=10.43, 3.31 S.D.



Figure. 16: Odd One Out (OOO) task and graphics as presented on the Ipad. The right panel represents that amount of time left whilst the thermometer indicates the current score achieved. The left panel demonstrates the stimulus presented. Individuals must tap on the shape they determine is the odd one out on the basis of rules inferred from the panel (e.g. number, colour, shape or combination of these factors).

2.1.2.6 HTT

In HTT, a tree shaped structure containing numbered beads is displayed. Participants must rearrange the beads so that they sit in ascending numerical order on the tree running from left to right and top to bottom (Fig. 17). The beads are highlighted as red when in an incorrect position and are green when located in the correct position on the tree. Participants must solve as many problems as possible in as few moves as possible within 90 seconds. Problems become progressively more difficult with the total number of moves required and complexity of planning increasing in each trial. Trials are aborted if the participant makes more than twice the number of moves required to solve the problem. After each trial, the score is increased by adding the minimum number of moves required multiplied by two, minus the number of moves actually made. This allows for efficient planning to be rewarded. The first trial can be solved in three moves. The outcome measure is the total score achieved after 90 seconds. Population mean is 32, 10.19 S.D.

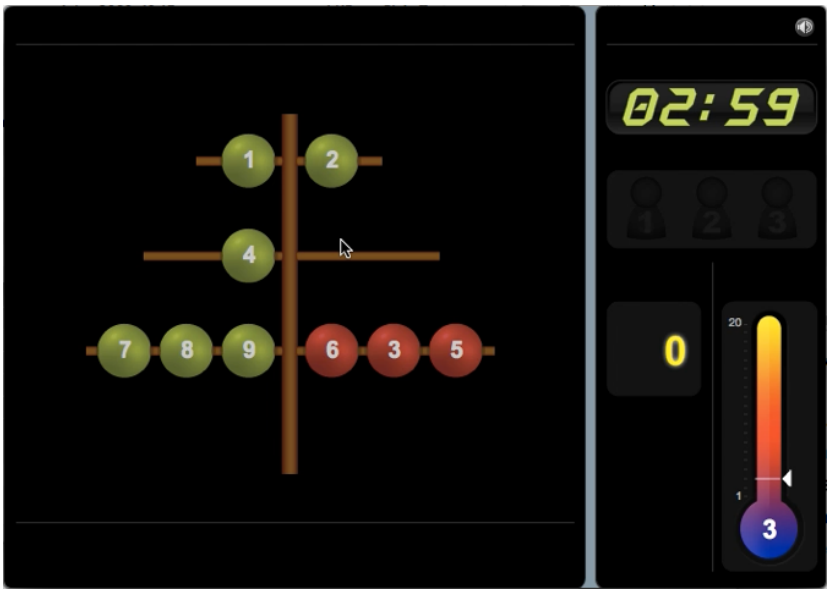


Figure 17: Hampshire Tree Task (HTT) and graphics as presented on the Ipad. The right panel presents the amount of time left as well as the current score achieved. The left panel demonstrates the problem to be solved. Individuals must tap on a ball and then tap to where they would like to move it. When a ball is in the correct location it will turn green, otherwise it remains red.

2.1.3 Modified Paired associates learning task

As part of a wider study, computerised cognitive tasks were refined, and graphics updated on the basis of patient feedback and assessment of sensitivity to impairments in the TBI population. This resulted in the selection of the PAL as an outcome measure for a longitudinal study of a subacute TBI population recruited from St Mary's hospital major trauma centre. The data from this is presented in chapter five. The paradigm of the PAL did not change (e.g. the rules, starting difficulty level and scoring), however the graphics and instructions given to patients did. Instructions were re-worded and presented in a sequential manner alongside a GIF of the task being performed. The graphics of the task were updated to include new background colours, objects and a larger grid surface area for object presentation (Fig. 18). Furthermore, the PAL was tested using a different tablet (a Galaxy Samsung Tablet A, 32Gb). Alterations to the task and device may therefore make comparison between previous PAL data challenging, until within-subject comparisons across the tasks are made and effects quantified. Therefore, no comparisons between the two versions of this task are made for this thesis.

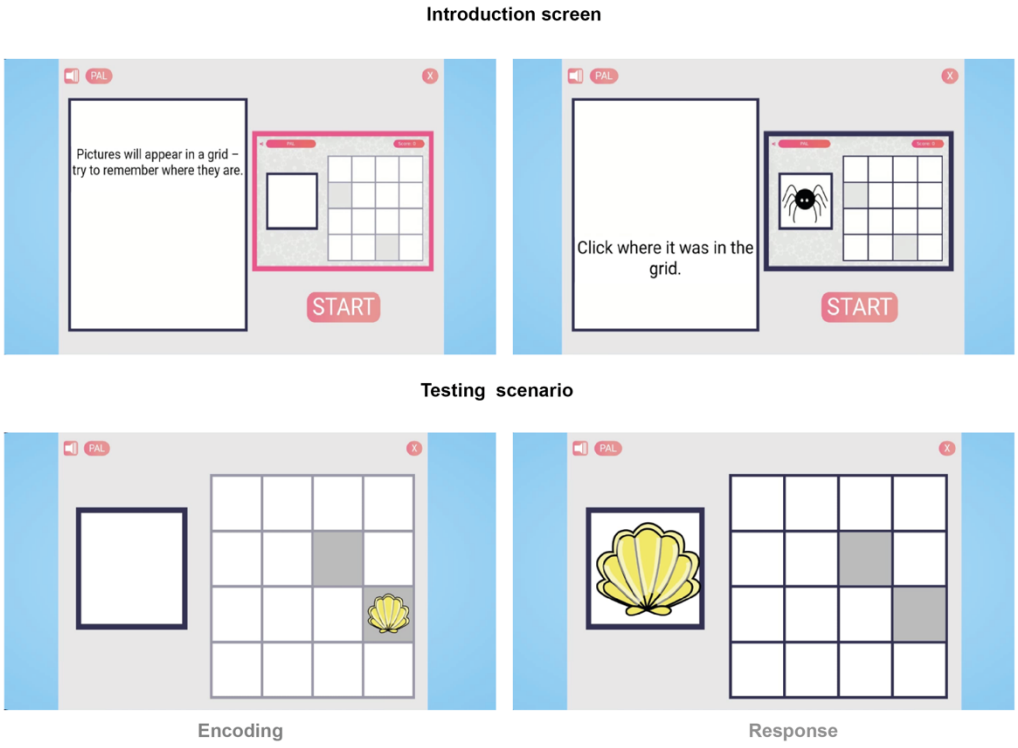


Figure 18: Modified PAL task graphics. Introduction screen demonstrates sequential presentation of instructions with gif. Testing scenario demonstrates updated encoding and response screen along with new objects and clearer spatial grid.

2.2 Imaging structural and functional changes in the brain after TBI

2.2.1 Principles of MRI

MRI is achieved through the measurement of magnetic fields associated with the movement of hydrogen atoms located in the water of cells within the human body. In water, hydrogen ions are positively charged (e.g. they have a greater number of protons than electrons) meaning that the constituent parts of their nuclei demonstrate "spin" properties. In simplest terms, a hydrogen nuclei's "spin" creates a magnetic moment that in turn produces a magnetic field, possessing north and south poles that align to the axis of its rotation. When an external magnetic field is applied such as to

the brain via MRI, hydrogen nuclei align to the direction of this field, and precession (rotation) around its axis occurs in a similar manner to gyroscopes (Fig. 19).

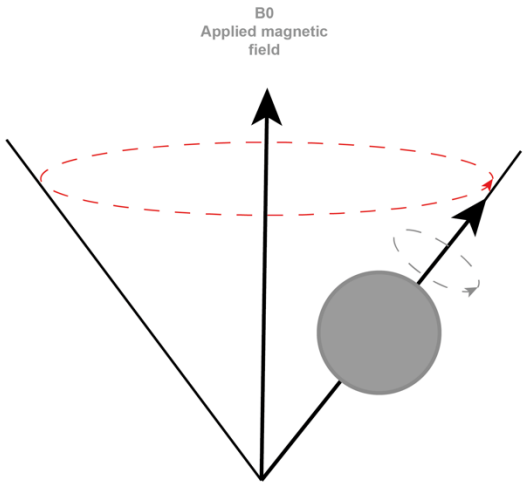


Figure 19: Example of hydrogen nuclei alignment to external magnetic field and precession properties. Grey sphere represents hydrogen nuclei. Grey dashed line represents spin property of hydrogen nuclei. Red dashed line represents precession of nuclei around magnetic field axis.

This property is termed the Larmour precession (or Larmour frequency, $\omega 0$) and refers to the velocity at which the nuclei rotates around the external magnetic field axis. The Larmour frequency proportional to the applied magnetic field strength.

Larmour frequency : $\omega 0 = \gamma B0$

Where γ is the gyromagnetic ratio and B0 is the strength of the applied magnetic field.

In neuroimaging, the head is placed into a uniform magnetic field to induce alignment of the hydrogen nuclei within the brain, parallel to the external field. Next, a radio-frequency pulse equal to the Larmour frequency is applied perpendicular to the magnetic field in short pulses (microseconds), causing the magnetic moment (e.g. the magnetic strengths and orientation of nuclei) to move away from the aligned axis. As the radio-frequency is removed, the nuclei realign, enabling the net magnetic moment to become parallel with the magnetic field again. This process is referred to as relaxation, during which the hydrogen nuclei lose energy and emit their own radio frequency known as the free-induction decay (FID) response signal. To improve

signal-to-noise ratio (SNR), multiple RF pulses will be used during acquisition to obtain numerous FID response signals which are then averaged. These signals are measured by a conductive coil placed around the head and are subsequently reconstructed into a 3D grey-scale MR image using a Fourier transformation.

In order to achieve 3D images, FID response signals must be quantified within the axial, coronal and sagittal dimensions. This is achieved by creating spatial variations to the magnetic field strength (B0) within the MRI using gradient magnetic fields via three gradient coils (Gx, Gy, Gz). Spatial variations in field strength leads to faster or slower precession of hydrogen nuclei dependent upon their location, thus providing spatially relevant information (Fig. 20).

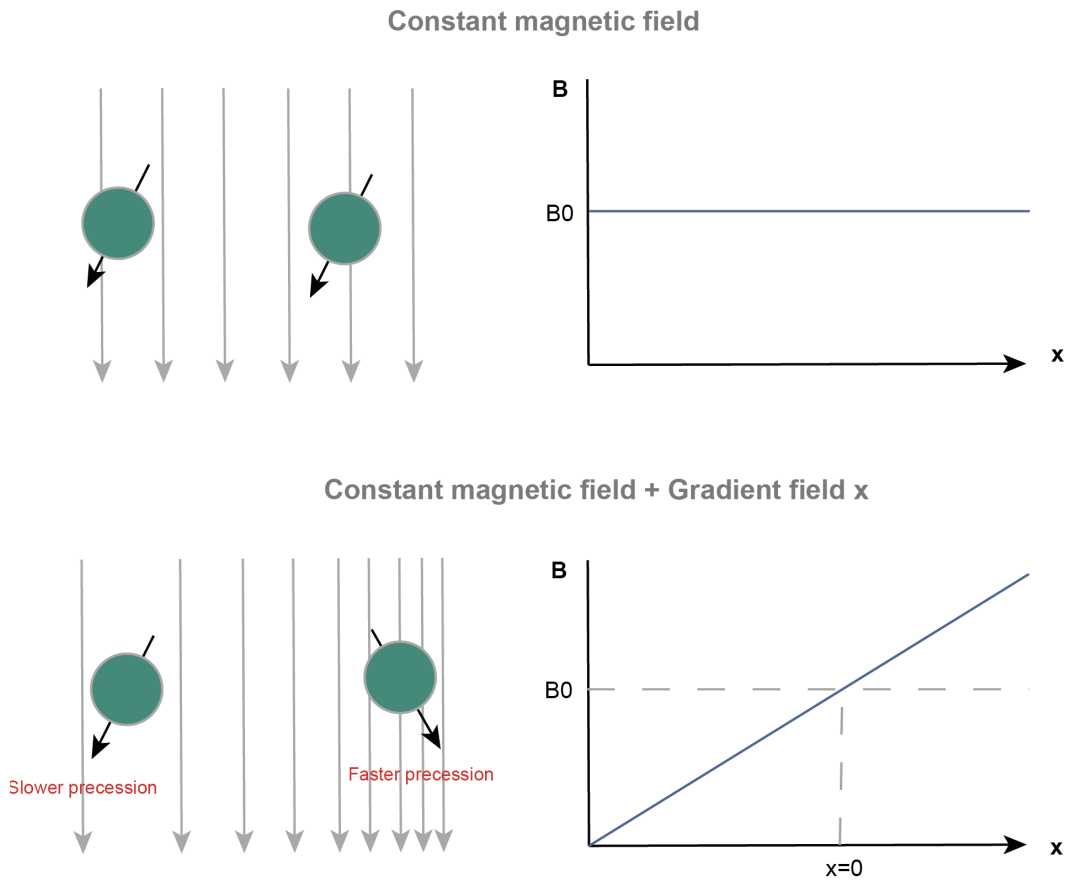


Figure 20: Example of gradient fields and impact on hydrogen nuclei precession. Green spheres represent hydrogen nuclei, and black arrows represent the nuclei magnetic axis. Grey arrows represent the precession speed around magnetic field. Plots on the right side of the figure represent magnetic field strengths on y axis (from high to low), x axis represents gradient field x applied to the magnetic field. Blue line represents magnetic field gradient, grey dashed line represents Larmour frequency.

Within the brain, the intensity of an MR image can vary dependent upon the tissue type (e.g. white matter or grey matter). These variations in intensity can be attributed to the differences in proton density (more specifically hydrogen ions) which in turn impact upon the strength of the FID response signal. Furthermore, contrasts in MRI between tissue types are also impacted by their differing longitudinal relaxation (T1) and transverse relaxation times (T2). In T1-weighted imaging, the manipulation of time between RF pulses, known as the repetition time (TR) is implemented to enable clearer contrast between cerebrospinal fluid (CSF) and fatty tissue (e.g. grey and white matter) which possess different relaxation times.

2.2.2 Diffusion tensor imaging (DTI) and fractional anisotropy

Diffusion tensor imaging (DTI) is an advanced MRI technique designed to quantify microstructural changes in white matter *in vivo* (Basser et al., 1994). Although computed tomography (CT) and standard MRI is currently used to assess DAI via surrogate markers such as microbleeds and white matter lesions clinically (Adams et al., 1989), DTI has become a popular method within TBI research due to its sensitivity and accuracy in detecting white matter damage (Laitinan et al., 2015; Rutgers et al., 2008). DTI is achieved through diffusion weighted imaging (DWI), by measuring the direction and magnitude of water molecule diffusion within the brain, which varies dependent upon the microstructure of tissue (Mori & Zhang., 2006).

Water molecules follow Brownian motion principles such that when unconstrained, molecules will move equally in all directions (e.g. isotropic). In the brain, water diffusion may be restricted by tissue microstructure, particularly within the white matter where movement is greater in one direction (e.g. anisotropic), providing a means to image these microstructures. To quantify water molecule motion in three-dimensional space, diffusion weighted imaging utilises gradient fields to derive an image that is sensitive to diffusion in a given direction. As water molecules move during application of the gradients, differing magnetization will occur compared to neighbouring molecules, leading to differences in the image contrast. More specifically, the introduction of gradient pulses leads to a phase shift for diffuse water molecules, leading to the signal

of diffusion in a given direction to be lost. White matter fibres that are parallel to the gradient direction applied will therefore be dark within the diffusion weighted image for that direction (Fig. 21). This process is subsequently repeated in a minimum of six non-colinear gradient directions with an additional non-gradient weighted (B0) image to provide a three-dimensional model of water diffusion known as a tensor.

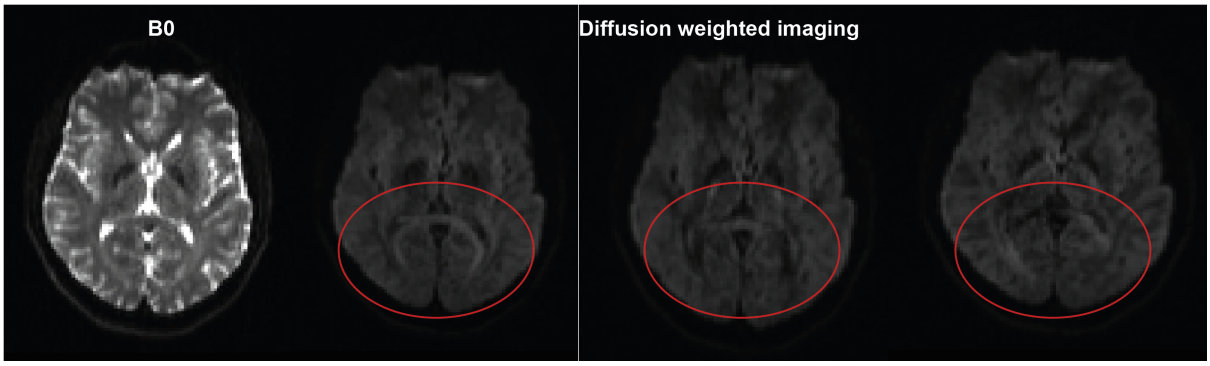


Figure 21: Example images of B0 diffusion image and several diffusion weighted images across different directions. Red circle highlights regions for comparison across directions to demonstrate diffusion signal.

The diffusion tensor is mathematically calculated using a 3x3 symmetric matrix consisting of three orthogonal eigenvectors and three eigenvalues (λ1, λ2, λ3) (Fig. 22). This 3x3 array represents the diffusion rates in each combination of directions. Each gradient direction that is applied measures the movement along the direction of that gradient. The diagonal elements of this array (Dxx, Dyy and Dzz) represent the diffusion coefficients along each of the x, y and z axis. The remaining six measures represent the correlation of motions between each pair of directions. When diffusion is purely isotropic, the non-diagonal elements equal zero and the diagonal elements are the same (e.g. diffusion is equal in each of the x, y and z planes). For anisotropic diffusion which is seen within the white matter structures, diagonal elements are unequal and the surrounding elements in the array provide information about the direction of greatest diffusion.

$$\begin{bmatrix} Dxx & Dxy & Dxz \\ Dxy & Dyy & Dyz \\ Dxz & Dyz & Dzz \end{bmatrix}$$

Figure 22: Example of 3x3 diffusion array.

To provide the measurements needed to fill in the matrix, the six or more non-colinear gradients are summed using the following equation:

$$S_k = S_0 e^{-b\hat{g}_K^T \boldsymbol{D} \hat{g}k.}$$

Where S_0 is the original image intensity at a voxel (e.g. B0 with no diffusion gradient) and S_k is the intensity measured after the application of the kth diffusion weighted gradient in the direction $\hat{g}k$. The product $\hat{g}_K^T \boldsymbol{D} \hat{g}k$ is the diffusitivty in direction $\hat{g}k$.

The measurements calculated within this array can be used to create an ellipsoid of diffusion whereby the axes of the ellipsoid are the eigenvectors and the measurement of their lengths are the eigenvalues. The major eigenvector will be pointed in the direction of fastest water diffusion, as quantified by eigenvalues, and can be viewed as representative of the white matter tract fibre axis (in regions where no crossing fibres are present). Where diffusion is isotropic, the tensor will form a spherical shape whilst in anisotropic regions, the tensor will have an ovoid shape (Fig. 23).

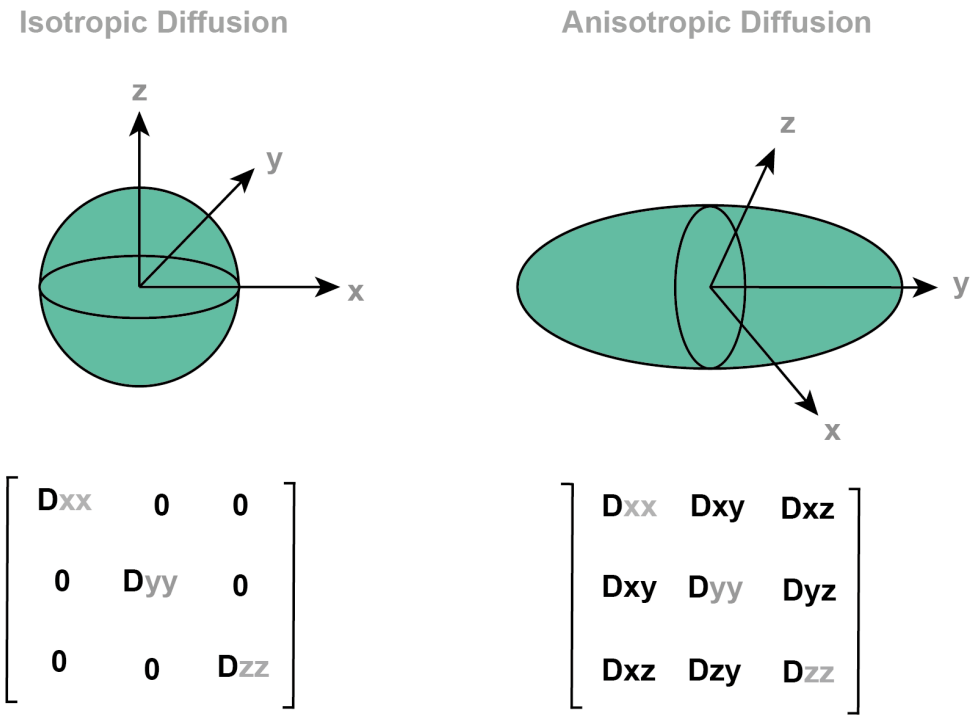


Figure 23: Example of diffusion tensor and diffusion array for isotropic and anisotropic water movement.

Although a number of measures can be derived from the tensor (e.g. axial, radial and mean diffusivity), fractional anisotropy (FA) is most commonly used as a proxy for white matter integrity. Fractional anisotropy provides a scalar value of water diffusion between 0 and 1 where lower values represent more isotropic movement (e.g. freely moving molecules in any direction) and higher values represent more anisotropic movement (e.g. movement is greater in one direction). FA is ratio measure that is calculated from the eigenvalues of the diffusion tensor ($\lambda 1$, $\lambda 2$, $\lambda 3$), providing a description of the shape of the ellipsoid (Fig. 24). In the context of the healthy brain, lower values of FA are likely to be observed in CSF in the ventricles whereas higher values would be expected to be seen in white matter structures. In studies of TBI, widespread significant reductions in FA in the white matter are observed (Sharp et al., 2011; Palacios et al., 2012) as axons are damaged, changing the diffusion of water (Budde et al., 2011). FA has been validated as representative of white matter damage on the basis of its correlation to histological findings (Leergaard et al., 2010; Seehaus

et al., 2013) and is therefore used as the primary measure of white matter damage in this thesis.

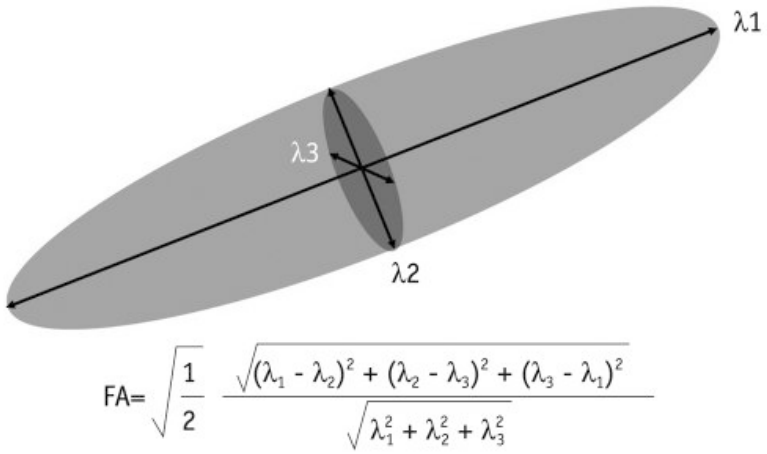


Figure 24: Example of diffusion tensor and equation for the calculation of FA. Figure reproduced from Ahn S, Lee SK. Diffusion tensor imaging: exploring the motor networks and clinical applications. *Korean J Radiol*. 2011;12(6):651-661.

2.2.3 ^{123}I-Ioflupane SPECT

^{123}I-Ioflupane single photon emission computed tomography (SPECT) or DaTscan, is a computerized tomography imaging technique designed to measure levels of Dopamine transporter (DaT) within the brain. SPECT is a functional imaging measure that quantifies the spatial concentration of radio compounds that are injected into a participant and taken up by different organs in the body. Radiopharmaceutical compounds such as ^{123}I-Ioflupane which are designed to bind presynaptically to DaT within the brain are radioactively-labelled, emitting γ-ray photons that can be detected using a scintillation camera with a lead collimator. As γ-ray photons pass through the scintillation camera, their energy is converted into lower energy photons that are then converted into electrical signals. These signals are processed to provide information regarding the location at which the photon reached the scintillation camera, resulting in a two-dimensional image of the distribution of the ^{123}I-Ioflupane uptake in the brain. In order to construct a three-dimensional image, multiple two-dimensional images are

acquired at different views around the head and combined using image reconstruction techniques (Tsui et al., 1994).

To quantify the levels of DaT within the brain, the striatal binding ratio (SBR) is subsequently calculated from the reconstructed 3D-image.

$$SBR=\frac{Striatal\ region}{Reference\ region}-1$$

As DaT is primarily located within the striatum, high uptake of ^{123}I-Ioflupane and therefore high signal in this region is observed (Fig. 25). The amount of binding in this region relative to non-specific binding regions such as the occipital lobe can therefore be calculated as measure of DaT (Watanabe et al., 2017). Alterations in DaT have previously been shown in patients with TBI (Jenkins et al., 2018) and are associated with working memory deficits within this population (Newsome et al., 2015).

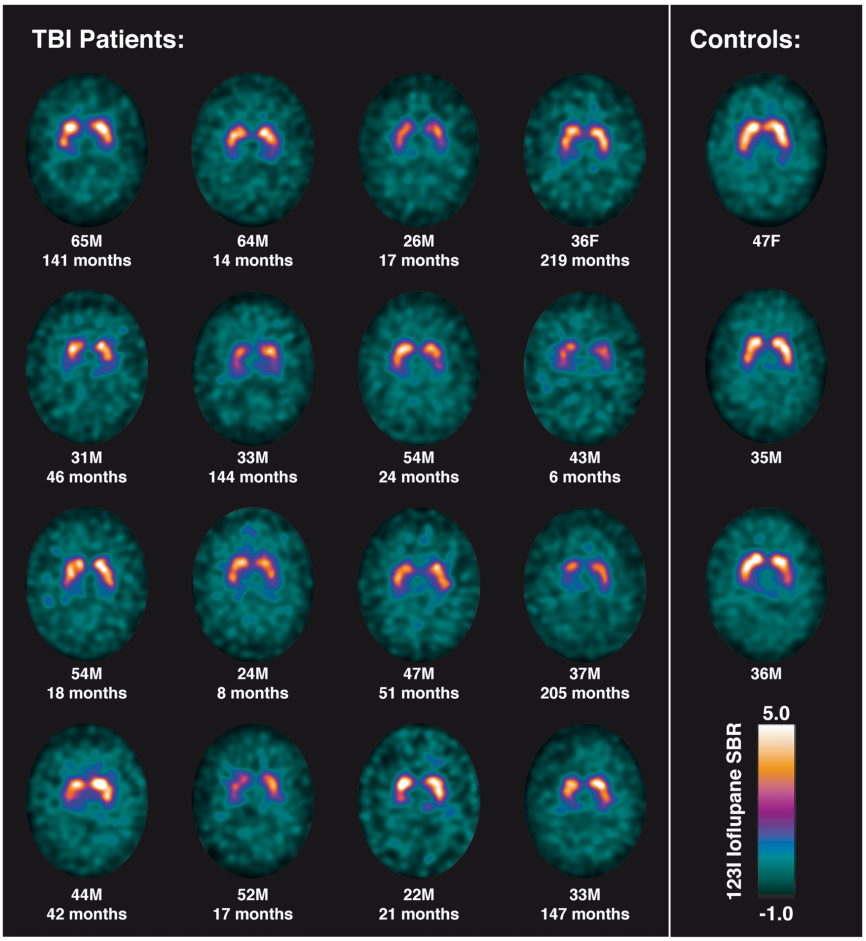


Figure 25: ^{123}I-Ioflupance SPECT scans of TBI patients and healthy controls. Illustrating uneven comma shape of striatum in patients where reductions in DaT are observed as quantified by SBR. Figure reproduced from *Jenkins et al., 2018 Brain*, Volume 141, Issue 3, March 2018, Pages 797–810.

2.2.4 Resting state functional connectivity

Resting state functional connectivity is a functional MRI measure used to investigate which regions of the brain are functionally connected with one another when not performing an explicit task. This is achieved by measuring the similarity in spontaneous blood-oxygen level dependent (BOLD) fluctuations between different regions in the brain. Where two regions show similarities in BOLD signals over time, as quantified using Pearson's correlation coefficients, it is assumed that they are functionally connected.

The BOLD signal is an indirect measure of neuronal activity and is generated by action potentials passing though axonal tracts to other cells. Here, a process known as the haemodynamic response (HR) occurs, where increases in blood flow locally to provide oxygen and glucose to active neuronal tissue, leads to an increase in oxygenated blood. As oxygenated and deoxygenated haemoglobin (oxyhaemoglobin and deoxyhaemoglobin respectively) have differing magnetic field properties, changes in local neural activity can be detected by MRI as increases in the local magnetic signal caused by increased oxygenated blood flow. Although the haemodynamic response has a lag of approximately 5-6 seconds from the time of neuronal excitation, this measure has proved highly beneficial in exploring connectivity within the brain for healthy individuals and patients with TBI (De Simoni et al., 2018; Yeo et al., 2011).

In this thesis, I utilise the cortico-striatal resting-state functional connectivity measures derived by De Simoni et al., 2018 in TBI patients and healthy controls. In summary, De Simoni et al defined striatal subdivisions and cortico-striatal functional connectivity in a large cohort of healthy controls (n=100, males 41, age 22-36) from the Human Connectome Project (HCP). A masked ICA (mICA) approach was then performed to extract 12 independent components using a striatal mask from the Harvard-Oxford anatomical atlas (thresholded at 50%). Next, the striatum was parcellated into 12 subdivisions on the basis of z-transforms from the ICA. A combined mICA and dual regression approach was then used to delineate cortico-striatal functional connectivity networks using the large HCP cohort rs-fMRI, by applying 12 group-level striatal independent components to produce subject-specific cortico-striatal functional connectivity networks. Next, a permutation-based one-sample t-test is applied to provide group-level maps of functional connectivity for each component, and networks were defined using non-parametric testing. The networks derived from this process were then thresholded and binarized for use in TBI patients and controls within this thesis.

Twelve dual regressions were performed by De Simoni et al., 2018, with each dual regression representing a different striatal independent component constrained to voxels within the corresponding whole-brain network identified using the HCP cohort.

A total of 24 FC measures were therefore derived (12 dual regressions, left and right) for TBI patients and controls for comparison and are used as a measure within chapter six of my thesis.

2.2.5 Lesion segmentation

In house software (ImSeg) was used to delineate focal contusions and areas of missing brain as lesion masks on T1-weighted MPRAGE images in chapters three, four, five and six. Lesion masks were manually drawn with FLAIR images overlaid to aid identification of boundaries of lesioned areas. All masks were drawn in native space and subsequently registered to standard space. This was achieved by first registering an individual's T1 to MNI152 1mm space using FIMRIB's linear image registration tool (FLIRT) (Jenkinson et al., 2001; Jenkinson et al., 2002) and applying the resulting transformation matrix to lesion masks to warp into standard space. Masks were subsequently thresholded and re-binarized.

2.3 Structural MRI and SPECT acquisition parameters

2.3.1 Structural MRI acquisition

Structural MRI included a high-resolution T1-weighted MPRAGE (106 1-mm-thick transverse slices, TR=2300ms, TE=2.98 ms, FA=9°, in-plane resolution=1x1mm, matrix size= 256x256, filed of view=25.6x25.6cm) and diffusion weighted imaging (64 directions, b=1000s/mm^2 with four interleaved b=0s/mm^2, TE/TR 103/9,500ms, 64 contiguous slices, FoV 256mm, voxel size 2mm^3).

2.3.2 SPECT acquisition

Patients were first provided with 2x60mg of potassium iodide tablets to minimize radiation exposure to the thyroid gland. An hour later, individuals received a bolus

intravenous injection of ^{123}I-Ioflupane (mean activity 185 MBq). SPECT images for all subjects were acquired using the same Symbia T16, Siemens Healthcare dual-head gamma camera 180 minutes post-injection with LEHR collimators (128x128 matrix, 1.45 zoom, 128 projections and 30s per projection).

2.4 Structural MRI and SPECT pre-processing

2.4.1 DTI

Diffusion weighted images were processed using FSL's diffusion toolkit (FDT) in the following steps: Eddy current correction was applied to diffusion weighted images to correct for distortions and movement. BVECs were rotated using the output from eddy correction and brain extraction (BET) was applied to the eddy corrected data. Tensor fitting was performed using DTIFIT with a weighted least squares approach. Individual fractional anisotropy (FA) maps constructed from DTIFIT were registered to standard MNI152 space using the FIMRIB 1mm FA atlas and tract-based spatial statistics (TBSS) (Smith *et al*., 2006). Concatenated standard space FA maps of TBI patients and controls were skeletonised at 0.2 threshold to sample from the centre of the white matter in order to avoid partial volume effects.

2.4.2 T1-MPRAGE

T1 images for patients and controls were first segmented into grey and white matter and registered to standard MNI152 space (including modulation to retain accurate volumetric measures) using the DARTEL toolbox in spm12 (Ashburner et al., 2007). Normalised grey matter was smoothed (4mm full-width-at-half maximum) and a grey matter mask was derived using the group average grey matter segmentation (thresholded at 0.2).

2.4.3 ^{123}I-Ioflupane SPECT

Details regarding the pre-processing of SPECT imaging can be found in Jenkins et al., 2018. In summary, data was reconstructed using an ordered subsets expectation-

maximization (OSEM) algorithm (HybridRecon, HERMES Medical Solutions; Stockholm, Sweden) which included corrections for scatter, resolution and attenuation. Images were then co-registered to subjects native T1. The flow-fields derived from DARTEL when registering T1 images to standard space were subsequently applied to SPECT images to also register them to standard space (without modulation). Striatal binding ratio was then calculated.

2.5 Quantifying structural network topology from diffusion tensor imaging

2.5.1 Graph theory

Graph theory is a mathematical method used to model relationships between pairs of objects defined within a graph as a series of nodes (vertices) and their respective connections (edges). Recently, this method has been applied to neuroimaging in order to model the complex networks that exist in the brain. In anatomical terms, structural networks in the brain, which I examine within this thesis, are composed of nodes representing grey matter regions and edges representing white matter tracts that connect them. In graph theory, two categories of graphs can be constructed; an undirected graph where edges link two nodes symmetrically, or a directed graph, where the edges that link two nodes are asymmetrical. In simplest terms, an undirected graph provides no information about the direction of information flow between two nodes and is bidirectional, whilst a directed graph consists of edges with start and end points between nodes (one-way edges) that provide information about the direction of information flow (Fig. 26).

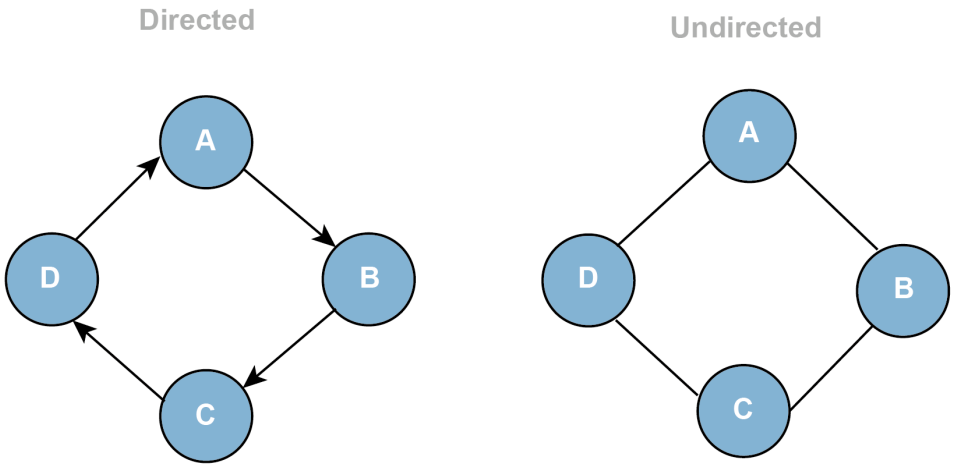


Figure 26: Example of directed vs undirected graphs used in graph theory. Blue circles represent nodes in the graph, black lines represent edges (vertices) within the graph with or without directionality.

In addition to directionality, graphs can be weighted or unweighted dependent on how edges are defined. Weighted graphs refer to weights being applied to edges to represent the magnitude of a relationship between nodes. In contrast, unweighted graphs provide no measure of the magnitude of relationship between two nodes but rather demonstrate whether a relationship between two nodes exist. For example, if an edge between nodes i and j=0, then no relationship exists between them. If an edge between nodes I and j=1 ($e_{i,j}$) then a relationship between these nodes exist.

2.5.2 Defining the structural connectome to assess network topology

For this thesis, structural connectomes, which represent the structural networks in the brain, are created by first defining nodes using grey matter anatomical parcellations from the Desikan-Killiany atlas (Desikan et al., 2006) and edges that connect these nodes using the Illinois institute of Technology (IIT) human brain white matter atlas (Zhang et al., 2018). Edges are defined using the track density images (TDI, standardised to MNI152 space) of 72 healthy controls created by MRIIIT for the atlas by first parcellating structural T1 images into 90 cortical and subcortical grey matter regions using the Desikan-Killiany grey matter parcellation scheme (Desikan *et al.*, 2006). Individual grey matter parcellations of the 72 healthy controls were

subsequently registered to standard MNI152 space and probabilistic tractography between all regions was performed creating TDI's for each region to region connection where they existed. Track density images, region labels, number of streamlines and the IIT white matter atlas were obtained from an online archive (https://www.nitrc.org/projects/iit/). Please refer to Zhang *et al*., 2018 for more details.

Next, each region to region connection (TDI) from the IIT atlas was thresholded and binarised to create an edge mask. Masks were then intersected with each participant's skeletonised FA map to extract the mean FA for that connection, resulting in a 90 by 90 connectivity matrix, weighted by FA, for each participant. When no connection was present between regions in the connectivity matrix, a value of zero is included. As directionality or effective connectivity cannot be derived from DTI, undirected weighted connectomes are used within this thesis as the graphs to examine network topology in patients and controls.

A number of pre-processing steps were applied to ensure structural connectomes are robust against choices of thresholding and to control for weak connections (i.e. small tracts with low FA) which can increase noise and impact upon graph theory measures (Li *et al*., 2013). First, each connection in a participant's connectivity matrix was multiplied by the number of streamlines used to create the connection to ensure greater weight was applied to larger tracts. Secondly, the mean and standard deviation (SD) of each connection in the connectivity matrices of all healthy controls was calculated. This produced two 90 by 90 connectivity matrices representing the mean FA and standard deviation of each connection in the healthy population. Next, ten thresholding limits were calculated using the same scheme as Fagerholm et al., (2015) ranging from 0.5 to 5 SD units in increments of 0.5. This was achieved by multiplying the control SD connectivity matrix by the threshold value (e.g. 0.5 or 5) and subtracting this from the control mean connectivity matrix. The resulting values derived from this calculation were then applied to each patient and control's individual connectivity matrix such that any value less than the value calculated for a connection, was removed (e.g. replaced with a zero). This process was repeated for each of the ten thresholds. For ease of presentation, all findings will be presented using the moderate threshold (2.5 SD units) with all other thresholding results reported within the supplemental data.

2.5.3 Small-world topology

In the human brain, an optimal balance between global integration and local segregation has been observed in both structural and functional networks using graph theory (Bullmore & Sporns., 2009; He & Evans., 2010). This balance is referred to as small-world network topology and is associated with supporting healthy cognitive function (Bassett & Bullmore., 2006). Unsurprisingly, alterations to small-world topology after TBI is associated with cognitive impairment (Pandit et al., 2013). In structural networks, this alteration is related to disruption to white matter connections (edges) in the network between nodes. Due to the biomechanics of strain forces applied during TBI (Ghajari et al., 2016), long range white matter connections are most vulnerable to damage, leading to a loss of long-range connections and a move towards more lattice-like network topology configurations (Fig. 27).

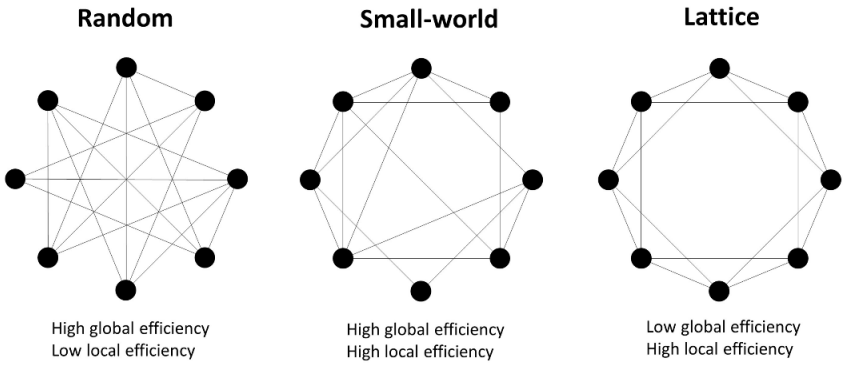


Figure 27: Figure from Imms et al., 2019 Demonstrating impact of edge connectivity on small-world network topology. Figure reproduced from *Imms et al., 2019, The structural connectome in traumatic brain injury: A meta-analysis of graph metrics, Neuroscience & Biobehavioral Reviews,Volume 99,2019,Pages 128-137.*

In this thesis, I therefore employ measures of global integration, local segregation and connectivity to investigate structural networks and examine whether small-world topology is disrupted. This is achieved by quantifying measures of global and local efficiency, clustering coefficient and degree centrality. A description of the measures used, and mathematical formula employed to calculate these are found below.

2.5.3.1 Global efficiency

Global efficiency (E_{glob}) provides a measure of information flow or overall network integration, and is defined as the inverse of all shortest path lengths in a given network (Latora & Machiori, 2001). Put simply, it is the average of efficiencies across all pairs of nodes within the network. In the context of white matter, global efficiency is particularly influenced by long-range connections that enable the rapid transfer of information across distal regions. When long-range white matter connections are lost via axonal injury, global efficiency decreases within the network. Global efficiency is calculated as:

$$E_{glob} = \frac{1}{N(N-1)} \sum_{j \neq i \epsilon G} \frac{1}{l_{ij}}$$

Where N is the group of nodes within the network and l_{ij} is the shortest path (e.g. the number of steps length between nodes).

2.5.3.2 Local Efficiency

Local efficiency (E_{loc}) provides a measurement of information flow at the individual nodal level (Onnela et al., 2005, Klados et al., 2013) and is related to network segregation. Local efficiency is calculated as:

$$E_{loc} = \frac{1}{N_{Gi}(N_{Gi}-1)} \sum_{i,j \in Gi} \frac{1}{l_{ij}}$$

Where N is the group of nodes within the network, G_i is the subgraph that contains the set of nodes that are direct neighbours of node L and L_{ij} is the shortest path (e.g. the number of steps) between nodes i and j within the network.

It is associated with short-range connections between nearby regions that enable modularity of information processing in a network (Latora & Macrchiori, 2001). This measure represents how interconnected neighbouring nodes are to one another (Fig. 28).

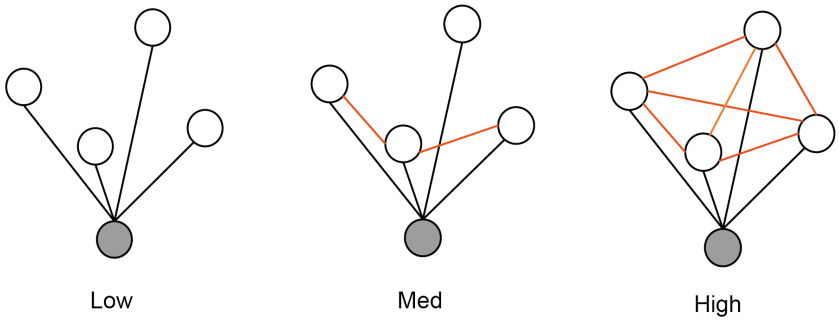


Figure 28: Example of Local Efficiency at different scales. Grey node represents the node currently being used to quantify local efficiency. Black lines represent the edges within the network that connect the node of interest to other nodes and are used to measure local efficiency. Orange lines represent where additional edges can change the scale of local efficiency from low to high for the grey node (e.g. the interconnections of neighbouring nodes).

When short-range connections are lost between the interconnections of neighbours connected to the node of interest via white matter damage, the local efficiency of a node may reduce (Fig. 29). In contrast, increases in local efficiency of a given node can also occur in the presence of axonal injury. Local efficiency may increase due to the loss of connections between the node of interest (L) and other nodes that themselves are not highly interconnected to neighbouring nodes in the defined sub-graph. Here, increases in the calculation of local efficiency can occur as the node of interest is now only connected to nodes with high interconnectivity within the subgraph, increasing local efficiency measures (e.g. less average number of steps between nodes in the sub-graph) (Fig 29). This is particularly demonstrated in graph network simulations where manipulation of topology via the removal of edges demonstrates decreases in global efficiency and increases in local efficiency when moving from small-world to lattice configurations (Imms et al., 2016).

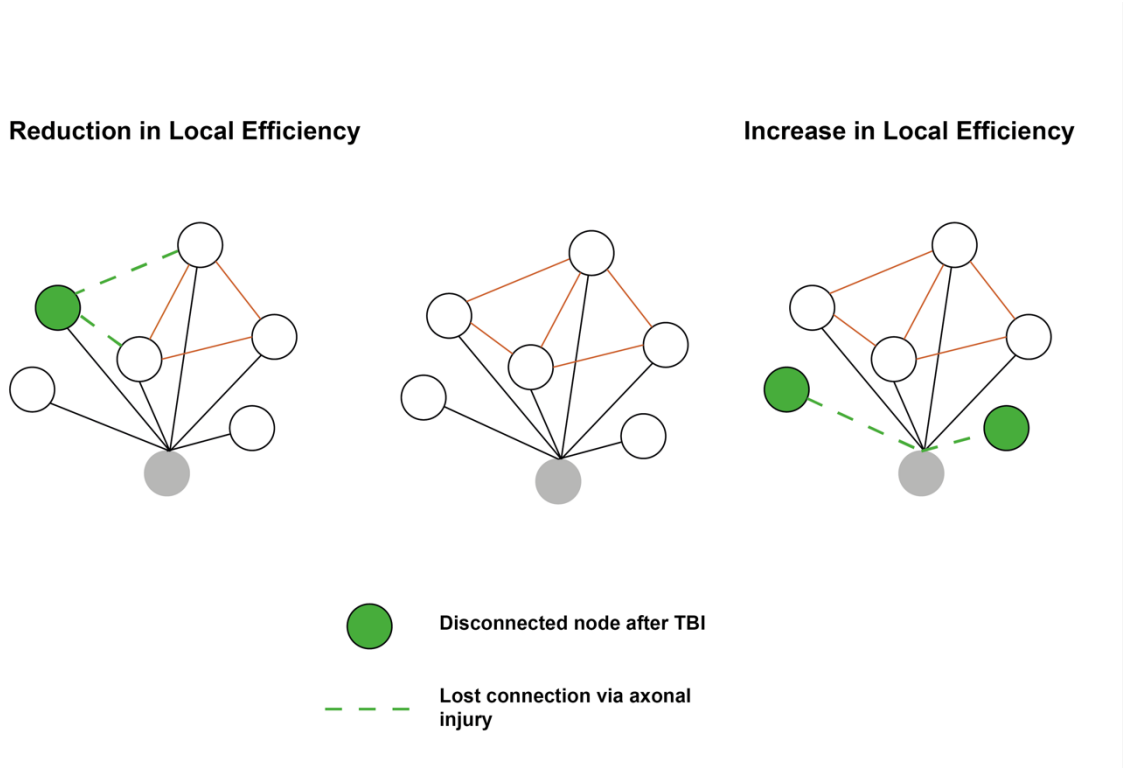


Figure 29: Example of impact of axonal injury on local efficiency measures of a given node. Grey node represents the node being measured for local efficiency. Green nodes represent node that is disconnected due to axonal injury.

2.5.3.3 Degree centrality

Degree centrality refers to the number of neighbours connected to a given node where Kij represents a connection between node i and node j (Fig. 30). If Kij=0, there is no connection whereas Kij>0 represents a connection (Sporns, 2003; Gottlich et al., 2013). Degree centrality is therefore calculated as:

$$K_i = \sum_{j \in G} a_{ij}$$

Where K_i represents the degree of node K calculated as the number of edges linking to that node and where a_{ij} is the ith row and jth column element of the connectivity matrix.

A loss of white matter connections to a given node via axonal injury will therefore result in a reduction of degree centrality for that node.

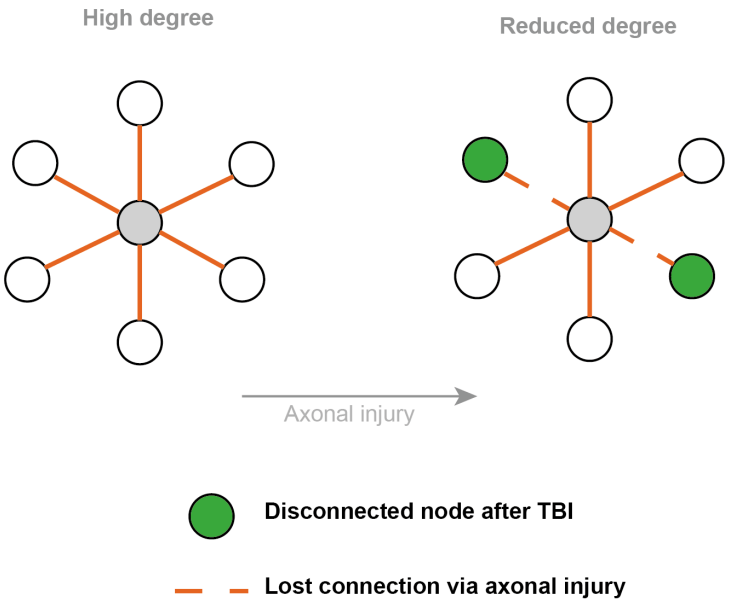


Figure 30: Example of degree centrality. Grey circle represents the node currently being measured for degree centrality. Orange lines represent the number of connections from the grey node to other nodes within the network. Green circle represents the node that is disconnected via axonal injury.

2.5.3.4 Clustering coefficient

Finally, the clustering coefficient provides a measure of the extent to which nodes tend to group together (Fig. 31). The clustering coefficient is defined as the number of 'triangles' on the nodal level (Watts & Strogatz., 1998, Onnela et al., 2005) or the probability that neighbours connected to the node of interest are also connected.

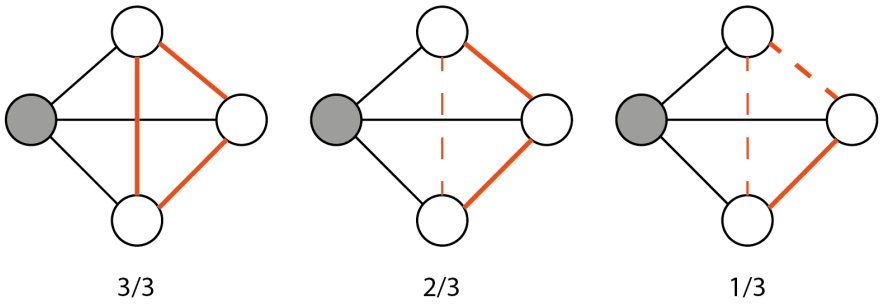


Figure. 31: Example of Clustering coefficient. Grey circle represents the node being measures for clustering coefficient. Black lines represent the connections between nodes. Orange lines represent the measurement of the connectivity between neighbouring nodes connected to the same node. Dashed orange line represents where removal of a connection can alter the clustering coefficient.

The clustering coefficient is calculated as:

$$C=\frac{2C}{N(N-1)}$$

Where C is the number of present connections, N is the number of nodes and N-1 is the maximum number of connections a node can have, resulting in a total of N(N-1) connections.

In TBI, a loss of short-range connections that connect the neighbours associated with a given node can lead to reductions in clustering coefficient, if this loss removes a 'triangle' within the subgraph. Increases in clustering coefficient can also occur due to the loss of connections. In this instance, the loss of a connection from the node of interest to a sparsely connected node (e.g. that is not well connected to neighbours) can lead to an increase in the clustering coefficient as the number of 'triangles' do not change but the number of connections to the node do (Fig. 32).

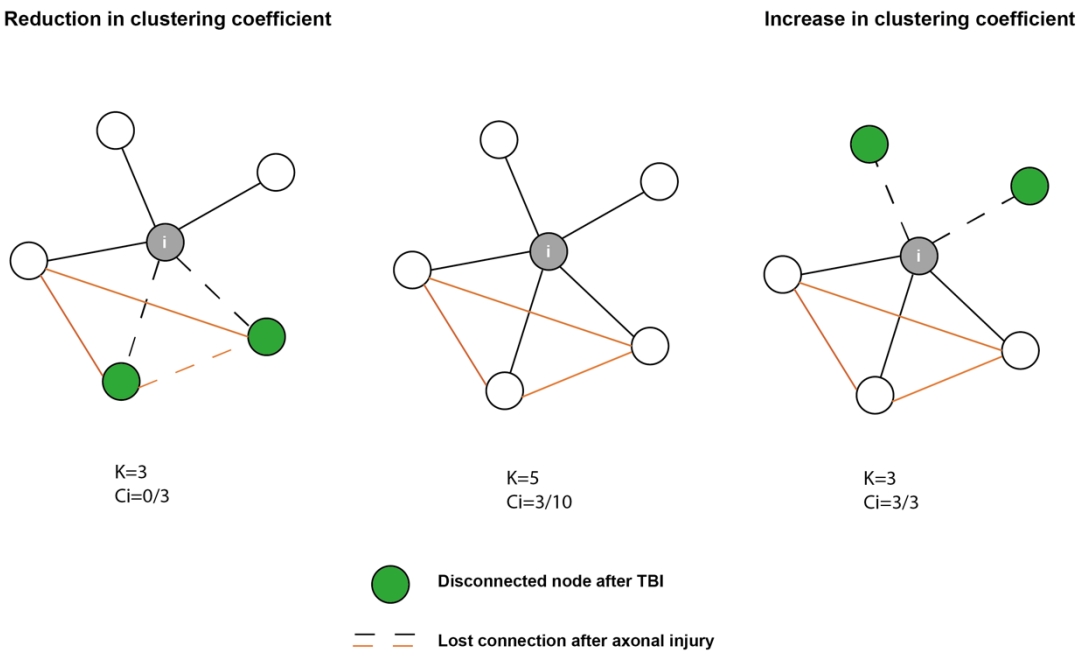


Figure 32: Example of alterations to clustering coefficient due to axonal injury. K represents the number of nodes connected to node of interest; Ci represents the clustering coefficient for node. Grey circle represents the node measured for clustering coefficient. Green circle represents node disconnected due to axonal injury.

2.6 Multivariate statistical analysis

2.6.1 Canonical correlation analysis method

Canonical correlation analysis (CCA) is a multivariate statistical method that investigates the relationship between two datasets with multiple variables. This method extends beyond simple linear regression by using multiple independent and dependent variables. In CCA, the relationships between X set of variables and Y set of variables are explored (Fig. 33) to find multiple linear combinations of the two variable datasets that best describe the correlations between them. These linear composites are known as canonical variates (V and U), with the correlations between the corresponding pairs of canonical variates being referred to as the canonical correlation (r). The number of canonical correlations (or canonical modes) produced from a CCA will relate to the smallest number of variables from either dataset X or Y. Therefore, if a CCA is performed between dataset X with two variables and dataset Y with nine, two canonical modes will be produced. If more than one significant mode is observed, more than one relationship is observed between the two datasets that are dissociable from one another.

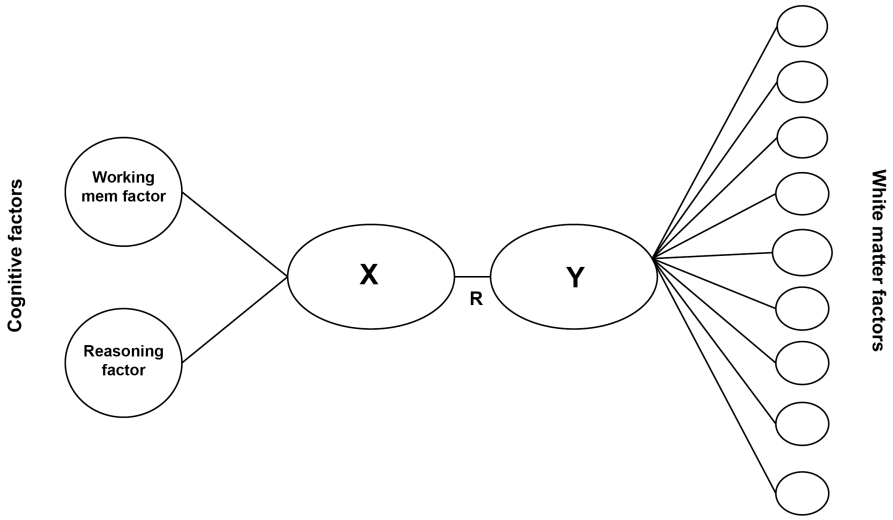


Figure 33: Example of CCA structure and input data. Here two data matrices containing cognitive (x) and white matter (y) measures are included in the CCA. Linear combinations of the two data matrices that best describe the correlations between the two datasets are derived as canonical variates. The relationship (R) between these variates are represented as canonical modes.

2.7 Machine learning

2.7.1 Classification and regression-based machine learning

In this thesis, I utilise machine learning methods inclusive of classification and regression-based models. Both of these methods are included within the area of supervised machine learning whereby algorithms learn information using known data (e.g. a training dataset) to make predictions. The difference between the two methods relates to the output variable and questions explored. For classification, the output is categorical (discrete) and is commonly used to classify between different groups based on information from the input data. For example, exploring whether neuroimaging data can be used to accurately classify patients from controls (Hellyer et al., 2013). One of the most common algorithms used within this method is a binary support vector machine (BSVM). In this algorithm, a hyperplane is constructed that seeks to separate all data points of one class from the other (e.g. patients from controls). The greater the margin between the two classes using the hyperplane, the better the hyperplane and model (Fig. 34).

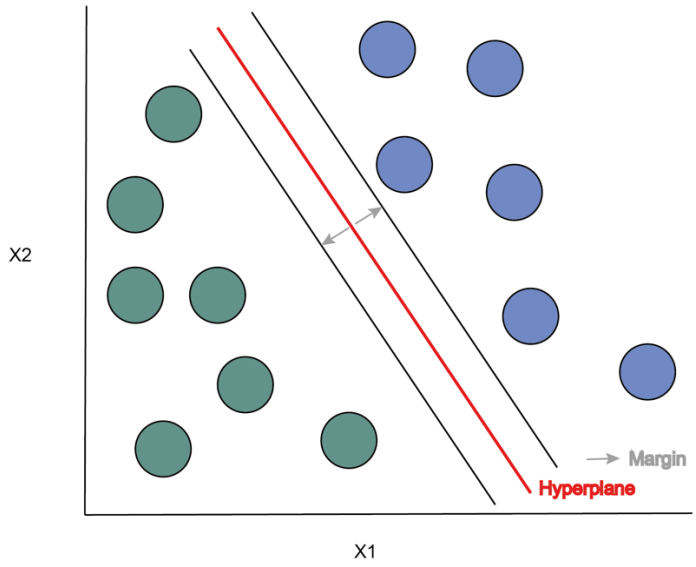


Figure 34: Example of classification problem with hyperplane. Green and blue dots represent different groups. Red line represents the optimal hyperparameter that has accurately separated the two classes of data. Grey arrows illustrate the margin between the hyperplane and the data points within each class.

Regression-based machine learning seeks to predict a dependent variable on the basis of an independent variable via regression. The better the model, the smaller the error between predicted and actual (target) values (Fig. 35). An example of this method would be to use neuroimaging data to predict a cognitive score. One of the most common algorithms used is a kernel ridge regression (KRR) which is able to account for non-linearity within the data and handle instances of collinearity.

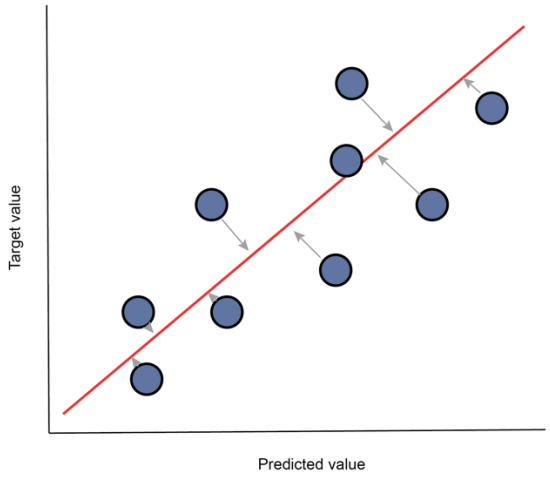


Figure 35: Example of regression using machine learning. Red line represents the regression line fitted by the algorithm. Blue dots the predicted value plotted on predicted vs actual (target) value. Grey arrows represent the distance from the perfect prediction (e.g. error).

2.7.2 Validating machine learning models: Cross-validation

Validation of machine learning models is fundamental for their interpretation and implementation. This method aims to test whether the model derived is accurately identifying patterns in the data with relatively low error, such that low bias and variance is observed. After a model is trained, residuals can be evaluated by quantifying the difference between predicted and target values (in both classification and regression-based machines). Although useful in examining the model's performance on the dataset used, using validation in this way is limited as it cannot evaluate how well the model can generalise to independent unseen data, preventing assessment of whether a model is over or underfitting.

Cross-validation is therefore commonly used to assess model accuracy and generalisability by partitioning data into training and test (validation) sets. Here, the model is trained on a subset of the data available and then validated by applying to the remaining test data to determine the error observed between predicted and actual values. As data is limited, partitioning data into training and test sets can pose risks whereby the training set is too small for actual patterns in data to be detected leading to increases in error. K-fold cross-validation is therefore commonly used as a means

to deal with this potential underfitting problem by ensuring a large proportion of data is partitioned into a training set with a large enough sample retained for validation.

2.7.2.1 K-fold cross-validation

K-fold cross validation divides data into k subsets, where one subset is used as the test (validation set) and the remaining data (k-1) is used to train the model. This process is repeated k times so that every data point is included in the validation set once and is included in the training set k-1 times (Fig. 36). This method therefore allows for bias in model fitting to be reduced as most of the data is used to train the model whilst variance is also reduced as most of the data is also used in the test set. In the example depicted in figure 36, a 5-fold cross validation scheme is applied to the data. Here, data is equally divided into 5 subsets. For the first of the 5 folds in the cross validation, the remaining four subsets (80% of the data) is used as the training set whilst the remaining subset is used for validation. Upon completion, this set is placed back, and a new subset is held out as the test/validation set whilst the remaining become the training set. The average of all folds is then used as the overall model performance measures. I implement 5-fold cross validation for machine learning models detailed in chapters 5 and 6 of the thesis.

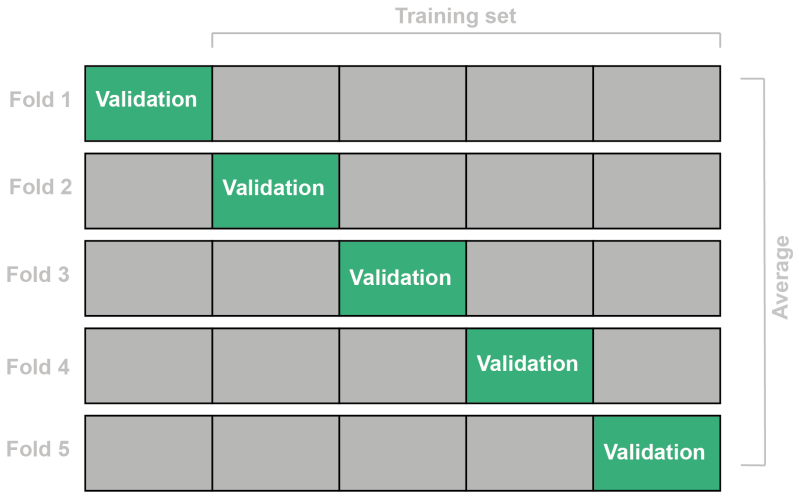


Figure 36: Example of 5-fold cross-validation. Green squares represent the proportion of data held-out as the validation/test set. Grey squares represent the training data used to create the model that is then tested against the validation data.

2.7.3 Hyperparameter optimisation and nested cross-validation

Hyperparameter optimization, also referred to as 'tuning' is a method of choosing hyperparameters that provide the most optimal model for machine learning. This is defined on the basis of a loss function, where an evaluation of how well the machine is able to model the given data is calculated from the deviations of predicted values from the target data. Therefore, hyperparameters with the smallest loss function are most optimal for the machine. In order to optimise hyperparameters automatically without biasing model evaluations and leading to overfit, a nested cross validation scheme can be employed. This is used so that the same test set from the data is not used to select the values of the hyperparameter and evaluate the model. Here, two loops are present within the k-fold cross validation scheme so that different test sets are used to evaluate the best hyperparameter and subsequently the overall model using the selected hyperparameter. The inner loop is used for hyperparameter optimisation, tuning the parameters and selecting the best model, whilst the outer loop is used to assess the performance of the model selected within the inner loop (Fig. 37).

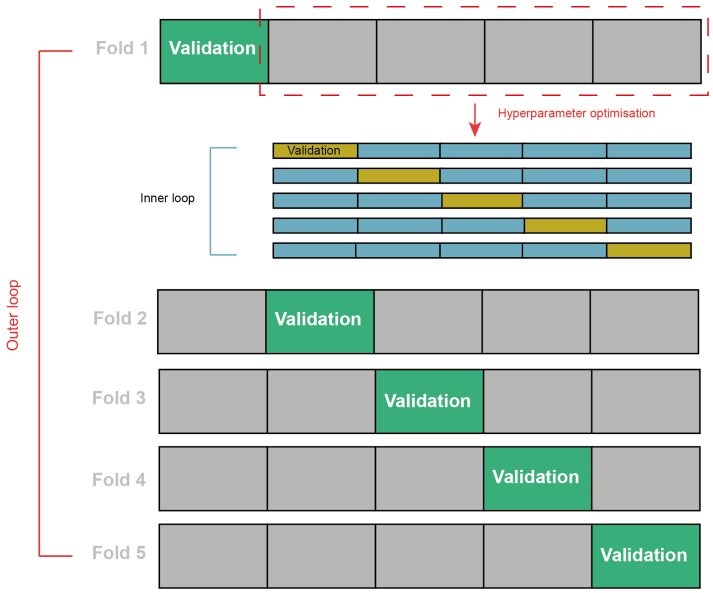


Figure 37: Example of hyperparameter optimisation during k-fold cross validation. Inner loop represent partition of training data identified in the outer loop for that particular fold. This inner loop subsequently trains and tests using different hyperparameters.

2.7.4 Evaluating model performance in machine learning

After cross-validation, a number of metrics are provided as a means to evaluate how well the model has performed in generalising to new data. The better the performance, the greater the likelihood the model will be able to accurately predict of classify new unseen data which is fundamental to its utility. Performance is calculated and then averaged across the folds used in cross-validation to provide an overall measure for the model.

2.7.4.1 Evaluating classification models

In classification-based machine learning models, measures of accuracy, and area under the curve (AUC) are commonly used. Classification accuracy is used to measure how well the model is able classify data and is calculated as:

$$\text{Accuracy (\%)}=1-\frac{1}{N}\sum_n l_{01}(y_n, f(x_n))$$

Where $l_{01}(y_n, f(x_n))$ represents a loss function that calculates correct classifications as 0 and incorrect classifications as 1.

This measure is useful when the two samples to classify are of equal size. If class sample sizes vary greatly, balanced accuracy measures are used instead to avoid bias. For example, if the data consisted of 90% of one class and 10 % of the other, a high accuracy rate could be derived if the model classified all data as the larger class. Balanced accuracy accounts for the variation in sample size between the two classes by averaging the proportion of correct classifications for each class individually:

$$\text{Balanced accuracy (\%)}=\frac{1}{C}\sum acc_c$$

Where C represents the class to be calculated for accuracy.

The AUC represents how well a classification model is able to distinguish between different classes of data. This is calculated using a ROC curve that is plotted as true positive rates versus false positive rates of a classifier. The higher the value, the better the classification model's performance is viewed to be with a value of 0.5 representing random classification (e.g. chance) and 1 representing perfect classification.

2.7.4.2 Evaluating regression models

For regression-based machine learning models, measures such as the correlation coefficient, mean squared error (MSE) and R^2 are commonly used to assess performance. The correlation coefficient represents the Pearson's correlation between the predicted versus target data in the model. Where the model is able to perfectly predict data, a correlation coefficient of 1 would be observed whilst a correlation coefficient of 0 would represent no relationship between predicted and target data from the model. The MSE also provides a measure of model error and represents the average of the squared differences between the predicted and target values produced by the model. MSE is calculated as:

$$MSE=\frac{1}{n}\sum(y-\hat{y})^2$$

Where n is the number of data points, y is the values of the variable being predicted, $\hat{y}$ is the predicted values and $(y-\hat{y})^2$ represents the squares of the errors.

The R^2 or coefficient of determination represents how close the data are to the fitted regression line and is a measure of goodness-of-fit. In other terms, it represents the percentage of variation explained by the model. R^2 can be a value between 0 and 1, with higher values indicating better model performance. R^2 is calculated as:

$$R^2=1=\frac{SS(residual)}{SS(total)}$$

Where *SS(residual)* represents the residual sum of squares from the model (e.g. the sum of squares of the perpendicular distance between the data and the fitted regression line), and *SS(total*) represents to the total sum of squares (e.g. the sum of squares of perpendicular distance between the average line and data)

2.7.4.3 Permutation testing

A fundamental part of assessing model performance is to determine whether the model is significant from the null hypothesis (e.g. the model is able to classify or predict above chance). This can be achieved using non-parametric permutation testing which calculates confidence intervals and p values for the given model. Permutation testing is achieved by randomly shuffling the data with the resulting value included as part of the null distribution. Next, the distribution from the randomly permuted data is compared to the distribution of interest to determine whether there are significant differences. If a significant p value is observed, the model performance can be determined to be significantly better than the null. For this thesis, 1000 permutations were applied to each machine learning model to assess significance.

2.7.5 The Pattern recognition for neuroimaging toolbox (PRoNTo)

Identifying features of damage that are common amongst patients and can predict the development of working memory impairment after TBI is a core aim of this thesis. In heterogeneous populations like TBI, this can be difficult when using mass-univariate approaches that may not be optimal with large individual differences. One way to overcome this issue is to identify the patterns of damage that are common within the brain. The Pattern Recognition for Neuroimaging Toolbox (PRoNTo, Schrouff et al.,

2013) is a widely available toolbox that enables this to be achieved by utilising a multivariate pattern recognition (MVPA) approach. PRoNTo enables both classification and regression-based models to be implemented within various modalities of neuroimaging data. Furthermore, PRoNTo is able to work with both 3D images as well as 2D data frames containing measurements derived from neuroimaging such as functional connectivity metrics. Importantly, PRoNTo has recently developed the means to use multi-modal imaging within the same machine learning model. This is achieved through the use of a multi-Kernel learning algorithm (MKL) that can examine the relative contributions of each modality to the model and the regional contributions provided within each modality using anatomical maps in a hierarchical fashion (Fig. 38). In this way, more biologically informative models can be derived using multimodal imaging to provide a holistic overview of the brain.

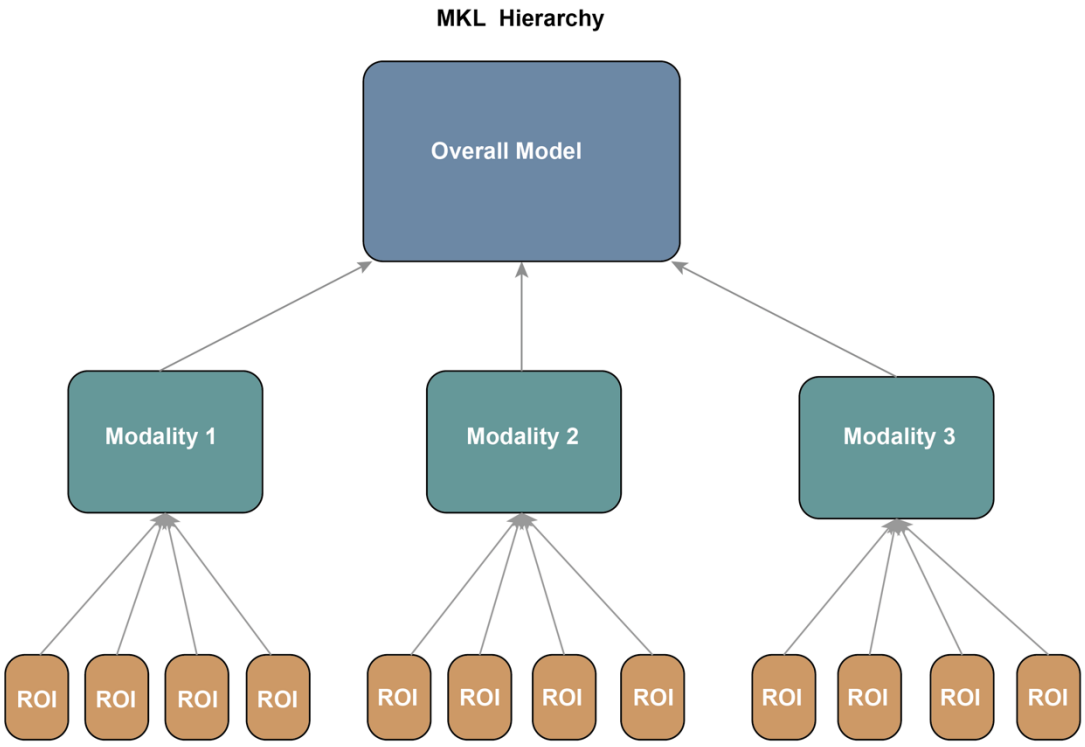


Figure 38: Schematic of hierarchical nature of MKL algorithm for machine learning. The overall classification/regression model is derived and the relative contribution (weights) of each modality calculated. Within each modality, the relative weights from voxelwise and region of interest (ROI) kernels are calculated in parallel and contribute to the modality kernel in a hierarchical manner.

When using MKL in PRoNTo, standard space 3D images or 2D arrays containing imaging data can be used in parallel to build both classification and prediction models. The kernel within MKL is considered to represent a linear combination of 'basis' kernels such as individual imaging modalities and their respective features. The features for each imaging modality can be either voxels or ROI's as defined using an imaging modality specific atlas. MKL is therefore viewed as a feature selection technique whereby each kernel corresponds to different subsets of features (such as ROIs) at the single imaging modality level, and the overall model kernel is composed of features selected across each of the imaging modalities included. Model weights for MKL models subsequently provide information about the contribution of each feature to the overall model. Weights can be plotted spatially within the brain to provide anatomical insights. Importantly, these weights are derived at two levels: first, the weight contribution of each region and the weights for each voxel. The weights at the voxel level can help to provide insights into the homogeneity of discriminative patterns within the regions. Importantly, weights are ranked according to their contribution to the model averaged across folds. Only weights with a positive (non-null) contribution to the decision function are displayed. The stability of these regions in their contribution to the kernel across the folds of cross-validation are also computed as the Expected ranking (ER), which provides the average ranking across folds.

The recent implementation of a fast, multi-kernel learning (MKL) is an important step in allowing research to move beyond single imaging modality studies into more biologically representative models of damage and its associated impact on working memory (McAllister et al., 2009). For example, neuroimaging studies have demonstrated that working memory impairments are related to a wide range of pathophysiological changes after TBI, such as alterations in task-activation, functional connectivity, structural connectivity, grey matter volume and dopamine function (Palacios et al., 2011; Konstantinou et al., 2018; Newsome et al., 2007; McAllister et al., 2004). These abnormalities are highly inter-related and therefore lend themselves to an MKL based approach which seeks to combine different concepts of similarity via different sources of data (Gonen & Alpaydun., 2011). Critically, by modelling features of damage across different systems in the brain, we can begin to better understand the mechanisms of working memory impairment and the biological factors associated with its successful treatment and is therefore applied within this thesis.

Chapter 3

Detecting axonal injury in individual traumatic brain injury patients

In this chapter I develop a novel pipeline to assess and diagnose the presence of axonal injury in individual patients. I test this pipeline against a number of common methodological issues and examine the cognitive and functional outcomes of patients identified as having axonal injury using this method.

3.1 Abstract

Diffuse axonal injury is important for predicting outcomes after TBI, but its assessment remains limited in the clinical setting. Currently, axonal injury is diagnosed on the basis of clinical presentation, visible damage to the white matter or via surrogate markers of axonal injury such as microbleeds. These do not accurately quantify axonal injury leading to misdiagnosis in a proportion of patients. Diffusion tensor imaging provides a quantitative measure of axonal injury *in vivo*, with fractional anisotropy (FA) often used as a proxy for white matter damage. Diffusion imaging has been widely used in TBI, but is not routinely applied clinically. This is in part due to the fact that robust analysis methods to diagnose axonal injury at the individual level have not yet been developed.

Here, I present a pipeline for diffusion imaging analysis designed to accurately assess the presence of axonal injury in large white matter tracts in individuals. Average FA is calculated from tracts selected on the basis of high test-retest reliability, good anatomical coverage and their association to cognitive and clinical impairments after TBI. I test this pipeline for common methodological issues such as the impact of varying control sample sizes, focal lesions and age-related changes to demonstrate high specificity, sensitivity and test-retest reliability. I assess 92 individual moderate-severe TBI patients in the chronic phase (≥6 months post-injury), 25 patients in the subacute phase (10 days – 6 weeks post-injury) with six-month follow-up and a large control cohort (n=103).

Evidence of axonal injury is identified in 52% of chronic and 28% of subacute patients. Those classified with axonal injury had significantly poorer cognitive and functional outcomes than those without, a difference not seen for focal lesions or microbleeds. Almost a third of patients with unremarkable standard MRI's had evidence of axonal injury, whilst 40% of patients with visible microbleeds had no diffusion evidence of axonal injury. More diffusion abnormality was seen with greater time since injury, across individuals at various chronic injury times and within individuals between subacute and 6-month scans.

I provide evidence that this pipeline can be used to diagnose axonal injury in individual patients at subacute and chronic timepoints, and that diffusion MRI provides a sensitive and complementary measure when compared to susceptibility weighted imaging, which measures diffuse vascular injury. I discuss the guidelines for the implementation of this pipeline in a clinical setting.

3.2 Introduction

Long-term outcomes are often poor after traumatic brain injury (TBI) and it is challenging to understand the causes of its varying effects (McMillan et al., 2011; Colantonio et al., 2004; Menon et al., 2009). A key reason for this is that diffuse axonal injury (DAI) is difficult to measure clinically. However, DAI plays a fundamental role in the pathophysiology of TBI and is an important predictor of outcome (Sidaros et al., 2008). Axons and axoplasmic membranes are injured by initial shearing forces produced at the time of injury (Smith et al., 2003). This impairs axonal transport, disrupts brain network function and results in delayed axonal damage. There are currently limited diagnostic tools to measure axonal injury. A key goal for TBI research is to develop and validate sensitive and specific measures of DAI that can robustly identify the extent of injury.

Currently, diagnosis of diffuse axonal injury after TBI relies upon the clinical presentation of a patient and the presence of observable damage to the white matter using computed tomography (CT) or MRI imaging (Adams et al., 1989; Marshall et al., 1991; Gallagher et al., 2007). For example, the Adams diffuse axonal injury classification provides useful guidelines for determining the presence and severity of DAI (Adams et al., 1989). However, this method is likely to underestimate DAI when conventional imaging approaches are used (Cicuendez et al., 2017) as they do not provide a sensitive measure of the microstructural changes to white matter that are present in DAI, but not visible on routine MRI (Sharp et al., 2014; Hellstrom et al., 2017).

Advances in magnetic resonance imaging (MRI) allow axonal injury to be sensitively detected after TBI (Kinnunen et al., 2011; Bonelle et al., 2012; MacDonald et al., 2007; MacDonald et al., 2011). The development of diffusion tensor imaging (DTI) has provided a quantitative method to assess white matter structure *in vivo* with measures of fractional anisotropy (FA) used as a proxy for white matter integrity (MacDonald et al., 2007). This technique has demonstrated an improved ability to detect and quantify diffuse axonal injury in patients (Basser et al., 1996, Sidaros et al., 2008) as witnessed by the identification of abnormalities in the context of an otherwise normal scan (Hashim et al., 2017, Corbo et al., 2004; Hellstrom et al., 2017). Furthermore, DTI proved to be a valid measure of white matter integrity after TBI in animal models of traumatic injury (MacDonald et al., 2007a), and provides a sensitive structural measure of damage to white matter that becomes abnormal in the first hours after injury (MacDonald et al., 2007b) and remains abnormal into the chronic phase (Laitinen et al., 2015). Importantly, DTI has also helped to predict long-term clinical outcomes after TBI (Sidaros et al., 2008; Kumar et al., 2009) and can be used to explain abnormalities of brain function seen after injury (Sharp et al., 2014). The location of diffusion abnormalities has been shown to predict many types of cognitive problems that patients often experience after TBI, particularly in large long-range white matter connections, which are integral in supporting functional networks of cognition (Sharp et al., 2014; Hellyer et al., 2013; Fagerholm et al., 2015).

Despite the clear evidence of the utility of diffusion MRI in the assessment of TBI, it is not widely used clinically. A key challenge is to define analysis methods that are robust to the challenges of clinical imaging data and that can be used to provide diagnostic information at the level of individual patients. Here I present a pipeline for diffusion imaging that is robust to common methodological challenges, including the impact of focal lesions, variation in FA with age and test-retest reliability issues. The pipeline produces results with high sensitivity and specificity, test-retest reliability and that correlate with common clinical outcomes after TBI. This is achieved using measures of fractional anisotropy (FA) in large white matter tracts to calculate whether significantly abnormal FA is observed in individual TBI patients compared to healthy individuals. I first apply a data-driven approach to identify large white matter tracts with high reliability across time by investigating test-retest reliability of FA at three time points across a two-year period. I select tracts that include association, projection and

commissural pathways to provide good anatomical coverage. I demonstrate the rates of axonal injury identified in individual patients and investigate associations with cognitive, psychiatric and functional outcomes. Finally, I examine the impact of age, sample size, focal lesions and time since injury on diagnostic results to provide pragmatic guidelines for the use of this pipeline.

3.3 Methods

3.3.1 Participants

Data from 92 patients (mean age 42.9, 12.02 SD years, 19 females) and 103 healthy controls (mean age 44.5, 14.76 SD years, 35 female) were included in this study. Patients and controls had no history of psychiatric illness, drug or alcohol dependence and were not undergoing any litigation. Controls had no neurological history including traumatic brain injury. There was no significant difference in age between the two groups ($t(192)=0.84, p=0.4$). All patients were classified as moderate-severe as defined by the Mayo criteria (Malec et al., 2007) and were recruited from Neurology outpatient clinics at St Mary's hospital, London, within the chronic phase of their injury (mean time since injury 130 months, range 6-497 months). Further information regarding patient's mechanism of injury and current medications can be found in Table 2. All patients and controls underwent advanced structural MRI. Of the 92 patients included, 16 had no visible evidence of injury on routine MRI (e.g. contusion or microbleeds), 11 had evidence of microbleeds, 36 had a focal contusion and 29 patients had both contusions and microbleeds as classified by a consultant neuro-radiologist. All patients completed standard neuropsychological testing and questionnaires to determine functional outcomes after injury. A sub-group of the controls (n=35) also completed neuropsychological testing. Written informed consent was obtained for all participants in accordance with the Declaration of Helsinki. The studies were approved by the West London and GTAC Research Ethics Committee (14/LO/0067, 13/LO/1678, 14/LO/1998).

Age	Gender	Severity	Cause	PTA	Contusion	Microbleeds	Medication
65	M	Mod/Sev	RTA	>7 days	Y	N	nil
38	M	Mod/Sev	violence/assault	2 days	N	Y	nil
51	F	Mod/Sev	incident fall	2 days	unknown	unknown	Lansoprazole 15mg od
31	M	Mod/Sev	RTA	90 days	Y	Y	nil
54	M	Mod/Sev	RTA	5 days	N	N	Citalopram 30mg, thyroxine 150 mcg
20	M	Mod/Sev	incident fall	28 days	N	Y	nil
36	M	Mod/Sev	violence/assault	3 days	Y	N	nil
44	M	Mod/Sev	RTA	90 days	Y	Y	nil
51	M	Mod/Sev	RTA	several weeks	Y	Y	nil
64	M	Mod/Sev	RTA	few hours to a day	Y	N	Omeprazole 40mg, Levothyroxine 75mcg
58	M	Mod/Sev	RTA	1 month	Y	N	nil
34	M	Mod/Sev	other	6 weeks	Y	Y	nil
45	M	Mod/Sev	RTA	2 weeks	N	Y	nil
20	M	Mod/Sev	RTA	2 months	Y	Y	nil
52	M	Mod/Sev	RTA	5 days	N	Y	nil
45	M	Mod/Sev	other	14 days	N	N	nil
31	M	Mod/Sev	violence/assault	months	Y	Y	nil
49	M	Mod/Sev	other	yes but unknown duration	Y	Y	Loperamine 2mg
24	M	Mod/Sev	RTA	14 days	N	N	nil
52	M	Mod/Sev	incident fall	21 days	Y	Y	Levetirecetam 1250mg bd, perindopril 2mg od
54	M	Mod/Sev	violence/assault	15 days	Y	Y	nil
26	M	Mod/Sev	violence/assault	56 days	Y	N	Amitriptyline 10mg, Sodium Valproate 100mg
21	F	Mod/Sev	RTA	35 days	N	Y	Fluoxetine 20mg
39	F	Mod/Sev	incident fall	2 days	N	N	nil

47	M	Mod/Sev	RTA	3 days	Y	Y	nil
22	M	Mod/Sev	RTA	450 days	Y	Y	nil
34	M	Mod/Sev	incident fall	0 days	Y	N	nil
48	M	Mod/Sev	RTA	60 days	Y	N	Amitriptyline 20mg tds, Fexofenadine 180mg od, Esomeprazole 40mg od Solifenacin 5mg od Loperamine 10mg od
38	M	Mod/Sev	violence/assault	700 days	Y	N	nil
49	F	Mod/Sev	violence/assault	10 days	Y	N	Levothyroxne 150mcg od, omeprazole
36	F	Mod/Sev	RTA	120 days	Y	Y	nil
43	M	Mod/Sev	RTA	42 days	N	Y	nil
31	M	Mod/Sev	violence/assault	21 days	Y	N	Growth Hormone 2mg, Lamotrigine 50mg bd
37	M	Mod/Sev	incident fall	120 days	Y	N	Tegretol CR 400mg BD
33	M	Mod/Sev	RTA	30 days	Y	Y	Citalopram 10mg OD, Baclofen 20mg OD
35	M	Mod/Sev	incident fall	7 days	Y	Y	nil
33	M	Mod/Sev	RTA	28 days	Y	N	Symbicort
52	M	Mod/Sev	violence/assault	4 days	Y	N	Lansoprazole 15mg od
38	M	Mod/Sev	violence/assault	14 days	unknown	unknown	nil
31	M	Mod/Sev	RTA	120 days	unknown	unknown	nil
39	M	Mod/Sev	RTA	2 weeks	Y	N	nil
24	F	Mod/Sev	RTA	120 days	unknown	unknown	Citalopram 40mg OD
35	M	Mod/Sev	incident fall	3 days	unknown	unknown	Salbutamol, Beclomethasone
42	M	Mod/Sev	RTA	unknown	N	N	Modafinil 300od, citalopram 20 OD,
37	M	Mod/Sev	RTA	4 days	Y	N	Omeptrazol 40mg OD, Gabapentin 900mg OD
6	M	Mod/Sev	incident fall	4-6 hours	N	N	nil
59	M	Mod/Sev	RTA	7 days	N	Y	nil
57	F	Mod/Sev	incident fall	1-7 days	Y	Y	Demeclocycline 300g bd, ramipril 5mg od,

							salbutamol brn,
54	M	Mod/Sev	incident fall	2 days	Y	N	nil
39	M	Mod/Sev	RTA	unknown	N	Y	nil
44	M	Mod/Sev	RTA	6 days	Y	Y	unknown
48	M	Mod/Sev	violence/assault	24-48 hours	N	N	Carbamezipine 200mg
65	M	Mod/Sev	unknown	unknown	Y	Y	unknown
59	M	Mod/Sev	RTA	1-7 days	Y	N	Lansoprazole 30mg od
37	M	Mod/Sev	incident fall	1 days	Y	N	nil
26	M	Mod/Sev	RTA	3 days	Y	Y	nil
24	M	Mod/Sev	RTA	unknown	Y	N	nil
39	M	Mod/Sev	violence/assault	3 weeks	Y	N	nil
53	M	Mod/Sev	incident fall	unknown	Y	Y	nil
29	F	Mod/Sev	RTA	still in PTA	Y	Y	Lansoprasine 30mg, Phenytoin 300mg,
51	M	Mod/Sev	unknown	unknown	Y	Y	Gabapentin 300mg tds, Amitriptyline 50 mg
52	M	Mod/Sev	Incident fall	24-48 hours	Y	Y	nil
57	M	Mod/Sev	RTA	4 days	Y	N	unknown
40	M	Mod/Sev	RTA	42 days	Y	N	nil
42	F	Mod/Sev	RTA	3 days	Y	Y	nil
40	F	Mod/Sev	unknown	unknown	Y	N	unknown
31	M	Mod/Sev	incident fall	unknown	N	Y	nil
34	M	Mod/Sev	unknown	3 days	Y	N	nil
49	F	Mod/Sev	incident fall	24-48 hours	Y	N	Ibuprofen
39	M	Mod/Sev	unknown	7 days	Y	N	ramipril
44	F	Mod/Sev	RTA	unknown	Y	N	unknown
49	M	Mod/Sev	RTA	unknown	unknown	unknown	nil
61	F	Mod/Sev	RTA	120 days	Y	Y	Citalopram 10mg od
39	F	Mod/Sev	RTA	unknown	Y	Y	citalopram 20mg OD
49	M	Mod/Sev	unknown	unknown	Y	N	phenytoin 35omg OD, Omnitrope GH 0.3mg/0.4mg, Bendroflumethiazide 2.5mg,

							Thiamine 300mg OD, Quetiapine 100mg OD, Mirtazapine 45mg OD, Atorvastatin 40mg OD, Amlodipine 10mg OD, Ramipril 7.5mg OD, Pregabalin 300mg OD
72	M	Mod/Sev	unknown	unknown	Y	N	nil
40	F	Mod/Sev	RTA	unknown	Y	N	Tegretol, propranolol
65	M	Mod/Sev	incident fall	14 days	N	N	amlodipine, simvastatin, ramipril,
54	M	Mod/Sev	RTA	10 days	Y	Y	Tegretol 200mg BD, Amytriptyline 100mg
56	F	Mod/Sev	RTA	several months	Y	N	ventolin, seretide
43	M	Mod/Sev	RTA	unknown	Y	N	pregabalin 75mg bd, ventolin, cetirizine, omeprazole, lamotrigine 50mg bd
39	M	Mod/Sev	RTA	unknown	Y	N	tegretol 400mg bd
57	M	Mod/Sev	RTA	unknown	Y	N	nil
31	F	Mod/Sev	unknown	unknown	unknown	unknown	unknown
38	M	Mod/Sev	unknown	unknown	unknown	unknown	unknown
51	M	Mod/Sev	incident fall	unknown	unknown	unknown	nil
54	M	Mod/Sev	RTA	1 days	N	N	nil
46	F	Mod/Sev	incident fall	4 weeks	unknown	unknown	nil
43	M	Mod/Sev	RTA	no	N	N	nil
55	M	Mod/Sev	violence/assault	4 days	N	N	Levetiracetam, Salbutamol
48	M	Mod/Sev	RTA	no	N	N	Salbutamol, Seretide
57	M	Mod/Sev	RTA	no	N	N	nil

Table 2: TBI patient demographics. M=male, F=female, N=no, Y=yes, RTA=road traffic accident, PTA=post traumatic amnesia, OD=once daily, BD=twice a day, Mod/Sev=Moderate-severe TBI.

To investigate the impact of time since injury, an additional 25 moderate-severe TBI patients (mean age 49.36, 13.45 SD years, 7 females) with subacute longitudinal diffusion weighted imaging data collected on the same scanner, were included. Patients within this subset were scanned at subacute (10 days-6 weeks) and chronic (~6 months) timepoints. Patients were scanned no less than 10 days post-injury to allow for stabilisation of FA measures which can be transiently elevated soon after injury (MacDonlad et al., 2007a). Further information regarding time since injury, scanning interval and mechanism can be found in Table 3.

Age	Gender	Severity	Mechanism of injury	PTA duration	Time since injury at sub-acute (days)	Time since injury at chronic (days)
22	Male	Mod-severe	RTA	1to7days	11	170
24	Male	Mod-severe	Assault	NK	26	179
45	Male	Mod-severe	RTA	1to7days	29	191
41	Male	Mod-severe	Assault	None	28	188
55	Female	Mod-severe	Fall	1to24Hour	29	249
56	Female	Mod-severe	RTA	NK	49	175
40	Male	Mod-severe	Assault	1to24Hour	50	189
52	Male	Mod-severe	RTA	1to29Minute	29	191
70	Male	Mod-severe	Fall	1to24Hour	25	193
58	Male	Mod-severe	Fall	1to24Hour	13	196
42	Male	Mod-severe	Fall	None	28	226
67	Female	Mod-severe	RTA	1to7days	20	183
26	Male	Mod-severe	Fall	None	13	181
60	Female	Mod-severe	Fall	None	12	186
43	Male	Mod-severe	Fall	1to24Hour	25	203
47	Male	Mod-severe	Fall	None	22	183
45	Male	Mod-severe	RTA	1to24Hour	16	190
52	Female	Mod-severe	RTA	1to7days	44	177
49	Male	Mod-severe	Fall	1to7days	26	219
75	Female	Mod-severe	Fall	None	44	183
70	Male	Mod-severe	RTA	1to7days	14	196
44	Male	Mod-severe	Fall	NK	24	166

47	Male	Mod-severe	Fall	1to7days	21	176
41	Female	Mod-severe	Fall	NK	20	235
60	Male	Mod-severe	Sports	NK	35	203

Table 3: Patient demographics of additional longitudinal subacute TBI patient cohort (n=25). M=male, F=female. RTA=road traffic accident, PTA=post traumatic amnesia. NK=not known, Mod-Severe=Moderate-to-severe TBI.

3.3.2 Neuropsychological and functional outcomes assessment

A standardized neuropsychological battery previously used to investigate cognitive impairment after TBI was implemented (Kinnunen et al., 2011; De Simoni et al., 2018). Tests were designed to investigate executive function, memory, processing speed and reasoning and included; the Trail Making Test (TMT) and Delis-Kaplan Executive Function systems (D-KEFS) Colour-Word Interference (Stroop) test to assess processing speed and executive function (Delis et al., 2001); the Peoples Test (PT) from the doors and peoples test to measure episodic memory (Weschler, 1945) as well as the Weschler Abbreviated Scale for Intelligence (WASI) Matrix reasoning task to assess abstract reasoning ability (Weschler, 1945). An additional computerised battery including three working memory tests was also included to assess working memory performance (Hampshire et al., 2012). Tasks included the Monkey Ladder (MKL), Paired Associates Learning (PAL) and Self-Ordered Search (SOS). For further details regarding cognitive tasks please refer to methods chapter 2, section 2.1. Self-report measures of functional outcomes, mood and sleep after injury were assessed using the Glasgow Outcome Scale-Extended (GOSE) (Jennett et al., 1981, Jennett & Bond., 1975), the Hospital Anxiety and Depression Scale (HADS) (Snaith., 2003) and the Pittsburgh Quality of Sleep Index (PSQI) (Buysse et al., 1989).

3.3.3 Structural MRI acquisition

Structural MRI was acquired using a 3T Siemens Magnetom Verio Syngo with a 32-channel head coil. All patients and controls were scanned using the same MRI machine and acquisition parameters. Structural MRI included a high-resolution T1-weighted MPRAGE, diffusion weighted imaging and fluid-attenuated inversion recovery (FLAIR) to identify focal lesions. Further details regarding acquisition parameters can be found in methods chapter two, section 2.3.

3.3.4 Delineation of focal lesion location

In house software (ImSeg) was used to delineate focal contusions and areas of missing brain as lesion masks on T1-weighted MPRAGE images. This allows to identify, and exclude, areas in a white matter tract that may bias the overall mean FA that are not representative of axonal injury. Lesion masks were manually drawn with FLAIR images overlaid to aid identification of boundaries of lesioned areas. All masks were drawn in native space and subsequently registered to standard space. Further details can be found in methods chapter two, section 2.2.5.

3.4 Statistical analysis

3.4.1 Diffusion tensor imaging group-level analysis

Diffusion weighted images (DWI) were processed using FSL's diffusion toolkit (FDT) and standard pre-processing techniques (Behren's et al., 2003) as outlined in methods chapter two section 2.4.1. To extract mean FA values for each tract region-of-interest (ROI) for each patient and control, the concatenated skeletonised images derived from TBSS were separated using fslsplit into their individualised FA skeleton maps. Tract ROI masks were then intersected with each individual skeletonised FA map to extract the mean FA for each individual within the selected ROI's using fslstats. As a summary measure to capture FA across the whole white matter, whole brain mean FA was also extracted for each individual by intersecting skeletonised FA maps with the whole brain mean FA skeleton mask derived from TBSS. This provides further investigation of the presence of generalised reductions in FA that may not be detected by the individual ROI's selected but remains an important factor in relation to cognitive and clinical outcomes (Kinnunen et al., 2010, Jenkins et al., 2017).

A group-level comparison of FA for patients and controls was applied using a repeated measures ANOVA across tract ROI's (excluding whole brain FA) to determine whether the patient cohort demonstrated evidence of axonal injury. To investigate the presence of axonal injury at the individual patient level, FA for all controls and the patient of

interest were used in the pipeline. A summary of the ROI's selected for use in the pipeline and the methodology to detect axonal injury are described in the following sections.

3.4.2 Pipeline for the diagnosis of axonal injury in individual patients

A summary of the methods used in the diagnostic pipeline can be found in Figure 39. Briefly: 1) skeletonised FA maps of the healthy control cohort and individual TBI patient are constructed using the TBSS pipeline. 1.1) If there is evidence of contusion/missing brain in the TBI patient, a lesion mask is manually delineated using ImSeg. The binarized lesion mask is then registered to standard space by first registering the subjects T1 to MNI152 1mm space using FLIRT and applying the transformation matrix to the lesion mask. The standardized lesion mask is then used to exclude lesioned areas from the tract ROI's by subtracting from all tract ROI masks using fslmaths. In this way, any tract ROI where an area of lesion overlaps is redefined to exclude this area from FA sampling. The mean FA for the resulting tract ROI masks is extracted for both the patient and the control cohort to allow for comparison of FA and used in the subsequent steps of the tool. If the mask includes a correction for the presence of a lesion, the control group FA is specifically calculated for this corrected mask. 2) Skeletonised FA maps (of the patient and control group) are intersected with tract ROI masks to extract mean FA for each ROI for each participant. 3) Checks for assumptions of normality are performed across each tract to determine whether parametric methods are appropriate. Distribution of FA and QQ plots in the healthy population are plotted and shapiro-wilks tests applied. 3.1) If assumptions of normality are not met, a rank-inverse normalisation can be applied to the data (i.e., applying the transformation to the control group and patient together) to provide ranked data with normal distribution. 4) Next, the mean and standard deviation of FA for each tract ROI across the control cohort is then calculated. 5) Patient Z-scores are then calculated for each ROI by subtracting the control groups FA from the individual patients and dividing by the control groups standard deviation ($z= (x-\overline{x})/\sigma$). A negative Z-score indicates a patients FA is lower than the control means 6) Z-scores are converted to P-values (two-tailed, with 95% confidence interval) and corrected for multiple comparisons across all tract ROI's investigated using FDR. Whole brain FA skeleton

values extracted using the whole brain mean FA skeleton mask are calculated as a stand-alone summary measure and is therefore not included in multiple comparisons correction. The patient FA is then plotted against the control cohort for each tract ROI to demonstrate abnormal tracts (e.g. tracts that have significantly lower FA in the patient compared to the control group, $p<0.05$, FDR corrected) for ease of interpretation for the user.

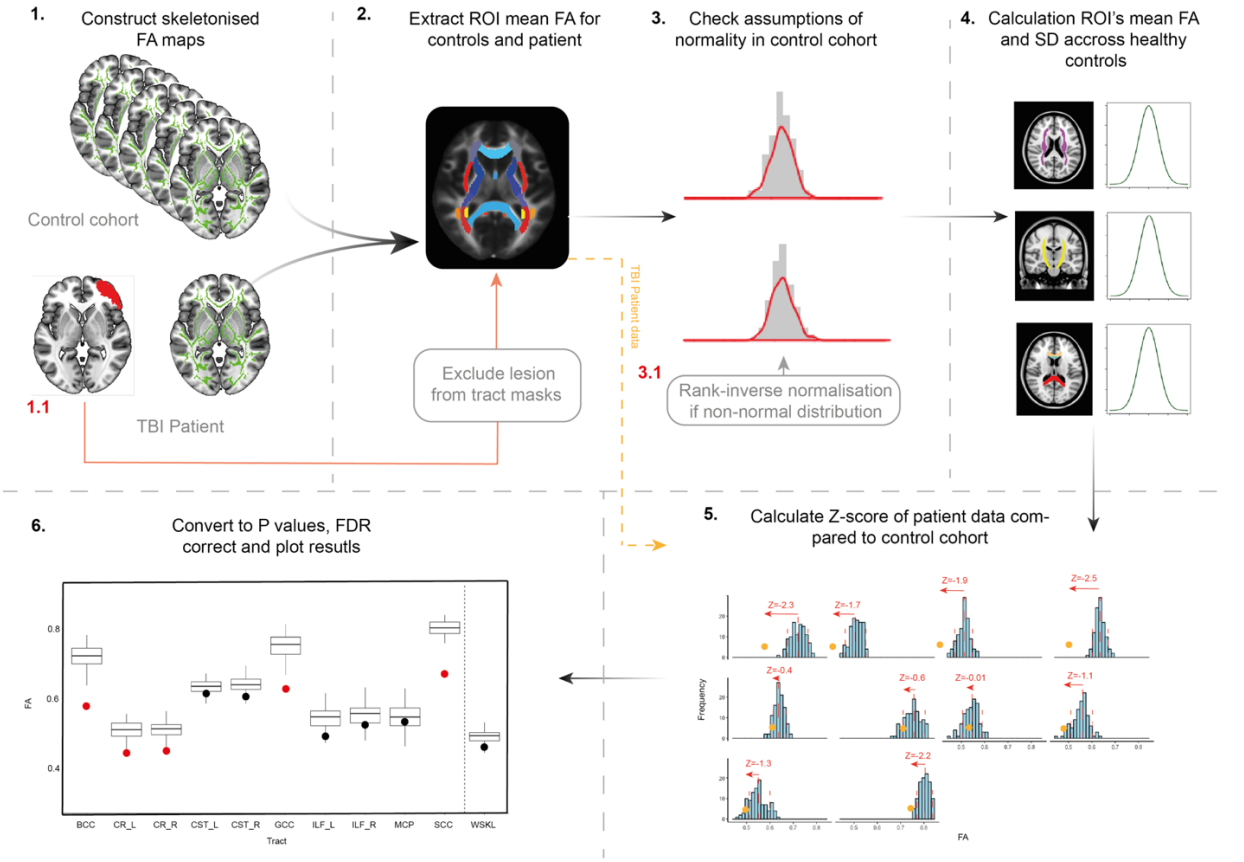


Figure 39: DTI diagnostic pipeline processing steps. 1. Skeletonised FA maps are derived for the patient of interest and the comparative control group using TBSS. 1.1. If a patient has evidence of contusion or missing brain, these areas are manually delineated using in house software (ImSeg) to produce a lesion mask. The lesion mask is then registered to standard MNI152 1mm space and subtracted from tract masks so that these regions are excluded from influencing subsequent FA measures. 2. Skeletonised FA maps from controls and individual patients are tract masks to extract mean FA value for each ROI for each individual. 3. Control FA distributions are assessed for assumptions of normality using histograms, QQ plots and Shapiro-Wilks tests. 3.1 If assumptions of normality are violated, rank-inverse normalisation is applied. 4. Control group mean FA and SD for each ROI is then calculated for use in Z-scoring. 5. Z-scores for each patient are calculated. 6. Z-scores for a patient are then converted to p-values (95% confidence interval, two tailed) and corrected for multiple comparisons using FDR. Whole brain FA skeleton is calculated as a stand-alone test Individual patient

data is then plotted against control group and significantly lower FA in patients are highlighted in red for ease of interpretation.

3.4.3 Selection of white matter tract ROI's for use in diagnostic tool

A total of 46 white matter tract ROI's were considered for use in the diagnostic tool (Table 4). Tracts were derived from the ICBM-81-DTI white matter atlas and included cortical and subcortical white matter projections. Details regarding the delineation of these regions have been previously reported (Oishi et al., 2008). To select the most reliable tracts with good sensitivity to axonal injury and high clinical relevance to impairments after TBI, a set of criteria was applied in a stepwise data-driven approach. It consisted of: 1) the exclusion of small tracts (tracts with number of voxels below median of all candidate tracts); 2) the identification of high reliability as quantified using intra-class correlation coefficient (ICC); 3) good anatomical coverage and sampling of association, projection and commissural white matter projections (Mori et al., 2008); and 4) clinical relevance to traumatic brain injury as defined by prior evidence of relationship to motor, cognitive and functional outcomes. We aimed at selecting ~10 tracts, to provide balance between good white matter coverage and power to detect axonal injury after correction for multiple comparisons. To allow comparison across hemispheres, tracts included both left and right hemispheres where possible.

Tract	Abbreviation
Anterior limb of internal capsule L	ALIC_L
Anterior limb of internal capsule R	ALIC_R
Body of corpus callosum	CCB
Cerebral peduncle L	CP_L
Cerebral peduncle R	CP_R
Cingulate_cing_L	CC_L
Cingulate_cing_R	CC_R
Cingulum_Hippocampus_L	CH_L
Cingulum_Hippocampus_R	CH_R
Corona Radiata L	CR_L
Corona Radiata R	CR_R

Corticospinal_L	CST_L
Corticospinal_R	CST_R
External capsule L	EXC_L
External capsule R	EXC_R
Fornix	Fnx
Fornix cres L	FC_L
Fornix cres R	FC_R
Genu of corpus callosum	CCG
Inf_fronto-occipital_fasc_L	IFOF_L
Inf_fronto-occipital_fasc_R	IFOF_R
Inf_longitudinal_fasc_L	ILF_L
Inf_longitudinal_fasc_R	ILF_R
Inferior cerebellar peduncle L	ICP_L
Inferior cerebellar peduncle R	ICP_R
Medial lemniscus L	ML_L
Medial lemniscus R	ML_R
Middle Cerebellar Peduncle	MCP
Pontine crossing tract	PCT
Posterior limb of internal capsule L	PLIC_L
Posterior limb of internal capsule R	PLIC_R
Posterior thalamic radiation L	PTR_L
Posterior thalamic radiation R	PTR_R
Retrolenticular part of internal capsule L	RLIC_L
Retrolenticular part of internal capsule R	RLIC_R
Splenium of corpus callosum	CCS
Superior cerebellar peduncle L	SCP_L
Superior cerebellar peduncle R	SCP_R
Superior fronto-occipital fasciculus L	SFOF_L
Superior fronto-occipital fasciculus R	SFOF_R
Superior longitudinal fasciculus L	SLF_L
Superior longitudinal fasciculus R	SLF_R
Tapetum L	TP_L
Tapetum R	TP_R
Uncinate fasciculus L	UF_L
Uncinate fasciculus R	UC_R

Table 4: List of candidate tracts considered for use in the diagnostic pipeline. L=left, R=right. Tracts were derived from the ICBM-81-DTI white matter template (Mori et al., 2008).

First, median tract size (number of voxels) was calculated across all 46 ROI's. Tracts with a total number of voxels lower than the median were excluded from the candidate pool. This ensures only the largest tracts are considered as previous evidence indicates erroneous and variable tensor fitting (thus low reliability) specific to FA in smaller tracts (Sairanen et al., 2017). The remaining candidate tracts were then tested for test-retest reliability by examining the average ICC of FA in twenty healthy controls scanned across three timepoints (year 1, 2 and 3). An ICC value above 0.6 indicates good reliability (Chinchetti., 1994), I therefore selected this as the threshold for the inclusion or exclusion of tracts. The remaining tracts were examined to determine good coverage of association, commissural and projection pathways as well as their relevance to TBI. Providing good anatomical coverage of the white matter in all directions ensures I am able to detect axonal injury due to rotational/shearing forces applied to the brain within a given direction (Ghajari et al., 2016). Additionally, white matter tracts relating to motor and cognitive impairments, as well as functional outcomes after TBI when damaged (Kinnunen et al., 2011, De Simoni et al., 2018, Jenkins et al., 2017), were considered as priority to retain if more than 20% of candidate tracts remained after application of the previous criteria.

3.4.4 Testing the effect of age on diagnosis

Normal aging is associated with changes in FA (Pfefferbaum et al., 2000) and may impact upon classification of normal vs. abnormal tracts if the patient and control cohort differs greatly in age. A repeated measures ANOVA was therefore applied to control data to examine if there was a main effect of age on FA across tracts. A one-way ANOVA was also applied to whole brain FA to examine the impact of age. I quantified the impact of ageing on diagnosis by comparing: 1) diagnosis of axonal injury without accounting for age using all controls; and 2) diagnosis of axonal injury using control data with the effect of age regressed out of the control and patient data. In the first method, each of the 92 patients were individually compared to all healthy controls using the diagnostic pipeline. The number of patients diagnosed as having a tract abnormality (as defined by one or more significantly abnormal tracts, $p<0.05$ FDR corrected, excluding the whole brain measure) were quantified. In the second method, all 92 patients and 103 controls were included in a multiple linear regression to regress age and age^2 out of FA to account for any non-linear relationships between age and

FA. The residuals from this regression were then used and each individual patient was compared to all 103 controls using the diagnostic pipeline.

3.4.5 Testing the impact of control sample size on diagnosis

The sample size of controls required to produce stable diagnosis performance is an important aspect. As diagnosis is derived using Z-scores, potential bias arises from small control sample sizes. I therefore investigated the effect of varying sample size on diagnostic rates using the whole control cohort (n=103). I randomly subsampled the control cohort to produce samples of 10, 20, 30, 40 and 50. Mean FA and its standard deviation from each ROI was then used to re-classify each of the 92 patients. This process was repeated 100 times for each control sample size and each individual patient to improve reliability of the estimate. The reliability of diagnosis within a given sample size was calculated using ICC of p values (FDR corrected) derived using the pipeline across all of the 100 sample size iterations for each patient. A high ICC indicates that the results derived for patients across all 100 sub-samples of a control N are reliable.

I then calculated rates of type 1 and type 2 errors at varying sample sizes by comparing diagnostic results to those derived using the whole control cohort. Taking the results of all 100 iterations for a patient, I deemed an abnormal tract (e.g. axonal injury) to be present if more than 5% of the 100 test iterations identified it as such. In this way, I assumed a tract to be deemed abnormal if diagnosed as such above an expected 5% false positive rate when testing at a given sample size 100 times. I quantified the number of false positives (a patient is identified as having evidence of a white matter abnormality in at least one tract in the smaller sample size but not with the whole control cohort), false negatives (a patient is not deemed abnormal in contrast to the whole control cohort diagnosis), true negatives (a patient is not deemed abnormal in agreement with the whole control cohort diagnosis) and true positives (a patient is deemed abnormal in agreement with the whole control cohort diagnosis). Finally, I calculated measures of sensitivity (accurately identifying a patient as abnormal) and specificity (accurately identifying a patient as normal), positive predictive values (PPV) (the probability of patients being identified as abnormal using the smaller sample size are abnormal using all controls) and negative predictive values as measures of

'diagnostic accuracy' in the context of a smaller sample size compared to diagnosis derived from the whole control cohort.

3.4.6 Testing the specificity of the diagnostic pipeline

To test the specificity of the diagnostic pipeline, I then applied the diagnostic process to each of the 103 healthy controls using a leave-one-out approach. This allowed the rate of false positive tracts to be identified. Diagnosis was performed on non-age regressed data. If the pipeline had low specificity to axonal injury in TBI we would expect to see false positive rates exceed an acceptable rate of 5% in healthy controls. This process was also repeated using varying sample sizes in the same manner as TBI patients to determine whether smaller sample sizes impacted on false positive rates in healthy controls.

3.4.7 Neuropsychological assessment and functional outcomes

Performance on individual neuropsychological tests were compared between TBI patients and controls. As data was not normally distributed, non-parametric tests (Wilcoxon rank sum tests) were used. To account for the issue of multiple comparisons, a false discovery rate (FDR) correction was applied within each cognitive domain assessed. Composite scores for each cognitive domain (executive function, information processing, reasoning and episodic memory) were calculated by averaging across tasks within a given cognitive domain. Scores were then normalized for comparison across domains. In addition, a composite measure was derived across three computerised working memory tasks and performance compared between patients and controls for each task using a repeated measure ANOVA. Next, patients with a DTI abnormality as determined by the diagnostic pipeline, were compared to those with no abnormality and healthy controls using a factorial ANOVA's with age included as an independent variable to determine if this was associated to cognitive performance (CogScore~Diagnosis+Age). Functional outcomes, mood and sleep assessed using the GOSE, HADS and PSQI respectively were also compared between patients with or without abnormalities. Furthermore, to assess whether certain tracts had a greater association to cognitive composite measures, correlational analysis was performed between each tract and each composite measure for patients. Due to high collinearity between tracts, multiple linear regression was not applied.

Results from correlational analysis were therefore corrected for multiple comparisons using an FDR approach.

3.4.8 Testing the effect of time since injury on diagnosis

An important issue when examining FA alterations after TBI is the effect of time since injury. After the initial injury, dynamic changes to FA can occur leading to elevated FA acutely and progressive reductions chronically, via neuroinflammatory processes (Werner & Engelhard., 2007; Sharp et al., 2014). These longitudinal alterations may impact upon the detection of abnormalities across different phases of injury and is an important consideration when implementing the pipeline. From a clinical perspective, detection of axonal injury at an acute timepoint may be particularly beneficial in guiding the initial management of patients but may be challenging if fluctuations in FA are present and reliability is low. I therefore investigate the relationship between time since injury (in months) and diagnosis using the pipeline in two patient cohorts. First, I investigate whether significant differences in time since injury are present in the large cohort of chronic patients (n=92) identified with or without abnormalities using an unpaired two-tailed t-test. I apply bivariate correlations to determine whether there is a significant relationship between time since injury and FA across all tracts and mean whole brain skeleton in patients after correcting for age and multiple comparisons using FDR.

Next, I investigate the reliability of the diagnostic pipeline in the subacute phase of injury using an additional cohort of patients (n=25) scanned during subacute (10 days-6 weeks) and chronic phases (~6 months) of injury. I compare measures of FA across the two timepoints for all tracts using a repeated measures ANOVA and for whole brain skeleton using a paired t-test. Next, I examine the diagnostic results of patients using the pipeline, and investigate the reliability of diagnosis by calculating the intraclass correlation coefficients of tract abnormalities between the two timepoints (as quantified by Z-score and p values, FDR corrected, as derived from the diagnostic pipeline). To ensure comparisons within subjects across the two time-points are consistent, I exclude areas of lesion (inclusive of oedema) identified at the subacute phase of injury from the analysis at both timepoints.

3.5 Results

3.5.1 Tract selection

Of the 46-candidate tract ROI's considered, a total of seven tracts (10 ROI's) were selected for use in the diagnostic tool after application of a stepwise selection process. First, I considered the size of the tracts. Fractional anisotropy (FA) calculated from smaller tracts can be unreliable, in part because of errors in tensor construction (Sairenan et al., 2017) and problems skeletonising the ROI leading to partial volume effects (Smith et al., 2006; Bach et al., 2014). Hence, I focused analysis on the largest tracts in the set of ROIs by excluding those smaller than the median voxel size, leaving a total of 20 ROI's (Fig. 40A).

Next, I calculated the reliability of these tracts by measuring the test-retest reliability of FA using data from 20 healthy controls scanned across three timepoints approximately 12 months apart (Fig. 40B). Intraclass correlation coefficients (ICC) were calculated to quantify reliability and tracts with a good ICC (>0.6) were retained (Chichetti, 1994). This criterion led to the posterior thalamic radiations being removed (Fig 40C). A total of 11 tracts (18 separate ROI's) remained after these criteria were applied. Fractional anisotropy values within these tracts were normally distributed as defined using the Shapiro-Wilks test of normality ($p>0.05$) confirming that the use of parametric Z-scoring to identify abnormalities was appropriate.

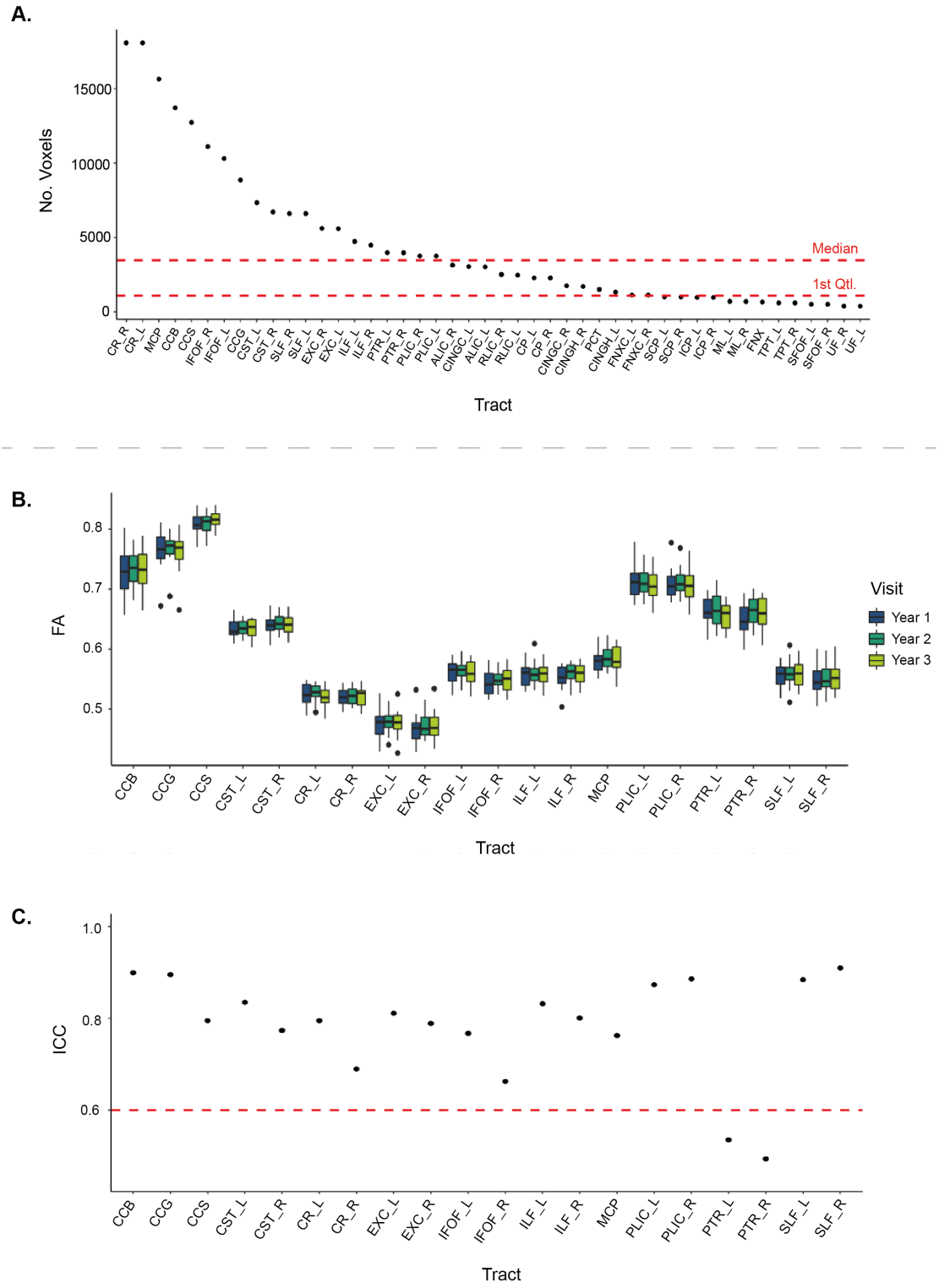


Fig 40: Data-driven tract selection. A: Voxel size of all 46 candidate tracts ordered from largest to smallest. Median and first interquartile range demonstrated on red dashed lines. **B.** Standard deviation of mean FA in each of the remaining candidate tracts across healthy control population with longitudinal

data (n=20). **C.** Reliability of tracts calculated using intraclass correlation coefficient (ICC) using longitudinal data from healthy control subset.

From these 18 ROIs, 10 were selected to provide sampling of the projection, association and commissural pathways that are commonly affected after TBI and relate to the motor, cognitive and emotional symptoms often observed. Tracts selected were: the body, genu and splenium of the corpus callosum (CCB, CCG, CCS), the corticospinal tract (left and right; CST_L, CST_R), the corona radiata (left and right; CR_L, CR_R), the inferior longitudinal fasciculi (left and right; ILF_L, ILF_R) and the middle cerebellar peduncle (MCP) (Fig. 41). The corpus callosum is commonly disrupted after TBI due to high strain forces (Ghajari et al., 2017), is associated with cognitive impairment (Kinnunen et al., 2010; Arenth et al., 2016) and is the largest among the commissural fibres. The corticospinal tracts consist of major projection fibres and are associated with motor deficits after TBI (Caeyenberghs et al., 2011; Choi et al., 2012). The corona radiata is a large projection fibre tract and is associated with motor and cognitive impairments after TBI when damaged (Caeyenberghs et al., 2011; Kraus et al., 2007). The inferior longitudinal fasciculi are association tracts in the inferior portion of the brain and are associated with cognitive and functional outcomes after TBI (Edlow et al., 2016). Finally, the middle cerebellar peduncle was selected due to cerebellar atrophy and damage observed after TBI and its association with cognitive and vestibular/balance symptoms after TBI (Drijkoningen., 2011; Cole et al., 2018). Importantly, these tracts have varying anatomical orientations, which is likely to be important in assessing diffuse axonal injury because high strain rates are likely to have distinct effects depending on the orientation of the tracts assessed (Colgan et al., 2010; Halabieh & Wan., 2008; Parizel et al., 1998).

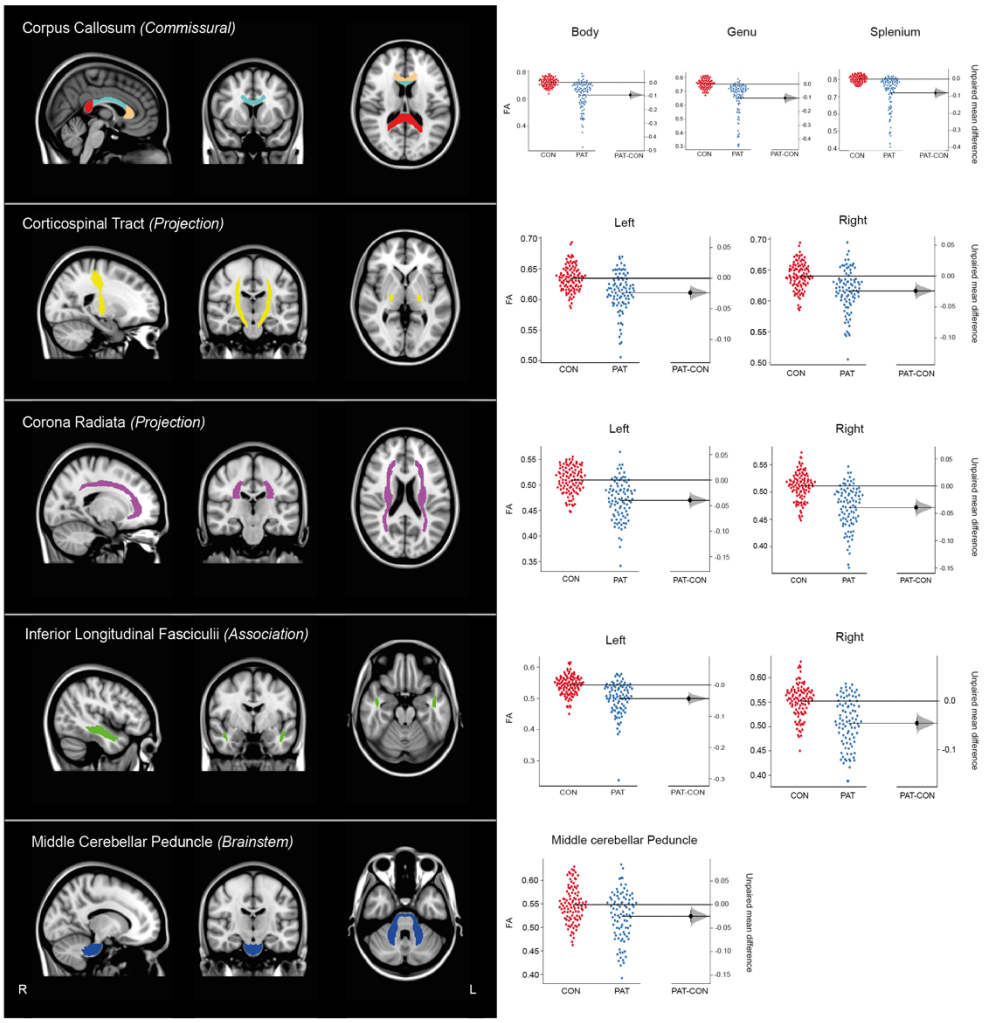


Figure 41: Tracts selected for use in diagnostic pipeline. Rendering of tracts selected for use in the DTI pipeline. The corpus callosum demonstrates the three subdivisions as; red=splenium, blue=body and orange=genu. L=left, R=right. Estimation plots representing individual mean FA values for TBI patients and controls. Black lines represent group level means. A measure of effect size and its 95% confidence intervals calculated through nonparametric bootstrap resampling are plotted on the vertical bar on a separate but aligned axes (Ho et al., 2019).

3.5.2 TBI patients demonstrate significant group-level reductions in FA

Comparison of TBI and control data showed significant reductions in FA in patients. A repeated measures ANOVA revealed a significant main effect of group ($F(1,1960)=456.57, p<0.001$) such that TBI patients had lower FA compared to controls. A significant tract by group interaction was also observed ($F(9,1960)=15.17, p<0.001$) with post-hoc t-tests revealing significantly lower FA in the body, genu and splenium of the corpus callosum, the corona radiata and inferior longitudinal fasciculi in patients ($p<0.001$). Comparison of whole brain mean FA

skeleton revealed significantly lower FA in patients compared to controls ($t(123.4)=5.84, p<0.001$). There were no group level differences in the corticospinal tracts or middle cerebellar peduncle, although there were individuals who showed clearly abnormally low FA in these tracts, illustrating the importance of developing the individual tool for DTI testing (Fig. 41).

3.5.3 An individual test of white matter damage

I next applied an individualised approach to diagnosis axonal injury based on the assessment of whether FA in each patient's white matter tract was significantly different from the normal range after correction for multiple comparisons. An example of an individual patient's diagnostic results can be found in Figure 42A. Highly variable patterns of tract abnormalities were seen in patients. Of the 92 patients individually compared to the healthy control population, a total of 48 patients (52%) were identified as having at least one tract abnormality compared to the healthy population after FDR correction. Of the patients classified as abnormal, over two thirds had abnormalities in four or more tracts. 35 patients (38%) were also found to have an abnormal whole brain mean FA compared to healthy individuals with only one patient demonstrating an abnormal whole brain mean FA with no evidence of abnormalities in any tracts. The body, genu and splenium of the corpus callosum showed the highest rates of abnormalities within the patient population (>35%) with the lowest percentage of abnormalities observed in the middle cerebellar peduncle (15%) (Fig. 42B).

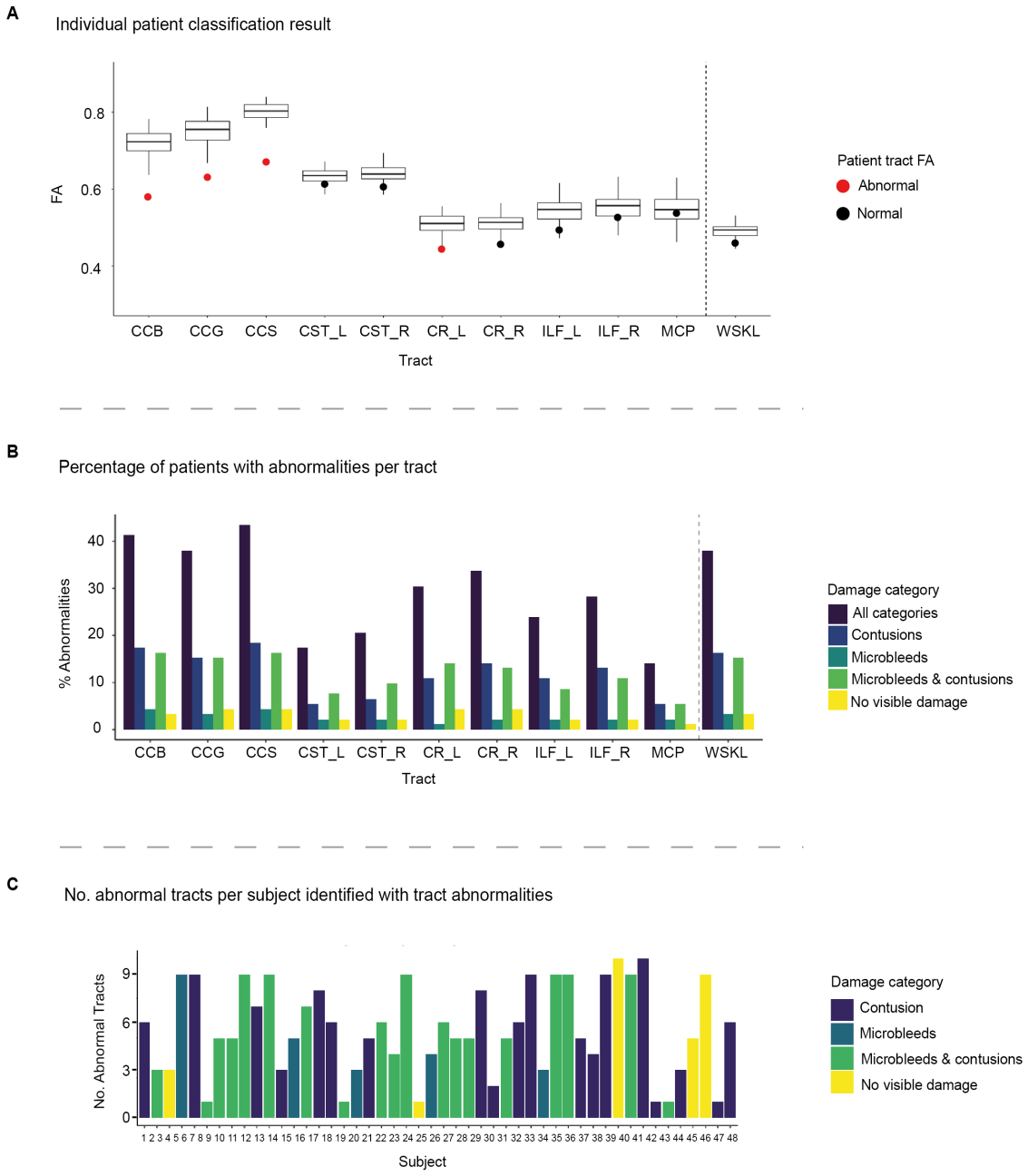


Figure 42: Diagnostic results using the DTI diagnostic pipeline for each individual TBI patient. A. Example of individual patient diagnostic results across all tracts and whole brain skeleton. Individual points denote the individual patient FA. Boxplots represent the distribution of mean FA for a given tract across all healthy controls (n=103). A red point indicates a significantly abnormal FA value for the individual patient compared to controls ($p<0.05$, 95% confidence interval, FDR corrected). Black point represents patients mean FA value within normal ranges compared to healthy controls ($p<0.05$, 95% confidence interval, FDR corrected). **B.** Percentage of patients identified as having an abnormality in tract ROI's and whole brain skeleton as quantified by diagnostic pipeline p-value (two-tailed, 95% confidence interval, FDR corrected). All categories=total percentage of abnormalities across all damage

categories. **C.** Number of tract abnormalities per patient identified as abnormal using diagnostic pipeline compared to 103 healthy controls. Colours represent damage category of a patient, e.g. yellow indicates where a TBI patient has tract abnormalities but no evidence of damage on routine clinical MRI sequences.

3.5.4 Diffusion abnormalities in relation to other imaging measure of TBI

I next examined how DTI abnormalities related to the presence or absence of other imaging evidence of brain injury (contusion, microbleed, microbleed and contusion or none visible). Patients in all four categories were found to have tracts abnormalities (Fig. 42C). 19 out of 36 patients with contusions (52%) and 19 out of 29 patients with both contusions and microbleeds (65%) were found to have tract abnormalities. Five out of the 11 patients with only microbleeds (45%) were also identified as having tract abnormalities. Importantly, five out of 16 patients with no other evidence of brain injury (31%) were identified as having tract abnormality. For the whole brain white matter measure, 14 patients had abnormal whole brain FA measures in patients with both contusion and microbleeds (48%), 15 with contusions (42%), three with microbleeds (27%) and two with no visible damage on MRI (31%).

3.5.5 Susceptibility weighted imaging and diffusion MRI provide distinct information

Microbleeds have sometimes been used as a surrogate marker of DAI (Scheid et al., 2006), but are actually a marker of diffuse vascular injury. This may co-occur with DAI but can be distinct (Kinnunen et al., 2011; Griffin et al., 2019). Hence, it is important to understand the relationship between DTI and SWI findings. SWI abnormalities were distinct from diffusion abnormalities as illustrated by the distinct groups of patients identified with or without microbleeds. In one subgroup, patients had microbleed abnormalities (microbleeds or microbleeds and contusions) but no diffusion abnormalities (n=16, 40%). A second subgroup had diffusion abnormalities and no microbleed abnormalities (n=24, 46%), whilst a third subgroup had both microbleed and diffusion abnormalities (n=24, 60%).

3.5.6 Controlling for the presence of focal lesions

Focal lesions are commonly seen after TBI and can produce diffusion abnormalities, simply because of obvious disruption to white matter structure within a focal lesion.

My main goal is to quantify white matter structure in regions without obvious focal injury. Therefore, my analysis pipeline controls for the presence of focal lesions by excluding them on a case-by-case basis. I investigate the impact of this by calculating FA measures with and without the control of focal injury. Lesion masks were generated for brain injury using T1 and FLAIR imaging. These areas were then excluded from the calculation of tract FA and classification performed. 64 patients were identified as having a focal contusion/area of missing brain in a typical distribution for TBI (Fig. 43A). Of those patients, 38 were also identified as having an abnormality in at least one tract. 29 patients with abnormalities in a tract were also found to have abnormal whole brain skeleton FA values when including lesioned areas in my classification. After exclusion of areas of lesion for each patient and the whole control cohort, 36 of the 38 patients remained abnormal. All 29 patients showed whole brain FA abnormalities also demonstrated these after exclusion of lesioned areas (Fig. 43B). A summary of the classification results with and without correction for lesion can be found in appendix table 1.

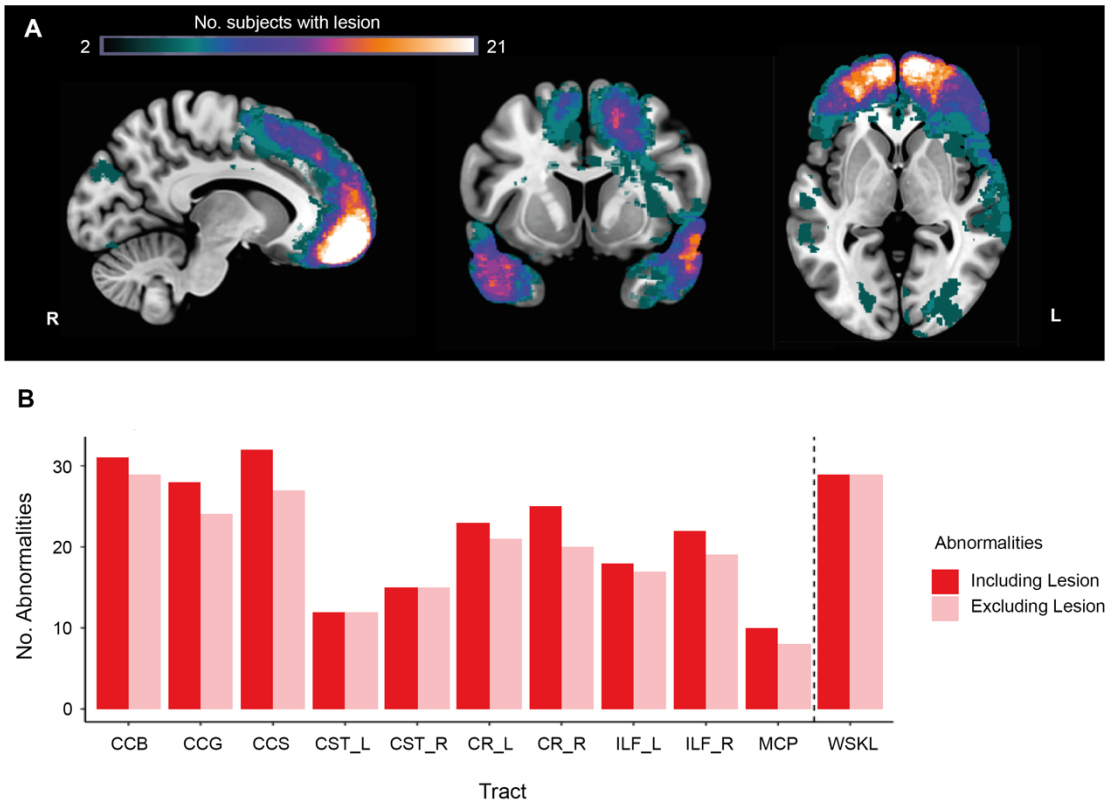


Figure 43: Diagnostic results when including or excluding areas of lesion. A. Lesion overlap map of the 64 patients identified as having a contusion/area of missing brain. Lesion masks are averaged

across patients to demonstrate areas of high overlap (bright white) and areas of low overlap (dark green) across patients. **B.** Tract abnormality rates within the 64 patients when including lesioned areas (red) and when excluding areas of lesion (pink).

3.5.7 Individual case studies

The results of the diagnostic pipeline are illustrated with four case studies, which highlight how variable DTI findings can be in relation to conventional imaging results, as well as functional, cognitive and psychiatric outcomes (Fig. 44). Case study one is a 51-year-old male with moderate-severe traumatic brain injury as a result of a road traffic accident (lowest GCS 3, PTA>7 days). Conventional MRI showed evidence of frontal contusions and microbleeds. Upper/moderate disability was present (GOSE=6) with no severe sleep disturbances (PSQI=7), but significant depressive symptoms (HADS anxiety=4, depression=17). Cognitive testing showed performance across cognitive domains to be within normal ranges when compared to healthy individuals (reasoning z=0.92, memory z=0.19, executive function z=-0.90 and information processing z=-0.3975212). DTI diagnostics showed no abnormalities.

Case study two is a 20-year-old male with moderate-severe TBI resulting from of a fall from height (>1m) onto concrete (lowest GCS 3, PTA 28 days). Conventional MRI showed extensive microbleeds but no focal injury. Upper-moderate disability was present (GOSE=6), no severe sleep disturbances (PSQI=6) and no anxiety or depression (HADS anxiety=1, depression=1). Cognitive testing demonstrated significantly poorer performance on memory ($z=-3.14, p<0.001$), executive function ($z=2.90, p<0.001$) and information processing ($z=7.14, p<0.001$) compared to healthy controls. Extensive white matter abnormalities were identified in 9 out of the 10 tracts as well as abnormalities in whole brain FA.

Case study three is a 43-year-old male with moderate/severe TBI resulting from road traffic accident in childhood (~two weeks of loss of consciousness, GCS/PTA unknown). Conventional MRI showed no evidence of contusions or microbleeds. There was a good functional recovery (GOSE=8), no sleep difficulties (PSQI=4) and no anxiety or depression (HADS=0). Cognitive impairments in memory ($z=-2.33$, $p=0.02$) and executive function ($z=2.19$, $p=0.03$) were observed when compared to

healthy controls. Diagnosis using the pipeline provided evidence of axonal injury in the three subdivisions of the corpus callosum as well as the corona radiata bilaterally.

Case study four is a 35-year-old male with moderate/severe TBI resulting from assault with a weapon (LOC several minutes, GCS unknown, 2 days PTA). Conventional MRI showed microbleeds and superficial siderosis. There was a good outcome (GOSE=8), with sleep disturbances (PSQI=8), and no severe anxiety or depression (HADS, anxiety=3, depression=0). Performance across all four cognitive domains was within normal ranges when compared to healthy controls (memory $z=-0.50$, reasoning $z=0.91$, executive $z=-0.15$, information processing $z=0.13$, $p>0.05$). Results from the diagnostic pipeline indicated no evidence of axonal injury in any tract or within whole brain FA.

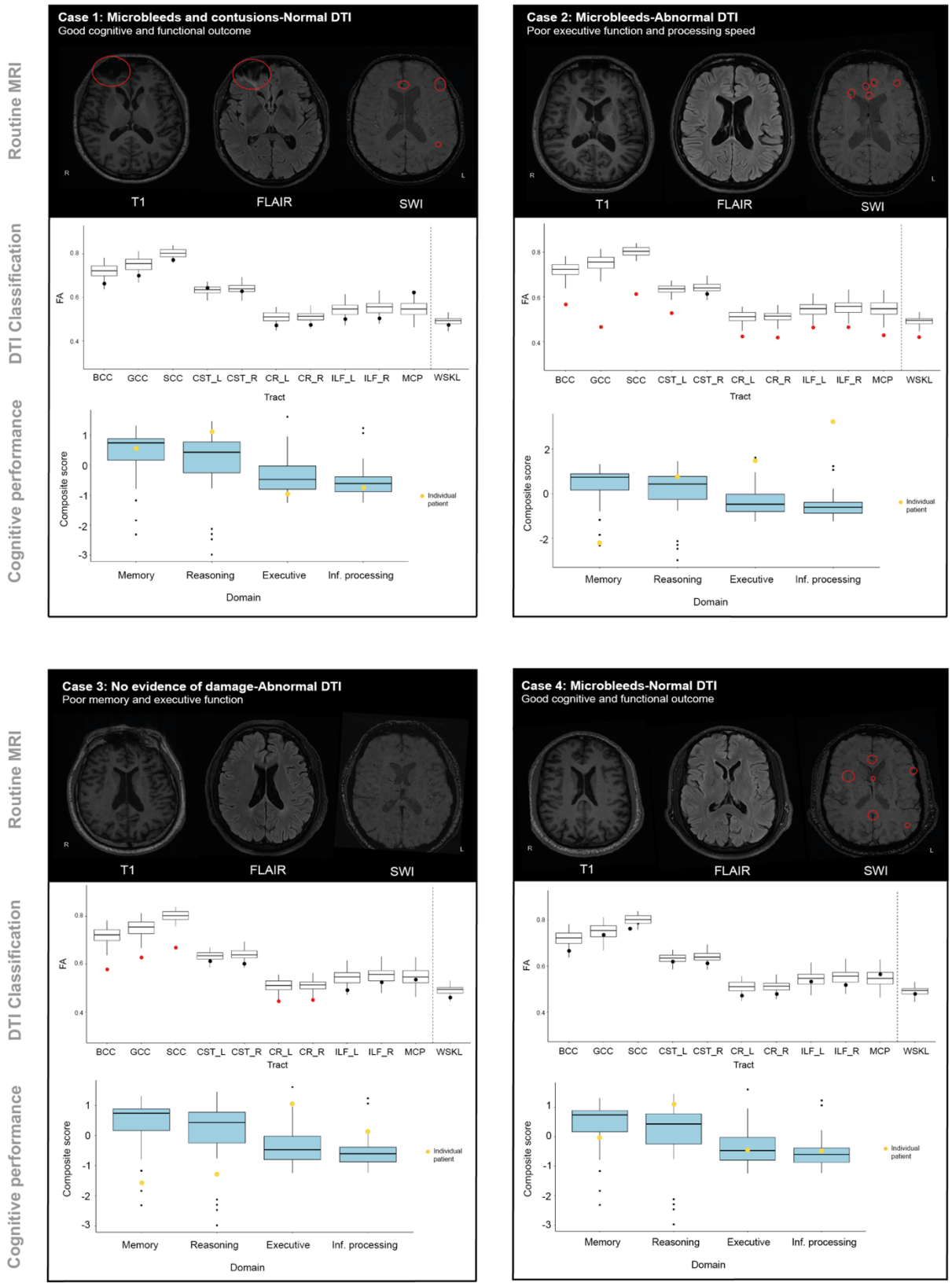


Figure 44: Individual case studies. Routine MRI scans including T1-MPRAGE, SWI and FLAIR of four moderate-severe TBI patients classified using the diagnostic pipeline are observed on the top row of the case study boxes. Areas of visible contusion or microbleeds are highlighted by red circles and

confirmed in radiological reports by a consultant neuroradiologist. The second row of the case studies box demonstrates the patients individual DTI diagnostic results. Boxplots represent FA of the control cohort used in the tool (n=103). Single points on the plot represents the individual patient assessed with the tool. Black dots represent where a patients does not have a significantly abnormal FA within a given ROI. Red points indicate where patients have a significantly abnormal FA compared to the healthy control cohort, $p<0.05$, 95% confidence interval, FDR corrected. Bottom row of the case studies illustrate individual patients' cognitive performance (yellow dot) compared to the control cohort (n=35) highlighted as blue boxplots. Lower scores in the memory and reasoning domains indicate poorer performance whilst higher scores in the executive and information processing domains indicate poorer performance due to slower reaction times.

3.5.8 Controlling for age in diffusion measurements

Ageing impacts on diffusion MRI measures (Fig. 45). Hence, the relationship between FA and age could influence diagnostic results. This is supported by a significant main effect of age ($F(1,1010)=79.7, p<0.01$) as FA is lower in older individuals. As expected, a significant main effect of age on whole brain mean FA skeleton was also observed ($F(1,101)=18.74, p<0.001$).

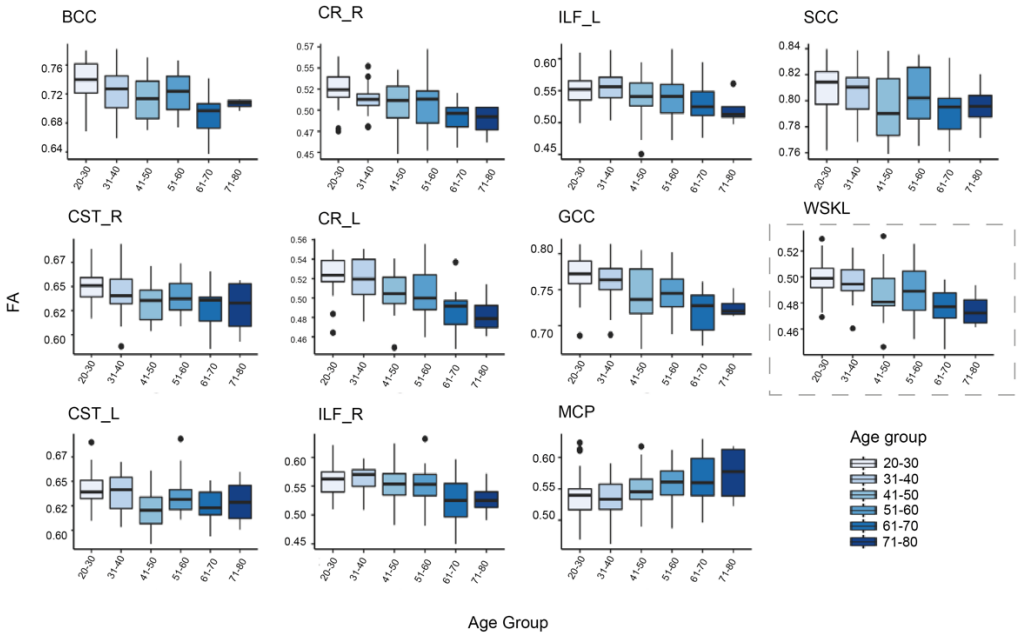


Figure 45: Tract mean FA for healthy control cohort, grouped by age. BCC=Body of corpus callosum, CR_R= right Corona Radiata, ILF_L=Left inferior longitudinal fasciculus, SCC=Splenium of corpus callosum, CST_R=right corticospinal tract, CR_L= left corona radiata, GCC=Genu of corpus callosum, WSKL=Whole brain white matter skeleton, CST_L=left Corticospinal tract, ILF_R=right inferior longitudinal fasciculus, MCP=Middle cerebellar peduncle.

Therefore, I examined the impact of accounting for age when using the diagnostic tool. I repeated classification of the same 92 patients and healthy controls using FA data with the effect of age regressed out. Both Age and Age^2 was regressed out of FA using multiple linear regression and the residuals were then used in the diagnostic tool. As with non-age regressed data, the same 48 patients (52%) were identified as having at least one abnormal tract compared to healthy controls (Fig. 46). A summary of individual classification results with and without age correction can be found in Table 5.

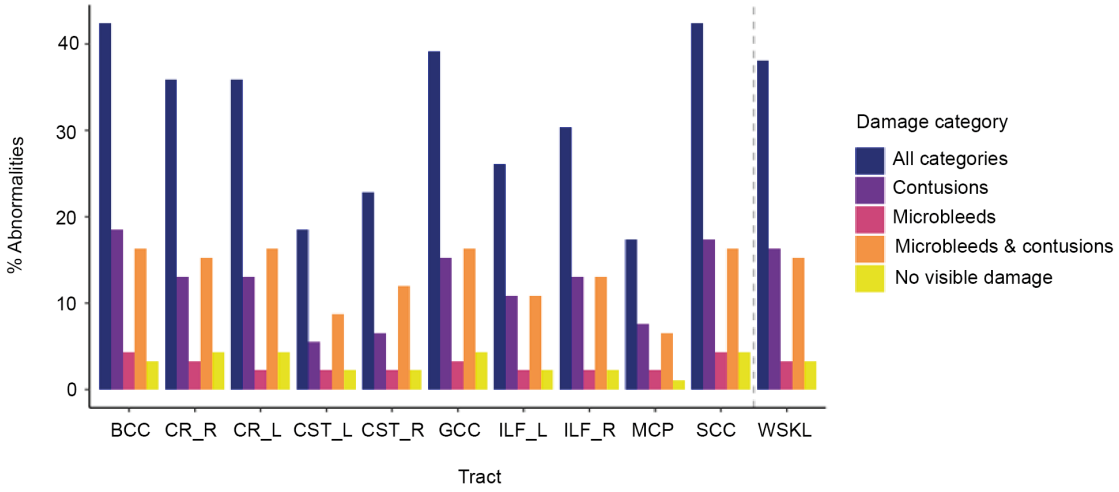


Fig 46: Diagnostic results for each tract when controlling for age. Percentage of patients identified as having an abnormality in tract ROI's and whole brain skeleton as quantified by diagnostic pipeline p-value when regression age and age^2 out of FA (two-tailed, 95% confidence interval, FDR corrected). All categories=total percentage of abnormalities across the four damage categories defined using MRI.

Routine MRI findings	No. of abnormal tracts	No. abnormal tracts (accounting for age)	Whole brain white matter skeleton	Whole brain white matter skeleton (accounting for age)
Contusion	6	7	Abnormal	Abnormal
Microbleed	0	0	Normal	Normal
Contusion & Microbleed	3	7	Abnormal	Abnormal

No visible damage	3	3	Normal	Normal
Microbleed	9	9	Abnormal	Abnormal
Contusion	0	0	Normal	Normal
Contusion & Microbleed	0	0	Normal	Normal
Contusion & Microbleed	0	0	Normal	Normal
Contusion	9	9	Abnormal	Abnormal
Contusion & Microbleed	1	4	Normal	Abnormal
Microbleed	0	0	Normal	Normal
Contusion & Microbleed	5	5	Abnormal	Abnormal
Microbleed	0	0	Normal	Normal
No visible damage	0	0	Normal	Normal
Contusion & Microbleed	5	7	Abnormal	Abnormal
Contusion & Microbleed	9	9	Abnormal	Abnormal
No visible damage	0	0	Normal	Normal
No visible damage	0	0	Normal	Normal
Contusion	7	7	Abnormal	Abnormal
Contusion & Microbleed	9	10	Abnormal	Abnormal
Contusion & Microbleed	0	0	Normal	Normal
Contusion	3	5	Abnormal	Abnormal
Microbleed	5	7	Abnormal	Abnormal
Contusion & Microbleed	0	0	Normal	Normal
Contusion & Microbleed	7	9	Abnormal	Abnormal
Contusion	0	0	Normal	Normal
Contusion	8	9	Abnormal	Abnormal
Contusion	6	6	Normal	Normal

No visible damage	0	0	Normal	Normal
Contusion & Microbleed	1	1	Normal	Normal
Microbleed	3	3	Normal	Normal
Contusion	0	0	Normal	Normal
Contusion	5	5	Abnormal	Abnormal
Contusion & Microbleed	6	6	Normal	Normal
Contusion & Microbleed	0	0	Normal	Normal
Contusion	0	0	Normal	Normal
Contusion	0	0	Normal	Normal
Contusion & Microbleed	0	0	Normal	Normal
Contusion & Microbleed	4	7	Abnormal	Abnormal
Contusion	0	0	Normal	Normal
Contusion & Microbleed	9	9	Abnormal	Abnormal
Contusion	0	0	Normal	Normal
No visible damage	0	0	Abnormal	Abnormal
No visible damage	0	0	Normal	Normal
Contusion	0	0	Normal	Normal
No visible damage	1	1	Normal	Normal
Microbleed	4	4	Normal	Normal
Contusion & Microbleed	6	6	Abnormal	Normal
Contusion	0	0	Normal	Normal
Microbleed	0	0	Normal	Normal
Contusion & Microbleed	5	6	Normal	Abnormal
No visible damage	0	0	Normal	Normal
Contusion & Microbleed	5	3	Abnormal	Normal

Contusion	0	0	Normal	Normal
Contusion	8	7	Abnormal	Abnormal
Contusion & Microbleed	0	0	Normal	Normal
Contusion	2	2	Normal	Normal
Contusion	0	0	Normal	Normal
Contusion & Microbleed	0	0	Normal	Normal
Contusion & Microbleed	0	0	Normal	Normal
Contusion & Microbleed	5	5	Abnormal	Abnormal
Contusion	0	0	Normal	Normal
Contusion	0	0	Normal	Normal
Contusion	6	6	Abnormal	Abnormal
No visible damage	0	0	Normal	Normal
Microbleed	0	0	Normal	Normal
No visible damage	0	0	Normal	Normal
Contusion	9	9	Abnormal	Abnormal
Microbleed	3	3	Abnormal	Abnormal
Contusion & Microbleed	9	8	Abnormal	Abnormal
Contusion & Microbleed	9	9	Abnormal	Abnormal
Contusion	5	6	Abnormal	Abnormal
Contusion	4	3	Abnormal	Abnormal
Contusion	9	9	Abnormal	Abnormal
No visible damage	10	10	Abnormal	Abnormal
Contusion & Microbleed	9	9	Abnormal	Abnormal
Contusion	10	10	Abnormal	Abnormal
Contusion	0	0	Normal	Normal
Contusion	1	1	Normal	Normal
Contusion & Microbleed	1	1	Normal	Normal
Contusion	3	3	Abnormal	Abnormal

No visible damage	5	5	Normal	Normal
No visible damage	0	0	Normal	Normal
No visible damage	9	9	Abnormal	Abnormal
No visible damage	0	0	Normal	Normal
Contusion	1	1	Normal	Normal
Contusion & Microbleed	0	0	Normal	Normal
Contusion	0	0	Normal	Normal
Microbleed	0	0	Normal	Normal
Contusion	0	0	Normal	Normal
Contusion	0	0	Normal	Normal
Contusion	6	6	Abnormal	Abnormal

Table 5: Diagnostic results for individual patients with and without accounting for age.

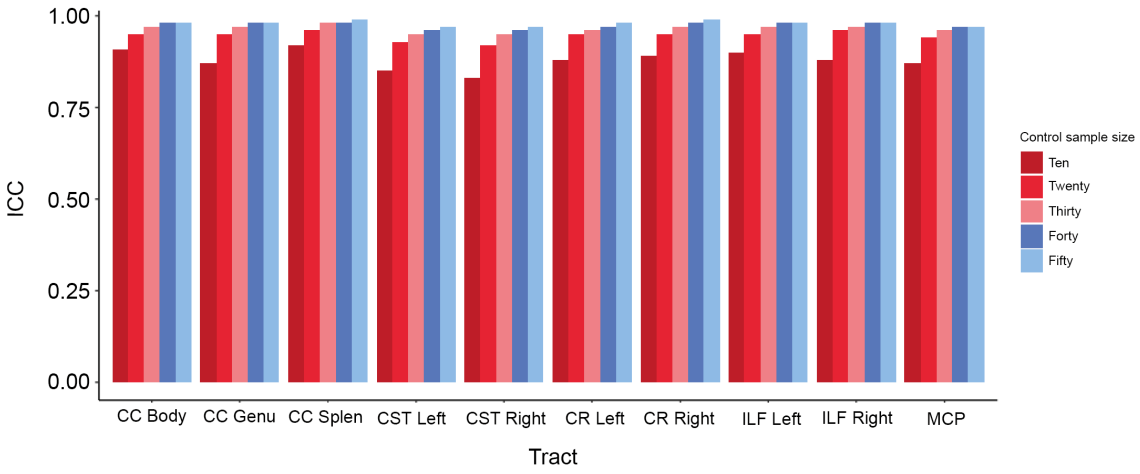
3.5.9 Control sample size influences specificity of diagnosis

An important practical consideration is the size of a control group collected on the same scanner that is necessary to produce stable diagnostic results. To investigate this, I examined diagnostic rates of patients (e.g. normal or abnormal) across a range of control group sample sizes (10, 20, 30, 40 and 50). Intraclass correlation coefficients were calculated for tract corrected p values derived for each patient across 100 iterations for each sample size (Fig. 47A). High ICC was observed for all tracts and sample sizes (e.g. greater than 0.67), however smaller sample sizes demonstrated the lowest ICC indicating lower reliability.

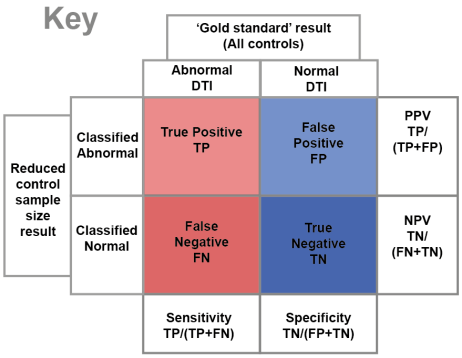
To assess the impact of control group sample size on sensitivity and specificity, type 1 and type 2 errors were quantified (Fig. 47B). When compared to the diagnostic rates using the whole control cohort, no false negatives were observed across any of the sample size results i.e. no patient was diagnosed as having normal DTI in smaller control group sample size tests when also diagnosed as having abnormal DTI using the whole control cohort. Similarly, all patients diagnosed as abnormal using the whole control group, were also found to be diagnosed as abnormal across all smaller sample size tests, demonstrating 100% sensitivity. In contrast, higher rates of false positives

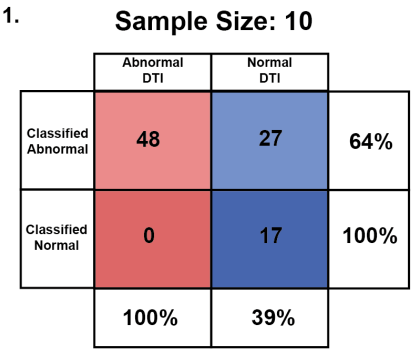
(patients deemed abnormal in smaller sample sizes in contrast to the whole control group) were observed when smaller the control group sample size used. The smallest sample size of 10 identified 27 additional patients leading to a 39% specificity rate. Specificity more than doubled when using a control sample size of 30 (specificity=80%) and only incrementally improved when using 40 (82%) or 50 healthy controls (84%) to classify DTI abnormalities in individual patients. Similarly, the positive predictive value increased by 20% between sample size of 10 to 30, only incrementally increasing with sample sizes greater than 30.

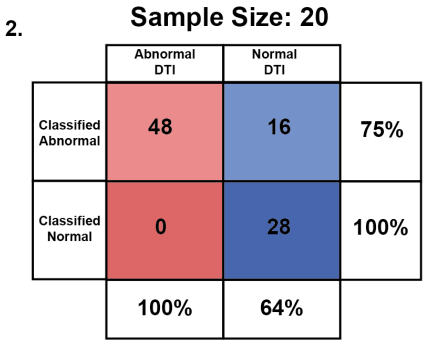
A.

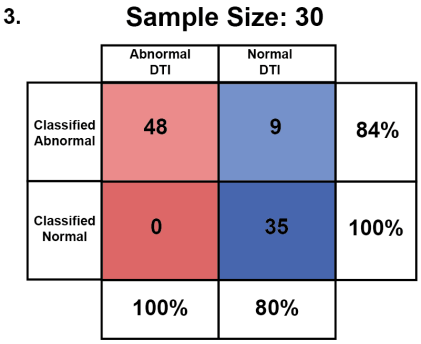

1.00
0.75
0.50
0.25
0.00
ICC
CC Body
CC Genu
CC Splen
CST Left
CST Right
CR Left
CR Right
ILF Left
ILF Right
MCP
Tract
Control sample size
Ten
Twenty
Thirty
Forty
Fifty

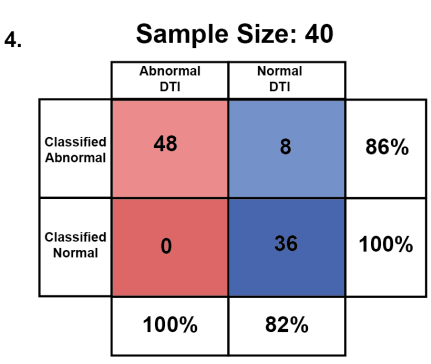
B.


Key
'Gold standard' result (All controls)
Abnormal DTI
Normal DTI
Reduced control sample size result
Classified Abnormal
Classified Normal
True Positive TP
False Positive FP
False Negative FN
True Negative TN
PPV TP/ (TP+FP)
NPV TN/ (FN+TN)
Sensitivity TP/(TP+FN)
Specificity TN/(FP+TN)


1.
Sample Size: 10
Abnormal DTI
Normal DTI
Classified Abnormal
Classified Normal
48
27
64%
0
17
100%
100%
39%


2.
Sample Size: 20
Abnormal DTI
Normal DTI
Classified Abnormal
Classified Normal
48
16
75%
0
28
100%
100%
64%


3.
Sample Size: 30
Abnormal DTI
Normal DTI
Classified Abnormal
Classified Normal
48
9
84%
0
35
100%
100%
80%


4.
Sample Size: 40
Abnormal DTI
Normal DTI
Classified Abnormal
Classified Normal
48
8
86%
0
36
100%
100%
82%

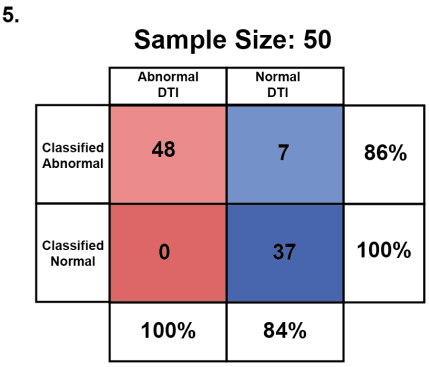

5.
Sample Size: 50
Abnormal DTI
Normal DTI
Classified Abnormal
Classified Normal
48
7
86%
0
37
100%
100%
84%

Figure 47: Reliability and accuracy measures using smaller control group sample sizes to identify DTI abnormalities in individual TBI patients. A. Intraclass correlation coefficient values derived from the FDR corrected p values of individual patient's tract FA when compared to randomly subsampled control groups of a given N over one hundred iterations. Sample sizes ranged from 10-50 and were randomly selected from the total control cohort (n=103). **B.** Calculation of type 1 and type 2 errors and related measures of sensitivity, specificity, positive and negative predictive value for diagnostic rates of individual TBI patients when compared to a control group of a given N (e.g. 10-50 in increments of 10). Values are calculated by comparing results of smaller control group to the 'gold standard' results derived for each patients when compared to all 103 healthy controls.

3.5.10 High specificity for identifying abnormalities in traumatic brain injury patients compared to healthy controls

To determine whether the methods applied are specific to TBI, I applied the same diagnostic pipeline to each individual control, who were compared to the rest of control group. Of the 103 healthy controls individually assessed against the remaining control cohort, three (2.9%) were found to have a single abnormal tract using my diagnostic pipeline. Six controls were found to have an abnormal whole brain skeleton (5.8%) when individually compared to the remaining control cohort. These rates of false positive are within the expected statistical range. With smaller control sample sizes (e.g. group size of 30), no healthy controls were diagnosed as having axonal injury.

3.5.11 Functional and cognitive impairments are greater in patients with evidence of axonal injury

Groups with and without abnormalities were compared across functional, cognitive and psychiatric outcomes. TBI patients in general showed a typical pattern of cognitive impairment in classical neuropsychology tests. Impairments were seen in memory, processing speed and executive functioning after FDR correction. Specifically, TBI patients performed significantly poorer on the people's test immediate ($t(64.39)=2.84, p<0.01$) and delayed recall $t(63.07)=2.39, p<0.02$), trail making test A ($t(111)=-4.89, p<0.001$), trail making test B ($t(115)=-4.44, p<0.001$) and A Minus B ($t(109.7)=-3.36, p<0.01$) as well as sub-scores of the DKEFS Stroop test (colour naming; $t(90.18)=-5.67, p<0.001$; word reading ($t(79.19)=-4.65, p<0.001$) and inhibition switch ($t(101)=-3.69, p<0.001$). When examining performance across computerised working memory tasks, a significant main effect of group was observed

($F(1,375)=15.23, p<0.001$) such that TBI patients performed worse on tasks than healthy controls.

Patients with evidence of axonal injury were more impaired across all cognitive domains using classical neuropsychological tests compared to patients without DTI abnormalities. For memory, a factorial ANOVA including group (controls, abnormal and normal DTI) and age revealed a significant main effect of group ($F(2,124)=13.147, p<0.001$). Post-hoc Tukey t-tests showed this effect was driven by significantly lower scores for patients with abnormal DTI compared to patients with normal DTI ($p<0.001$) and controls ($p<0.0001$). There was no significant difference between controls and patients with normal DTI ($p=0.66$) (Fig. 48A). There was no main effect of age or interaction of age with group on memory scores. For executive function, ANOVA showed a main effect of group ($F(2,124)=17.088, p<0.001$). This was driven by slower performance in patients with abnormal DTI relative to patients with normal DTI ($p<0.001$) and healthy controls ($p<0.001$). A main effect of age was also observed ($F(1,124)=6.55, p<0.05$) but no interaction between group and age ($p=0.138$). For information processing, there was a significant main effect of group ($F(2,124)=24.524, p<0.001$), driven by patients with abnormal DTI performing more slowly than patients with normal DTI ($p<0.001$) and controls ($p<0.001$). There was no difference between patients normal DTI and controls ($p=0.230$). There was no main effect of age nor an interaction with group. A significant main effect of group ($F(2,124)=4.463, p<0.05$) was also observed when performing a repeated measures ANOVA for reasoning scores, driven by lower performance in patients with abnormal DTI compared to patients without DTI abnormalities ($p=0.029$). There was a difference between patients diagnosed with abnormal DTI and controls of borderline significance ($p=0.051$) but no difference between patients with normal DTI and controls ($p=0.98$). There was also a significant main effect of age ($F(1,124)=7.99, p<0.01$), however there was no interaction between group and age (Fig. 48B).

Similarly, for working memory performance, a repeated measures ANOVA revealed a significant main effect of group ($F(2,124)=8.18, p<0.001$), driven by patients with DTI abnormalities performing worse on working memory tasks that healthy controls ($p<0.001$) and patients with no DTI abnormalities ($p<0.05$). No significant difference was observed between patients without abnormalities and healthy controls ($p=0.27$).

The Glasgow Outcome Scale (Extended) provided a summary measure of clinical outcomes. Patients with abnormal DTI showed lower scores on the GOSE than patients with normal DTI ($t(80.65)=2.59, p<0.02$). There were no significant differences between patient groups on measures of sleep disturbance (PSQI) or measures of psychiatric state provided by the anxiety and depression subscales of the HADS questionnaires ($p>0.05$) (Fig. 48C).

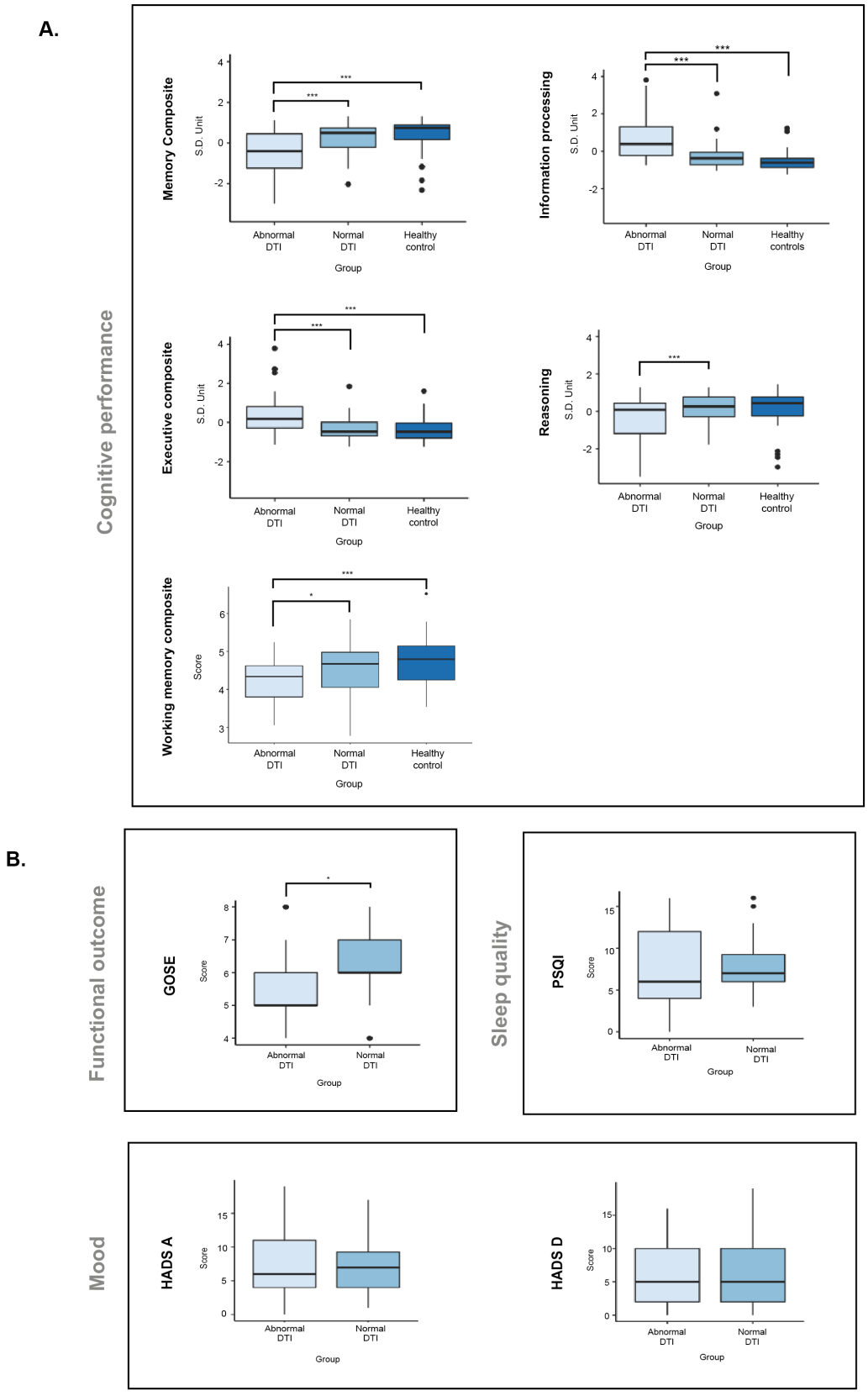


Figure 48: Cognitive and functional outcomes in patients diagnosed with and without axonal injury A. Comparison of composite scores for the four cognitive domains selected between healthy controls and patients identified as having either normal or abnormal DTI using the diagnostic pipeline.

Diagnosis of normal vs. abnormal DTI was determined using the whole control cohort (n=103), not accounting for age. **B.** Comparison of functional outcome measures between patients identified as having normal vs. abnormal DTI using the pipeline. ***=p<0.001, *=p<0.05.

I also investigated whether variable patterns of DTI abnormality in different tracts related to cognitive performance. Bivariate correlations were performed between all ten tracts and each of the cognitive composite measures, correcting for multiple comparisons within each cognitive domain. For executive function, significant negative correlations were observed in the Body (p<0.004), Genu (p<0.0.001), Splenium (p<0.001), left and right inferior longitudinal fasciuculi (p<0.004 and p<0.001, respectively) and middle cerebellar peduncle (p<0.01), (Appendix figure 1.1). For memory, positive correlations with the Genu of the corpus callosum were seen (p<0.05) (Appendix figure 1.2). For information processing speed, negative correlations with FA in the corpus callosum body (p<0.001), genu (p<0.001), splenium (p<0.001), right corona radiata (p<0.05), left and right inferior longitudinal fasciculus (p<0.01 and p<0.001 respectively) and middle cerebellar peduncle (p<0.001) were observed (Appendix figure 1.3). Finally, correlations between reasoning and tract FA were observed in the corpus callosum body (p<0.01), genu (p<0.01) and splenium (p<0.05) as well as the left and right inferior longitudinal fasciculi (p<0.05 and p<0.01, respectively) as well as the left and right corona radiata (p<0.01 and p<0.01, respectively) and middle cerebellar peduncle (p<0.01) (Appendix figure 1.4).

3.5.12 Functional and cognitive impairments do not differ between patients when categorised on the basis of visible damage on MRI

To assess whether the cognitive and functional differences observed between patients with or without diffusion abnormalities are specific to this feature, patients were also compared on the basis of visible damage on routine MRI. For example, patients with or without microbleeds and patients with or without focal lesions were compared across the four cognitive domains and GOSE. When grouping patients by microbleeds (n=40) vs. no microbleeds (n=52), cognitive performance did not significantly differ between the groups for any of the four cognitive domains (p>0.1, FDR corrected) (Appendix figure 1.5). Similarly, no significant difference was observed between

patients for GOSE scores (t(61.36)=0.16,p=0.87) (Appendix figure 1.6). When comparing cognitive performance between patients with (n=65) or without (n=27) focal lesions (Appendix figure 1.7), no significant differences were observed across any of the cognitive domains (p>0.05, FDR corrected). In addition, no significant difference was observed between GOSE scores (t (27.87)=-0.20,p=0.84) (Appendix figure 1.8).

3.5.13 Greater intervals between injury and MRI are observed in patients diagnosed with axonal injury using the pipeline

The relationship between time since injury and diagnosis of axonal injury using our pipeline was explored. Patients identified with axonal injury had significantly greater time since injury than patients without (t (86.14)=3.13, p<0.01), although widespread intervals were observed in both groups (group with tract abnormalities range 6-441 months, group without range 6-497 months since injury). There was no significant correlation between the number of tracts identified as abnormal and time since injury in patients with axonal injury (r=0.17, p=0.26). Bivariate correlations between individual tract FA and time since injury revealed significant relationships (p<0.05, FDR corrected) in the body (r=-0.38), genu (r=-0.38) and splenium of the corpus callosum (r=-0.43) as well as the right corona radiata (r=-0.24), and middle cerebellar peduncle (r=-0.27) such that the greater the time since injury the lower FA. When correlating time since injury with whole brain mean FA, a significant negative correlation was also observed (r=-0.37, p<0.001).

3.5.14 Diagnosis of axonal injury in subacute TBI patients is reliable but longitudinal assessments are recommended

I examined whether the application of the diagnostic pipeline to a subacute TBI cohort was able to reliably identify axonal injury. At the individual level, a total of 7 out of 25 patients were found to have an abnormality (28%). Of those patients, six had abnormalities in at least one tract in addition to the whole brain skeleton, whilst an additional patient showed only abnormalities in the whole brain skeleton. When assessed at the chronic timepoint (~6 months), a total of eleven patients (44%) had abnormalities. All seven patients with subacute abnormalities remained abnormal at six months, with the same tracts and/or whole brain skeleton abnormalities being observed across the two timepoints. A repeated measures ANOVA revealed no

significant main effect of timepoint on the number of abnormalities observed across tracts ($F(1,18)=0.05, p=0.9$). Of the four additional patients diagnosed with axonal injury at the chronic time point, one had tract abnormalities and the remaining three demonstrated abnormalities in the whole brain skeleton (Fig. 49A). Calculation of the intraclass correlation coefficient of Z-scores derived from the diagnostic pipeline revealed good reliability across tracts (mean ICC=0.89, range 0.77-0.96) between the two timepoints. When examining the ICC of p values (FDR corrected) derived from the diagnostic pipeline between the two timepoints (Fig. 50), average reliability remained high, although greater variability was observed across tracts, likely reflecting the changes in FA longitudinally (mean ICC=0.76, range 0.59-0.86). Examination of ICC for whole brain mean skeleton between acute and chronic timepoints revealed high reliability for Z-scores (ICC=0.92), and good reliability for p values (FDR corrected) derived from the diagnostic pipeline (ICC=0.70).

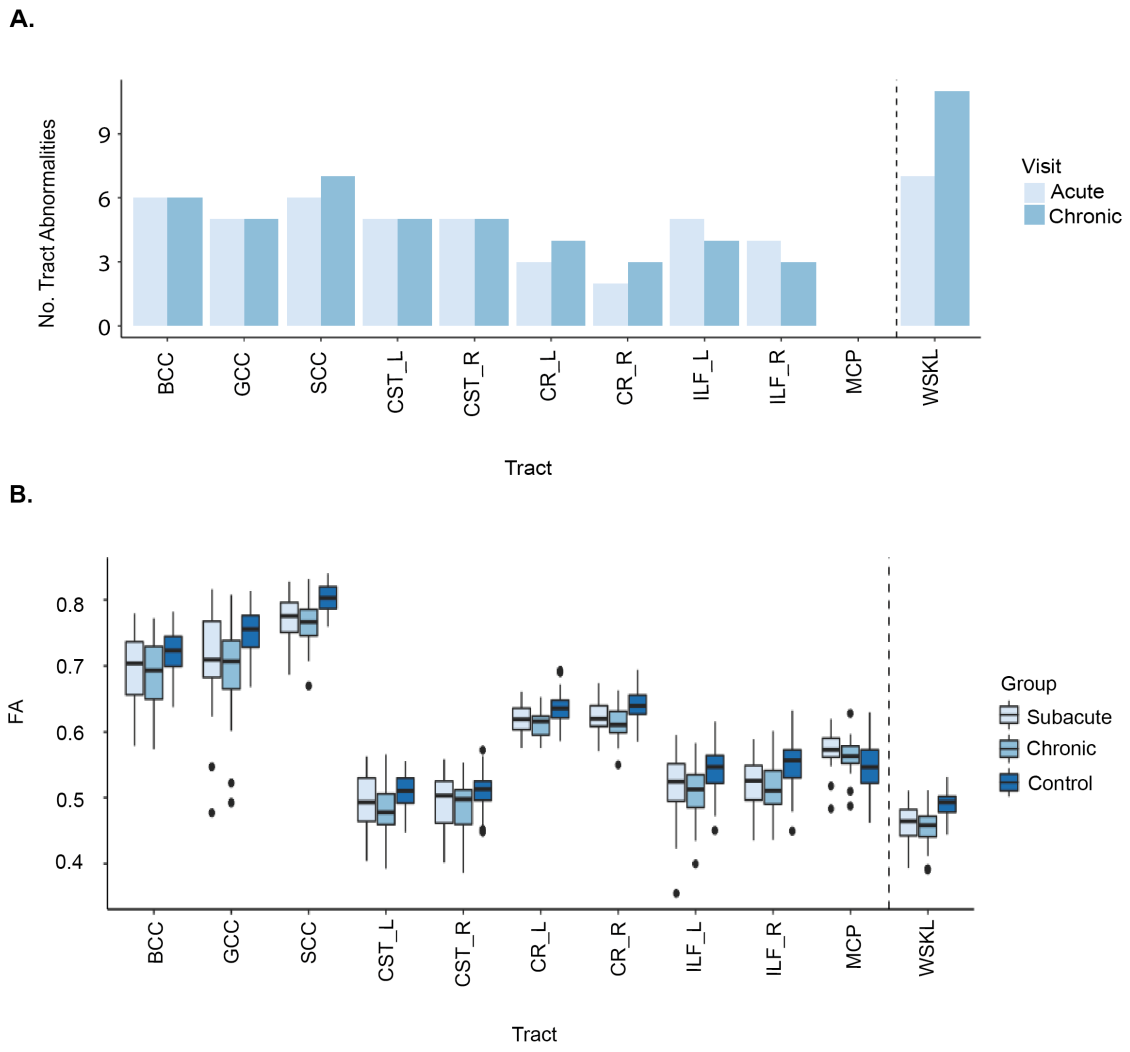


Figure 49: Longitudinal diagnostic results of subacute TBI cohort. A. Number of abnormal tracts identified in subacute TBI cohort using diagnostic pipeline for subacute (10 days-6 weeks) and chronic (~6 months) timepoints. **B.** Tract fractional anisotropy measures from subacute and chronic timepoints, as well as controls.

At the group level, there was evidence of reductions in FA in patients at both subacute and chronic timepoints compared to controls (Fig. 49B). In subacute scans, a factorial ANOVA revealed a significant main effect of group ($F(1,1270)=79.195$, $p<0.001$), such that patients had significantly lower FA than healthy controls. A significant group by tract interaction was also observed ($F(9,1270)=5.534$, $p<0.001$) with post-hoc Tukey tests revealing that this interaction was driven by significantly lower FA in the genu ($p<0.001$) and splenium ($p<0.01$) of the corpus callosum as well as the left and right inferior longitudinal fasciculi ($p<0.02$ respectively). Comparison of whole brain

skeletonised FA revealed significantly lower FA in patients at the subacute timepoint compared to controls (t(30.27)=-4.66, p<0.001). When comparing FA at the six-month follow-up to healthy controls, factorial ANOVA revealed a significant main effect of group (F(1,1270)=171.49, p<0.001) such that patients had lower FA than controls, as well as a significant group by tract interaction (F(9,1270)=6.36, p<0.001). Post-hoc Tukey tests revealed that this interaction was driven by significantly lower FA in the body (p<0.001), genu (p<0.001) and splenium (p<0.001) of the corpus callosum as well as the left and right corona radiata (p<0.01 and p<0.02, respectively), right corticospinal (p<0.05) and left and right inferior longitudinal fasciculi (p<0.001, respectively). Comparison of whole brain skeleton FA also revealed a significant reduction in patients at the six-month follow up compared to controls (t(30.27)=-5.70, p<0.001).

When comparing patients between the two timepoints, repeated measures ANOVA revealed a significant main effect of time (F(1,500)=5.619, p=0.02) such that lower FA was observed in the chronic compared to subacute phase of injury across all tracts. No significant tract by time interaction was observed. No significant difference was observed for whole brain skeletonised mean FA between the two timepoints (t(49.95)=0.88, p=0.39).

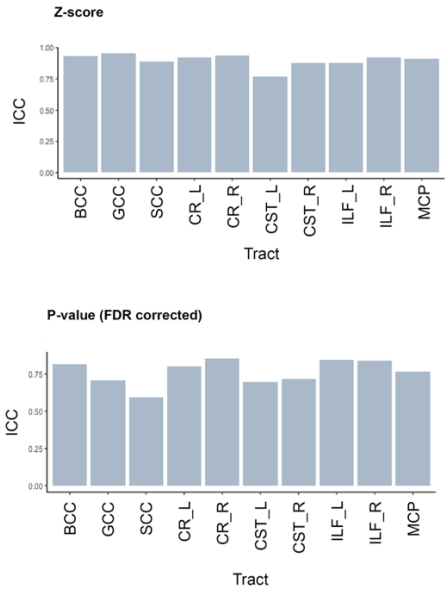


Figure 50: Intraclass correlation coefficient (ICC) of diagnostic results (z-scores and FDR corrected p values) between subacute and chronic timepoints in TBI patients.

3.6 Discussion

This work showed that diffusion tensor imaging can be informative for evaluating the white matter structure in individual patients. I describe a robust approach to the calculation of fractional anisotropy (FA) that controls for a number of important methodological constraints. Diffusion MRI abnormalities indicative of DAI are common in the chronic phase after moderate/severe TBI (~48% of cases) and provide distinct information from other commonly used diagnostic approaches. The location of DAI in the brain is variable, so an individualized tract-based assessment method is necessary. Importantly, some patients without visible damage according to standard MRI, including SWI, show clear evidence of diffuse axonal injury on diffusion measures. In addition, patients with evidence of DAI show cognitive impairments and poorer functional outcomes which cannot be attributed to psychiatric difference. I therefore provide a framework and methodology for the use of diffusion MRI in the assessment of DAI that provides clinically useful information in individual patients.

A number of measurements can be calculated from diffusion MRI. I focus on fractional anisotropy (FA) as it provides a measure of white matter tract integrity that has been widely studied in previous TBI work (MacDonald et al., 2007; Sidaros et al., 2008). Fractional anisotropy calculations are based on patterns of water diffusion that are normally highly directional in much of the white matter because of the directional organization of axons (Mori & Zhang., 2006). Mechanical forces applied to white matter tracts at the time of an injury damage the normal axonal structure producing more random patterns of water diffusion along a tract (Song et al., 2002; Budde et al., 2011). Alterations in FA have been validated as a measure of axonal injury in animal models of TBI, with reductions in FA associated with disrupted white matter structure and the associated inflammatory response (MacDonald et al., 2007a; MacDonald et al., 2007b, Laitinen et al., 2015).

I extend previous studies by demonstrating a robust method for measuring white matter tract FA at the individual level. My research group and other laboratories have previously shown the value of diffusion MRI in assessing patterns of white matter injury in groups of TBI patients. Widespread evidence of DAI is almost always when

moderate/severe TBI patients are studied. The location and severity of injury relates to patterns of cognitive and functional outcomes (Bonnelle et al., 2011; Kinnunen et al., 2011; Sidaros et al., 2008; Kumar et al., 2009). However, the significant inter-individual heterogeneity in the location and severity of DAI motivates the need for individualized assessments. Here I showed that ~48% of moderate/severe TBI patients have diffusion abnormalities indicative of DAI and that these abnormalities are often missed using T1, FLAIR or SWI imaging. Hence, clinicians will often be falsely re-assured about the absence of DAI using the standard neuroimaging investigations.

I showed that diffusion MRI provides information that is distinct from other assessments of post-traumatic injury. DAI can occur in the absence of focal brain injury, which is seen in the sub-group of patients who have diffusion abnormalities in the absence of any evidence of focal injury. In addition, I confirm that diffusion MRI provides complementary information to SWI, which identifies microbleeds. Although SWI has previously been thought of as a surrogate marker of DAI (Scheid et al., 2006), recent work confirms that microbleeds are a marker of diffuse vascular injury (Liu et al., 2014; Costello et al., 2013; Zhu et al., 2013a). DAI can occur with or without diffuse vascular injury (Liu et al., 2014). I demonstrate that only 45% of patients with microbleeds were found to have evidence of axonal injury. Conversely, more than a third of patients with no visible damage on conventional MRI had evidence of axonal injury. Diagnosis may be made on the basis of microbleeds where no axonal injury is present and secondly where an unremarkable MRI leads to diagnosis being determined on clinical symptoms which may not be reliable.

Diffuse axonal injury is an important predictor of cognitive and functional outcomes (Menon et al., 2014; Katz et al., 1994; Scheid et al., 2006; Weiss et al., 2007). I showed that individuals with evidence of DAI show more cognitive impairments in all four cognitive domains assessed. In contrast, patients without evidence of DAI showed no cognitive abnormalities. In addition, patients with evidence of DAI had significantly poorer functional outcomes, emphasizing the importance of DAI for real-world clinical outcomes. Differences in cognitive and functional outcomes between these two patient groups were not obviously attributable to mood, as patients with and without evidence

of DAI showed similar levels of depressive and anxiety symptomatology. In addition, the presence of focal injury and diffuse vascular injury was not associated with worse cognitive or functional outcomes: diffusion MRI provides specific information about that is related to chronic impairments after TBI that is not provided by more conventional neuroimaging.

Patterns of white matter damage vary across individuals, which reflects the variable biomechanics of different head injuries. Tract damage is produced by large forces exerted at the time of an injury and the location of these forces is highly dependent on the specific features of a head impact (Ghajari et al., 2017), with rotational forces having differential effects depending on the direction of the axons and force (Colgan et al., 2010; Halabieh & Wan., 2008). Hence, it is necessary to estimate injury from a range of different tracts. I described a principled selection process for choosing the final set of tracts I study. These tracts are large enough to reliably estimate white matter structure (Sairanen et al., 2017). They have good test-retest reliability, which I demonstrate in data from healthy controls scanned multiple times over a two-year period. They were selected to have different anatomical orientations so the impact of a range of biomechanical forces can be assessed (Colgan et al., 2010; Halabieh & Wan., 2008; Parizel et al., 1998), and also to include association, projection and commissural pathways so the impact of DAI on varying types of brain networks can be measured.

The distribution of white matter tract damage is known to relate to patterns of cognitive impairment (Kinnunen et al., 2011; Palacios et al., 2004; Bonnelle et al., 2012). Hence, the distribution of damage to specific tracts may explain patterns of post-traumatic impairments. This principle has previously been demonstrated by the association of corticospinal tract damage to motor deficits (Choi et al., 2010; Caeyenberghs et al., 2011). Here I report clear correlations between diffusion abnormalities and a range of cognitive impairments for a number of the tracts studied. For example, significant negative correlations were observed between executive function and the three subdivisions of the corpus callosum, the inferior longitudinal fasciuli, the middle cerebellar peduncle and executive function. In addition, when examining information processing and reasoning, significant correlations were observed with the three

subdivisions of the corpus callosum, the corona radiata bilaterally, the inferior longitudinal fasciuli and the middle cerebellar at varying degrees.

I have considered a range of potential limitations for the use of diffusion MRI in this context and address a number of practical issues relevant to the widespread adoption of diffusion MRI for the diagnosis of DAI in clinical practice. One barrier is the need to compare individual diffusion measures to control data collected on the same scanner. Currently, this is necessary because the between-scanner variability of diffusion measures is high enough to impact in an unpredictable way on patient classification. Hence, an important consideration is establishing the minimum size of a control group that is necessary for adequate sensitivity and specificity. I explored this issue by bootstrapping the classification analysis using different control groups of differing sizes. I concluded that a control sample size of around 30 with a range of ages provides acceptable 'specificity' and 'sensitivity'. I would therefore recommend that clinical units collect around 30 control subjects using the same diffusion sequence parameters to form the comparative dataset for the DAI analysis pipeline I provide. This recommendation may change in the future as very recent work indicated that diffusion data can be harmonized across scanners using groups of around 15 control subjects to identify the scanner dependent variability from the diffusion signal, prior to analysis (Karayumak et al., 2019).

Another factor that should be considered when comparing FA across individuals is their age. There is a non-linear relationship between age and FA which could impact on the identification of diffusion abnormalities (Pfefferbaum et al., 2000). I explicitly investigated this issue by comparing diagnostic results before and after statistically controlling for the age of the patients and the comparative control group. Regressing age and age^2 out of the patient and control data had little impact on the diagnostic result i.e. the same patients were identified as having evidence of DAI with and without when accounting for age. Nevertheless, I recommend the use of age-regression when using the pipeline as this might correct differences in age between other control cohorts and patient groups. Hence, my method allows for the inclusion of healthy individuals somewhat older or younger than the patient without biasing the results, which may prove useful in clinical settings where data is sparse.

The presence of focal lesions also potentially impacts on the reliability of FA estimates. This is an important consideration when assessing DAI in individual patients as the mean FA across a tract is calculated and may therefore be biased if a portion is missing. I provided a solution to this issue by excluding areas of the focal lesion from white matter tract estimating in both the patient and controls. This had a small effect on the diagnostic results, with three out of the 38 patients no longer found to have evidence of axonal injury. These findings illustrated the specificity of the pipeline in primarily detecting axonal injury but also highlights that it is possible for large lesions to bias results if not accounted for. I therefore recommend excluding areas of focal lesion/missing brain from the pipeline to accurately quantify DAI.

Finally, it is important to consider the timing of diffusion MRI acquisition relative to the injury. I have primarily evaluated our pipeline for use in the assessment of a chronic TBI population with moderate-severe injuries but have begun to provide some assessment of its utility within a subacute population. TBI produces dynamic changes in diffusion measures including increases in FA in the initial days (MacDonald et al., 2007a), and progressive reductions many years after injury, due to neuroinflammation (Sharp et al., 2014). In this chronic TBI population, patients identified with axonal injury had significantly greater intervals between their date of injury and MRI, than those without. Furthermore, significant negative relationships between FA and time since injury were observed in a number of tracts. These findings may suggest that my diagnostic pipeline is more sensitive in detecting axonal injury when the progression of FA abnormalities is advanced, however I demonstrate using an additional dataset that this pipeline is able to reliably detect axonal injury at the subacute phase of injury. The identification of abnormalities in four additional patients at the chronic timepoint does however support the notion that axonal injury is not a static event, and my pipeline provides accurate quantification of axonal injury at the time of assessment. Follow-up assessments may therefore be beneficial after the initial months of injury where the greatest changes in FA occur. Further application of this method in a larger subacute population would be beneficial to determine whether diagnosis sub-acutely corresponds to cognitive and functional outcomes within the chronic phase.

In summary, I described a pipeline for diffusion MRI assessment of diffuse axonal injury and provide data and code for use by others. I showed that this is a robust approach to the calculation of fractional anisotropy (FA) that controls for a number of important methodological constraints. Diffusion MRI abnormalities indicative of DAI are common in the chronic phase after moderate/severe TBI (~50% of cases) and provide diagnostic information that is distinct from other commonly used neuroimaging approaches that provide clinically valuable information.

Chapter 4

Dissociable structural sub-networks underlie working memory and reasoning deficits after traumatic brain injury

In this chapter I investigate the patterns of white matter damage associated with working memory and reasoning impairment using diffusion tensor imaging and computerised cognitive testing. I apply graph theory to examine these associations from a network perspective.

4.1 Abstract

Chronic cognitive impairments after traumatic brain injury (TBI) relate to diffuse axonal injury (DAI) and widespread disruption of brain connectivity. However, the pattern of DAI varies greatly between patients as does their profile of cognitive deficits. This heterogeneity is poorly understood, presenting a challenge for prognostication and treatment.

Deficits in working memory and reasoning are some of the most common cognitive problems after TBI. Previous functional magnetic resonance imaging (fMRI) in controls has associated these aspects of cognition with distinct, but partially overlapping, networks in the brain. It is therefore likely that differences in the integrity of the white matter tracts that connect these networks should predict variability in the type and severity of cognitive deficits after TBI.

I use diffusion-weighted imaging (DWI), cognitive testing and graph theory network analyses to test this prediction. I define functionally distinct sub-networks of the structural connectome by intersecting previously published fMRI maps of the brain regions activated during working memory and reasoning tasks, with the white-matter tracts that connect them. I then examine how graph theoretic measures within these sub-networks relate to the performance of the same tasks in a cohort of 92 moderate-severe TBI patients.

Principal component analysis of behavioural performance demonstrate that reasoning and working memory form distinct components of cognition, which are both vulnerable to TBI. Importantly, impairments in these abilities correlate in a dissociable manner with the topology of the networks that they are associated with. This dissociation is illustrated when examining degree centrality measures of the networks using a canonical correlation analysis. Notably, the dissociation is prevalent across a number of nodal/local measures and is asymmetrical: disruption to the working memory network relates to both working memory and reasoning performance whereas disruption to the reasoning network relates to reasoning performance, supporting

classical hierarchical models of working memory, where reasoning is dependent on working-memory capacity.

I propose that TBI patients may be profiled using combined behavioural and structural imaging measures to identify the brain networks that are deficient. This finer grained diagnostic information may be useful for future applications that attempt to predict long-term cognitive outcomes or develop therapies that are tailored to individual patient profiles.

4.2 Introduction

Traumatic brain injury (TBI) can lead to a variety of reasoning and working memory impairments that persist across the lifespan, impacting on quality of life and contributing to poor functional outcomes (Ponsford et al., 2014; McAllister et al., 2014). The role of diffuse axonal injury (DAI) in the development of cognitive deficits is well established (Palacios et al., 2011; Kinnunen et al., 2011; Palacios et al., 2012; Zappala et al., 2012); however, the ability to accurately predict the type and severity of deficits that each patient will suffer from is limited.

Neuroimaging has highlighted the importance of the structural connectome in supporting higher-order cognition and has begun to characterise the mechanisms of impairment after TBI. Studies that analyse the brain as networks have motivated a more holistic perspective on cognition by illustrating that functionally specialised regions of the brain dynamically form temporary networks in order to support different cognitive processes (Beckman et al., 2005; Smith et al., 2009; Hampshire et al., 2016; Soreq et al., 2019), which are facilitated by white matter structural connectivity (van den Huevel et al., 2009). In the context of TBI, damage to structural networks produced by DAI has been demonstrated to disrupt functional connectivity, impairing information transfer across distal brain regions (Sharp et al., 2014) and producing cognitive deficits (Kim et al., 2009; Bonelle et al., 2011; Palacios et al., 2011; Bonelle et al., 2012).

The utilisation of graph theory with neuroimaging data has extended this by demonstrating that TBI alters network structure, moving it away from an optimal small-world topology where a balance between network integration and modularity is observed (Bassett and Bullmore., 2006; Braun *et al*., 2015) to a more segregated architecture where coordinated information processing across systems is hindered (Pandit *et al*., 2013; Caeyenberghs *et al*., 2014; Fagerholm *et al*., 2015). Changes to network efficiency have been proposed to be due to the loss of long-range white matter connections (Achard *et al*., 2006; Bullmore and Sporns., 2009), supported by previous work investigating network structure and function following TBI (Pandit *et al*., 2013; Fagerholm *et al*., 2015). These altered structural network properties have been observed to correlate with cognitive impairments in TBI patients and have been used to robustly classify patients with chronic cognitive problems (Fagerholm *et al*., 2015), highlighting their potential for predicting cognitive outcomes.

Describing the impact of brain injury in terms of changes to structural networks promises to inform our understanding of the basis of variable cognitive impairments after TBI. It also provides insights into the neural mechanisms that underlie cognitive systems. For example, deficits in working memory and reasoning are common after TBI (Palacios *et al*., 2011; Kinnunen *et al*., 2011; Palacios *et al*., 2012; Zappala *et al*., 2012) yet the incidence and extent of these impairments vary greatly across patients. One potential reason for this is the heterogeneity in the spatial distribution of damage to the structural connectome after TBI and is likely important when considering the impact of structural disconnection on distinct cognitive processes. Most relevantly, in previous studies (Hampshire *et al*., 2012; Daws *et al*., 2017; Hampshire *et al*., 2019) principal component analysis of two large cohorts of healthy individuals (N=44,600 & N=18,455), supported the view that working memory and reasoning form distinct cognitive components of cognitive ability. In a smaller subset of controls, it was also shown that independent component analysis of brain activity during the performance of these tasks produces the same working memory vs. reasoning component structure that relates to spatially different but partially overlapping networks in the brain (Hampshire *et al*., 2012). It was therefore proposed that individual differences in the functionality of these networks may underpin distinct axes of cognitive ability; however, this interpretation was controversial (Haier et al., 2014).

Here, I use a combination of cognitive testing, diffusion weighted imaging and graph theoretic analyses to examine whether working memory and reasoning abilities are differentially affected by TBI dependent on the post-injury integrity of these functionally distinct networks. Critically, the impact of TBI on working memory and reasoning has seldom been investigated in parallel, yet cognitive tasks typically involve some mixture of both. I therefore apply principal component analysis to data from 92 TBI patients and 105 matched controls who performed six of the tasks reported in Hampshire *et al*., 2012. I seek to confirm the previously reported dissociation of behavioural factors and to extract working-memory and reasoning scores in an unbiased data-driven manner. I test whether there are deficits in both behavioural components in the TBI population and investigate how the component scores covary with the integrity of the structural connectome in TBI patients. I define working memory and reasoning sub-networks of the structural connectome by intersecting the whole brain fMRI activation maps from Hampshire *et al*., 2012 (Fig. 51) with an established atlas of the white matter tracts that connect the grey matter regions of the brain. I test whether working memory and reasoning performance have dissociable relationships to variability in graph theory measures of connectivity (degree centrality), integration (global efficiency) and modularity (local efficiency, clustering coefficient), of their associated structural sub-networks. I demonstrate evidence of a dissociation in a purely data-driven manner by using canonical correlation analysis to identify modes that relate variability in working memory and reasoning performance to white matter measures across the whole structural connectome. I further illustrate this dissociation using correlation analysis across functional sub-networks and graph theory measures. Furthermore, I seek to replicate previous findings that disconnection of network hubs (highly interconnected regions) have the strongest association with cognitive performance in patients (Fagerholm *et al*., 2015). Finally, I examine the relationship that exists between white matter measures, component scores from the computerised reasoning and working memory tests, and the measures provided by neuropsychological tests that are widely used to assess cognitive problems in the clinical setting.

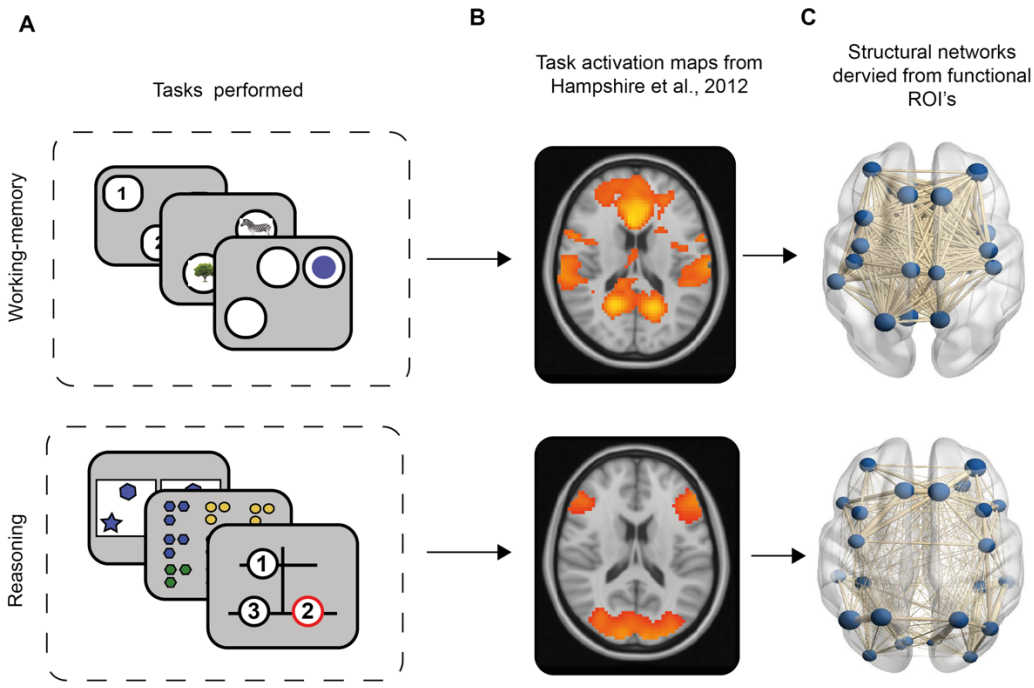


Figure 51: Illustration of extraction of structural connectomes from task-activation maps produced by Hampshire *et al*., 2012. A) Cognitive tasks used, and cognitive component structure created from principal component analysis revealing a working memory vs. reasoning component structure. **B)** Working memory and reasoning activation maps derived from task-fMRI relative to rest in healthy controls performing the cognitive tasks. **C)** Construction of structural connectomes in current study using activation maps from Hampshire *et al*., 2012 intersected with Desikan-Killiany grey matter atlas to define nodes (regions of grey matter) and subsequent edges between nodes as white matter connectivity. *Figure reproduced from Jolly et al., 2020, Distinct patterns of structural damage underlie working memory and reasoning deficits after traumatic brain injury,* Brain*, Volume 143, Issue 4, April 2020, Pages 1158–1176 under Creative Commons CC BY license.*

4.3 Materials and Methods

4.3.1 Participants

Data from ninety-two patients (19 female, mean age 42.9, SD 12.40 years) with a moderate-severe TBI as classified using the Mayo criteria (Malec *et al*., 2007) were included in this study. Patients were recruited from Neurology clinics in London within the chronic phase of injury (≥ 6 months post injury). Average time since injury was

130.4 months (SD 154, range 6-497 months). Findings from routine MRI, mechanism of injury and current medications can be found in Table 6. Inclusion criteria were: age 18-80 years (range 20-80 years), no significant neurological or psychiatric history or previous TBI, no history of alcohol or substance abuse and able to understand English. Exclusion criteria were: contraindication to MRI or a positive urine drug screen. Written informed consent was obtained from all patients in accordance with the Declaration of Helsinki. The studies were approved by the West London and GTAC Research Ethics Committee (14/LO/0067, 13/LO/1678, 14/LO/1998). All patients completed structural MRI, a computerised cognitive battery and a standard neuropsychological test battery.

One-hundred and five healthy controls were included (35 female, mean age 44.98, SD 15.16 years). Controls had no history of neurological or psychiatric illness, TBI or alcohol and substance abuse. All participants gave written informed consent and completed structural MRI. A subset (n=35, 8 females, mean age 44, SD 13.05) also completed the computerised cognitive battery and standard neuropsychological tests.

Age	Gender	Severity	Cause	PTA	Contusion	Microbleeds	Medication
65	M	Mod/Sev	RTA	>7 days	Y	N	nil
38	M	Mod/Sev	violence/assault	2 days	N	Y	nil
51	F	Mod/Sev	incident fall	2 days	unknown	unknown	Lansoprazole 15mg od
31	M	Mod/Sev	RTA	90 days	Y	Y	nil
54	M	Mod/Sev	RTA	5 days	N	N	Citalopram 30mg, thyroxine 150 mcg
20	M	Mod/Sev	incident fall	28 days	N	Y	nil
36	M	Mod/Sev	violence/assault	3 days	Y	N	nil
44	M	Mod/Sev	RTA	90 days	Y	Y	nil
51	M	Mod/Sev	RTA	several weeks	Y	Y	nil
64	M	Mod/Sev	RTA	few hours to a day	Y	N	Omeprazole 40mg, Levothyroxine 75mcg
58	M	Mod/Sev	RTA	1 month	Y	N	nil
34	M	Mod/Sev	other	6 weeks	Y	Y	nil
45	M	Mod/Sev	RTA	2 weeks	N	Y	nil
20	M	Mod/Sev	RTA	2 months	Y	Y	nil
52	M	Mod/Sev	RTA	5 days	N	Y	nil
45	M	Mod/Sev	other	14 days	N	N	nil

31	M	Mod/Sev	violence/assault	months	Y	Y	nil
49	M	Mod/Sev	other	yes, but unknown duration	Y	Y	Loperamine 2mg
24	M	Mod/Sev	RTA	14 days	N	N	nil
52	M	Mod/Sev	incident fall	21 days	Y	Y	Levetiracetam 1250mg bd, perindopril 2mg od
54	M	Mod/Sev	violence/assault	15 days	Y	Y	nil
26	M	Mod/Sev	violence/assault	56 days	Y	N	Amitriptyline 10mg, Sodium Valproate 100mg
21	F	Mod/Sev	RTA	35 days	N	Y	Fluoxetine 20mg
39	F	Mod/Sev	incident fall	2 days	N	N	nil
47	M	Mod/Sev	RTA	3 days	Y	Y	nil
22	M	Mod/Sev	RTA	450 days	Y	Y	nil
34	M	Mod/Sev	incident fall	0 days	Y	N	nil
48	M	Mod/Sev	RTA	60 days	Y	N	Amitriptyline 20mg tds, Fexofenadine 180mg od, Esomeprazole 40mg od Solifenacin 5mg od Loperamine 10mg od
38	M	Mod/Sev	violence/assault	700 days	Y	N	nil
49	F	Mod/Sev	violence/assault	10 days	Y	N	Levothyroxine 150mcg od, omeprazole
36	F	Mod/Sev	RTA	120 days	Y	Y	nil
43	M	Mod/Sev	RTA	42 days	N	Y	nil
31	M	Mod/Sev	violence/assault	21 days	Y	N	Growth Hormone 2mg, Lamotrigine 50mg bd
37	M	Mod/Sev	incident fall	120 days	Y	N	Tegretol CR 400mg BD
33	M	Mod/Sev	RTA	30 days	Y	Y	Citalopram 10mg OD, Baclofen 20mg OD
35	M	Mod/Sev	incident fall	7 days	Y	Y	nil
33	M	Mod/Sev	RTA	28 days	Y	N	Symbicort

52	M	Mod/Sev	violence/assault	4 days	Y	N	Lansoprazole 15mg od
38	M	Mod/Sev	violence/assault	14 days	unknown	unknown	nil
31	M	Mod/Sev	RTA	120 days	unknown	unknown	nil
39	M	Mod/Sev	RTA	2 weeks	Y	N	nil
24	F	Mod/Sev	RTA	120 days	unknown	unknown	Citalopram 40mg OD
35	M	Mod/Sev	incident fall	3 days	unknown	unknown	Salbutamol, Beclomethasone
42	M	Mod/Sev	RTA	unknown	N	N	Modafinil 300od, citalopram 20 OD,
37	M	Mod/Sev	RTA	4 days	Y	N	Omeprazole 40mg OD, Gabapentin 900mg OD
6	M	Mod/Sev	incident fall	4-6 hours	N	N	nil
59	M	Mod/Sev	RTA	7 days	N	Y	nil
57	F	Mod/Sev	incident fall	1-7 days	Y	Y	Demeclocycline 300g bd, ramipril 5mg od, salbutamol brn,
54	M	Mod/Sev	incident fall	2 days	Y	N	nil
39	M	Mod/Sev	RTA	unknown	N	Y	nil
44	M	Mod/Sev	RTA	6 days	Y	Y	unknown
48	M	Mod/Sev	violence/assault	24-48 hours	N	N	Carbamazepine 200mg
65	M	Mod/Sev	unknown	unknown	Y	Y	unknown
59	M	Mod/Sev	RTA	1-7 days	Y	N	Lansoprazole 30mg od
37	M	Mod/Sev	incident fall	1 days	Y	N	nil
26	M	Mod/Sev	RTA	3 days	Y	Y	nil
24	M	Mod/Sev	RTA	unknown	Y	N	nil
39	M	Mod/Sev	violence/assault	3 weeks	Y	N	nil
53	M	Mod/Sev	incident fall	unknown	Y	Y	nil
29	F	Mod/Sev	RTA	still in PTA	Y	Y	Lansoprazole 30mg, Phenytoin 300mg,
51	M	Mod/Sev	unknown	unknown	Y	Y	Gabapentin 300mg tds, Amitriptyline 50 mg
52	M	Mod/Sev	Incident fall	24-48 hours	Y	Y	nil

57	M	Mod/Sev	RTA	4 days	Y	N	unknown
40	M	Mod/Sev	RTA	42 days	Y	N	nil
42	F	Mod/Sev	RTA	3 days	Y	Y	nil
40	F	Mod/Sev	unknown	unknown	Y	N	unknown
31	M	Mod/Sev	incident fall	unknown	N	Y	nil
34	M	Mod/Sev	unknown	3 days	Y	N	nil
49	F	Mod/Sev	incident fall	24-48 hours	Y	N	Ibuprofen
39	M	Mod/Sev	unknown	7 days	Y	N	ramipril
44	F	Mod/Sev	RTA	unknown	Y	N	unknown
49	M	Mod/Sev	RTA	unknown	unknown	unknown	nil
61	F	Mod/Sev	RTA	120 days	Y	Y	Citalopram 10mg od
39	F	Mod/Sev	RTA	unknown	Y	Y	citalopram 20mg OD
49	M	Mod/Sev	unknown	unknown	Y	N	phenytoin 35omg OD, Omnitrope GH 0.3mg/0.4mg, Bendroflumethiazide 2.5mg, Thiamine 300mg OD, Quetiapine 100mg OD, Mirtazapine 45mg OD, Atorvastatin 40mg OD, Amlodipine 10mg OD, Ramipril 7.5mg OD, Pregabalin 300mg OD
72	M	Mod/Sev	unknown	unknown	Y	N	nil
40	F	Mod/Sev	RTA	unknown	Y	N	Tegretol, propranolol
65	M	Mod/Sev	incident fall	14 days	N	N	amlodipine, simvastatin, ramipril,
54	M	Mod/Sev	RTA	10 days	Y	Y	Tegretol 200mg BD, Amitriptyline 100mg
56	F	Mod/Sev	RTA	several months	Y	N	Ventolin, Seretide

43	M	Mod/Sev	RTA	unknown	Y	N	pregabalin 75mg bd, Ventolin, cetirizine, omeprazole, lamotrigine 50mg bd
39	M	Mod/Sev	RTA	unknown	Y	N	Tegretol 400mg bd
57	M	Mod/Sev	RTA	unknown	Y	N	nil
31	F	Mod/Sev	unknown	unknown	unknown	unknown	unknown
38	M	Mod/Sev	unknown	unknown	unknown	unknown	unknown
51	M	Mod/Sev	incident fall	unknown	unknown	unknown	nil
54	M	Mod/Sev	RTA	1 days	N	N	nil
46	F	Mod/Sev	incident fall	4 weeks	unknown	unknown	nil
43	M	Mod/Sev	RTA	no	N	N	nil
55	M	Mod/Sev	violence/assault	4 days	N	N	Levetiracetam, Salbutamol
48	M	Mod/Sev	RTA	no	N	N	Salbutamol, Seretide
57	M	Mod/Sev	RTA	no	N	N	nil

Table 6: Demographics of TBI patients. M=Male, F=Female, Mod/Sev=Moderate-severe TBI injury. RTA=Road traffic accident. PTA=Post traumatic amnesia. N=No, Y=Yes. OD=Once daily. BD=twice a day.

4.3.2 Structural MRI acquisition

Structural MRI was acquired using a 3T Siemens Magnetom Verio Syngo scanner with a 32-channel head coil. All participants were scanned using the same acquisition parameters. Structural MRI included a high-resolution T1-weighted MPRAGE, diffusion weighted imaging and fluid-attenuated inversion recovery (FLAIR) to identify focal lesions. See methods chapter two section 2.4 for full acquisition details.

4.3.3 Neuropsychological assessment

4.3.3.1 Computerised cognitive assessment

A computerised battery was used to assess working memory and reasoning in patients and controls (Fig. 52). This battery consisted of six tasks, designed and programmed

by Dr Hampshire. Tasks were based on classical paradigms used to measure working memory and reasoning performance. These were identified as the minimal set required to reliably differentiate working memory and reasoning abilities based on sub-sampling data from previous studies with two large cohorts of Internet users (Hampshire *et al*., 2012, Daws *et al*., 2017; Hampshire *et al*., 2019). The tasks were deployed on iPads via a custom-programmed App and included: 1) Monkey Ladder (MKL), 2) Paired Associates Learning (PAL) 3) Self-Ordered Search (SOS) 4) Feature Match (FTM) 5) Odd One Out (OOO) and 6) The Hampshire Tree Task (HTT).

All tasks were adaptive to performance, e.g. increasing and decreasing the speed of delivery or number of stimuli, or the complexity of problems on completion of each trial. For tasks without time limits, three errors triggered the end of the task. Detailed information about the task designs has been reported previously (Hampshire *et al*., 2012) and can be found in methods chapter two section 2.1.2.

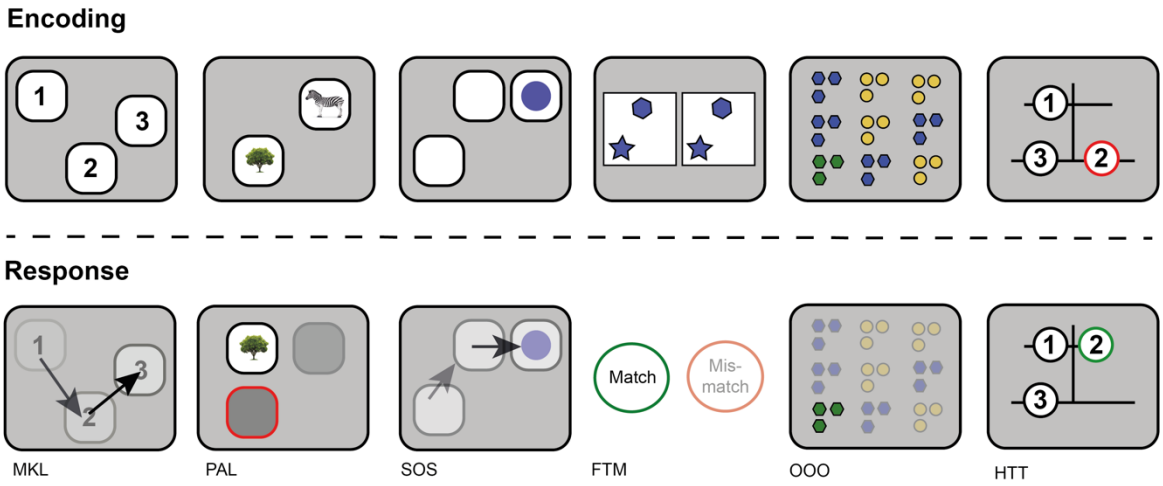


Figure 52: Schematic of the six computerised cognitive tasks used to assess TBI patients and controls. From left to right, working memory tasks MKL=Monkey ladder task, PAL=Paired associates learning, SOS=self-ordered search, and reasoning tasks FTM=feature match, OOO=odd one out, HTT=Hampshire tree task. Encoding demonstrates the initial presentation of stimuli for each task and response demonstrates the method in which to complete the task correctly. *Figure reproduced from Jolly et al., 2020, Distinct patterns of structural damage underlie working memory and reasoning deficits after traumatic brain injury,* Brain*, Volume 143, Issue 4, April 2020, Pages 1158–1176 under Creative Commons CC BY license.*

4.3.3.2 Standard neuropsychological assessment

In addition to computerised testing, all TBI patients and a subset of 35 healthy controls completed a standard pen and paper neuropsychological assessment commonly used to assess cognitive function in TBI (Kinnuen et al., 2011; De Simoni et al., 2018; Jenkins et al., 2018). This provides comparative, clinically validated measures to determine the relevance of computerised tasks to the clinical gold standard. The test battery included; 1) the Wechsler test of Adult reading (WTAR) and the matrix reasoning subtest from the Weschler adult intelligence scale (WAIS-III) to assess intellectual function (Weschler, 1945), 2) the peoples test (PT) from the peoples and door test (Weschler., 1945) and logical memory subtest of the Weschler memory scale (Weschler, 1945) to assess memory and 3) the colour-word interference (Stroop) test from the Delis-Kaplan executive function system (DKEFS, Delis et al., 2001) and trail-making task (A & B) to assess executive function. Further details about these tasks can be found in methods chapter two, section 2.1.

4.3.4 Diffusion tensor imaging

Diffusion weighted images were pre-processed using FSL's diffusion toolkit (FDT). Details of the pre-processing steps are detailed in methods chapter two section 2.4. Voxelwise non-parametric permutation analysis was undertaken using randomise in FSL to examine patterns of white matter damage (as quantified using FA) in the TBI cohort relative to controls. Specifically, FA skeleton maps were compared between patients and controls in a voxelwise manner with 10000 permutations forming the null distribution. Age was included as a covariate and results were threshold-free cluster corrected to account for multiple comparisons.

4.3.5 Behavioural data

Cognitive data for TBI patients and controls were pre-processed in the following steps. Multiple linear regression was applied to regress out age, age-squared and age-cubed from the data, accounting for non-linear relationships between age and cognitive performance. A rank based inverse transform was then applied to the extracted

residuals to ensure assumptions of normality were met. All pre-processing and analyses were performed in MATLAB (R2017b). For computerised cognitive data, performances across the six tasks were compared between TBI patients and controls using a repeated measures ANOVA. Performance across paper neuropsychological test measures were also compared using a repeated measures ANOVA. To confirm that the six computerised tasks mapped onto working memory and reasoning components as per previous research (Hampshire *et al*., 2012), a principal component analysis (PCA) with varimax rotation was applied to patients' task scores. A PCA with varimax rotation was also applied to patient and control data combined to determine whether a similar factor structure was observed. The Kaiser convention was used to threshold out components that had eigenvalues < 1 prior to rotation.

Bivariate correlations were performed to determine the degree to which the computerised tasks captured the same variance in patients as standard neuropsychological assessment. For dimensionality reduction, age-regressed and rank inverse normalised data from patients using the standard neuropsychological battery were included in a principal component analysis with varimax rotation. Components that had eigenvalues < 1 prior to rotation were removed. The components that remained were then correlated to the computerised task components and FDR corrected for multiple comparisons. A PCA with varimax rotation was also applied to patient and control neuropsychological data combined to determine whether a similar factor structure was observed.

4.3.6 Graph theory analysis

A summary of the analysis methodology applied to our graph theory analysis can be found in Figure 52. To investigate structural network topology and efficiency, a graph theoretical approach was applied to the skeletonised FA maps of patients and controls. As tractography is susceptible to issues when fractional anisotropy values are low (Squarcina *et al*., 2012), I used a large set of pre-defined white matter tractography masks from healthy controls to define region-to-region connectivity for the creation of connectivity matrices. (Fig 53A). This was achieved using the track density images (TDI) created for the construction of the Illinois Institute of Technology (IIT) human brain atlas of white matter (Zhang *et al*., 2018) developed by the Magnetic Resonance

Imaging Laboratory (MRIIT). Details about the construction of the whole brain connectome can be found in the methods chapter two, section 2.5.2.

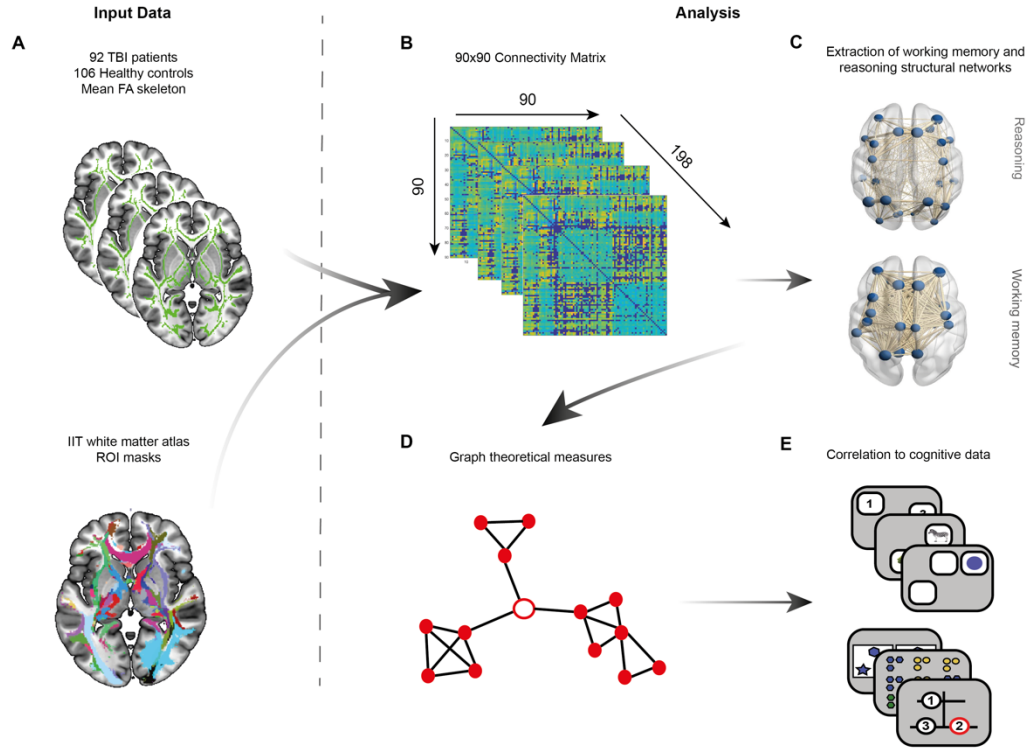


Fig 53: Overview of graph theory analysis methods. A. Skeletonised FA maps for the 92 TBI patients and 106 healthy controls were intersected with region-to-region, thresholded and binarized Track density images (TDI's) created using probabilistic tractography for the IIT white matter atlas. Mean FA for each ROI was therefore extracted for all patients and controls **B.** Mean FA for each ROI derived from the 90 region-to-region connections were then used to create a 90x90 connectivity matrix for all 198 subjects and weighted by number of streamlines to account for weak connections. A thresholding approach using the mean and standard deviation of healthy controls for each connection was then applied to all controls and patients to remove weak connections. **C.** Using task-fMRI activation maps from Hampshire *et al*., 2012, working memory and reasoning structural networks were derived from the 90x90 connectivity matrices by selecting nodes that overlapped with activation maps and their respective connections **D.** Graph theoretical measures were subsequently derived from these two structural networks including global/local efficiency, degree centrality and clustering coefficient **E.** Graph theory metrics for each network were then correlated to performance on cognitive tasks associated with working memory and reasoning in patients. *Figure reproduced from Jolly et al., 2020, Distinct patterns of structural damage underlie working memory and reasoning deficits after traumatic brain injury,* Brain*, Volume 143, Issue 4, April 2020, Pages 1158–1176*
under Creative Commons CC BY license.

4.3.7 Connectivity matrix pre-processing and extraction of reasoning and working memory networks for graph theory analysis

I applied the same approach as reported by Fagerholm *et al*., 2015 when pre-processing structural connectivity matrices (Fig. 53B). The aim was to ensure results were robust against different choices of thresholding whilst controlling for weak connections (i.e. small tracts with low FA) which can increase noise and impact upon graph theoretical analysis (Li *et al*., 2013). Further details regarding the pre-processing of structural connectomes can be found in methods chapter two, section 2.5.2.

In order to determine whether impairments of working memory and reasoning performance relate to disruption of different systems in the brain, I focused my graph theory analysis on networks previously associated with these two aspects of cognition when using the same tasks (Hampshire *et al*., 2012). I therefore extracted the whole brain working memory and reasoning activation maps from a study that measured changes in functional MRI activation for the same tasks relative to rest (Hampshire *et al*., 2012). This resulted in two distinct networks associated with reasoning and working memory (Fig 53C). The structural connectivity matrices were intersected with each of these maps, so that two sub-networks comprising of nodes that overlapped with the activation maps and their connections (edges) were produced.

4.3.8 Graph theory measures

Graph theoretic measures were extracted from the structural connectivity matrices of reasoning and working memory networks using the brain connectivity toolbox (BCT) (Rubinov and Sporns., 2010) (Fig 53D). Network hubs were identified by determining the top 20% of nodes with the highest average degree within healthy controls (van den Huevel *et al*., 2009) to determine whether dysconnectivity had a strong relationship to cognitive impairment as per previous research (Fagerholm *et al*., 2015). Global and local properties of each network for patients and controls were examined. For global measures, global efficiency, average local efficiency and average degree centrality were quantified. For local measures, local efficiency, degree centrality and local clustering coefficient were extracted. Measures were selected on the basis of previous

literature examining TBI (Pandit *et al*., 2013, Fagerholm *et al*., 2015) and for their quantification of network integration (global efficiency, average degree centrality), modularity (local efficiency, clustering coefficient) and disconnection (degree centrality) associated with small-world topology. These measures have been shown to be sensitive to structural alterations after TBI (Pandit et al., 2013; Fagerholm et al., 2015) and provide a focused summary of network topology in the brain. Further information about these metrics can be found in methods chapter two, section 2.5.1.

4.3.9 Multivariate correlational analysis of reasoning/working memory performance and structural networks

Canonical correlational analysis (CCA) was applied as a preliminary statistical analysis to confirm that multiple latent variables relate network dysconnectivity (as quantified using degree centrality) to working memory and reasoning impairment. This method allows multivariate relationships between two sets of variables to be statistically tested in a data-driven manner (see methods chapter two for a detailed description of CCA). For my analysis, I explored the relationships between behavioural data and degree centrality of all 90 nodes that were defined within the whole-brain structural connectome. To overcome the problem of overfit due to the large number of nodes, a PCA was applied prior to CCA, reducing measures to a set of components that captured 90% of the variance. The resultant component scores were input to the CCA along with the patient's cognitive component scores. If more than one canonical correlation coefficient (or mode) is significant as calculated using robust permutational testing, evidence of multiple, differential relationships between behaviour and structural data can be inferred. To determine the relative contribution of the two sets of variables to each mode, back projection of canonical variates to raw task and node degree data using Pearson's r correlation was applied. A custom sub-sampling routine with separate train and test data was applied to determine the generalisability of the canonical model and degree of overfit. In summary, the CCA analyses were repeated in an iterative loop, whereby the data were randomly sub-sampled, the model trained, then applied to the held out data to which it was naiive. This process was repeated with systematic variation in the trained (N samples) and held out samples ratio, with r values averaged over 1000 iterations at each point. The process was then repeated using permuted data to derive a null model and assess overfit.

4.3.10 Cross-sectional and correlational analysis of graph theory measures

Global network measures were compared between patients and controls using t-tests to determine whether significant differences in the overall information processing properties of the structural connectome were observed. Data was checked for assumptions of normality and results FDR corrected across the 12 comparisons. Next, to determine whether there was any relationship between network properties and corresponding cognitive performance in patients, global graph theoretic measures of reasoning and working memory networks were correlated to the cognitive components derived from patient-only PCA (Fig. 53E). These comparisons were repeated across non-corresponding network-behavioural component pairs, e.g. global properties of the working memory network were correlated to the reasoning cognitive component and global properties of the reasoning network were correlated to the working memory cognitive component. Results were corrected for multiple comparisons across the 12 correlations using FDR correction.

Local network measures were also compared between patients and controls using t-tests. Cross-sectional local network measures were corrected for multiple comparisons across network nodes using FDR correction. Local measures of the nodes in each sub-network were then correlated to reasoning and working memory cognitive component scores derived from patient-only PCA to quantify the relationship between node properties and cognitive performance in patients. Similar to global network analysis, correlations were repeated across non-corresponding network-behavioural component pairs. For each network, correlational results were corrected for multiple comparisons across network nodes using FDR correction.

4.4 Results

4.4.1 TBI patients perform significantly less well on cognitive tasks and have widespread diffuse axonal injury

Repeated measures ANOVA across the six cognitive tasks revealed a significant main effect of group ($F(1,126)=10.554, p=0.001$) such that TBI patients performed significantly less well than healthy controls. There was no significant group by task interaction indicating that all tasks could be affected by TBI to similar degrees, although numerically the PAL showed the greatest sensitivity (Fig. 54A). When examining standard neuropsychological test scores, repeated measures ANOVA did not reveal a significant main effect of group ($F(1,15)=3.652, p=0.056$). However, a significant group by task interaction was observed ($F(15,1856)=12.920, p<0.001$) with post-hoc t-tests revealing that this interaction was driven by lower performance on 12 out of the 16 test scores. This included; the WTAR, Trail Making Test scores, the four subtests of the Colour-Word (Stroop) Interference Task, Peoples Test total score, Peoples Test delayed score, Logical Memory total score for subtests 1 and 2 and Logical Memory retention scores (Table 7).

Domain	Task	Control mean n=35	Patient mean N=92	Difference
Intellectual ability	WTAR Scaled	114.8	108.3	**6.5****
	Matrix reasoning	27.76	26.93	0.83
Information processing	Trail Making A	20.55	32.49	**-11.94****
	Stroop Word reading	20.41	25.18	**-4.77****
	Stroop colour naming time	27.95	34.92	**-6.97****
Executive function	Trail Making B minus A	-0.47	0.07	**0.54****
	Stroop Inhib time	52.77	60.59	**-7.82***
	Stroop Inhib switch time	57.2	71.02	**-13.82****
	Stroop contrast inhib vs colour naming	24.83	25.66	-0.83
	Stroop Contrast Inhib switch vs Inhib	4.43	10.44	-6.01
	Stroop Contrast Inhib switch vs combi baseline	34.91	39.99	-5.08
Memory	Peoples Test total	27.58	22.82	**4.76***
	Peoples test delayed	9.79	8.18	**1.61***
	Logical memory 1 total	50.26	38.35	**11.91****
	Logical memory 2 total	32.55	23.24	**9.31****
	Logical memory retention	89.62	80.42	**9.2***

Table 7: Standard neuropsychological test battery performance for patients and controls. Data in bold represent significant differences in performance between patients and controls as quantified using post-hoc Tukey HSD contrasts from a repeated measures ANOVA. *=p<0.05, **=p<0.01, ***=p<0.001. WTAR=Weschler test of adult reading.

Voxelwise tract-based spatial statistics indicated that patients on average had significantly lower FA compared to controls, TFCE corrected (p<0.05). White matter damage was distributed widely throughout the brain (Fig. 54B). No significant increases in FA were observed in patients.

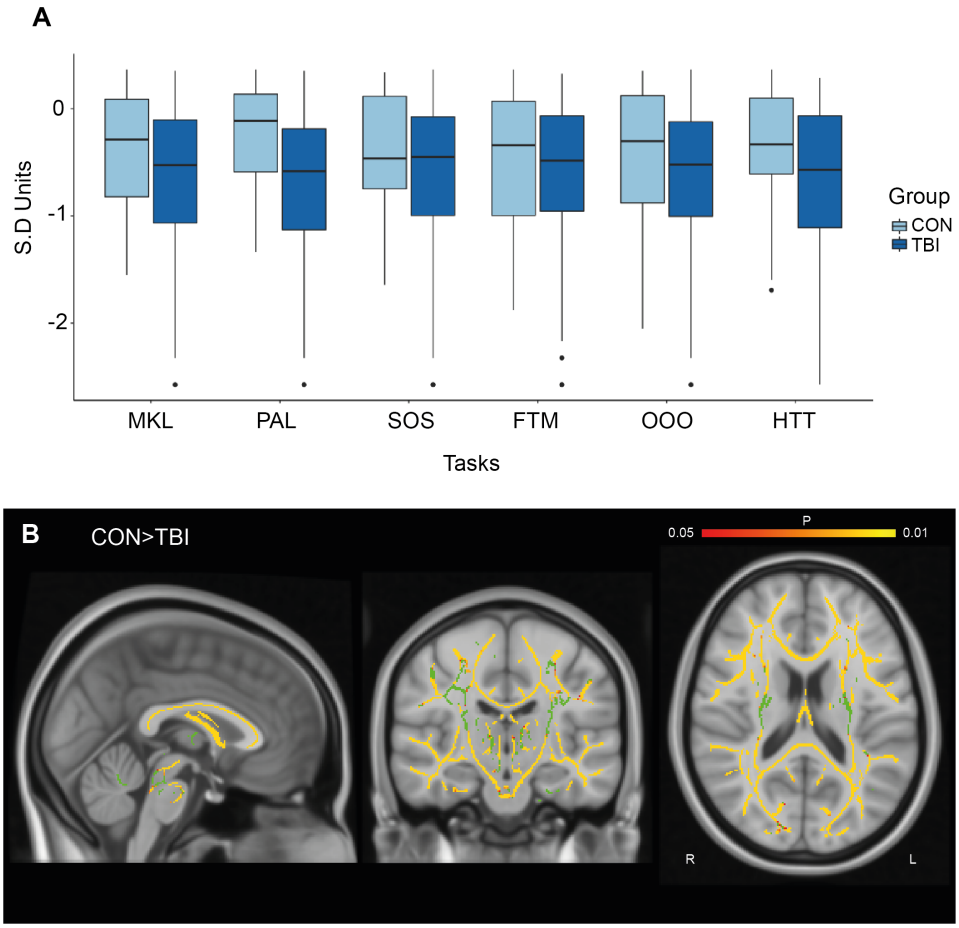


Figure 54. Cross-sectional analysis of TBI patients and controls for cognitive performance and whole-brain fractional anisotropy. A. Performance across the six cognitive tasks in TBI patients and healthy controls. MKL=Monkey ladder, PAL=Paired associates learning, SOS=Self ordered search, FTM=Feature match, OOO=odd one out and HTT=Hampshire tree task. Y axis is in SD units. **B.** Voxelwise analysis using TBSS, TFCE corrected with age as a covariate. Yellow indicates voxels with significantly higher FA in controls than patients (p<0.05). Green indicates the group averaged mean FA skeleton mask. *Figure reproduced from Jolly et al., 2020, Distinct patterns of structural damage underlie*

working memory and reasoning deficits after traumatic brain injury, Brain*, Volume 143, Issue 4, April 2020, Pages 1158–1176 under Creative Commons CC BY license.*

4.4.2 Computerised tasks load onto two distinct cognitive components

A PCA of the patient cognitive data indicated two significant components (Appendix figure 1.9). Orthogonal rotation replicated the previously reported pattern of task-component loadings, where psychometric analyses were applied to data from 44,600 members of the general public (Hampshire *et al*., 2012) (Fig. 55). The rotated components explained 54.27% of the variance with component 1 explaining 27.17 % and component 2 explaining 27.10%. Higher loadings of the FTM, OOO and HTT tasks onto component 1 demonstrate a distinct reasoning ability. Higher loadings of the MKL, PAL and SOS onto component 2 demonstrate a distinct working memory ability. A similar structure was observed when applying PCA with varimax rotation to all patient and control cognitive data combined, with two components explaining 42.33% of the variance in the data. Component 1 explained 21.17% and had highest loadings for the reasoning tasks (FTM, OOO, HTT) whilst component 2 explained 21.16% and had the highest loadings for working memory tasks (MKL, PAL, SOS).

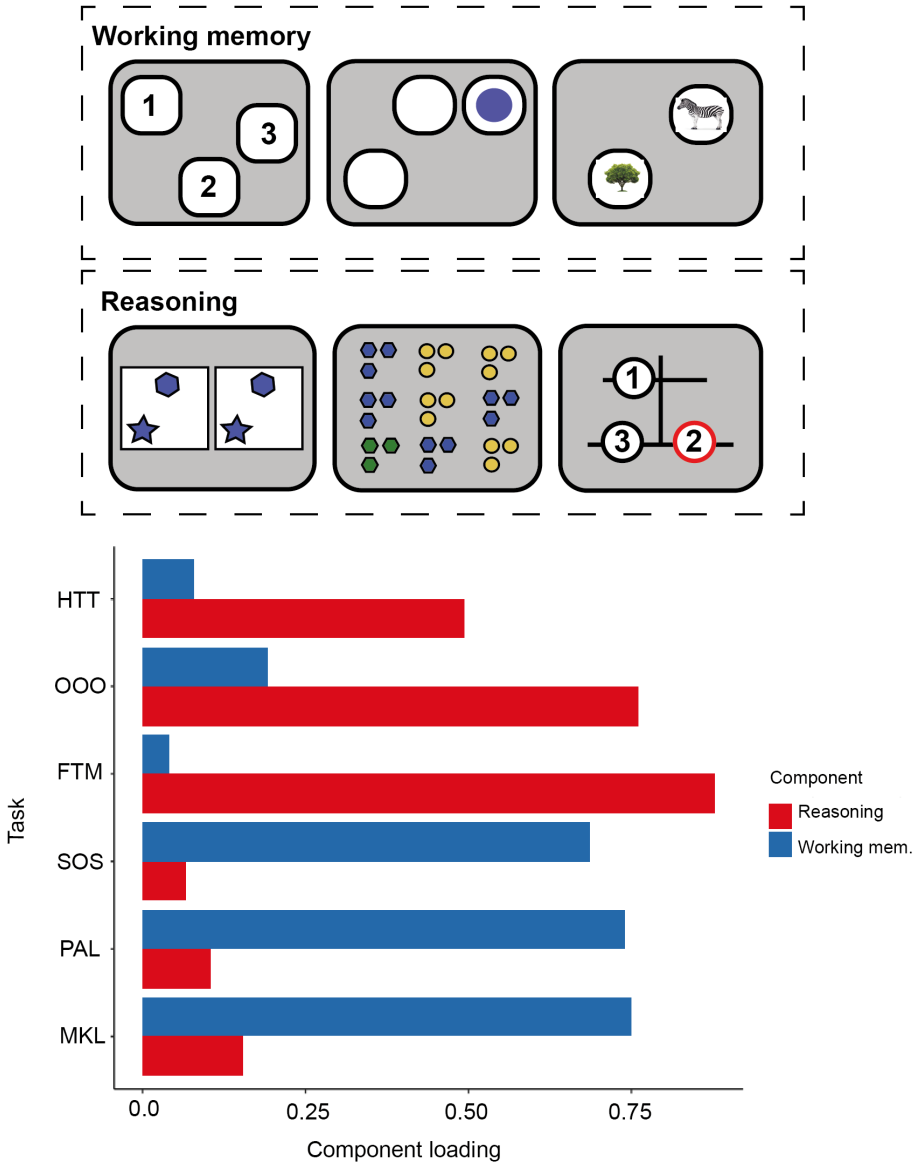


Figure 55: Principal component analysis of patient cognitive data. Component loadings for each task demonstrate higher loadings onto component 1 for reasoning-based tasks such as the HTT, OOO and FTM. Greater loadings to component 2 were observed in working memory-based tasks including MKL, PAL and SOS. *Figure reproduced from Jolly et al., 2020, Distinct patterns of structural damage underlie working memory and reasoning deficits after traumatic brain injury,* Brain*, Volume 143, Issue 4, April 2020, Pages 1158–1176 under Creative Commons CC BY license.*

4.4.3 Reasoning and working memory tasks correlate to standard clinical neuropsychological tests

I examined the relationship between the components derived from computerised tasks and the standard paper neuropsychological tests in patients (Fig. 56A). A principal components analysis of standard neuropsychological tests revealed four significant components that explained 69.93% of the total variance (Fig. 56B). A principal components analysis with both patients and controls revealed the same factor structure. Bivariate correlations between computerised and neuropsychological cognitive components revealed a significant relationship between reasoning and neuropsychological component 1 (r=-0.32,p=0.016, FDR corrected) and a significant relationship between working memory performance and neuropsychological component 3 (r=0.37,p<0.01, FDR corrected) (Fig. 56C). Task loadings revealed that component 1 was primarily associated with executive function measures such as the Colour-Word Interference Task sub-scales (Stroop) and Trail Making Tasks whilst component 3 was associated with memory measures such as the Peoples Test and to a lesser extent, Logical Memory sub-scores (Fig. 56D).

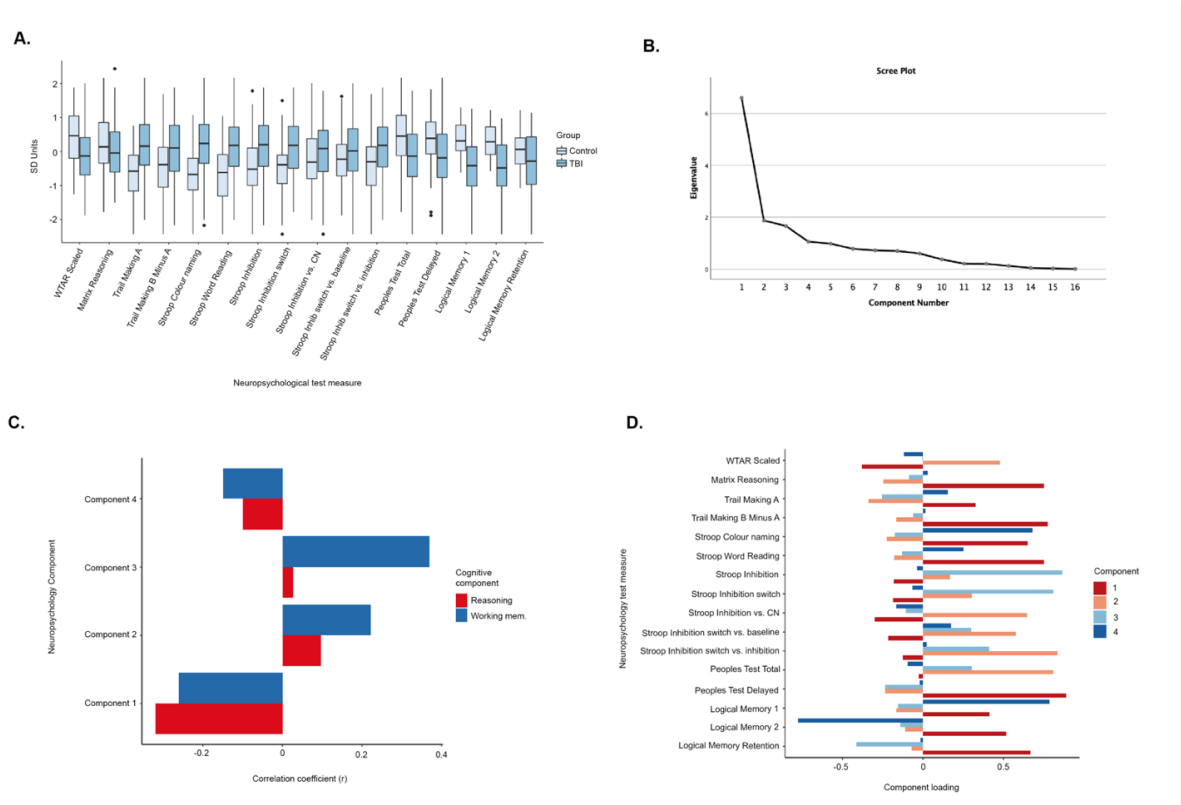


Figure 56: Association between working memory/reasoning performance derived from computerised tasks and classical neuropsychological test performance in patients. A.

Performance as quantified in SD units on 16 sub-tests of the standard neuropsychological test battery previously used to assess TBI patients (Kinnunen *et al*., 2011; De Simoni *et al*., 2018). **B**. Component eigenvalues derived from principal component analysis (PCA) of standard neuropsychological test performance in TBI patients. **C.** Bivariate correlations between working memory and reasoning performance derived from PCA of computerised task data with the four cognitive components derived from PCA of standard neuropsychological tests in the same patient cohort. **D.** Component loadings of each individual neuropsychological sub-test. *Figure reproduced from Jolly et al., 2020, Distinct patterns of structural damage underlie working memory and reasoning deficits after traumatic brain injury,* Brain*, Volume 143, Issue 4, April 2020, Pages 1158–1176 under Creative Commons CC BY license.*

4.4.4 Abnormal working memory and reasoning structural networks after TBI

Extraction of working memory and reasoning networks by intersection of the Desikan-Killiany grey matter atlas with task-based activation maps from Hampshire *et al*., 2012 resulted in a working memory network consisting of 31 nodes and a reasoning network consisting of 26 nodes (Table 8). In network science, nodes can be members of multiple networks. Here, nine nodes shared membership across the two networks including; left lateral orbitofrontal, left precentral gyrus, left rostral middle frontal, left superior frontal, right caudate middle frontal, right precentral, right rostral middle frontal, right superior frontal and right superior parietal lobe. Six hubs were identified in the working memory network and included: left caudate, right pallidum, insula bilaterally, right precuneus and the right superior parietal cortex. In the reasoning network, five hubs were identified: the left rostral middle frontal cortex, left superior frontal cortex, superior parietal cortices and right inferior parietal cortex. Three of the hubs within the reasoning network formed nodes within the working memory network. Hub classification was consistent across all analysed thresholds.

Working Memory network nodes	Reasoning network nodes
Caudate.L†	CaudMidFront.L
Pallidum.L	Cuneus.L
Hippocampus.L	Fusiform.L
Caudate.R	InfParietal.L
Pallidum.R†	InfTemporal.L
Hippocampus.R	LatOcc.L
CaudAntCing.L	**LatOrbFront.L**

LatOrbitoFront.L	ParsOperc.L
Paracentral.L	Pericalcarine.L
PostCentral.L	**Precentral.L**
PostCingulate.L	**RosMidFront.L**†
Precentral.L	**SupFront.L**†
Precuneus.L	SupParietal.L†
RosAntCing.L	**CaudMidFront.R**
RosMidFront.L	Cuneus.R
SupFront.L	Fusiform.R
Insula.L†	InfParietal.R†
CaudaAntCing.R	InfTemporal.R
CaudMidFront.R	LateralOcc.R
LatOrbitoFront.R	Lingual.R
Paracentral.R	ParsOperc.R
PostCentral.R	Paricalcarine.R
PostCingulate.R	**Precentral.R**
Precentral.R	**RosMidFront.R**
Precuneus.R†	**SupFront.R**
RosAntCing.R	**SupParietal.R**†
RosMidFront.R	
SupFront.R	
SupParietal.R†	
SupraMarg.R	
Insula.R†	

Table 8: List of nodes for working memory and reasoning networks. Nodes defined using activation maps from Hampshire et al., 2012. †Network Hub as defined using node degree (highest 20% degree in healthy controls). Highlighted nodes in bold indicate overlap between working memory and reasoning networks.

Cross-sectional analysis of global network measures using graph theory demonstrated that TBI patients had significant alterations in both working memory and reasoning networks compared to controls. TBI patients had significantly lower global efficiency in working memory ($t(196)=6.04$, $p<0.001$, FDR corrected) and reasoning networks ($t(196)=5.29$, $p<0.001$, FDR corrected), significantly lower average degree centrality in working memory ($t(196)=8.82$, $p<0.001$) and reasoning networks ($t(196)=8.81$, $p<0.001$, FDR corrected) and significantly higher average local efficiency in working memory ($t(196)=-6.59$, $p<0.001$, FDR corrected) and reasoning networks

(t(196)=-3.35, p<0.001, FDR corrected) compared to controls. This was consistent across 80% of threshold iterations excluding the most extreme thresholds only.

4.4.5 Patients demonstrate alterations in local/nodal network properties

Individual node metrics in both the working memory and reasoning networks were compared between patients and controls (Fig. 57). Patients demonstrated significant reductions in degree for all nodes within the working memory and reasoning networks compared to controls (p<0.001, FDR corrected). In the working memory network, local efficiency was significantly higher in 81% of nodes (p<0.01, FDR corrected) and significantly lower in 6% of nodes (p<0.01, FDR corrected) compared to controls. Greater clustering coefficient were also observed in 68% of nodes (p<0.05, FDR corrected) in patients compared to controls (Appendix Table 2.1).

In the reasoning network, local efficiency was significantly greater in 62% of nodes (p<0.05, FDR corrected) and significantly lower in 23% of nodes (p<0.05, FDR corrected) in patients compared to controls. Clustering coefficient was significantly greater in 50% of nodes (p<0.01, FDR corrected) and significantly lower in 19% of nodes (p<0.01, FDR corrected) in patients compared to controls (Appendix Table 2.2).

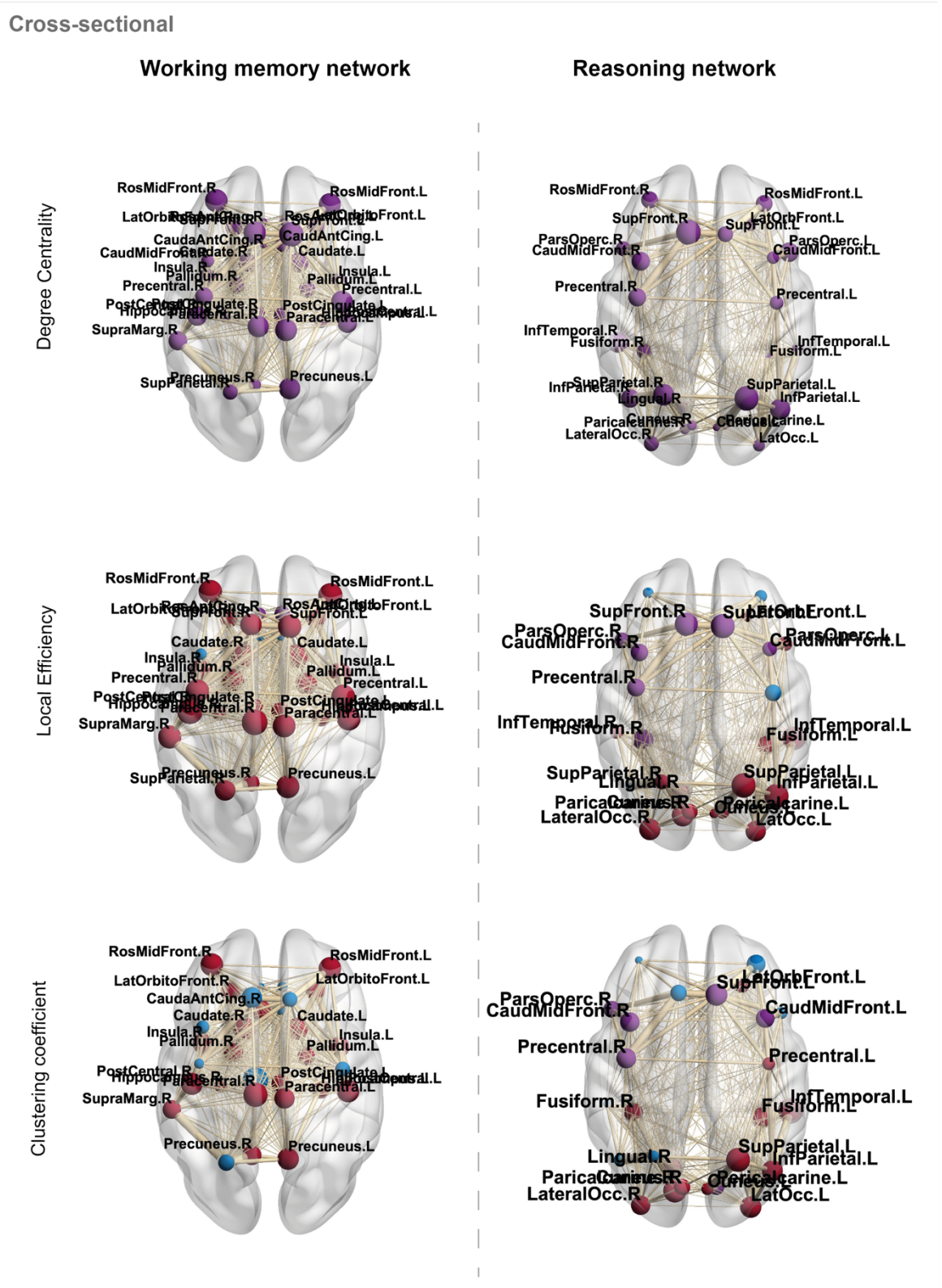


Figure 57: Cross-sectional analysis of local/nodal properties in TBI patients and controls. Blue nodes indicate non-significance, purple nodes indicate significantly lower values in patients compared to controls and red nodes indicate significantly greater values in patients compared to controls, FDR corrected. Node size=difference between patient and control local/nodal properties for each metric

examined. Edge width=weighted by FA and no. streamlines. Significant nodes are labelled for reference. *Figure reproduced from Jolly et al., 2020, Distinct patterns of structural damage underlie working memory and reasoning deficits after traumatic brain injury,* Brain*, Volume 143, Issue 4, April 2020, Pages 1158–1176 under Creative Commons CC BY license.*

4.4.6 Canonical Correlation Analysis confirms dissociable relationships between working memory/reasoning and structural networks

A CCA was conducted to test whether multiple latent variables captured shared variance between node degree centrality and cognitive measures. Data reduction using a principle component analysis was applied to all the nodes included in the whole brain structural connectome, resulting in a total of nine components capturing 90% of the variance. Scores for the two cognitive components formed the first matrix whilst scores for the nine node components formed the second matrix input to the CCA. To determine the significance of canonical correlation coefficients, a permutational test was conducted, where the subject labels were shuffled and the CCA repeated 10,000 times to produce null distributions for each canonical mode (Fig. 58).

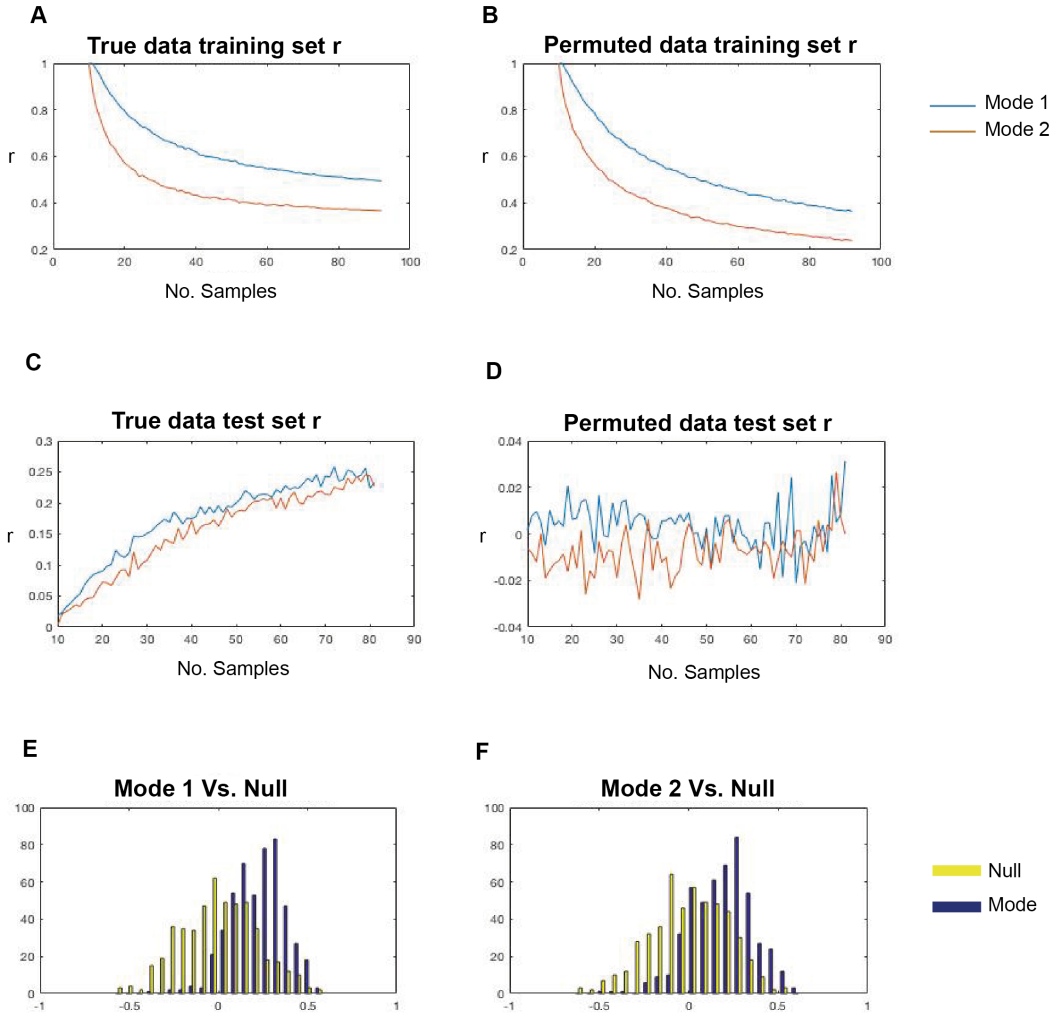


Figure 58: Sub-sampling canonical correlation analysis results to assess model genralisability and overfit. In order to quantify generalisability the CCA analyses were repeated in an iterative loop, whereby the data were randomly sub-sampled, the model trained, then applied to the held out data to which it was naiive. This process was repeated with systematic variation in the trained (N. samples) and held out (remaining samples) ratio, with r values averaged over 1000 iterations at each point. The process was then repeated using permuted data to assess overfit. **A.** Canonical r values for each mode calculated within the training set at varying sub-sample sizes. **B.** Canonical r values for each mode as calculated using the same training set data but with the labels permuted to break the behavioural-graph thery metric linkage. Note that although the r values are higher for the true data, they also are in the medium range for the permuted data. **C.** Canonical r values for the held out data, to which the model was naiive. **D.** Canonical r values calculated the same way as for 'C' but with the permuted data. Note that generalisation for the true data is in the r=0.25 range for both modes in the true data, but on average is close to 0 for the permuted data **E.** Distribution of canonical r values for Mode 1 using 1000 sub-samples at a 2:1 train/test ratio. Blue=true data, yellow = permuted data. **F.** The distribution of true and permuted canonical r values for Mode 2 for the same models as 'E'. *Figure reproduced from Jolly et al.,*

2020, Distinct patterns of structural damage underlie working memory and reasoning deficits after traumatic brain injury, Brain*, Volume 143, Issue 4, April 2020, Pages 1158–1176 under Creative Commons CC BY license.*

The results indicated two significant modes ($p<0.001$ & $p<0.02$) with canonical coefficient values (r) of .470 & .334 respectively. The means of canonical modes in the corresponding null distributions were (r) of .36 & .24 respectively. Back projection of canonical modes to raw task and node degree data revealed a greater contribution of reasoning tasks to mode 1 and greatest contribution of working memory tasks to canonical mode 2 (Fig. 59A). Of the 90 nodes included within the analysis, back projection revealed nodes associated with the reasoning sub-network contributed the greatest to canonical mode 1 whereas nodes associated with the working memory sub-network were found to contribute the greatest to canonical mode 2 (Fig. 59B).

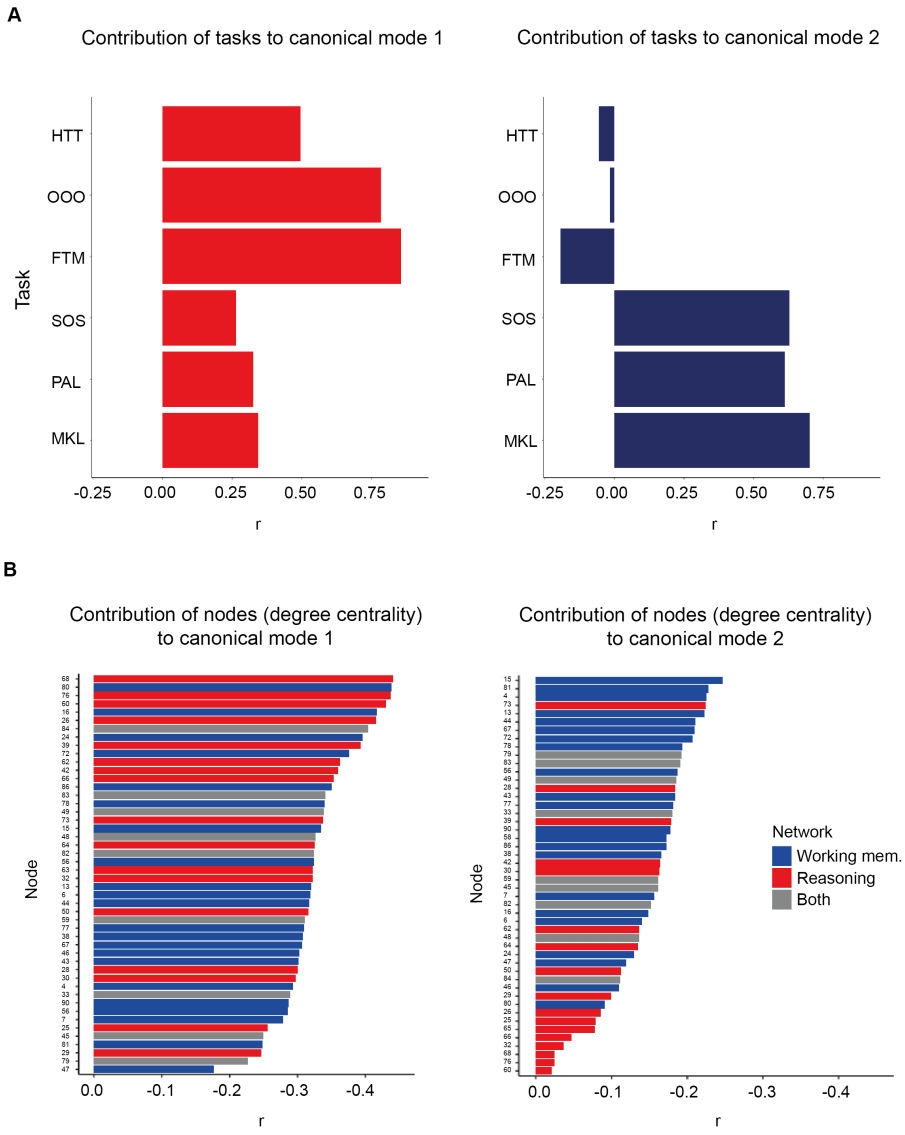


Figure 59: Back projection of canonical variates to task and node data from Canonical correlation analysis. Canonical correlation analysis produced two significant modes demonstrating two distinct relationships between cognitive variables and degree centrality of the 90 nodes defined in the whole brain connectome. **A.** Back projection of cognitive canonical variates to cognitive tasks demonstrated greater contribution of reasoning tasks (HTT, OOO and FTM) to canonical mode 1 and greater contribution of working memory tasks (MKL, PAL, SOS) to canonical mode 2. **B.** Back projection of node canonical variates to individual nodes and their measures of degree centrality revealed that dissociable patterns of nodes were associated with each canonical mode. Specifically, reasoning nodes (red bars) contributed the greatest to canonical mode 1and working memory nodes (blue bars) contributed the greatest to canonical mode 2. Grey bars denote where nodes are present within both structural networks. *Figure reproduced from Jolly et al., 2020, Distinct patterns of structural damage underlie working memory and reasoning deficits after traumatic brain injury,* Brain, *Volume 143, Issue 4, April 2020, Pages 1158–1176 under Creative Commons CC BY license.*

4.4.7 Correlation of global network properties with cognitive performance in patients

CCA's are useful insofar as they test how many latent variables relate two matrices of data in a data-driven and multivariate manner, however they are overfitted by definition and provide limited mechanistic insight. Therefore, calculation of the scale of relationships and interpretation require further analysis. First, global graph theoretic measures from the two sub-networks were compared to behavioural scores. The results showed significant but distinct relationships to cognitive performance whereby global efficiency of the working memory network correlated significantly and at the same approximate strength with both working memory ($r=0.22$, $p=0.042$, FDR corrected) and reasoning ($r=0.25$, $p=0.025$, FDR corrected) performance. Conversely, global efficiency of the reasoning network correlated significantly with reasoning ($r=0.32$, $p=0.024$, FDR corrected) performance, but not for working memory ($r=0.20$,$p=0.06$, FDR corrected). Mean local efficiency of the working memory network correlated significantly with both working memory ($r=-0.25$,$p=0.025$, FDR corrected), and reasoning ($r=-0.26$,$p=0.024$, FDR corrected) performance; whereas the average local efficiency of the reasoning network correlated significantly with reasoning ($r=-0.28$,$p<0.02$, FDR corrected) but not working memory ($r=-0.12$,$p=0.239$, FDR corrected) performance. Finally, mean degree centrality of the working memory network correlated at the same approximate strength with working memory ($r=0.28$,$p<0.02$, FDR corrected) and reasoning ($r=0.30$,$p<0.02$, FDR corrected); whereas average degree centrality in the reasoning network correlated more robustly with reasoning ($r=0.33$,$p<0.02$, FDR corrected) than working memory performance ($r=0.24$,$p=0.025$, FDR corrected).

4.4.8 Local/nodal level network properties correlate to cognitive performance in patients differentially

Next, local/nodal graph theoretical metrics were correlated to cognitive performance in patients (Fig. 60). Significant positive correlations were observed between working memory performance and degree centrality in 32% of nodes in the working memory network. Significant negative correlations were also observed between working

memory performance and local efficiency in 20% of nodes and between clustering coefficient and working memory performance in 3% of nodes (P<0.05, FDR corrected). When correlating reasoning performance to working memory network properties, significant positive correlations were observed to degree centrality in 70% of nodes and negative correlations to local efficiency and clustering coefficient in 42% and 35% of nodes respectively (P<0.05, FDR corrected). For network hubs including the left caudate, right pallidum and insula bilaterally, local efficiency and degree centrality were shown to be consistently related to working memory and reasoning performance. All nodes with significant correlations to reasoning and working memory performance had abnormal network properties compared to controls.

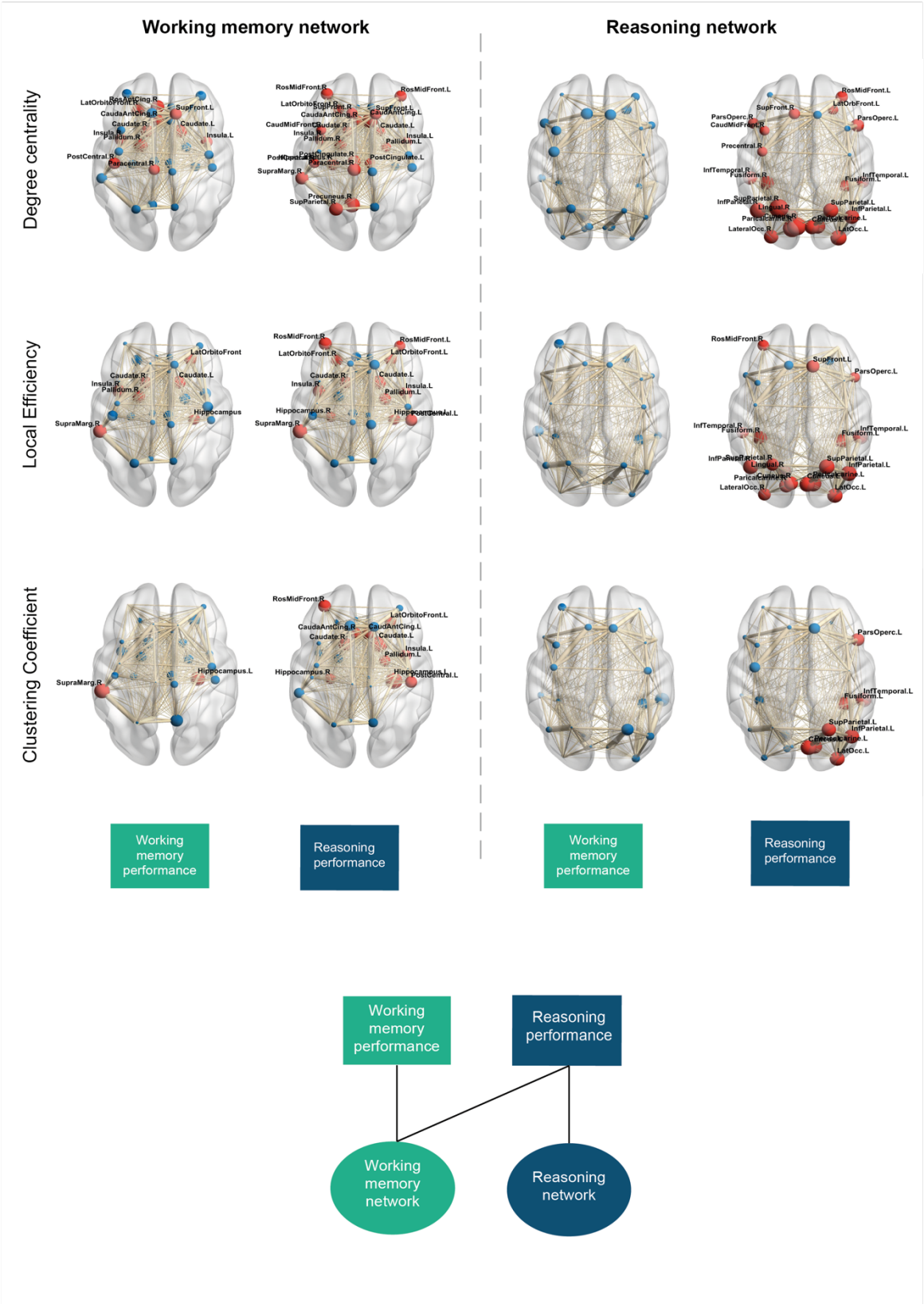


Fig 60: Local graph theory network measures and correlation to cognitive performance. Node size represents correlation coefficient (r, positive or negative). Red nodes demonstrate a significant

correlation to cognitive components (p<0.05, FDR corrected) blue nodes demonstrate non-significant correlations. For measures of degree centrality, red nodes denote significant positive correlations, FDR corrected. For measures of local efficiency and clustering coefficient, red nodes denote significant negative correlations, FDR corrected. Edge thickness demonstrates weight of a given connection (FA and no. streamlines). Boxes at bottom demonstrate which cognitive component is correlated to each of the networks and properties demonstrated. Bottom figure illustrates the dissociable relationship between cognitive components and working memory and reasoning structural network properties. *Figure reproduced from Jolly et al., 2020, Distinct patterns of structural damage underlie working memory and reasoning deficits after traumatic brain injury,* Brain*, Volume 143, Issue 4, April 2020, Pages 1158–1176, under Creative Commons CC BY license.*

In the reasoning network, significant positive correlations were observed in 81% of nodes between degree centrality and reasoning performance. A combination of negative (62%) and positive (8%) correlations was observed between local efficiency of nodes and reasoning performance. Significant negative correlations were also observed between clustering coefficient and reasoning performance in 31% of nodes (P<0.05, FDR corrected). In contrast, no significant correlations were observed between any node graph theoretic properties and working memory performance in the reasoning network. Four of the five network hubs related to reasoning in both degree centrality and local efficiency. All local/nodal correlations to cognitive components are provided in Appendix tables 2.3-2.22 and presented in figures 61 and 62.

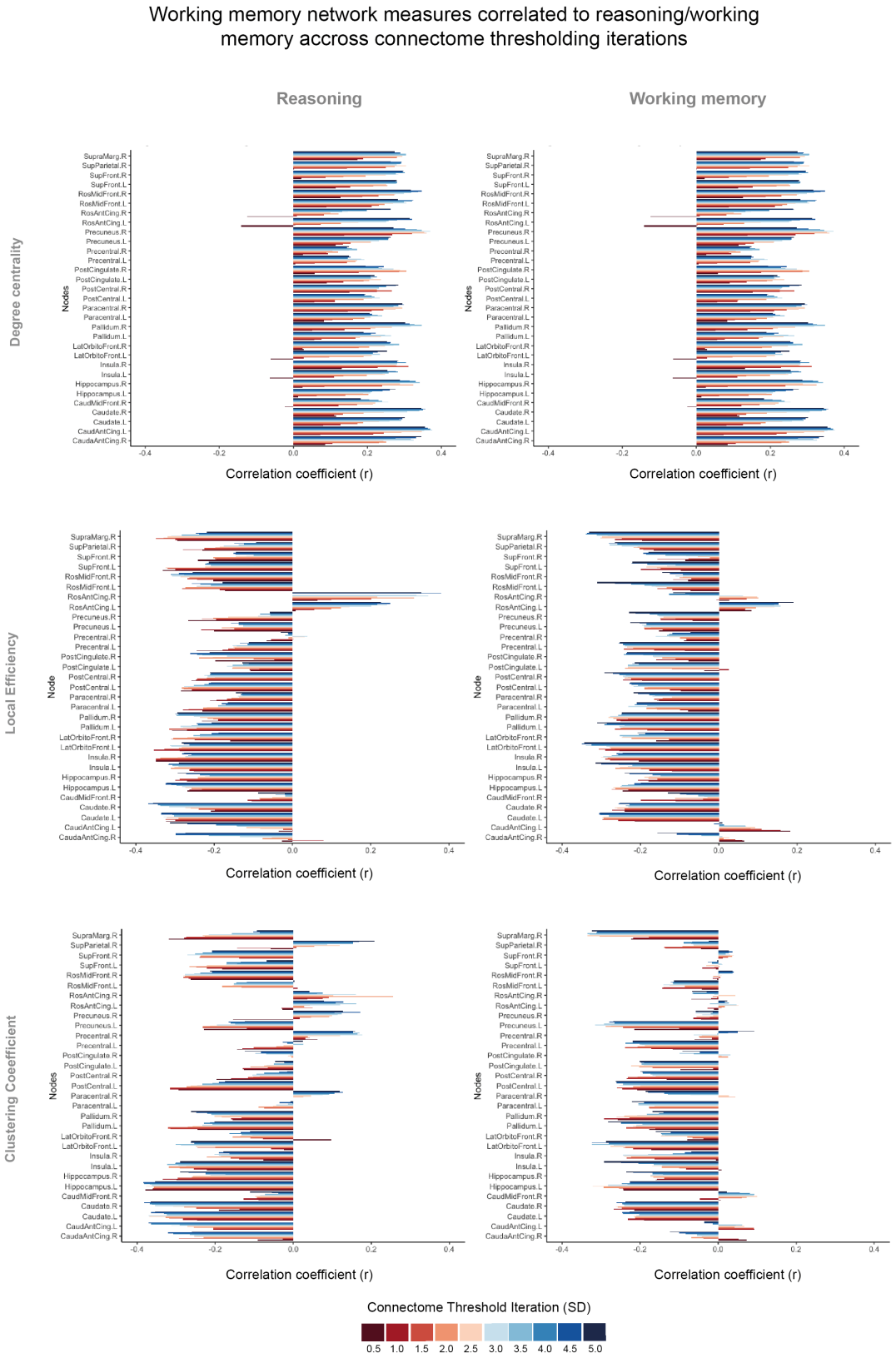


Figure 61: Correlation coefficients of local/nodal working memory network measures across the ten connectome threshold iterations. Plots on left illustrate correlation coefficients for working memory network node measures (degree centrality, local efficiency and clustering coefficient) to

reasoning performance across all ten connectome threshold iterations. Plots on right illustrate correlation coefficients for working memory network node measures (degree centrality, local efficiency and clustering coefficient) to working memory performance across all ten connectome threshold iterations. Connectome threshold iterations refer to multiplying the control SD connectivity matrix by the threshold value (e.g. 0.5, 1.0, 1.5, 2.0, 2.5, 3.0, 3.5, 4.0, 4.5 and 5.0 SD) and subtracting this from the control mean connectivity matrix. The resulting threshold values derived from this calculation were then applied to each patient and control's individual connectivity matrix such that any value less than the threshold value calculated for a connection was replaced with a zero. *Figure reproduced from Jolly et al., 2020, Distinct patterns of structural damage underlie working memory and reasoning deficits after traumatic brain injury,* Brain*, Volume 143, Issue 4, April 2020, Pages 1158–1176 under Creative Commons CC BY license.*

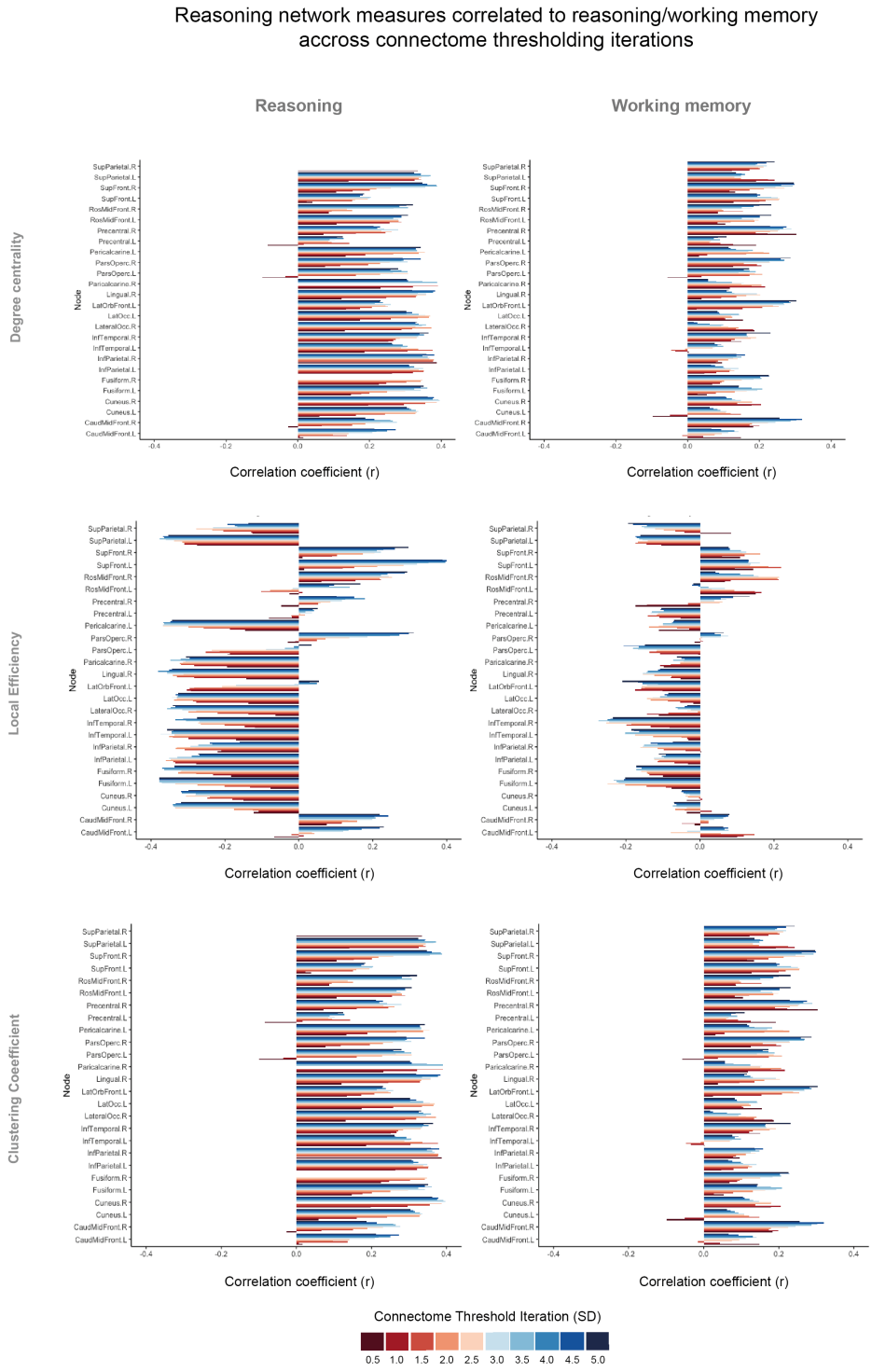


Figure 62: Correlation coefficients of local/nodal reasoning network measures across all ten connectome threshold iterations. Plots on left illustrate correlation coefficients for reasoning network node measures (degree centrality, local efficiency and clustering coefficient) to reasoning performance across all ten connectome threshold iterations. Plots on right illustrate correlation coefficients for reasoning network node measures (degree centrality, local efficiency and clustering coefficient) to working memory performance across all ten connectome threshold iterations. Connectome threshold iterations refer to multiplying the control SD connectivity matrix by the threshold value (e.g. 0.5, 1.0,

1.5, 2.0, 2.5, 3.0, 3.5, 4.0, 4.5 and 5.0 SD) and subtracting this from the control mean connectivity matrix. The resulting threshold values derived from this calculation were then applied to each patient and control's individual connectivity matrix such that any value less than the threshold value calculated for a connection was replaced with a zero. *Figure reproduced from Jolly et al., 2020, Distinct patterns of structural damage underlie working memory and reasoning deficits after traumatic brain injury,* Brain*, Volume 143, Issue 4, April 2020, Pages 1158–1176 under Creative Commons CC BY license.*

4.5 Discussion

My results provide evidence that working memory and reasoning deficits after TBI relate to dissociable patterns of white matter damage, as demonstrated by their differential relationships to distinct structural networks. I demonstrate for the first time that TBI impacts on both working memory and reasoning using a large cohort of patients. A strength of this approach is not only that it provides a further replication of the findings of Hampshire *et al*., 2012, by illustrating that working memory and reasoning form two distinct cognitive abilities; it demonstrates that TBI can impact on either one of these abilities when taking into account the other. This is an important point because cognitive tasks tend to tap multiple abilities and the behavioural basis of deficits can be hard to interpret if tasks are analysed in isolation. I also replicate the finding that disruption to network hubs has a particularly significant impact on the cognitive processes they support (Fagerholm *et al*., 2015). By intersecting an established atlas of white matter connections with reasoning and working memory task-fMRI activation maps, I provide evidence to support the hypotheses that individual differences in cognitive deficits relate to the integrity of information processing architecture within functionally-distinct sub-networks of the structural connectome.

Broadly speaking, this supports Hampshire et al., 2012, where it was observed that tasks that activate the same functional networks also tend to load on to similar behavioural abilities when factor analysing inter-subject variability in their behavioural scores. This interpretation was controversial when first proposed (Haier et al., 2014) and my hypothesis sought to extend this by investigating whether damage to a functionally distinct sub-network would impact on the associated axes of cognitive ability. Here my results confirm this hypothesis and provide refinement in our

understanding of the way in which functionally distinct structural sub-networks support reasoning and working memory abilities. More specifically, whilst the expected dissociation between reasoning and working memory structural networks was evident, the association to working memory and reasoning performance unexpectedly provided evidence of a hierarchal functional relationship between the two networks.

Behavioural data confirmed the hypothesis that working memory and reasoning are distinct aspects of cognitive ability that can be differentially affected by axonal injury. Previous studies investigating impairment after TBI have shown that tasks that tap either of these aspects of cognition can be affected by traumatic brain injury (Kinnunen *et al*., 2011; Palacios *et al*., 2011; McAllister *et al*., 2014; De Simoni *et al*., 2018). However, working memory and reasoning have seldom been investigated in parallel, limiting our understanding of the varied prevalence of impairments after TBI and the mechanisms contributing to them. In studies of healthy individuals, factor analyses of >44,600 members of the general public have demonstrated that working memory and reasoning are distinct axes of cognitive ability (Hampshire *et al*., 2012; Daws *et al*., 2017). Here I observed relatively uniform impairments in the performance of all six computerised tasks when comparing mean scores for TBI patient's relative to controls. This indicated that they were all similarly susceptible to neurotrauma. Nonetheless, principal components analysis of the cognitive data replicated the two cognitive components observed in previous literature (Hampshire *et al*., 2012; Daws *et al*., 2017) such that tasks involved in maintaining information in working memory (MKL, PAL, SOS) loaded onto one principal component whereas tasks that involved transforming information according to rules (FTM, OOO, HTT) loaded onto another.

Widespread diffuse axonal injury was also observed in patients compared to controls, suggesting disruption to these networks may impact upon cognition, as per previous research (Fagerholm *et al*., 2015). The impact of DAI on cognition may be best understood mechanistically from a graph theoretic perspective as the balance between network integration (global efficiency) and segregation (clustering coefficient/local efficiency) is described as key in the emergence of small-world organisation of networks that support cognition (Bullmore and Sporns., 2009; Braun *et al*., 2015; Cohen and D'esposito., 2016). Alterations to this balance reflects aberrant information processing properties that may lead to impaired cognition. Here, analysis

of global graph theoretic measures revealed abnormalities in both the working memory and reasoning networks of TBI patients compared to controls, remaining consistent across 80% of the alternative thresholds examined. I replicated the observation of a move away from optimal small-world topology as illustrated by a reduction in global efficiency and increase in local efficiency which has previously been shown in TBI (Pandit *et al*., 2013). Evidence of reduced average degree in networks suggest that this move away from small-worldness may in part be due to loss of long-range white matter connections (Sharp *et al*., 2014).

The results from the canonical correlation analysis further supported my hypothesis that multiple latent variables or 'modes' relate working memory and reasoning abilities to measures of white matter tract integrity throughout the brain. An advantage of this method is that it identifies the number of latent variables that are common across different matrices of data in an unbiased, data-driven manner. Back-projection of the canonical variates onto the behavioural matrix reproduced the working memory vs. reasoning dissociation whilst back projection onto the node degree centrality matrix partially dissociated the nodes of the working memory and reasoning networks. These results provide further confirmation of the differential impact of DAI on working memory and reasoning in white matter previously associated to impairment after TBI (Kinnunen *et al*., 2011; Palacios *et al*., 2011; McAllister *et al*., 2014; De Simoni *et al*., 2018) and support the initial graph theory findings. However, the main limitations of CCA are that the models are, by design, overfitted. I directly tested this limitation using a sub-sampling permutation test and illustrated that the two modes differed from the null distribution, demonstrating that real dissociable relationships existed. Nevertheless, CCA analyses do not provide mechanistic insights regarding the impact of observed individual differences on network information processing properties and therefore require other complementary analysis to gauge the scale of relationship and aid interpretation.

When cross-correlating behavioural components and graph theoretic measures for these sub-networks, I found similar correlations between reasoning performance and global graph theoretic measures in the reasoning and working memory sub-networks, but only significant correlations between working memory performance and the working memory sub-network. This one-way dissociation was more pronounced in the

analysis of node-centric graph theoretic measures. Abnormalities in degree centrality, local efficiency and clustering coefficient for a large proportion of nodes within the working memory and reasoning networks were observed in patients, and was robustly replicated across 80% of the alternative thresholds. When correlated to cognitive components, similar significant correlations to degree centrality, local efficiency and clustering coefficient were observed with consistently strong relationships in network hubs, supporting previous literature demonstrating the impact of hub disconnection on cognitive impairment (Fagerholm *et al*., 2015). Importantly, cross-correlation revealed a distinct and strong relationship of reasoning performance to these metrics in both the working memory and reasoning sub-networks, but for working memory performance there were significant relationships to nodes within the working memory network only. This one-way dissociation was very robust, being evident in 70% of the threshold iterations (i.e., excluding the most liberal and strict thresholds).

Although I had not predicted this hierarchy when planning the study, this dissociation is precisely what is posited in classic hierarchal models of working memory (Petrides., 1989; Petrides., 1994; D'Esposito *et al*., 1999). More specifically, these models proposed that information must first be maintained in working memory before it can be processed according to task rules. In accordance with this, disruption to the working memory network correlates with impairments in both working memory and reasoning, whereas disruption of the reasoning network is more selectively correlated to reasoning scores. From this perspective, it is interesting to note the relationship of reasoning and working memory abilities to distinct but partially overlapping brain regions. This overlap is unsurprising from a network neuroscience perspective, as the same nodes typically contribute to multiple networks, but in different combinations – indeed this has been shown to be the case for the tasks applied here (Lorenz *et al*., 2018; Soreq *et al*., 2019). Here, three of the five reasoning hubs were also present as nodes within the working memory network, providing clues regarding how networks may operate cooperatively to support the processing of actively maintained information.

From a clinical perspective, the dissociation of working memory and reasoning impairments provides new insights into the systems-level basis for heterogeneity in the cognitive impairments that TBI patients suffer from. These impairments have

severe consequences on a patient's quality of life and highlight the need for improved therapies to be developed. An exciting avenue of research has begun to attempt to treat these impairments via pharmacological interventions, neurostimulation (e.g. tDCS and tACS) and cognitive rehabilitation, however, there remains much debate about the efficacy of these treatments in TBI with little to no standard framework that can be translated into real-world clinical practice. This is likely due to the need to tailor treatments dependent on the type of impairments that patients have. A connectomic description is likely to have value for predicting cognitive impairments or developing individually tailored therapies. One way to achieve this would be to consider concurrently the behavioural profile of impairment and the damage to networks in the brain of the individual.

This profiling could also be used to classify patients when validating pharmacotherapies, cognitive interventions, and other therapeutics such as neurostimulation (Violante *et al*., 2018; Li *et al*., 2019). For example, individuals with deficits due to damage to functionally distinct parts of the structural connectome are likely to respond best to different treatments. Indeed, it has recently been reported that the efficacy of dopaminergic therapy can be predicted based on the degree of striatal dopamine transporter disruption after TBI (Jenkins *et al*., 2017). Furthermore, it has been illustrated that the efficacy of modulating functional networks using tDCS relies upon the structural connectivity underlying the stimulation target (Li et al., 2019). Here I provide a complementary way to further subdivide the patients according to the cortico-cortical networks that are affected.

Nevertheless, there are several potential limitations that should be considered. Firstly, although the network measures demonstrate potential in predicting cognitive performance in patients, the application of machine learning models to determine whether such measures can significantly predict cognitive impairment in patients would be beneficial. Secondly, longitudinal changes in graph theoretical measures of the structural connectome have been demonstrated to be beneficial to cognitive outcomes (Kuceyeski et al., 2019) and future research would therefore benefit from utilising and refining these sub-network graph theory measures to predict the evolution of reasoning and working memory impairments in acute TBI. Thirdly, working memory and reasoning are themselves complex constructs (Hampshire *et al*., 2012;

Christophel *et al*., 2017; Soreq *et al*., 2019) that subdivide the networks examined here at a finer grain. A recent study has demonstrated a paradigm that could be used for this diagnostic purpose because it strongly differentiates multiple aspects of working memory based on network connectomics with high reliability (Soreq *et al*., 2019). Fourthly, a broader characterisation of the types of deficits that are relevant to TBI is required. Indeed, the comparison of standard neuropsychological tests to computerised measures highlights this point. Although substantial variance was shared between the two assessments, the structure of that variance differed such that standard neuropsychological assessments demonstrated additional factors that were affected by TBI that our tasks did not measure. This suggests a broader characterisation of the distinct behavioural abilities that are most commonly affected in TBI and how they map to different patterns of damage within the structural connectome. Achieving this is a focus of current research. Finally, in the current work I have not taken into account the presence of focal lesions which may impact upon network functionality and properties which would be advantageous to explore further. Nevertheless, nodes within these networks do not overlap with lesion overlap maps constructed for this patient cohort, supporting a broader view that impairments primarily relate to disruption to connectivity via the white matter as opposed to damage localised within the grey matter (Gaffan., 2005).

In summary, TBI has a dissociable impact on working memory and reasoning due to the differential disruption of information processing properties of the structural networks that underpin these functions. This work provides new mechanistic insights by demonstrating that the nature of this dissociation is one sided, supporting multifactorial accounts of human cognitive ability (Hampshire *et al*., 2012) and hierarchical accounts of reasoning systems (D'Espoito and Postle., 2015). My work provides potential markers for the identification of patients likely to develop working memory and reasoning impairments. Further investigation utilising these measures in the prediction of cognitive outcomes, particularly in acute patients may prove beneficial. Identifying the properties of aberrant networks and their relationship to working memory and reasoning impairments also provides opportunities for individually targeted therapeutic interventions to be explored.

Chapter 5

Longitudinal changes in structural network topology and its association to working memory performance after TBI

In this chapter I test whether the working memory network metrics previously defined in chapter four can be used to predict working memory in a subacute TBI population. I also investigate the longitudinal changes in structural network topology and its association to working memory outcomes.

5.1 Abstract

In chapter four of this thesis, I demonstrated that distinct patterns of white matter damage associated with disruption to the working memory structural connectome, correlated with impairment after TBI. This work provided a means to quantify individual differences in structural dysconnectivity and its relationship to working memory whilst providing a discrete set of nodes to explore as potential prognostic markers. Previous studies investigating the prognostic value of graph theory measures have shown promising results, however this has largely been demonstrated in chronic TBI. From a clinical perspective, predicting working memory outcomes after TBI is most valuable at more acute phases of injury where decisions regarding the management of patients are made.

This study therefore seeks to explore whether subacute graph theoretical measures of the working memory network nodes identified in chapter four, can accurately predict working memory outcomes. I examine measures of network integration (global efficiency) and local/nodal measures of network segregation (degree centrality, local efficiency and clustering coefficient) in a cohort of 26 moderate-severe TBI patients in the subacute (10 days-6 weeks) and chronic (~6 months) phases of injury. I investigate whether 1) alterations in the working memory network are observed at either injury timepoint 2) whether longitudinal changes in network topology are related to working memory outcomes and 3) examine whether network measures at the subacute phase of injury can predict working memory at the chronic phase using a pattern recognition machine learning approach.

I demonstrate that local/nodal abnormalities in working memory network topology are observed at both the subacute and chronic timepoints. I find that significant changes in measures of local efficiency associated with network segregation are observed longitudinally and that greater increases in local efficiency are associated with better working memory performance in patients at follow-up. Furthermore, I demonstrate that the presence of focal lesions within working memory network nodes does not relate to performance in this cohort. Importantly, I illustrate that measures of degree centrality within the working memory network sub-acutely, can predict working memory

performance at the chronic phase of injury whilst measures of fractional anisotropy (FA) derived from the same connectome cannot.

These findings provide evidence in support of the prognostic value of graph theoretical measures, and begin to provide some mechanistic insights into the structural network changes associated with working memory performance after TBI.

5.2 Introduction

In studies of TBI, alterations in functional and structural network topology are observed, moving away from optimal small-world characteristics towards a regular lattice configuration (Imms et al., 2019). Increased modularity and reduced integration drive this shift as a result of a loss of long-range white matter connections that are prone to damage (Pandit et al., 2013). These alterations have been shown to correlate strongly with working memory deficits in chronic TBI patients, with structural dysconnectivity of network hubs (highly connected regions in a network) demonstrating the strongest associations (Fagerholm et al., 2015). In chapter four, I extended these findings by demonstrating that distinct patterns of white matter damage were associated with working memory impairment due to its impact upon working memory network topology, providing potential mechanistic insights into the heterogeneity of working memory after TBI.

A key motivation for understanding the mechanisms of working memory impairment in TBI is to improve prognosis. Currently, predicting impairment remains difficult (Mollayeva et al., 2019; Ruet et al., 2019), due to a lack of prognostic markers and the dynamic changes that can occur from acute to chronic phases of injury (Edlow et al., 2016; Yin et al., 2019). The findings from chapter four begin to address the first of these limitations by providing a discrete set of network measures that demonstrate prognostic potential insofar as their ability to map individual differences in working memory impairment after TBI. Indeed, previous studies attempting to predict cognitive impairment after TBI using graph theory have shown promise (Fagerholm et al., 2015; Hellyer et al., 2013), warranting the exploration of these measures further. However, the significant and varied changes that occur to the white matter microstructure during

the first year after injury (Sidaros et al., 2008; Wang et al., 2011) far exceed those in the chronic phase (Dinkel et al., 2014), posing a potential challenge for working memory network measures defined in chronic TBI. On the one hand, the relationship between long term cognitive outcomes and acute network topology may be too complex to effectively model, on the other, the metrics derived in a chronic TBI population may lack the sensitivity to detect relationships between acute structure and long-term cognitive outcomes.

Previous work exploring longitudinal changes in structural connectivity using graph theory have demonstrated that network reorganisation within the first year after injury is common and associated with working memory outcomes. Specifically, favourable working memory outcomes have been shown to relate to the development of hyper-connectivity in regions such as network hubs (Dall'Acqua et al., 2017) whilst increased network segregation over a six-month period was associated with better cognitive abilities (Kuceyeski et al., 2019). Importantly, longitudinal changes in network topology were also found be predictive of cognitive performance six months post-injury, suggesting changes in graph theoretical measures of the structural connectome provide valuable prognostic information. Nevertheless, from a clinical perspective, prognosis would be most advantageous with the use of a single imaging assessment soon after injury, rather than on the basis of longitudinal scans which can be limited in a clinical setting (Irimia et al., 2012).

This study therefore seeks to determine whether 1) structural connectivity abnormalities are observed sub-acutely and in the chronic phase of injury, similar to the findings of chapter four. 2) changes in network topology over time are associated with working memory outcomes and 3) whether network measures at the subacute phase of injury can predict working memory performance at the chronic phase. I examine graph theoretical measures of the working memory network at subacute (10 days-6 weeks) and chronic (~6 months) timepoints in a cohort of TBI patients and compare these to a large cohort of healthy controls. I first examine whether similar structural connectivity abnormalities are observed in subacute compared to chronic TBI and relate network measures from each timepoint to working memory performance in the chronic phase. Next, I examine whether lesions to network nodes are associated with working memory performance in patients. Then, I explore the

relationship between longitudinal changes in the working memory network and working memory performance. Finally, I examine whether local/nodal graph theoretic measures from the working memory network at the subacute phase of injury can predict working memory performance at the chronic phase, using the Pattern Recognition for Neuroimaging Toolbox (PRoNTo, Shcrouff et al., 2013). Finally, I compare model performance using graph theory measures vs. fractional anisotropy measures from the same working memory connectome, to determine whether graph theory is more informative in the prediction of working memory outcomes.

5.3 Materials and Methods

5.3.1 Participants

A total of twenty-six moderate to severe-TBI patients (7 females, mean age 49.36, SD 13.45 years) in the subacute phase (10 days-6 weeks) of their injury were recruited from the major trauma centre at St Mary's hospital, London. Patients were recruited no less than 10 days since injury to allow for the stabilisation of FA that has been shown to significantly increase in the first few days after injury and resolve within 10 days (MacDonald et al., 2007a). Inclusion criteria were; age over 16 years and a diagnosis of a traumatic brain injury (TBI) as classified using the Mayo criteria (Malec et al., 2007). Exclusion criteria were; unwillingness or inability to follow the procedures required and contraindication to MRI. Mean time since injury was 26 days (11.49 SD, range 11-50 days). Information regarding mechanism of injury, current medications and PTA duration can be found in Table 9. All patients completed structural MRI at the subacute (10 days-6 weeks) and chronic (~6 months) phases of injury on the same scanner. All patients completed cognitive assessments at the chronic phase of injury, inclusive of the Repeatable Battery for the Assessment of Neuropsychological Status (RBANS, Randolph et al., 1998) and a computerised visuospatial working memory task (the Paired Associates Learning task, PAL). A proportion of patients (n=11) also completed cognitive assessments at the subacute phase of injury, providing longitudinal cognitive measures.

One hundred and five healthy controls scanned using the same MRI and acquisition parameters (35 female, mean age 44.98, SD 15.16 years) were included for comparison of structural connectivity. A second cohort of 59 healthy controls (16 female, mean age 39.93, SD. 16.72. years) were included to compare cognitive performance. Controls who underwent cognitive testing completed the same computerised working memory task as patients, and a subset (n=20, 5 females, mean age 48.32, SD 17.23 years) also completed the RBANS. Exclusion criteria for healthy controls were; no history of significant neurological or psychiatric conditions. Written informed consent was obtained for all patients in accordance with the Declaration of Helsinki. The study was approved by the Camberwell St Giles research ethics committee (17/LO/2066).

Age	Gender	Severity	Mechanism of injury	PTA duration	Time since injury at subacute (days)	Time since injury at chronic (days)
22	Male	Mod-severe	RTA	1to7days	11	170
24	Male	Mod-severe	Assault	NK	26	179
45	Male	Mod-severe	RTA	1to7days	29	191
41	Male	Mod-severe	Assault	None	28	188
55	Female	Mod-severe	Fall	1to24Hour	29	249
56	Female	Mod-severe	RTA	NK	49	175
40	Male	Mod-severe	Assault	1to24Hour	50	189
52	Male	Mod-severe	RTA	1to29Minutes	29	191
70	Male	Mod-severe	Fall	1to24Hour	25	193
58	Male	Mod-severe	Fall	1to24Hour	13	196
42	Male	Mod-severe	Fall	None	28	226
67	Female	Mod-severe	RTA	1to7days	20	183
*26	Male	Mod-severe	Fall	None	13	181
60	Female	Mod-severe	Fall	None	12	186
*43	Male	Mod-severe	Fall	1to24Hour	25	203
*47	Male	Mod-severe	Fall	None	22	183
*45	Male	Mod-severe	RTA	1to24Hour	16	190
*52	Female	Mod-severe	RTA	1to7days	44	177

*49	Male	Mod-severe	Fall	1to7days	26	219
*75	Female	Mod-severe	Fall	None	44	183
70	Male	Mod-severe	RTA	1to7days	14	196
*44	Male	Mod-severe	Fall	NK	24	166
*47	Male	Mod-severe	Fall	1to7days	21	176
*41	Female	Mod-severe	Fall	NK	20	235
*60	Male	Mod-severe	Sports	NK	35	203
42	Male	Mod-severe	Fall	NK	26	189

Table 9: TBI patient demographics and time since injury at subacute and chronic assessments. M=Male, F=Female, RTA=road traffic accident, NA=not available, NK=Not known, PTA=post traumatic amnesia. * Patients with longitudinal data

5.3.2 Structural MRI acquisition

Structural MRI for patients and controls were acquired on the same scanner using a 3T Siemens Magnetom Verio Syngo with a 32-channel head coil. Structural MRI included a high-resolution T1-weighted MPRAGE and diffusion weighted imaging as well as fluid attenuation inversion recovery (FLAIR) and susceptibility weighted imaging (SWI) for the delineation of focal lesions and oedema in subacute scans. Patients repeated the same structural MRI acquisition at both timepoints. Further details regarding acquisition parameters can be found in methods chapter two section 2.3.1.

5.3.3 Cognitive assessment

5.3.3.1 Standard Neuropsychological testing

Standard neuropsychological testing was performed using the RBANS for TBI patients and controls to provide comparison of the computerised working memory task with gold standard measures currently used clinically. The RBANS is a classical test of neuropsychological function and is designed for longitudinal tracking of deficits within clinical populations inclusive of TBI in and outside of acute care settings (Randolph et al., 1998). This battery consists of 12 sub-tests designed to measure deficits within five cognitive domains broadly associated with 1) Immediate memory 2)

Visuospatial/Constructional 3) Language 4) Attention and 5) Delayed memory. For further details regarding the sub-tests associated with each domain please refer to table 10.

Domain	Sub-test	Brief Description
Immediate memory	List learning	Individuals are read a list of 10 words and asked to recall as many as possible four times to allow learning.
	Story memory	Individuals are read a short story and asked to recall as much of the story immediately. They are asked to perform this twice to allow for learning.
Visuospatial/Constructional	Figure copy	Individuals are presented with a picture comprising of different shapes. They are given a maximum of four minutes to copy the figure, the figure remains presented the whole time.
	Line orientation	Individuals are presented with two lines in different orientations and asked to match the lines to a several options presented below.
Language	Picture Naming	Individuals are presented with 10 pictures sequentially and asked to name them. They are provided with a semantic prompt if they cannot recognise what the picture is (e.g. “a tool”, “a kitchen appliance”).
	Semantic fluency	Individuals are given. Sixty seconds to generate as many words as possible belonging to a semantic category (e.g. musical instruments)

Attention	Digit span	Patients are read a sequence of numbers and asked to repeat these back in the exact order. The length of the sequence increases until an individual makes two consecutive errors on the same length sequence.
	Coding	Individuals are presented with boxes consisting of symbols and numbers associated with them. They are then given 90 seconds to complete empty boxes with the correct numbers corresponding to the symbols presented at the top of the page.
Delayed memory	List recall	Individuals are asked to recall as many of the words the were presented at the beginning of the battery without prompting.
	List recognition	Individuals are provided with words and asked to determine whether the word was in the list they were asked to remember at the beginning of the battery.
	Story recall	Individuals are asked to recall the story they were presented with earlier in the battery from memory.
	Figure recall	Individuals are asked to draw the figure from memory that they were presented with and drew earlier in the battery.

Table 10: List and description of sub-tests included within the RBANS. Domain index scores are calculated as total score across sub-tests within domain.

5.3.3.2 Computerised working memory task

A computerised visuospatial working memory task was used to assess working memory performance. The Paired Associates Learning (PAL) task is an object-location binding paradigm that has been applied to TBI patients previously (De Simoni et al., 2016) and modified for use in a TBI population. All Patients and controls completed the task using a Samsung touch-screen tablet (Tab A, version 10.3). Further details regarding the task paradigm can be found in methods chapter two, sections 2.1.2 and 2.1.3.

5.3.4 Image pre-processing

5.3.4.1 Diffusion tensor imaging

Diffusion tensor imaging was pre-processed using FSL's diffusion toolkit (FDT) in the same manner as detailed in methods chapter two, section 2.4.1. This was performed for both subacute and chronic timepoints in patients, and for healthy controls. Fractional anisotropy (FA) maps derived from FDT were subsequently registered to standard space and skeletonised using tract-based spatial statistics (TBSS, Smith et al., 2006). Next, whole brain 90x90 structural connectomes were constructed for controls and patients at both injury timepoints in the same manner as detailed in chapter four. This was achieved by extracting mean FA values from individual skeletonised FA maps using a set of predefined track density image (TDI) masks derived from the MRIIIT human white matter atlas (Zhang et al., 2018). Structural connectomes were weighted by FA and number of streamlines for a given connection. Connectomes were subsequently thresholded such that values below the defined standard deviation of healthy control data, was replaced with a zero. A range of standard deviation criteria were used (0.5 to 5 SD in increments of 0.5). For further details regarding the construction and pre-processing of connectomes, please refer to chapter two, section 2.5.2 and chapter four methods section 4.3.8. Finally, the 31 nodes previously defined as representing the working memory network in chapter four were extracted from the whole brain connectome to provide working memory network specific connectomes for use in graph theoretical analysis. To determine whether

graph theoretic measures provide additional information that cannot be derived from fractional anisotropy measures, mean FA for the whole working memory network (average FA across all working memory network nodes) and individual network nodes was extracted from the connectomes used to calculate graph theory measures. For comparison to the findings of chapter four, all results presented will be derived from structural connectomes thresholded by the moderate 2.5 SD criteria.

5.3.4.2 Delineation of focal lesions

For the delineation of focal lesions in patients in the subacute phase of injury, in house lesion drawing software (ImSeg) was used. Lesion masks were drawn using the native T1 image, guided by FLAIR and SWI and included oedema to account for potential confounds of blood in imaging statistical analysis. Native T1 images were subsequently registered to standard space using DARTEL as detailed in methods chapter two section 2.4.2. The flow-fields derived from registering individual T1 images to standard space were then applied to lesion masks using DARTEL to also register these to standard space. A group-level lesion overlap mask was subsequently derived by combining all individual masks and averaging the resulting image.

5.3.5 Statistical analysis

5.3.5.1 Cognitive assessment

Normalised Index scores from the RBANS representing performance across the five cognitive domains was first regressed for age and age^2 using multiple linear regression in matlab (2018a) to account for non-linear associations between cognition and age in patients at the chronic timepoint (n=26) and controls (n=20). A factorial ANOVA was used to investigate performance across the five cognitive domains between patients and controls (IndexScore~Domain*Group). For performance on the PAL task, patients and controls data had age and age^2 regressed out and the residuals from this regression were subsequently rank inverse normalised. Comparison between working memory performance for chronic TBI patients and controls with full cognitive datasets (n=20) was made using an unpaired two-sample t-test. An additional comparison

between patients and the larger control cohort (n=59) who completed the PAL task was also performed using an unpaired t-test to determine whether similar findings were observed. Finally, a bivariate correlation between the RBANS total index score (sum of all five domains) and PAL score for all patients and controls was performed to determine whether the two cognitive assessments shared the same variance in performance across patients and controls.

5.3.5.2 Longitudinal cognitive assessment

As an additional sub-analysis, data from the 11 TBI patients with cognitive scores inclusive of RBANS and PAL at the subacute and chronic timepoints was compared to healthy controls. Age and age^2 were regressed out of the raw data for all patients and controls using a multiple linear regression in the same manner as the larger cohort analysis. A factorial ANOVA was used to explore whether a significant main effect of group (subacute, chronic and control) was observed across the five RBANS index scores as well as any interactions (IndexScore~Domain*Group). A one-way ANOVA was applied to PAL scores to examine the effect of group (patients in subacute and chronic timepoints and controls) on working memory task performance.

5.3.5.3 Cross-sectional comparison of FA and assessment of longitudinal changes within patients

To examine whether axonal injury was present in TBI patients, a voxelwise non-parametric approach using randomise in FSL was applied (Winkler et al., 2014). First, skeletonised FA derived from patients subacute DTI was compared to healthy controls. Next, skeletonised FA derived from patient's chronic DTI was compared to healthy controls to examine whether abnormalities in FA were observed after six months. Finally, to determine whether significant changes in FA were apparent between subacute and chronic timepoints within patients, a single group paired difference (paired t-test) was applied. This was achieved by subtracting the concatenated 4D file of skeletonised FA for patients at the chronic timepoint from the concatenated 4D file of patient skeletonised FA at the subacute timepoint using fslmaths. The resulting 4D image provides a within-subject difference map of FA (FA

subacute-FA chronic). A non-parametric permutation test using randomise is then applied to determine whether the average difference between the two timepoints is greater than 0 (e.g. significant changes in FA over time). All voxelwise analysis was performed with 10000 permutations and excluded areas of focal lesion and oedema for individual patients using the standardised subacute lesion masks as an additional explanatory variable. Age was also included as a covariate and results TFCE cluster corrected for multiple comparisons.

5.3.5.4 Quantification of graph theory metrics

Graph theory measures of the working memory network previously defined in chapter four were extracted for all controls and patients at sub-acute and chronic timepoints using the Brain connectivity toolbox (Rubinov & Sporns., 2010) across each of the 10 connectome thresholding iterations. Measures were selected on the basis of my previous work exploring network topology changes and their association to individual differences in working memory impairment in chronic TBI in chapter four. First, global efficiency of the working memory network was calculated to provide a measure of overall network integration. Next, local/nodal measures of local efficiency and clustering coefficient (associated with network segregation) and degree centrality (associated with network dysconnectivity) were quantified for the working memory network to provide complementary measures associated with small-world topology. For further details regarding these network measures, please refer to methods chapter two section 2.5.

5.3.6 Cross-sectional analysis of working memory network topology

To determine whether significant differences in working memory network topology were observed in patients compared to controls, global and local/nodal graph theory measures were compared between patients at subacute and chronic timepoints with controls. First, for the subacute timepoint, global efficiency was compared using a two-tailed t-test. For local/nodal measures, two-tailed t-tests were performed and results FDR corrected for multiple comparisons across all 31 nodes, within each graph theory metric (degree centrality, local efficiency, clustering coefficient). Next, measures

derived from the chronic timepoint in TBI patients were compared to the same healthy control cohort in the same manner using two tailed t-tests and FDR correction.

5.3.7 Association between network measures at subacute and chronic timepoints to working memory performance

To determine whether network measures at both subacute and chronic timepoints were associated with cognitive performance, correlational analyses were performed in patients. First, measures of global efficiency at subacute and chronic timepoints were correlated to PAL performance at the chronic phase. Next, local/nodal measures from the subacute timepoint were correlated to performance on the PAL using bivariate correlations with FDR correction across the 31 nodes for each of the three graph theory metrics. Due to the number of comparisons and small sample size which may impact upon sensitivity to detect relationships after multiple comparisons correction, a network average for each local/nodal measure (e.g. average degree, average local efficiency or average clustering coefficient) was also calculated and correlated to PAL performance. This process was subsequently repeated using local/nodal graph theory measures from the chronic timepoint. For comparison of the strength of relationship of working memory performance to graph theory measures versus FA, mean FA derived for each network node at subacute and chronic timepoints was also correlated to PAL performance. Finally, the average working memory network FA at each timepoint was also correlated to PAL.

5.3.8 Calculation of longitudinal network changes and association to working memory performance

To examine longitudinal changes in working memory network topology after TBI, repeated measures ANOVA were performed using the local/nodal graph theoretic measures derived at each timepoint for patients (e.g. local/Nodal measure~timepoint). A paired two-tailed t-test was also applied to compare measures of global efficiency between the two timepoints. Next, for local/nodal graph theory measures that significantly differed over time within subjects, the difference (Δ) between subacute and chronic timepoints was calculated by subtracting chronic from subacute graph

theory measures. This provides a single measure of the magnitude of change across time for each patient at each node within the network. The local/nodal Δ derived in individual patients was then correlated to performance on the PAL at the chronic phase of injury and FDR corrected for multiple comparisons. In this way, any association between longitudinal changes at the nodal level and working memory performance at the chronic phase can be explored. As a large number of nodes are present within the network, the average Δ across the whole network was also calculated and correlated to working memory performance.

To provide further exploration between longitudinal network changes and their association to cognition, an additional sub-analysis using the 11 patients with longitudinal cognitive data was performed. Two-way ANOVA was first applied to scores on the RBANS to compare patients at subacute and chronic timepoints and healthy controls and to assess if any differences between the two timepoints occurred (IndexScore~Domain*Group). Next, one-way ANOVA was performed on PAL scores to examine the effect of group (subacute timepoint, chronic timepoint and controls). Finally, longitudinal graph theoretic changes Δ were correlated to PAL performance at the chronic phase of injury to determine if any relationships were observed. This was achieved by first correlating individual local/nodal measures and applying FDR correction across the 31 nodes, followed by bivariate correlation between the average network Δ and PAL performance at the chronic phase.

5.3.9. Quantification of lesion load within the working memory network

Evidence suggests that damage to hierarchically important nodes within the working memory system, such as the prefrontal cortex, may impact greatly upon its function (Duncan et al., 2001; McAllister et al., 2009; Aerts et al., 2016). I therefore quantified the presence of focal lesions in working memory network nodes to determine whether relationships to cognition would be observed. Individual standardised lesion masks were intersected with the Desikan-Killiany atlas used to define networks nodes to determine whether overlap was present. The number of lesions overlapping with working memory network nodes was subsequently calculated for each patient and correlated with working memory performance (PAL score) using bivariate correlations.

Total lesion burden across the whole patient group was also calculated for each node within the working memory network (e.g. number of patients with lesions in a given node) to determine where the greatest number of lesions were present within the network.

5.3.10 Using machine learning to predict working memory performance at the chronic phase of injury using subacute network measures

A regression-based machine learning approach was used to investigate whether values of local/nodal graph theory measures derived at the subacute phase of injury could predict working memory performance six-months post injury in patients. Using the Pattern Recognition for Neuroimaging toolbox (PRoNTo, Schrouff et al., 2013), local/nodal graph theory measures from the working memory network were used as independent variables and the PAL task score was used as the dependent variable in a kernel ridge regression (KRR) model with automated hyperparameter optimisation. Machine learning models were derived for each of the three graph theory measures (degree centrality, local efficiency, clustering coefficient).

Model validation was achieved using 5-fold cross validation to determine generalizability and permutation testing with 1000 permutations to derive a null distribution and p value for each model. Model accuracy was assessed using Pearson correlation coefficient between predicted and actual working memory scores derived from the model. The proportion of variance explained (R^2) and mean squared error (MSE) between predicted and actual PAL scores was also examined. As an additional step, computation of weights for each model was calculated to examine which nodes within a network were most informative to the model.

To determine whether graph theory measures derived from the working memory network provide prognostic value beyond standard fractional anisotropy measures, an additional regression-based model was tested. Average local/nodal fractional anisotropy measures from the working memory network nodes were used as the independent variables and performance on the PAL task at the chronic phase of injury as the dependent variable. Model performance was subsequently assessed using

Pearson correlation coefficient, R^2 and MSE measures and tested for significance using permutation testing with 1000 permutations.

5.4 Results

5.4.1 TBI patients demonstrate evidence of cognitive impairment

Factorial ANOVA revealed a significant main effect of group for performance on the RBANS ($F(1,243)=22.20, p<0.001$) such that TBI patients in the chronic phase of injury had lower scores than healthy controls (Fig. 63A). No significant group by domain interaction was observed ($F(4,243)=0.88, p=0.48$). At the group level, no significant difference in PAL performance was observed between patients and controls ($t(43.93)=-0.23, p=0.41$), although individual performance scores for patients was varied (Fig. 63B). Comparison of performance on the PAL task between patients and the larger cohort of controls with this data (n=59) further demonstrated no significant difference in scores ($t(65.47)=-1.13, p=0.13$). A significant positive correlation between performance on the PAL and total RBANS index score was observed across patients and controls ($r=0.34, p=0.04$) such that individuals with lower working memory scores also had lower total Index scores on the RBANS (Fig. 63C).

5.4.2 TBI patients demonstrate evidence of axonal injury at subacute and chronic timepoints

Tract-based spatial statistics demonstrated that TBI patients in the subacute phase of injury had significant lower FA than healthy controls in the three subdivisions of the corpus callosum (genu, splenium and body), the left cingulum hippocampus as well as the fornix crescent, anterior corona radiata, cerebral peduncle, inferior longitudinal fasciculus and inferior fronto-occipital tracts bilaterally (Fig. 63D). When comparing FA within the chronic phase of injury to controls, significantly lower FA was observed in more widespread regions of the white matter, including areas observed sub-acutely as well as bilaterally in the corticospinal, anterior limb of the internal capsule, retro-lenticular part of the internal capsule, posterior thalamic radiation, posterior corona

radiata and external capsule ($p<0.05$, FWE corrected). A comparison of FA within subjects between the two injury timepoints indicated significant reductions in FA occurred between subacute to chronic scans in the genu of the corpus callosum, left anterior corona radiata, left posterior thalamic radiation and the superior corona radiata bilaterally.

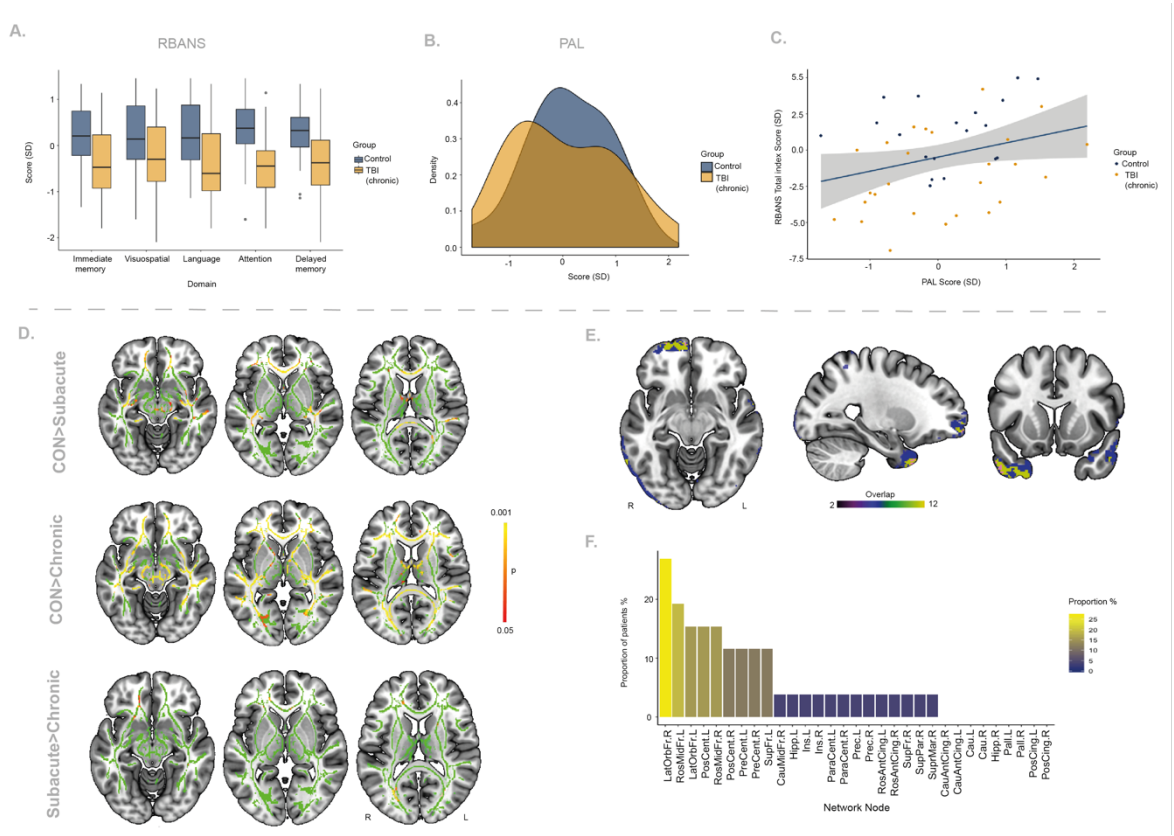


Figure 63: Cognitive and neuroimaging results A. Comparison of RBANS domain Index scores between TBI patients at the chronic phase of injury and healthy controls. **B.** Distribution of PAL task scores between patients at the chronic phase of injury and healthy controls. **C.** Scatterplot of total RBANS index score correlated to PAL task score in patients (at chronic phase) and healthy controls **D.** Comparing skeletonised fractional anisotropy of TBI patients in the acute phase of injury to healthy controls, TBI patients in the sub-acute phase of injury and healthy controls and finally the difference in FA between acute and sub-acute scans within TBI patients. Yellow-red voxels indicate significant differences (corrected for multiple comparisons). Green skeleton represents the groups averaged FA skeleton mask. CON=controls, Subacute=Subacute timepoint in TBI, Chronic=Chronic timepoint in TBI. **E.** Lesion overlap map for patients with focal lesions in the subacute phase of injury. Brighter colours represent greater overlap across patients **F.** Lesion load bar chart demonstrating proportion of patients

(%) with evidence of focal lesion within a given node of the working memory network defined in chapter 4.

5.4.3 TBI patients demonstrate evidence of focal lesions in regions associated with the working memory network

A total of 20 patients had evidence of focal lesion and/or oedema on subacute imaging (Fig. 63E). Delineation of focal lesions demonstrated areas of higher lesion load across patients in the temporal and frontal poles. Comparison of lesion distribution to the working memory network nodes revealed the highest proportion of lesions in patients to be in the right lateral orbitofrontal (27%), left rostral middle frontal (19.23%), left lateral orbitofrontal (15.38%), left posterior central (15.39%) and right rostral middle frontal nodes (15.38%) (Fig. 62F). When examining the five network hubs previously identified within chapter four, four hubs had evidence of focal lesion (right insula, left insula, right precuneus, right superior parietal) but in only a small proportion of patients (3.84%). Of the 20 patients with evidence of focal lesions, the number of nodes affected by lesion varied greatly between patients, ranging from 1 to 10 nodes. Correlation of lesion burden for patients (e.g. the number of working memory network nodes with evidence of lesion for a given patient) demonstrated no significant relationship to performance on the PAL ($r=0.15$, $p=0.55$) or total RBANS index score ($r=-0.133$,$p=0.62$).

5.4.4 Abnormal graph theory measures in the working memory network are present at the subacute and chronic phases of injury

Working memory network measures in the subacute and chronic phase of injury were compared to healthy controls to determine whether abnormalities existed at either timepoint (Fig. 64). In the subacute phase of injury, measures of global efficiency in the working memory network revealed no significant difference between TBI patients and controls ($t(129)=-0.31$,$p=0.76$). This finding was replicated across all ten thresholding iterations. Patients demonstrated significant reductions in degree centrality compared to controls in almost half (48%) of the network nodes.

Abnormalities were observed in the left caudate, left pallidum, right caudate, left caudal anterior cingulate cortex, left lateral orbito-frontal, left rostral anterior cingulate, left rostral middle frontal, left superior frontal, left insula, right caudal anterior cingulate, right lateral orbitofrontal, right post central, right rostral anterior cingulate, right rostral middle frontal and right superior frontal nodes. Measures of local efficiency also demonstrated significant abnormalities in patients compared to controls in 32% of nodes. Of the nodes with abnormal local efficiency measures, seven demonstrated significant increases including the left pallidum, left superior frontal, left insula and right caudal anterior cingulate and three demonstrated significant reductions including the left rostral anterior cingulate, right lateral orbitofrontal cingulate and right rostral anterior cingulate. Three nodes had significant clustering coefficient abnormalities in patients which comprised of reductions in the left rostral anterior cingulate node and increases in the left rostral middle frontal and right caudal anterior cingulate nodes. Abnormalities within each graph theory metric were consistent across 70% of threshold iterations (appendix tables 2.24-2.26).

In the chronic phase of injury, no significant difference in global efficiency of the working memory network was observed between TBI patients and controls ($t(129)=0.63$, $p=0.53$). This finding was replicated across all thresholding iterations. Examination of local/nodal network properties revealed abnormalities in the same nodes identified as such sub-acutely when compared to healthy controls. Furthermore, for measures of degree centrality, additional abnormalities were observed in the right pallidum, left posterior cingulate and right posterior cingulate. For measures of local efficiency, additional abnormalities were observed in the left caudate, left posterior central, left rostral middle frontal, right caudal middle frontal, right posterior central and right superior frontal nodes. No additional abnormalities were observed in measures of clustering coefficient. Abnormalities within each graph theory metric were consistent across 70% of threshold iterations (appendix tables 2.27-2.29)

Next, within subject's comparison of network measures between the two injury timepoints were made. Paired t-test revealed no significant difference in global efficiency between the two timepoints ($t(50)=-0.62$,$p=0.54$). For local/nodal measures of degree centrality, a repeated measures ANOVA revealed no significant main effect of time ($F(1,1550)=3.179$,$p=0.075$) and no significant time by node interaction

(F(30,1550)=0.13,p=1). In contrast, a significant main effect of time was observed for local/nodal measures of local efficiency (F(1,1550)=4.426,p=0.035) such that greater local efficiency metrics were observed at the chronic timepoint. No significant time by node interaction was found (F(30,1550)=0.457,p=0.995). For measures of clustering coefficient, no significant main effect of time was observed (F(1,1550)=2.167,p=0.141) nor significant time by node interaction (F(30,1550)=0.321,p=1).

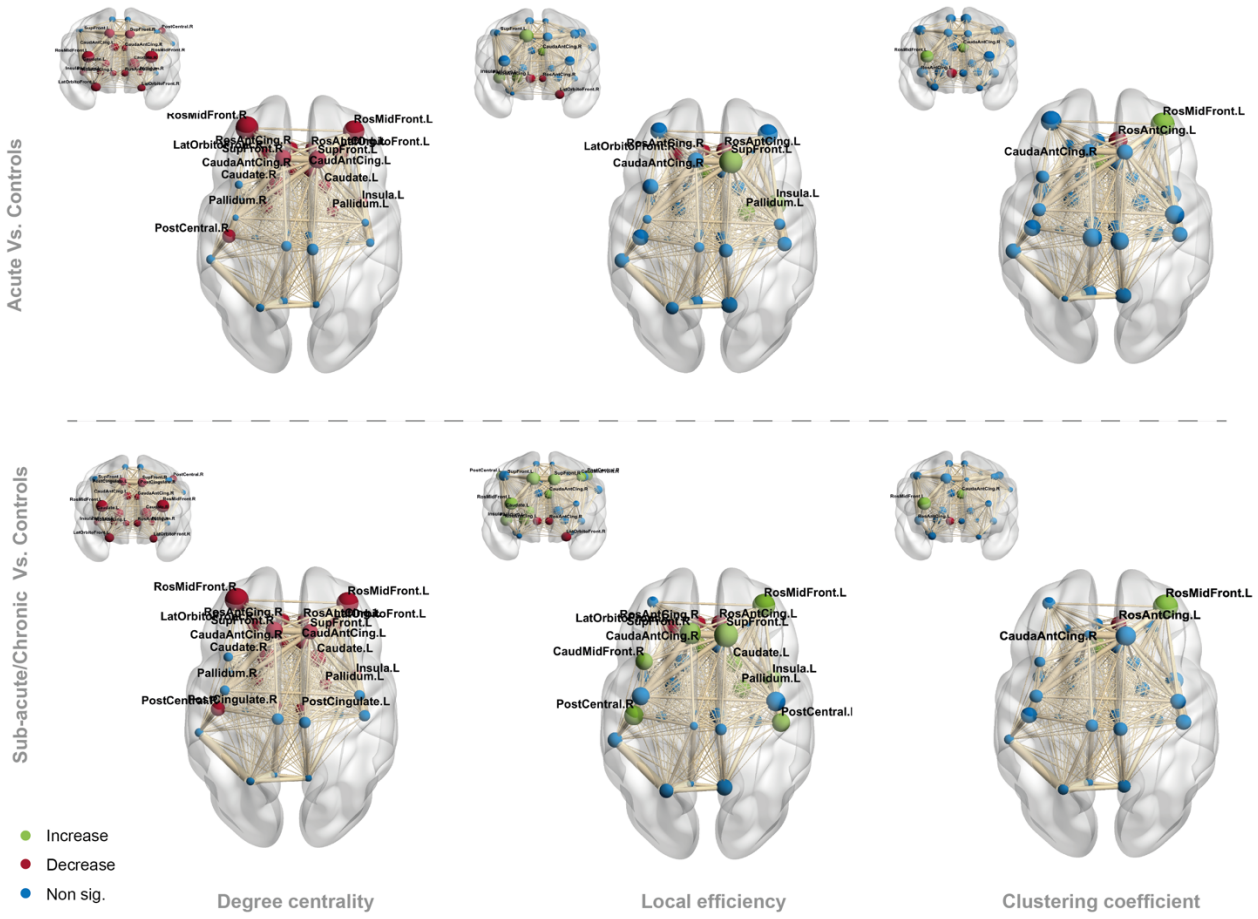


Figure 64: Local/nodal network measures in sub-acute and chronic phases of injury in TBI patients compared to controls. The top panel demonstrates cross-sectional comparison of the three graph theory measures for TBI patients in the sub-acute phase of injury and healthy controls. Lower panel represents comparison of same patients in the chronic phase (~6 months post injury) to healthy controls. Circles represent nodes within the working memory network, lines represent "edges" or white matter connections between nodes. The larger the node, the greater the difference between the two groups. The thicker the line the larger the white matter connection. Blue nodes indicate where no significant difference is observed between groups. Green nodes indicate where there is a significant

increase in value in TBI patients compared to controls. Red nodes indicate where there is a significant decrease in value in nodes of TBI patients compared to controls.

5.4.5 Average network measures of modularity are related to working memory performance at the chronic phase of injury

To examine the relationship between network measures and cognitive performance, correlation analysis between graph theory measures and performance on the PAL was performed in patients at both injury timepoints. For measures of global efficiency, no significant correlation was observed between performance on the PAL at the chronic phase of injury and subacute scans ($r=0.24, p=0.12$). At the chronic phase of injury, a significant positive correlation was observed such that greater global efficiency was related to higher scores on the PAL task ($r=0.35, p=0.04$). When correlating PAL performance to local nodal measures of degree centrality, no significant correlations were observed using subacute or chronic metrics after FDR correction ($p>0.05$). Average degree centrality measures of the whole working memory network revealed no significant relationships to PAL performance at both subacute ($r=-0.33, p=0.1$) and chronic timepoints ($r=-0.17, p=0.44$). For measures of local efficiency, bivariate correlations between PAL performance and local/nodal measures at either subacute or chronic timepoints was not significant ($p>0.05$, FDR corrected). When correlating average local efficiency measures across the whole network, no significant correlation was observed at the subacute phase ($r=0.19$, $p=0.17$) but a significant positive correlation at the chronic phase was observed ($r=0.43, p=0.03$). Local/nodal measures of clustering coefficient revealed no significant relationship to PAL performance at subacute or chronic timepoints ($p>0.05$, FDR corrected). However, a significant positive correlation was observed between average network clustering coefficient and chronic PAL performance at the chronic ($r=0.45, p=0.01$) but not subacute phase ($r=0.2, p=0.34$).

For comparison with graph theory measures, mean FA across the working memory network connectome at subacute and chronic timepoints was correlated to chronic PAL performance. No significant correlation between average node FA and PAL performance was observed at subacute or chronic timepoints ($p>0.05$, FDR corrected). When using subacute average network FA, no significant correlation was

observed (r=0.34,p=0.09), however a significant positive correlation was demonstrated when the chronic timepoint FA (r=0.41,p=0.04).

5.4.6 Longitudinal increases in local efficiency are associated with higher working memory scores in the chronic phase of injury

Next, changes in network topology (e.g. Δ) from subacute to chronic timepoints were correlated with working memory performance in patients to determine whether longitudinal network changes were associated with working memory outcomes. As a significant main effect of time was only observed in measures of local efficiency, analysis was focused on this measure. When correlating local/nodal measures of local efficiency to PAL performance, widespread associations were observed. However, only significant positive correlations remained after FDR correction in the left posterior cingulate (r=0.58,p=0.028) and right superior frontal nodes (r=0.63,p=0.015) (Fig. 65A-C). When taking the network average Δ of local efficiency for each patient, a significant positive correlation was observed (r=0.38,p=0.028) such that the greater the increase in local efficiency longitudinally, the higher the PAL score.

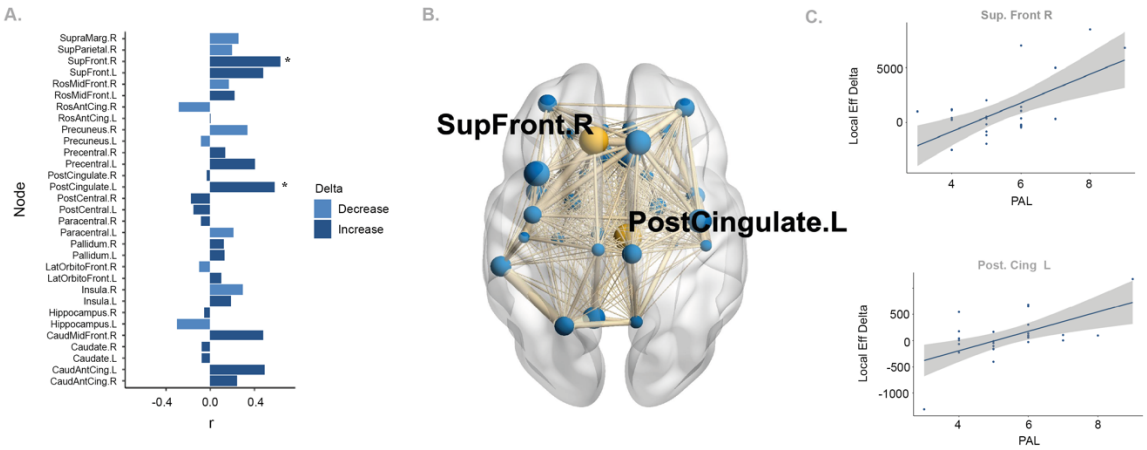


Figure 65: Association between local efficiency network changes between acute and sub-acute timepoints and working memory performance in patients. A. Bivariate correlations between local/nodal local efficiency Δ and working memory performance. *=significant correlation (p<0.05) after FDR correction across the 31 nodes. **B.** Illustration of significant nodes within the working memory structural network **C.** Scatterplots of correlation between local efficiency Δ and working memory performance for the two significant nodes.

An additional analysis including only patients with longitudinal cognitive and imaging data (n=11) was performed to determine if changes in cognition over time were present and to further investigate the relationship between longitudinal increases in local efficiency and working memory scores at the chronic phase of injury. Factorial ANOVA of RBANS scores revealed a significant main effect of group ($F(2,233)=14.99, p<0.001$) with post-hoc Tukey tests revealing that this was driven by significantly lower scores in TBI patients compared to controls at both subacute ($p<0.001$) and chronic ($p<0.001$) timepoints. No significant difference between subacute and chronic timepoints was present ($p>0.05$). No significant group by domain interaction was observed ($F(8,233)=0.76, p=0.64$). One-way ANOVA of PAL task performance revealed a significant main effect of group ($F(2,257)=27.97, p<0.001$) with post-hoc Tukey tests revealing that this was driven by significantly lower PAL scores in TBI patients in the subacute ($p<0.001$) and chronic ($p<0.001$) timepoints compared to controls, as well significantly greater PAL scores in patients at the chronic versus subacute timepoint ($p<0.02$). A significant positive relationship between average local efficiency Δ and performance on the PAL at the chronic phase of injury was observed ($r=0.62$, $p=0.04$) such that patients with greater increases in local efficiency over time across the working memory network had higher PAL scores. No significant correlations were observed between individual node changes in local efficiency and PAL scores after FDR correction.

5.4.7 Machine learning approaches using nodal measures of degree centrality sub-acutely predict working memory performance at the chronic phase of injury

A regression-based machine learning approach was used to examine whether local/nodal measures of working memory network topology at the subacute phase of injury could predict performance on the PAL task at the chronic phase in patients. A significant predictive model was observed when using measures of degree centrality within the working memory network ($r=0.60, p=0.005$; $R^2=0.46, p=0.035$; MSE=2.09, Norm MSE=2.33) (Fig. 66A). Computation of model weights indicated that the right hippocampus, left caudal anterior cingulate, left rostral middle frontal, left superior frontal, right rostral middle frontal, left paracentral, left precuneus, right postcentral,

right paracentral, and right caudal middle frontal nodes contributed the most to the model (Fig. 66B). Of the nodes most informative to the model, half demonstrated significantly lower degree centrality compared to controls, including the left caudal anterior cingulate, left rostral middle frontal, left superior frontal, right rostral middle frontal and right post central. No significant predictive models were observed for measures of local efficiency (r=0.16,p=0.29; R^2=0.23, p=0.47, MSE=2.36, Norm MSE=2.44) or clustering coefficient (r=0.38,p=0.07, R^2=0.31,p=0.24, MSE=2.57, Norm MSE=2.79).

To determine whether graph theoretic measures provide greater predictive value than FA measures, an additional model using the mean FA for each node within the working memory network as the independent variable and working memory scores at the chronic phase of injury as the dependent variable was constructed. No significant predictive model was observed (r=0.20, p=0.24, R^2=0.13,p=0.58, MSE=2.40, Norm MSE=2.69).

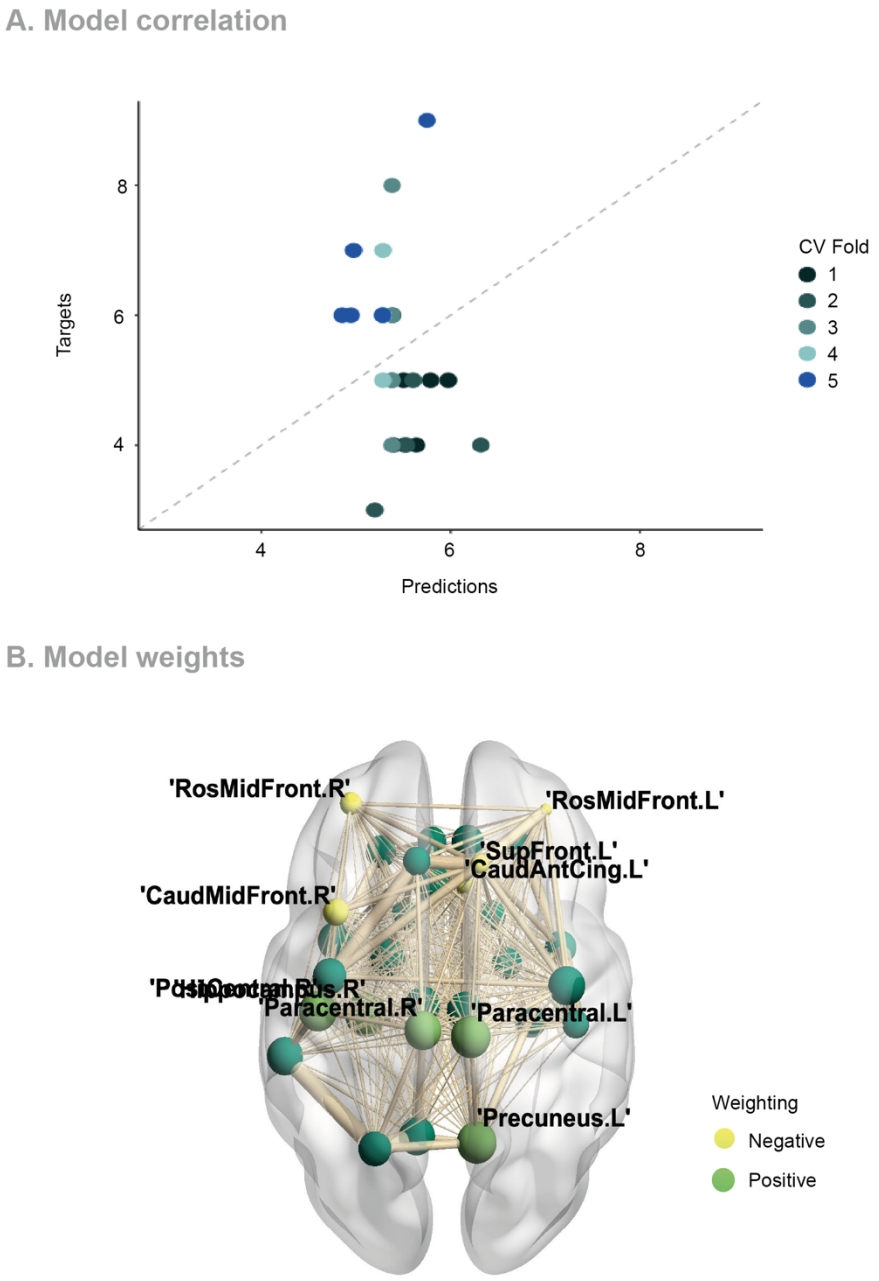


Figure 66: Regression-based machine learning results using acute local/nodal degree centrality measures to predict working memory performance at six months. A: Results from machine learning prediction model. Prediction of working memory score (predictions) compared to actual (target) score. Dashed line represents correlation coefficient of prediction model when r=1. Colour dots represent different folds from k-fold cross validation. **B:** Local/nodal weights derived from the prediction model. The greater the weight in either direction the greater the contribution of the nodal degree measure to the model. Labelled nodes represent the top 10% with greatest contribution to the model.

5.5 Discussion

This study extends the work of chapter four to determine whether measures from the working memory connectome sub-acutely can predict working memory performance in the chronic phase of injury. Here, I illustrate that graph theoretical measures of degree centrality, local efficiency and clustering coefficient (representing network connectivity and segregation respectively) are abnormal in the subacute and chronic phases of injury. I replicate the findings of chapter four by demonstrating that graph theory measures of the working memory network are altered after TBI and are associated with working memory performance in chronic TBI. Importantly, when using a machine learning approach, subacute measures of network connectivity (degree centrality) were able to predict working memory performance at the chronic phase where measures of FA could not. I illustrate that longitudinal increases in local efficiency relate to better working memory performance in patients, complimenting previous literature. These findings provide mechanistic insights into the heterogeneous nature of working memory outcomes in TBI and provide evidence in support of the prognostic value of graph theoretical network measures.

The role of axonal injury in disrupting the small-world topology of networks underpinning cognition is well established (Pandit et al., 2013; Caeyenberghs et al., 2013; Aerts et al., 2016). It is therefore unsurprising that in this moderate-severe TBI cohort I observed widespread abnormalities in FA and network topology at both timepoints. Similar to findings within my large chronic TBI population in chapter 4, decreased connectivity (e.g. reduced degree centrality) and increased modularity (e.g. increased local efficiency and clustering coefficient) was observed. However, no abnormalities in global efficiency were demonstrated between patients and controls at either timepoints. These findings demonstrate evidence of the working memory network moving away from small-world topology, but perhaps not as extensively as observed in more longer-term chronic TBI (Pandit et al., 2013; Jolly et al., 2020). When compared to the findings of chapter four, these results provide some insight into the working memory performance observed in patients at the chronic phase of injury compared to controls.

Although patients demonstrated generally greater variance in working memory performance than controls, with the distribution of scores being shifted more towards negative values, no group-level difference was observed. Taken together with the graph theoretical findings (where abnormalities are present at the local/nodal level but absent in global efficiency), a lack of impairment may represent network resilience to damage, where disruption to short-range connections within the network are not catastrophic to working memory processes, particularly where network integration remains. Indeed, measures of local efficiency are suggested to be representative of 'fault tolerance' within a network (Latora et al., 2001), providing high connectivity within a neighbourhood of nodes that means a loss of one connection does not result in the complete disconnection of information transfer from one node to another. However, TBI patients with longitudinal cognitive data demonstrated impairments in working memory at the subacute phase of injury that significantly improved at the chronic phase. This could suggest that working memory impairments resolved over time, resulting in impairments no longer being present, at least at the group level when assessed at follow-up.

Although this finding and its interpretation should be taken with caution given it represents less than half of the patient cohort, studies whereby increases in network modularity are associated with better cognitive outcome, and the correlational results from this study, provide some support (Dall'Acqua et al., 2017; Kuceyeski et al., 2019). In my findings, higher local efficiency was observed in patients at both subacute and chronic phases and was positively correlated to working memory performance at the chronic phase. Furthermore, significant increases in local efficiency were observed longitudinally and positively correlated to higher working memory scores at the chronic phase. This was also the case in the smaller subset of patients with longitudinal cognitive data.

Interestingly, longitudinal studies of TBI have illustrated that the development of hyper-connectivity (such as increased local efficiency) occurs in nodes with structural dysconnectivity and is associated with improved working memory performance after TBI (Dall'Acqua et al., 2017). This suggests that a loss of connectivity within nodes may drive increases in local efficiency. Although this may seem counterintuitive, the quantification of local efficiency is such that the loss of connections between the node

of interest and a node that is not highly interconnected to other nodes within a neighbourhood can result in increased local efficiency values. Indeed, in this study, nodes with abnormalities in degree centrality (relating to dysconnectivity) at the subacute phase were in general the same nodes with significant increases in local efficiency at the chronic phase. This finding is particularly interesting when considering the results of the predictive modelling.

Although an association is observed between longitudinal changes in local efficiency and working memory, subacute measures were not predictive of working memory outcomes when applied in a machine learning model. Regression-based machine learning demonstrated that only subacute measures of degree centrality could provide a significant predictive model. A potential explanation for this may be that degree centrality has a more direct association to long term working memory performance as it is the simplest measure of network dysconnectivity (Rubinov & Sporns., 2010; Bassett & Bullmore., 2017) and may underpin the propagation of longitudinal changes, as demonstrated by the patterns of local efficiency changes at the chronic phase of injury. Previous findings from chapter four also provide evidence in support of the informative nature of degree centrality by demonstrating that the strongest relationships observed between working memory performance and graph theory measures in patients were with measures of degree centrality. Critically, the inclusion of fractional anisotropy measures of network nodes resulted in non-predictive models when using machine learning. These findings suggest that measures of white matter connectivity in the subacute phase are most informative for the prediction of working memory outcomes, by providing perhaps more finer-grained detail that is not captured in simpler measures of FA (Palacios et al., 2012).

There are a number of limitations that should be considered within this study. Firstly, this study uses a relatively small number of patients for analysis and prediction models. Although this work compliments the findings from a chronic TBI population in chapter four and applies cross-validation methods, findings may not be generalisable to a wider subacute TBI population. For example, model overfitting can occur where the same cohort is used for cross-validation and may therefore over-estimate the predictive power of these measures (Ng., 2017). Future research would therefore benefit from applying these measures and methods to an additional subacute TBI

population for comparison. My current research is attempting to address this limitation. Additionally, long-term white matter pathophysiology and its association to cognitive decline after TBI is well established (Yin et al., 2019). Although this study has demonstrated clear predictive abilities within a six-month timeframe, it may be more valuable to examine whether subacute measures can predict much further into the chronic phase of TBI. This study is currently collecting working memory and diffusion data in the same cohort of patients 12 months post injury and will attempt to examine this in future research.

Finally, prediction of working memory outcomes was only made on the performance of a single task. Although the PAL has been demonstrated to be highly sensitive to TBI related impairment (De Simoni et al., 2016), working memory is a complex cognitive construct. In contrast to performance on the PAL working memory task, impairments on the RBANS were observed in patients at the chronic phase of injury. On the one hand, this may reflect the fact the RBANS is designed to assess other cognitive domains, on the other, these findings may demonstrate a lack of sensitivity to detect impairment in working memory when using a single coarse measure in comparison to an extensive cognitive battery. Indeed, a significant association between performance on the PAL and RBANS was observed, indicating some shared cognitive variance between the measures. More detailed measurements of working memory utilising a number of tasks may therefore be beneficial to further explore the role of longitudinal network changes.

In summary, this study provides evidence that subacute measures of degree centrality within a discrete working memory network can predict working memory in TBI patients at the chronic phase of injury. These findings provide a clear set of prognostic markers that may be useful within a clinical setting and warrant further exploration. Furthermore, evidence of longitudinal changes in local efficiency and its association to working memory performance provides insights into the potential resilience of structural networks and the differences in network changes that contribute to the varied outcomes in working memory performance in patients. By understanding the advantageous network changes within this population, the use of targeted interventions to support this resilience or identification of individuals where impairment may persist, is a promising avenue for future research to explore.

Chapter 6

Predicting the treatment effect of methylphenidate in working memory using multimodal imaging

In this chapter, I investigate whether the application of machine learning to neuroimaging data can successfully predict response to treatment with methylphenidate in TBI patients. I examine whether the use of multi-modal imaging improves predictive models by providing a more holistic overview of damage and investigate which regions in the brain are most informative to these models.

6.1 Abstract

Disruption to the dopaminergic system is common after traumatic brain injury (TBI) and has been associated with working memory impairment. Attempts to treat these deficits with pharmacological interventions that modulate dopamine, such as methylphenidate, have gained popularity in recent years, yet its efficacy varies greatly across individuals. This heterogeneity reflects the diverse ways in which TBI can disrupt brain systems. One option is to use imaging to target individuals who have damage to dopaminergic circuits that modulate the working memory system. However, studies seeking to use individual imaging modalities have had mixed results. Furthermore, working memory deficits in TBI relate to the disruption of both neuro-modulatory systems and cortical networks. I therefore hypothesised that accurately predicting responsiveness to pharmacological therapy may require a more holistic approach, where features from different imaging modalities are combined using multivariate machine learning algorithms.

In this study, I explored whether the application of the Pattern Recognition for Neuroimaging Toolbox (PRoNTo, Schrouff et al., 2013) to multimodal neuroimaging data can 1) accurately classify patients from controls and 2) predict improvements in working memory performance after treatment with methylphenidate. Thirty-three moderate-severe TBI patients and eighteen healthy controls underwent behavioural and neuroimaging assessment inclusive of diffusion tensor imaging (DTI), structural T1, resting-state functional MRI (rs-fMRI) and ^{123}I-Ioflupane SPECT at baseline. Patients subsequently completed two treatment blocks in a double-blind crossover design, completing further behavioural assessments to examine the impact of treatment with methylphenidate in comparison to placebo on working memory.

Classification of patients from controls was achievable using single imaging modality models, with incremental gain when using multimodal imaging, as ascertained using a rigorous k-fold cross-validation pipeline. Importantly, prediction of working memory treatment effect was only achieved using multimodal models. The model with greatest prediction accuracy featured measures of grey matter volume, white matter integrity and striatal dopamine transporter expression. My findings demonstrate the predictive

validity of machine learning models in TBI, and highlight their potential clinical utility particularly when applied to multimodal imaging to target therapeutic interventions.

6.2 Introduction

Chronic cognitive impairments are common after Traumatic Brain Injury (TBI) and contribute to poor functional outcomes in patients (Lovell et al., 2006; Rabinowitz et al., 2014; Stocchetti et al., 2016). Deficits in working memory are prevalent amongst these cognitive symptoms, (McAllister et al., 2004) and are associated with abnormalities within the dopaminergic system, representing a potentially useful therapeutic target (McAllister et al., 2009). In accordance with this view, some initial studies investigating the use of methylphenidate, a common dopaminergic modulator, to treat working memory impairments have reported promising results (Newsome et al., 2015; Manktelow et al., 2017).

Dopamine modulates working memory via cortico-striatal networks in the brain (Bales et al., 2008). This is achieved through dopaminergic signalling from the striatum via ascending white matter projections to the prefrontal cortex (PFC), a region fundamental to successful working memory function (Bjorkland & Dunnett., 2007; Kane & Engle., 2002). After TBI, damage can occur at diverse points within this circuitry (De Simoni et al., 2018; Jenkins et al., 2018). For example, the dopaminergic circuitry that modulates PFC function may be compromised, or the cortical networks that support the maintenance and manipulation of working memory representations may be disrupted. Consequently, to understand individual responsiveness to pharmacotherapy, it is likely necessary to consider the integrity of the working-memory system as a whole.

Indeed, in studies of rodents, the use of dopaminergic agonists to treat working memory impairment after injury to the dopaminergic system have been reported to be effective, except where damage to the PFC is present (Brozoski et al., 1979). Furthermore, in humans, it has been reported that reductions in striatal DAT are

associated with damage to nigrostriatal projections (Jenkins et al., 2018), but are present in only a proportion of patients, thus suggesting dopaminergic interventions are appropriate for only a subset of individuals. Therefore, variation in the efficacy of methylphenidate across patients is likely to be associated with the heterogeneity in damage to the complex systems that this intervention aims to modulate (Mehta et al., 2006; Jenkins et al., 2018; Jenkins et al., 2019).

Given the complexity of the underlying neural systems, modelling how pharmacotherapy can mitigate working memory deficits presents a poorly posed challenge for any single imaging modality. For example, measures of striatal DAT although useful in detecting subcortical damage, will be unable to quantify cortical network damage such as axonal injury, that may limit the effectiveness of an intervention. Machine learning offers a solution to this problem because it has the advantage of handling heterogeneous data by employing pattern recognition techniques (Gonen et al., 2011). With this approach, the identification of similarities or patterns within the data are derived in an automated fashion, utilising the most informative features within the model. To date, machine learning applied to TBI has proved promising in relating cognitive outcomes after TBI to a range of imaging modalities, including diffusion tensor imaging (DTI), computed tomography (CT) and resting state functional connectivity (rs-FC) (Hellyer et al., 2013; Vergara et al., 2017; Mitra et al., 2016). However, these models have been constrained to a single imaging modality, thereby providing fragmented mechanistic insights and likely limiting predictive accuracy.

Based on this, I hypothesised that modelling features of damage across different systems in the brain should provide more accurate predictions of who would benefit from pharmacological therapies. Furthermore, I posited that the resultant models should provide insights into the mechanisms of working memory impairment and the biological factors associated with successful treatment using methylphenidate (Mantkelow et al., 2017). To test these predictions, I analysed data from thirty-three moderate-severe TBI patients and eighteen healthy controls who had undergone a comprehensive behavioural and imaging assessment. I tested whether a machine

learning approach could 1) accurately classify patients and controls, and 2) accurately predict the impact of methylphenidate on working memory performance.

A key methodological challenge was to be able to combine imaging modalities that have different properties, e.g., in terms of signal strength, number of features and underlying neural properties that they measure, in a single model. To address this, I applied PRoNTo, which includes a fast, multi-kernel learning (MKL) algorithm for use with multi-modal imaging (Schrouff et al., 2013). I extracted imaging measures of 1) grey matter (GM) volume, 2) whole brain non-skeletonised fractional anisotropy (FA) 3) skeletonised FA and utilised measures of 4) ^{123}I-Ioflupane SPECT striatal binding ratio images (DaTscans) and 5) cortico-striatal rs-FC measures previously derived in the same cohort of patients (De Simoni et al., 2018; Jenkins et al., 2019). I assessed patient and control performance on three computerised working memory tasks at baseline and during treatment (methylphenidate vs. placebo). Then, I applied a thorough analysis of the most informative imaging modalities for classification and prediction models, using a Binary Support Vector Machine (BSVM) and Kernel Ridge Regression (KRR) machine respectively. Finally, I studied whether the use of multi-modal imaging using MKL improved these models and characterised which anatomical regions were the most informative to each model.

6.3 Materials & Methods

6.3.1 Participants

A total of 33 patients (mean age 39.44,11.58 SD, range 20-65 years, 3 females) with a moderate-severe traumatic brain injury as classified using the Mayo criteria (Malec et al., 2007) were included. Inclusion criteria were: aged between 20-65; no history of multiple traumatic brain injuries; at least three months since their injury and evidence of subjective complaints of cognitive impairments as reported by the individual, clinician or caregiver. Exclusion criteria included: a history of neurological or psychiatric illness prior to injury; history of drug or alcohol substance abuse/addiction; a positive urine drug screen; medications that were a contraindication to the use of methylphenidate; any contraindications to MRI or SPECT imaging and any clinical

evidence of parkinsonian motor signs as quantified using the Unified Parkinson's Disease Rating Scale (UPDRS; Fahn et al., 1987). Mean time since injury for patients was (72.79 months, SD 87,04, range 6-366). Further information regarding current medications and injury mechanism for patients can be found in table 11. In addition, eighteen age-matched healthy controls were also recruited (mean age 40.15, 12.93, range 21-61 years, 2 females). Controls had no previous history of psychiatric or neurological illness, no history of drug or alcohol dependence and no contraindications to MRI or SPECT scans.

Age	Gender	Time since Injury (months)	Length of PTA (Days)	Cause of Injury	Medications at Visit
65	M	141	60	RTA	None
51	F	37	2	Incident/ Fall	Omeprazole
31	M	46	60	RTA	Propranolol 80mg
54	M	18	5	RTA	Citalopram 30mg, Thyroxine 150mcg
20	M	24	30	Incident/ Fall	None
37	M	35	10	Violence	None
44	M	42	90	RTA	Amtripyline 40mg, Vitamin D, Lanzoprazole 15mg, Testosterone injections
51	M	266	21	RTA	None
64	M	14	4 hours	RTA	Omeprazole 40mg, Levothyroxine 75 mcg.
46	M	37	15	RTA	None

20	M	23	60	RTA	None
52	M	43	5	RTA	None
45	M	32	14	Other Non Intentional	None
31	M	73	90	Violence	None
24	M	8	14	RTA	None
52	M	17	21	Incident/Fall	Levetirecetam 1250mg BD, Perindopril 2mg OD
54	M	11	15	Violence	None
26	M	17	56	Violence	Amitriptylline 10mg OD, Sodium Valproate 100mg OD
39	F	6	2	Incident/ Fall	None
47	M	51	3	RTA	Atorvastatin 10mg, Growth Hormone
22	M	21	540	RTA	None
48	M	366	60	RTA	Amitrptylline 20mg TDS, Fexofenadine 180mg OD, Esomeprazole 40mg OD, Tramadol 50 mg TDS, Calcichew 1BD, Solifenacin 5mg TDS, Alvarine citrate 400mg BD,

					Botox injection 10mg OD, Mebeverine 500mg TDS, Loperamide 600mg TDS, Naproxen, Gabapentin 600mg TDS
38	M	210	720	Violence	None
49	F	158	7	Violence	Levothyroxine 150 mcg, Omeprazole, Gamolenic acid, Pyridoxine
43	M	6	42	RTA	None
37	M	205	120	Incident/ Fall	Tegetrol CR 400mg BD
33	M	147	28	RTA	Baclofen 20mg OD, Citalopram 10mg OD
34	M	9	7	Incident/Fall	None

32	M	73	28	RTA	Symbicort
52	M	23	4	Violence	Lanzoprazole 15 mg
38	M	9	14	Violence	None
31	M	112	120	RTA	None
39	M	33	8	RTA	None

Table 11: TBI patient demographics. RTA=road traffic accident, PTA=post-traumatic amnesia. OD=once daily, BD=two times a day, TDS=taken three times a day, PRN=as needed.

6.3.2 Study design

Patients and controls underwent baseline neuroimaging and computerised cognitive testing inclusive of three working memory tasks. In addition, patients completed two weeks of treatment with a placebo and two weeks of treatment with methylphenidate in a double-blind crossover design (Fig. 67). Patients were randomly allocated to one of two drug treatment orders (Placebo/Methylphenidate or Methylphenidate/Placebo). At the end of each two-week treatment block, patients attended a follow-up study visit to complete the final dose of medication and cognitive testing under the same conditions.

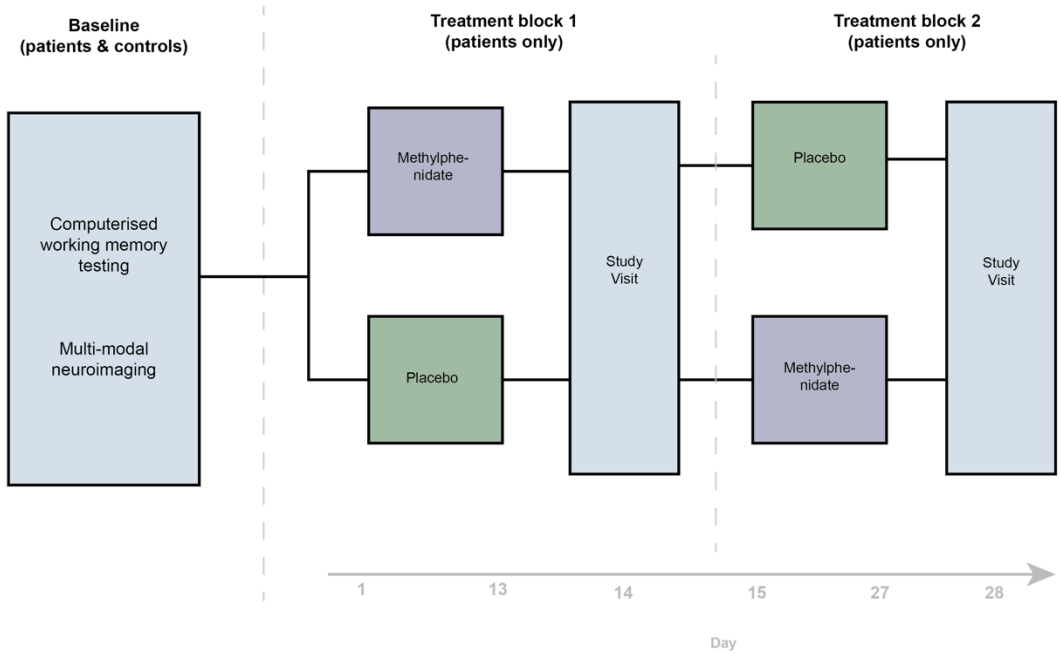


Figure 67: Study design for patients and controls. Baseline imaging and cognitive assessments were completed for both patients and controls. After baseline assessment, TBI

patients were randomly allocated to one of two drug treatment orders (Placebo/Methylphenidate or Methylphenidate/Placebo) where they would be administered two weeks of Methylphenidate or placebo and complete the alternative treatment the following two weeks. On days 14 and 28 (the final day for each drug treatment block) patients would attend a study visit to complete cognitive testing under the same controlled environment.

6.3.3 Study procedures

Multi-modal imaging was used to assess structural and functional properties of the brain in all TBI patients and controls at baseline. This included structural T1-MPRAGE to assess grey matter volume, diffusion weighted imaging (DWI) to examine white matter integrity as quantified using fractional anisotropy (FA), resting-state functional MRI (rs-fMRI) to investigate cortico-striatal functional connectivity and ^{123}I-Ioflupane SPECT to quantify endogenous dopamine transporter (DaT) in the brain. Computerised cognitive testing was completed to compare patients working memory performance with healthy controls at baseline and to assess the effect of drug treatment on working memory performance for patients at study follow-up visits.

6.3.4 MRI

For structural MRI, a high resolution T1 weighted MPRAGE image and diffusion weighted images were acquired. For further information regarding acquisition parameters please refer to methods chapter two section 2.3.1. Resting-state functional MRI was also acquired using gradient echo EPI. A total of 300 volumes of 35 interleaved slices (3mm thickness no interslice gap) were acquired over a 10-minute scan (TE=30ms, T1=2000ms, flip angle=80, in plane resolution=3x3mm, matrix=64x64, fov 19.2x19.2cm). Participants were asked to keep their eyes closed but not to fall asleep during the resting-state fMRI acquisition. Fluid attenuated inversion recovery (FLAIR) and susceptibility weighted imaging (SWI) were also acquired for the delineation of lesions.

6.3.5 ^{123}I-Ioflupance SPECT

A ^{123}I-Ioflupane SPECT scan was acquired to assess endogenous dopamine transporter (DaT) levels in patients and controls. Details of the acquisition methods can be found in methods chapter two (section 2.3.2).

6.3.6 Cognitive testing

To assess working memory performance, patients and controls completed three computerised working memory tasks using a custom app loaded onto an Ipad (Hampshire et al., 2012). Tasks included the Monkey ladder task (MKL); a numeric-spatial working memory task (Inoue and Matsuzawa., 2007), the Paired associates task (PAL); an object based visuo-spatial task reliant upon the binding of information (Gould *et al*., 2005) and finally the self-ordered search task; a strategy based visuo-spatial search task (Collins *et al*., 1998). For further information regarding the tasks, please refer to methods Chapter 2, section 2.1.2. These tasks have previously been shown to be associated with working memory function in a large cohort of healthy individuals (>44 600, Hampshire et al., 2101) and TBI patients (Jolly et al., 2020).

6.3.7 Structural MRI

T1 images for patients and controls were first segmented into grey and white matter and registered to standard MNI152 space (including modulation to retain accurate volumetric measures) using the DARTEL toolbox in spm12 (Ashburner et al., 2007). Normalised grey matter was smoothed (4mm full-width-at-half maximum) and a grey matter mask was derived using the group average grey matter segmentation (thresholded at 0.2). Diffusion weighted imaging was pre-processed using the standard FIMRIB diffusion toolbox (FDT, Behrens et al., 2007) in FSL. Details of DTI pre-processing can be found in methods chapter two (section 2.4.1).

6.3.8 Resting-state fMRI

Altered cortico-striatal functional connectivity (FC) has previously been associated with cognitive impairments after TBI inclusive of working memory function (Palacios et

al., 2012) and within this cohort (De Simon et al., 2017). I therefore included the cortico-striatal FC measures derived from the same cohort of patients and controls as detailed in De Simoni et al., 2018. In summary, De Simoni et al., 2018 removed the first two volumes of resting-state imaging to account for the T1 equilibrium effect. Next, rigid-body realignment to correct for motion was applied to individual resting-state fMRI images. Temporal frequency filtering using a high-pass filter (100 seconds) was used and spatial smoothing applied using a 6mm full-width at half-maximum (FWHM) kernel. Images were then registered to standard MNI152 space by first registering T1-weighted structural imaging to standard space using a linear registration (FLIRT) in FSL. Resting state images were then registered to standard space using boundary-based registration (BBR, Greve & Fischl, 2009) using the standard space transformation derived from T1 registration. Extraction of cortico-striatal functional connectivity measures was subsequently performed using 12 previously defined cortico-striatal networks. Further details regarding the definition of these networks can be found in methods chapter two section 2.2.4. A total of twenty-four FC measures (12 measures for each laterality) of functional connectivity between striatal and cortical regions were derived. This included FC between the anterior and posterior caudate (left and right) to the anterior cingulate cortex (ACC), posterior cingulate cortex (PCC), precuneus (PREC), Area 46, Area 9/46 dorsal and Area 94/6 ventral (regions of the dorsolateral prefrontal cortex) (Sallet et al., 2013).

6.3.9 Statistical analysis of neuroimaging data

Cross-sectional analysis was performed for each imaging modality to assess whether differences in brain structure and function were observed between patients and controls. Voxel based morphometry (VBM) was applied to standardised T1 images to quantify differences in grey matter volume across groups. The group average grey matter mask was used to constrain comparison to grey matter and age and total intracranial volume (ICV) were included as covariates. Skeletonised FA maps derived from TBSS were compared using non-parametric permutational testing in randomise to determine differences in FA. As age is associated with FA (pfefferbaum et al., 2003), this was included as a covariate and the group average skeletonised FA map was

used as a mask. Standardised DaT striatal binding ratio (SBR) images derived from ^{123}I-Ioflupane SPECT were compared across groups including age as a covariate. As DaT is principally located in the striatum, a striatal mask derived from the Harvard-Oxford atlas was thresholded at 50% and used in randomise. For T1, DTI and SPECT cross-sectional analysis, 10,000 permutations were implemented using randomise. Finally, the 24 FC measures were compared between patients and controls using a repeated measures ANOVA with post hoc Tukey t-tests.

6.3.10 Statistical analysis of cognitive data

Baseline cognitive data was first normalised in R statistical software package (version 3.5.3) to allow for comparison across tasks. A repeated measures ANOVA was applied to examine the effect of group and any interactions with working memory tasks. Finally, a principal components analysis (PCA) using SPSS was performed using the three working memory task scores for all patients and controls. This was to determine the latent variable structure within the data and derive a composite measure for machine learning prediction modelling.

To assess the impact of drug treatment on working memory performance, the difference (Δ) between working memory performance on methylphenidate (MPh) and placebo (Plc) at each study visit was calculated (Δ=working mem MPh-working mem Plc). In this way, individual differences in performance are accounted for by using a within-subjects comparison. Positive treatment effect (Δ) scores therefore demonstrate improved working memory performance on methylphenidate compared to placebo, whilst negative scores represent poorer performance when on methylphenidate compared to placebo. First, composite working memory scores were calculated for each study visit when on placebo or methylphenidate. This was achieved by first weighting (e.g. multiplying) raw working memory task scores by their factor loading derived from PCA of working memory data at baseline. Once weighted, the working memory scores were then averaged to provide a single composite measure for each drug treatment. Effect of drug treatment order (Mph/Plc vs. Plc/Mph) was examined using a one-way ANOVA (treatmentΔ~treatment order).

The relationship between baseline and treatment effect (Δ) working memory scores was explored. Bivariate correlations were applied to 1) all patients 2) patients who improved (Δ>0) and 3) patients who did not (Δ<0) whilst on methylphenidate compared to placebo. To determine whether the variance in the magnitude of treatment effect (e.g. Δ) significantly difference between the two patient response groups (improved vs did not), a coefficient of variance (CV) statistical test was applied.

6.3.11 Application of Machine learning to neuroimaging data

An overview of the machine learning methods used for 1) classification using baseline imaging and 2) prediction of treatment effect on working memory performance in patients, can be found in figure 68. In summary, classification and regression-based approaches were explored using all possible imaging modalities in unimodal models followed by all possible combinations of imaging for multimodal models. Comparison between unimodal and multimodal models were then made. A detailed description of each are described in the sections below.

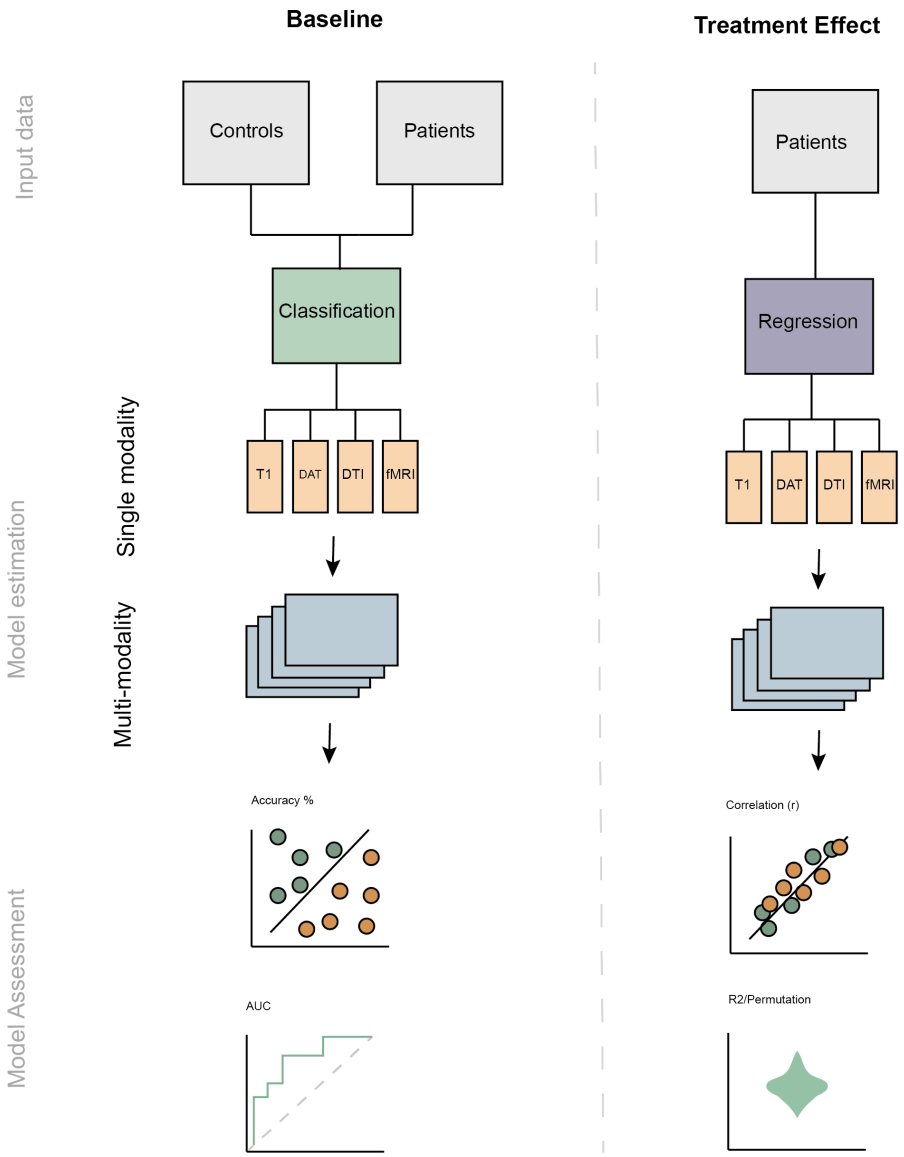


Figure 68: Schematic of machine learning research strands. Strand 1; classification models for each imaging modality as single models. Multimodal classification models using MKL with combination of imaging modalities also explored. Strand 2; regression-based machine learning models to predict response to methylphenidate in patients (Δ). All models used baseline neuroimaging. AUC=area under the curve. R^2=explained variance in the model.

6.3.12 Classification of patients and controls using machine learning

6.3.12.1 Single imaging classification models

Machine learning classification models were first constructed for each individual imaging modality (T1, DTI, rs-fMRI or SPECT) to investigate whether particular modalities outperformed others when classifying patients and controls (as quantified by balanced accuracy (BACC) and area under the curve (AUC)). This was achieved using a Binary Support Vector Machine (BSVM) in PRoNTo (Schrouff et al., 2013), where baseline imaging of patients and controls were used as the independent variable and class labels (e.g. TBI or Control) as the dependent variable for each model. For classification using T1, standardised grey matter (GM) segmentations derived using DARTEL were the input and masked using the group averaged GM segmentation to constrain the feature space to grey matter voxels only. For classification using DTI, two models were created using either standard space skeletonised FA maps or non-skeletonised standard space FA maps (whole FA), masked by the corresponding group averaged FA mask (mean FA skeletonised vs mean FA). Although skeletonised FA is commonly used to avoid partial volume effects (Smith et al., 2006), PRoNTo is particularly sensitive to subtle differences across the feature space. Classification performance may therefore improve when more features are available to the machine, particularly in cases where axonal damage is located at the edges of white matter rather than the centre. To avoid partial volume effects, a conservative threshold was therefore applied to the group averaged FA mask (0.2), which was included as the mask to constrain the feature space to within only these voxels. Previous research utilising both skeletonised and non-skeletonised FA images in PRoNTo within a different clinical population has demonstrated informative results in this approach (Schnyer et al., 2017). For classification with SPECT, standardised DaT images were used as the input with a striatal mask derived from the Harvard-Oxford atlas (Makris et al., 2006) to constrain the feature space. Finally, the 24 FC measures derived from rs-fMRI were input as a numerical 2D matrix for classification. The weights maps for each model were also derived to provide further insight into voxels within the imaging modality that are most informative for classification.

6.3.12.2 Multimodal classification models

Classification of patients and controls using multi-modal imaging via a L1-Multiple Kernel learning (MKL) machine was also explored. This was to determine whether the inclusion of multimodal imaging significantly improved model classification accuracy compared to single imaging modalities. All possible combinations of imaging modalities for the multimodal models was therefore explored, leading to a total of 26 models with varying numbers of imaging inputs (ranging from 2-5).

When using multimodal data with MKL, weights for each model are provided hierarchically, with relative contributions of each modality to the model being derived (e.g. the % contribution) as well as voxelwise weight maps. Furthermore, anatomically defined regional weights within each modality can also be calculated in parallel to voxelwise maps if an atlas is included as a second-level mask for the machine. This is a particular advantage of MKL as the inclusion of an atlas to construct regional weights provides more biologically interpretable information in comparison to voxelwise maps. Therefore, for models including T1 imaging, the AAL grey matter atlas was included (Tzourio-Mazoyer et al., 2012) providing 90 cortical and sub-cortical regions. For models including DTI imaging, the ICBM-81 DTI atlas consisting of 48 white matter tracts was included (Mori et al., 2008). Finally, for models including DaT imaging, the three structural subdivisions of the striatum derived by the Harvard-Oxford atlas were included (Makris et al., 2006). As FC measures are already extracted from cortico-striatal networks and included as a 2D input, no atlas was required. Expected ranking measures for each anatomical region within weights maps were also derived. This provides a measure of stability for the ranking of regions with greatest contribution to the model across each of the cross-validation folds.

6.3.12.3 Validation and assessment of classification models

For all classification models, hyperparameter optimisation with a 5-fold cross validation (CV) scheme was used to determine the generalisability of the classification model. For further details about this validation technique, please refer to methods chapter two, section 2.7.2. In order to evaluate model performance, total accuracy

(number of correct prediction/total number of predictions made quantified as a percentage), balanced accuracy (total accuracy accounting for unequal group sizes quantified as a percentage) and area under the curve (AUC) was calculated. For further details about these measures please refer to Methods chapter two, section 2.6.4. Performance metrics were calculated for each of the 26 possible models constructed and ranked from highest to lowest. The top five models were subsequently selected for comparison to single modality models. To determine whether models could significantly classify patients from controls, permutation testing using 1000 permutations was performed to derive a null distribution for the calculation of p values.

6.3.13 Prediction of response to Methylphenidate treatment using regression-based machine learning

6.3.13.1 Single imaging regression models

To determine whether individual imaging modalities could predict response to Methylphenidate in patients as quantified by Δ, a regression-based machine learning approach was applied using PRoNTo. This was achieved using a kernel ridge regression (KRR) machine where each patients baseline imaging was used as the independent variable and the Δ of working memory performance between Methylphenidate and Placebo as the dependent variable. Weights for each regression model were computed to identify the most informative voxels (or FC measures).

6.3.13.2 Multimodal regression models

To determine whether multi-modal imaging improved prediction of treatment effect compared to single imaging modality models, an MKL regression-based approach was applied. Here, all possible combinations of imaging modalities included in a model was tested, resulting in 26 prediction models with varying numbers of modalities. In addition to voxelwise weights maps, atlases for each imaging modality, as previously described within multimodal classification models, were included to derive anatomically interpretable weights maps.

6.3.13.3 Validation and assessment of regression-based models

To determine generalizability of regression models, a 5-fold CV scheme with hyperparameter optimisation was applied. Model accuracy was assessed using Pearson correlation coefficients between predicted and actual treatment effect working memory scores across the 5 folds. The proportion of variance explained (R^2) and mean squared error (MSE) were also examined to determine model accuracy. All models were ranked based on performance and the top five were selected for comparison of significant predictive power to single modality models. Permutation testing with 1000 permutations was performed to derive a null distribution and p value for the correlation coefficient and R^2 of each of the models to determine its accuracy and significance.

6.3.14 Assessment of single and multimodal model performance using a model comparison approach

Comparison of performance measures between single and all 26 possible multimodal models were performed. In this way, a direct test of the hypothesis that multimodal imaging will in general, significantly outperform single imaging modality models in classification and regression-based approaches could be made. For classification models, balanced accuracy measures were pooled for unimodal and multimodal models to create grand distributions for each family of models (e.g. Single vs Multi). For regression-based models, R^2 values were pooled for either unimodal or multimodal families. Next, a non-parametric one-tailed permutation test with 1000 permutations was applied using the Permutation Test function in Matlab (https://uk.mathworks.com/matlabcentral/fileexchange/63276-permutation-test), first for classification and then regression models. This function provides a non-parametric test for the difference in means between two samples. This test provides measures of the observed difference, effect size and statistical significance (p-value), thus providing a statistical means to determine whether multimodal models generally performed better than unimodal models.

For multimodal models, two additional correlational analyses were performed for each machine learning approach (e.g. classification and regression). First, a bivariate correlation analysis between the number of modalities and model performance measures (balanced accuracy for classification or R^2 for regression models) was performed to investigate whether the greater the number of modalities, the better the performance. Secondly, multiple linear regression was applied to determine whether the presence of a particular modality within multimodal models was significantly associated to model performance (e.g. Model performance~Modality).

6.4 Results

6.4.1 TBI patients demonstrate significantly poorer performance on working memory tasks

A repeated measures ANOVA revealed a significant main effect of group on working memory performance ($F(1,177)=7.619, p<0.01$) such that patients scored significantly lower than healthy controls. No interaction between group and task was observed. A principal components analysis was performed to determine the latent variable structure of the three working memory tasks. As per previous literature (Hampshire et al., 2012), all tasks loaded onto a single component explaining 56.44% of the variance in the data. A similar factor structure was observed when applying PCA to patient data only. Component scores from the PCA were therefore used as the composite measure of working memory ability (Fig. 69).

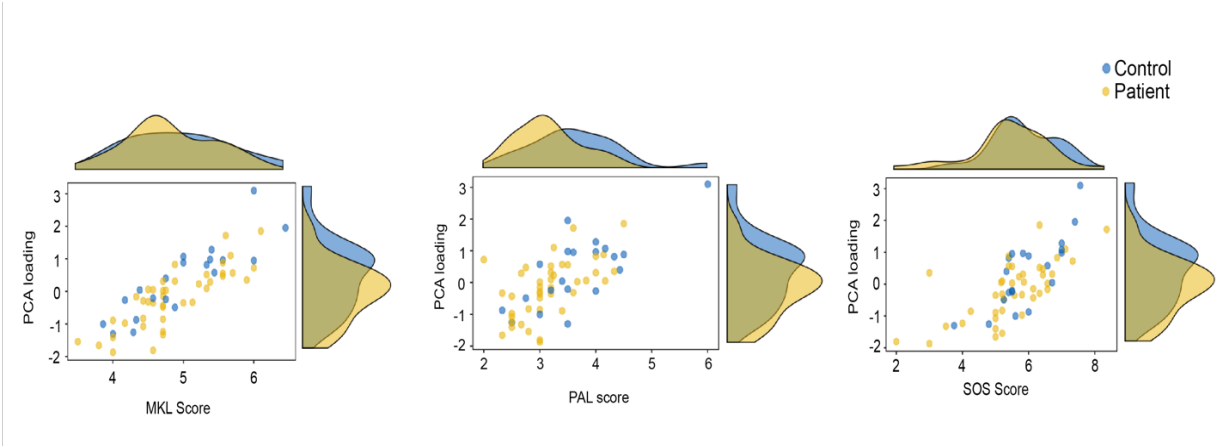


Figure 69: Associations between baseline working memory task performance in TBI patients and controls and PCA cognitive component loadings. Scatter and distribution plots of the association between tasks in patients and controls are plotted. Yellow represents TBI patients and blue represents healthy controls. PCA loading reflects the single cognitive component derived from the three working memory tasks.

6.4.2 Patients demonstrate abnormalities in brain structure and function

Lesion overlap masks derived for all TBI patients revealed a total of 23 patients (70%) had evidence of focal lesions. The highest density of lesions within this group was observed in the orbitofrontal cortex, in keeping with previous literature (Gurdjian., 1975; Bigler et al., 2007) (Fig. 70A). Cross-sectional analysis across all imaging modalities revealed significant abnormalities in TBI patients compared to controls. Voxel-based morphometry revealed significantly greater grey matter volume in healthy controls compared to TBI patients (tfce corrected, $p<0.05$) across a number of cortical and subcortical regions including the striatum, cerebellum, temporal and frontal lobes (Fig. 70B). No regions of increased volume were observed in patients compared to controls. Tract-based spatial statistics revealed significantly lower FA in TBI patients compared to controls (tfce corrected, $p<0.01$). Tracts with the largest difference in FA in TBI patients compared to controls included the corpus callosum (body, genu and splenium), the anterior and superior corona radiata, anterior limb of the internal capsule and posterior thalamic radiations (bilaterally) (Fig. 70C). No regions of greater FA were observed in patients. Comparison of DaT was also made between patients and controls. Significantly higher DaT was observed in healthy controls in the caudate bilaterally and the left putamen (tfce corrected, $p<0.05$) (Fig. 70D). A repeated measures ANOVA of cortico-striatal FC measures revealed a significant main effect

of group (F(1,1176)=104.667, p<0.001) such that TBI patients had more negative functional connectivity between caudate subdivisions and cortical regions than controls. No group by region interaction was observed (Fig. 70E-F).

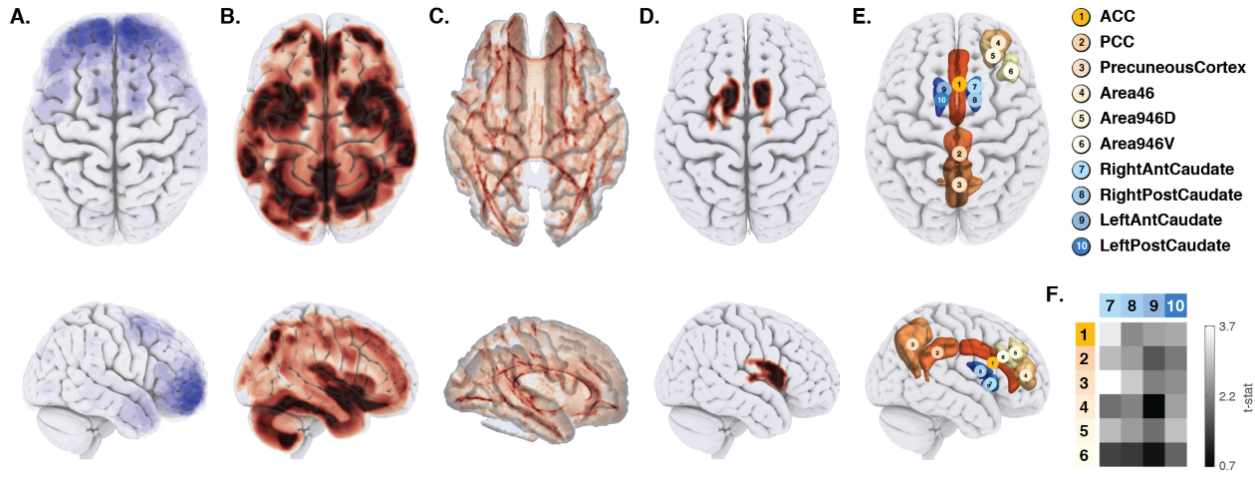


Figure 70: Cross sectional comparison of brain structure and function in TBI patients compared to healthy controls. A. Three-dimensional lesion overlap map. Darker colours represent greater overlap between patients with focal lesions. **B.** Voxel based morphometry results demonstrating significant reductions in grey matter volume, tfce cluster corrected (p<0.05). Darker colours represent greater statistical differences between groups. **C.** Tract-based spatial statistics results, dark red voxels represent statistically significant reductions in FA between TBI patients and controls, tfce cluster corrected (p<0.05). **D.** Voxelwise comparison of striatal DaT between. TBI patients and controls. Red represents voxels with significantly lower DaT (as quantified using SBR) in TBI patients compared to controls, tfce cluster corrected (p<0.05). **E.** Region of interest map displaying subdivisions of striatum and cortical regions defined for using in resting-state functional connectivity analysis. **F.** T-stat of differences in functional connectivity between TBI patients and controls between striatal subdivisions and cortical regions. Numbers represent region of interest labels defined in figure E.

6.4.3 Classification of patients and controls can be made using single imaging modalities

Classification of patients and controls using single modality inputs revealed significant models in both structural and functional measures of the brain. Permutational analysis demonstrated significant classification models for T1 grey matter imaging (total

accuracy 77.37%, balanced accuracy 73.21%, p<0.003, AUC 0.8, p<0.003), whole white matter fractional anisotropy (total accuracy 72.53%, balanced accuracy 71.79%,p<0.003, AUC 0.83, p<0.002) and DaT imaging (total accuracy 71.11%, balanced accuracy 68.45%, p<0.02, AUC 0.77, p <0.008). No significant classification model was observed when using skeletonised FA (total accuracy 58.99%, balanced accuracy 47.14%, p=0.71, AUC 0.57, p=0.29) or cortico-striatal FC measures (total accuracy 63.43%, balanced accuracy 59.17%, p=0.1, AUC 0.72, p=0.022), FDR corrected.

6.4.4 Multimodal imaging can improve classification accuracy

Classification using multimodal imaging demonstrated generally increased accuracy compared to single imaging models (Fig. 71). See Table 12 for all multimodal imaging model results. An MKL model consisting of T1 grey matter, whole white matter FA, DaT and FC provided the greatest classification accuracy (total accuracy 81.01%, balanced accuracy 79.29%, p=0.002; AUC 0.91, p=0.001, Fig. 71A). Computation of weights indicated that T1 imaging contributed the greatest to the model (50.60%) followed by whole white matter FA (31.70%), DAT imaging (12.16%) and FC (5.55%). Computation of regional weights within each imaging modality provided information regarding the anatomical regions most informative to the model (Fig. 52B). In T1 grey matter, regions of the right supplementary motor area (10.34%), left Cerebellum crus 2 (8.79%), left amygdala (4.61%), right lingual (4.30%), left paracentral lobule (3.89%), right caudate (3.66%), left middle temporal lobe (2.56%) left supplementary motor area (2.19%), left caudate (1.90%) and left thalamus (1.58%) contributed the greatest. For whole white matter FA, the left anterior corona radiata (10.21%), left cingulate gyrus (7.89%), right medial lemniscus (4.10%), left external capsule (2.83%), left fornix crescent (1.59%), left uncinate fasciculus (1.52%), left cingulum hippocampus (0.95%), left medial lemniscus (0.66%), left posterior limb of internal capsule (0.55%) and right superior longitudinal fasciculus (0.41%) contributed the greatest to the kernel. Regional weights within DaT revealed the caudate contributed the greatest to the model (9.27%), followed by the ventral striatum (2.88%). Finally, for FC measures, the greatest contributions to the model were the Anterior Right Caudate to precuneus

(0.47%), Posterior Right Caudate to precuneus (0.42%), Anterior Left Caudate to precuneus (0.5%) and Posterior Left Caudate to precuneus (0.33%).

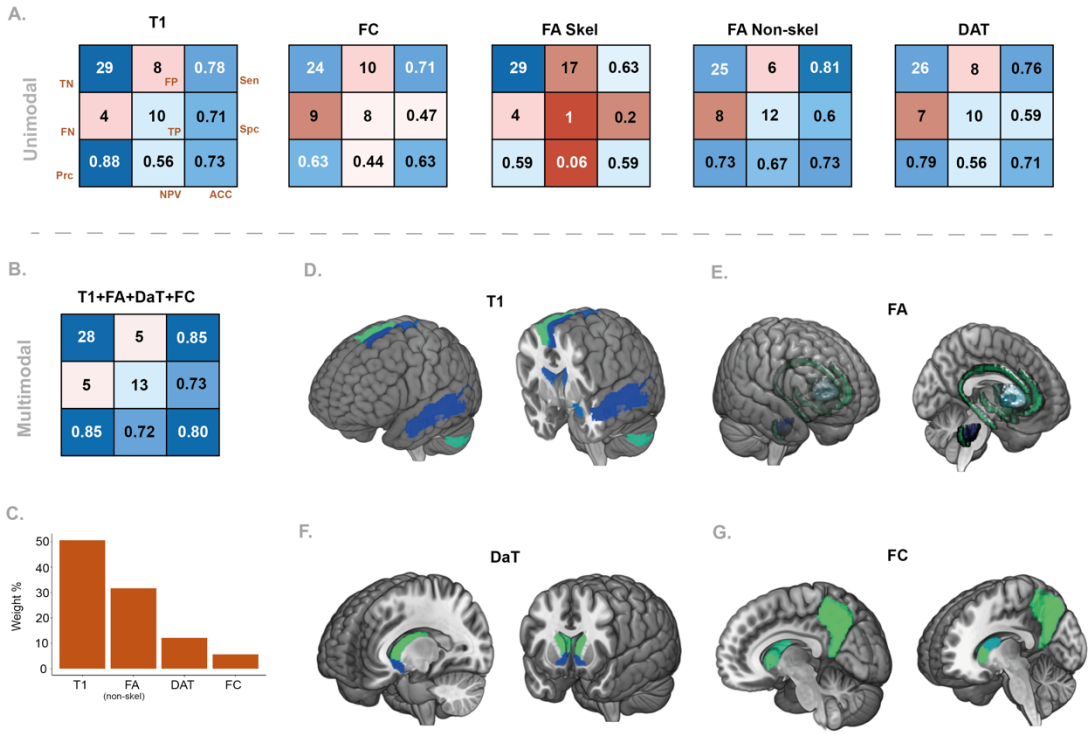


Fig 71: Uni- and multimodal classification results for TBI patient and control neuroimaging data. **A.** Unimodal classification confusion matrix plots for each imaging metric. **B.** Confusion matrix for multimodal classification model using MKL algorithm. **C.** Modality weights (% contribution to the model) for multimodal classification model. **D.** Top 10 regions with greatest contribution to the T1 modality kernel included within the multimodal classification model. **E.** Top 10 white matter tract regions with greatest contribution to FA imaging kernel included within the multimodal classification model. **F.** Striatal regions with greatest contribution to DaT imaging kernel included within the multimodal classification kernel. **G.** Functional connectivity (FC) subcortical and cortical regions with greatest contribution to FC kernel within the multimodal classification model. TN=True negative, TP=True positive, FN=False negative, FP=False positive, Prc=Precision, ACC=accuracy, NPV=Negative predictive value, Spc=Specificity, Sen=Sensitivity.

Permutation testing between measures of balanced accuracy for unimodal versus multimodal classification models revealed a moderate but significant effect size (d=0.36, p=0.048) such that greater balanced accuracy measures (indicative of model performance) was observed in multimodal models. Bivariate correlations between the number of imaging modalities included in multimodal models and balanced accuracy

revealed a significant positive relationship ($r=0.46, p<0.01$), such that the greater the number of modalities, the better the classification accuracy. When examining the relationship between inclusion of an imaging modality and balanced accuracy across multi-modal models using multiple linear regression, the model was not significant ($F(5,125)=2.237, p=0.055$).

Model	Rank	No.Modalities	B. Acc.	Acc.	AUC	T1	DAT	FA SKEL	FA MAP	FC
***T1FAMAPFC DAT**	**1**	**4**	**0.79**	**0.81**	**0.91**	**1**	**1**	**0**	**1**	**1**
***T1FASKELD AT**	**2**	**3**	**0.77**	**0.81**	**0.84**	**1**	**1**	**1**	**0**	**0**
***T1FASKELF AMAPFC**	**3**	**4**	**0.77**	**0.79**	**0.78**	**1**	**0**	**1**	**1**	**1**
***ALLMODALI TIES**	**4**	**5**	**0.77**	**0.79**	**0.86**	**1**	**1**	**1**	**1**	**1**
***T1FAMAPDA T**	**5**	**3**	**0.77**	**0.79**	**0.89**	**1**	**1**	**0**	**1**	**0**
FAMAPFC	6	2	0.77	0.79	0.88	0	0	0	1	1
FAMAPDAT	7	2	0.75	0.77	0.84	0	1	0	1	0
FASKELFAM APFCDAT	8	4	0.75	0.75	0.80	0	1	1	1	1
T1FAMAPSK ELDAT	9	4	0.74	0.77	0.85	1	1	1	1	0
FAMAPDATF C	10	3	0.74	0.77	0.85	0	1	0	1	1
FCDAT	11	2	0.74	0.77	0.77	0	1	0	0	1
T1FAMAPFC	12	3	0.73	0.75	0.82	1	0	0	1	1
T1FC	13	2	0.72	0.72	0.77	1	0	0	0	1
T1DATFC	14	3	0.72	0.76	0.87	1	1	0	0	1
T1FASKELDA TFC	15	4	0.71	0.74	0.83	1	1	1	0	1
T1DAT	16	2	0.71	0.76	0.85	1	1	0	0	0
FASKELFSM APFC	17	3	0.70	0.73	0.81	0	0	1	1	1
T1FASKELFA MAP	18	3	0.67	0.72	0.79	1	0	1	1	0
T1FASKEL	19	2	0.67	0.70	0.75	1	0	1	0	0
T1FAMAPS	20	2	0.66	0.69	0.75	1	0	0	1	0
FASKELFAM APDAT	21	3	0.65	0.67	0.75	0	1	1	1	0
FASKELFAM AP	22	2	0.64	0.69	0.73	0	0	1	1	0

T1FASKELFC	23	3	0.64	0.68	0.73	1	0	1	0	1
FASKELFCDAT	24	4	0.56	0.61	0.69	0	1	1	1	1
FASKELDAT	25	2	0.54	0.59	0.63	0	1	1	0	0
FASKELFC	26	2	0.54	0.64	0.59	0	0	1	0	1

Table 12: Multimodal classification model results using MKL. Rank represents model performance compared to all other multimodal classification models. B.Acc=Balanced accuracy, Acc=Total accuracy. AUC=Area under the curve. 1=Modality was present within the multimodal classification model, 0=Modality was not present within the multimodal classification model. Models highlighted in bold represent top five models selected for comparison to unimodal models and compared to null model using permutation analysis. *Represents significant models from permutation testing ($p<0.05$).

6.4.5 The impact of methylphenidate on working memory performance is variable

TBI patients demonstrated highly variable results in relation to treatment effects of methylphenidate on working memory performance (Fig. 72). A total of 15 patients (46%) were found to have improved working memory scores (e.g. $\Delta>0$) when on methylphenidate compared to placebo, however these effects varied greatly, ranging from score increases of 0.04 to 1 (SD=0.31). For patients who did not improve (e.g. $\Delta<0$) whilst on methylphenidate compared to placebo (n=18, 54%), decreases in working memory scores ranged from -0.11 to -0.79 (SD=0.17). Coefficient of variation tests revealed a significant difference between the variance in treatment effect for the two patient response groups (D'AD=2665,$p<0.001$), such that a greater spread of treatment effects was observed in patients who improved.

When examining the relationship between baseline working memory performance and response to methylphenidate (Δ) for all patients, a significant non-linear correlation was observed (rho=0.38,p=0.03), such that patients moderately below average on working memory performance at baseline tended to improve the most when on methylphenidate compared to placebo (Fig. 72). For patients who improved ($\Delta>0$), no significant relationship was observed (rho=0.34,p=0.19). No significant relationship between baseline working memory performance and treatment effect (rho=0.46, p0.08) was also observed for patients who did not improve ($\Delta<0$). No significant

difference between baseline working memory performance was observed in patients who improved compared to patients who did not with methylphenidate (t(26.13)=-1.25,m=0.22). One-way ANOVA revealed no significant main effect of treatment order (F(1,31)=0.001,p=0.975) indicating results are not impacted by which treatment block patients were randomly allocated to first.

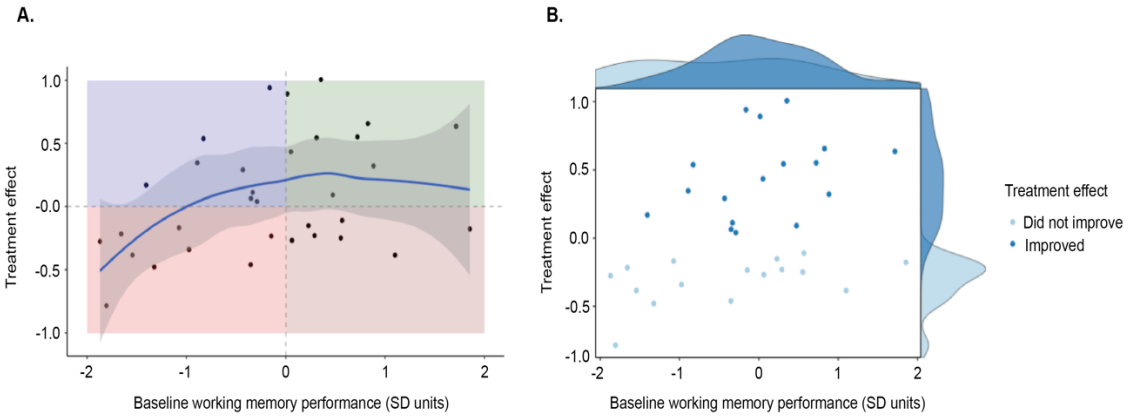


Figure 72: Treatment effect of methylphenidate on working memory performance in patients. Treatment effect is calculated as ∆=Working memory score with Methylphenidate-working memory score with placebo in patients. Positive value indicates higher working memory scores when treated with methylphenidate. Mph=methylphenidate, Plc=placebo. **A.** Scatter plot with LOESS regression line fitted to demonstrate non-linear association between baseline working memory performance (as defined by component loading) and treatment effect of methylphenidate (as defined by performance on methylphenidate-performance on placebo). Colour squares represent: 1) purple, cases where patients performed below average at baseline and improved when on methylphenidate 2) Light pink, cases where patients performed below average at baseline and performed worse when on methylphenidate compared to placebo 3) Green, cases where patients performed above average at baseline and improved when on methylphenidate, 4) Dark pink, cases where patients performed above average at baseline but performed worse when on methylphenidate compared to controls. **B.** Scatter and distribution plot of baseline working memory performance and treatment effect for patients who improved when on methylphenidate (dark blue) compared to placebo, and those that did not (light blue).

6.4.6 Multimodal imaging can predict treatment effect of methylphenidate on working memory performance where single modality models cannot

Regression-based machine learning to predict the treatment effect of methylphenidate on working memory performance in patients was explored (Fig. 73A). When applying machine learning regression to individual imaging modalities, no significant models were observed for T1 grey matter (r=-0.01, R^2=0.18, MSE=0.24, Norm MSE=1.21), skeletonised FA (r=-0.33, R^2=0.18, MSE=0.21, Norm MSE=1.02), whole white matter FA (r=-0.45, R^2=0.29, MSE=0.21, Norm MSE=1.03), DaT (r=0.17,p=0.29, R^2=0.26, p=0.20, MSE=0.22, Norm MSE=1.05) or FC (r=0.08, p=0.38, R^2=0.10, p=0.80, MSE=0.22, Norm MSE=1.06).

In contrast, a number of multi-modal imaging models were found to significantly predict a patient's response to methylphenidate. See Table 13 for all multimodal regression model results. The model with the highest accuracy included T1, skeletonised FA, DaT and FC imaging (r=0.63,p<0.007; R^2=0.42, p=0.016; MSE=0.14, Norm MSE=0.70) using an MKL machine (Fig. 73B). Computation of modality weights from this model indicated that T1 imaging provided the greatest contribution the model (74.1%), followed by skeletonised FA (22.10%), DaT (3.67%) and FC (0.20%) (Fig. 73C). Computation of regional weights within T1 imaging revealed areas of the right precentral gyrus (20.84%), Vermis 8 (9.39%), left cerebellum 10 (7.70%), right cerebellum 10 (7.52%) right cerebellum crus 1 (6.37%), right frontal middle orbital (2.67%), left middle temporal pole (2.20%), left precentral (2.19%), right paracentral lobule (2.12%) and left cuneus (2.03%) contributed the most (Fig. 73D). In skeletonised FA imaging, white matter tracts such as the right cingulate gyrus (8.53%), fornix (3.2%), left anterior limb of the internal capsule (2.68%), left uncinate fasciculus (1.2%), fornix crescent (1.12%), right sagittal stratum (inclusive of inferior longitudinal fasciculus and inferior fronto-occipital fasciculus), right superior cerebellar peduncle (1.06%), left superior cerebellar peduncle (0.7%), right superior fronto-occipital fasciculus (0.63%) and left inferior cerebellar peduncle (0.53%) contributed the greatest to the model (Fig. 73E). For DaT imaging, regional weights demonstrated that the ventral striatum (3.52%) and putamen (0.14%) contributed to the model (Fig. 73F).

Finally, for measures of FC, the right Anterior caudate to PCC (0.07%), right anterior caudate to the Precuneus (0.07%) and anterior right caudate to Area 94/6 ventral (0.06%) contributed to the model (Fig. 73G).

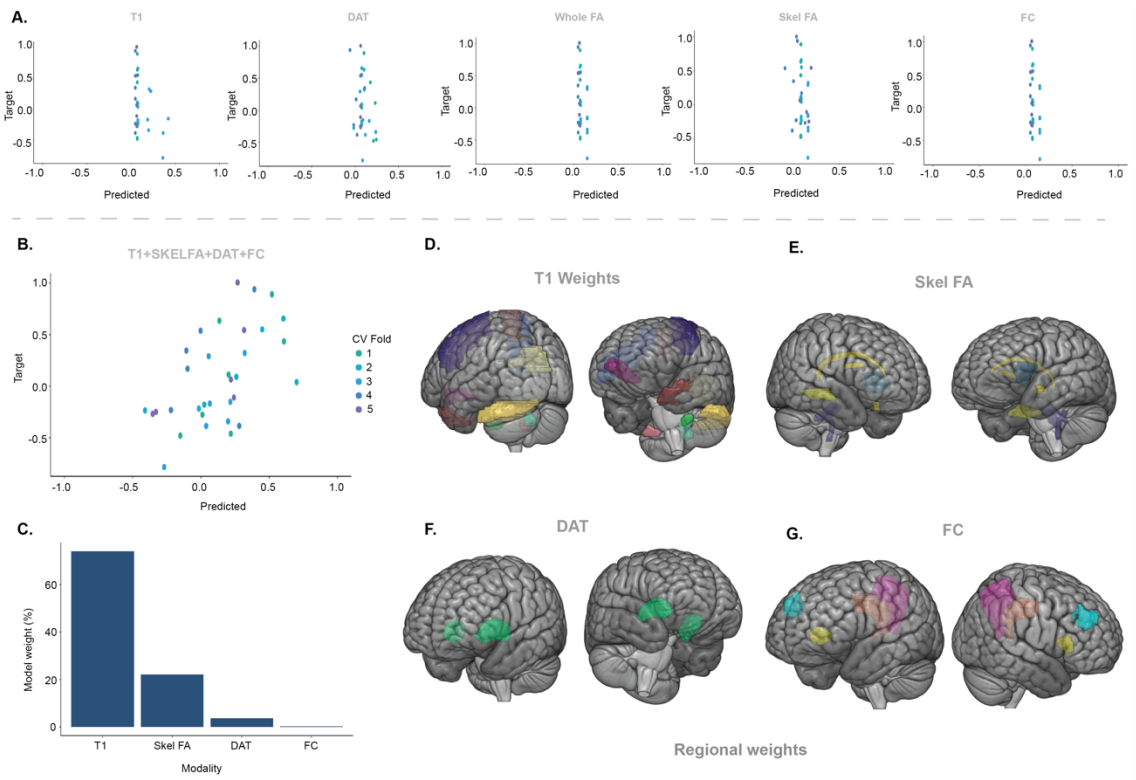


Figure 73: Results of multimodal regression-based model for the prediction of methylphenidate treatment effect of working memory performance in patients. A. Scatterplots of unimodal model results illustrating correlation between predicted and target working memory Δ scores across the 5-fold CV scheme. **B.** Scatterplot of best performing multimodal model illustrating correlation between predicted and target working memory Δ scores across the 5-fold CV scheme. **C.** Multimodal model modality weights. Bar plot represents % weight contribution of each imaging modality to the model. **D.** Regions of interest with greatest contribution to T1 imaging modality kernel within multimodal model. **E.** Regions of interest with greatest contribution to skeletonised FA imaging modality kernel within multimodal model. **F.** Regions of interest with greatest contribution to DaT imaging modality kernel within multimodal model. **G.** Regions of interest with greatest contribution to FC imaging modality kernel within multimodal model.

One-tailed permutation testing confirmed that multi-modal imaging outperformed single modality imaging models by demonstrating significantly greater R^2 measures ($d=0.59, p<0.01$) in this family. Bivariate correlations between the number of modalities and performance in models also demonstrated a significant positive correlation

(r=0.58,p<0.01) such that the greater the number of modalities included the greater the variance explained. A similar positive correlation was also observed for correlation coefficients of prediction models and number of modalities included (r=0.41,p<0.03), further demonstrating improved performance when more modalities are included. When assessing whether particular modalities had significantly greater associations to R^2 measures than others in multi-modal models using multiple linear regression, a significant model was observed ($F(5,18)=16.45$, $p<0.001$). Significant relationships were found between R^2 and the inclusion of T1 (beta=0.17,p<0.001) and non-skeletonised FA (beta=0.09,p<0.01) when accounting for other modalities.

Model	Rank	No.Modalities	Corr	R^2	MSE	DAT	FA MAPS	FA SKEL	FC	T1
***T1FASKELDATFC**	**1**	**4**	**0.63**	**0.42**	**0.14**	**1**	**0**	**1**	**1**	**1**
***T1FASKELDAT**	**1**	**3**	**0.63**	**0.42**	**0.15**	**1**	**0**	**1**	**0**	**1**
***T1DAT**	**3**	**2**	**0.62**	**0.42**	**0.15**	**1**	**0**	**0**	**0**	**1**
***ALLMODALITIES**	**4**	**5**	**0.62**	**0.42**	**0.16**	**1**	**1**	**1**	**1**	**1**
T1FASKELFC	**5**	**3**	**0.61**	**0.38**	**0.15**	**0**	**0**	**1**	**1**	**1**
T1FASKELFAMAPDAT	6	4	0.60	0.41	0.16	1	1	1	0	1
T1DATFC	7	3	0.60	0.42	0.16	1	0	0	1	1
T1FASKEL	8	2	0.59	0.37	0.16	0	0	1	0	1
T1FC	9	2	0.58	0.37	0.18	0	0	0	1	1
T1FASKELFAMAP	10	3	0.55	0.35	0.18	0	1	1	0	1
T1FAMAP	11	2	0.33	0.52	0.22	0	1	0	0	1
T1FAMAPDAT	12	3	0.27	0.49	0.24	1	1	0	0	1
T1FAMAPDATFC	13	4	0.27	0.49	0.24	1	1	0	1	1
T1FAMAPFC	14	3	0.26	0.44	0.24	0	1	0	1	1
T1FASKELFAMAPFC	15	4	0.23	0.41	0.23	0	1	1	1	1
FASKELFC	16	2	-0.10	0.02	0.24	0	0	1	1	0
DATFC	17	2	-0.14	0.16	0.29	1	0	0	1	0

FASKELDATFC	18	3	-0.16	0.23	0.26	1	0	1	1	0
FASKELFAMAP	19	2	-0.16	0.31	0.27	0	1	1	0	0
FASKELDAT	20	2	-0.17	0.24	0.26	1	0	1	0	0
FASKELFAMAPFC	21	3	-0.18	0.29	0.27	0	1	1	1	0
FASKELFAMAPDAT	22	3	-0.19	0.30	0.28	1	1	1	0	0
FASKELFAMAPDATFC	23	4	-0.19	0.30	0.27	1	1	1	1	0
FAMAPFC	24	2	-0.26	0.28	0.28	0	1	0	1	0
FAMAPDAT	25	2	-0.26	0.28	0.28	1	1	0	0	0
FAMAPFCDAT	26	3	-0.32	0.32	0.28	1	1	0	1	0

Table 13: Multimodal regression model results using MKL. Rank represents model performance compared to all other multimodal regression models. Corr=Pearson's' correlation coefficient between. predicted and actual treatment effect scores, R^2=variance explained/goodness of fit. MSE=Mean squared error. 1=Modality was present within the multimodal regression model, 0=Modality was not present within the multimodal regression model. Models highlighted in blue represent top five models selected for comparison to unimodal models and compared to null model using permutation analysis. ***** represents models that were significant after permutation testing ($p<0.05$).

As baseline working memory performance was found to significantly correlate to treatment effect in patients, an additional post-hoc model was constructed to determine whether inclusion of baseline information improved model performance. The imaging modalities from the best performing prediction model (T1, skeletonised FA and DAT) were therefore used as input and each patient's treatment effect (Δ) weighted (divided) by baseline working memory score as the dependent variable. A significant model was achieved (r=0.66, p<0.006 R2=0.44, p=0.015, MSE=0.04, Norm MSE=0.73) with incremental gain on r and R^2 compared to the multi-modal model not weighted by baseline performance. Computation of model weights revealed similar modality and regional contributions to the multimodal regression model not scaled by baseline working memory performance. For example, T1 imaging provided the greatest contribution to the model (75.27%), followed by skeletonised FA (19.32%) and DAT imaging (5.41%). Regional weights for each modality demonstrated the same regions in the same order of greatest to lowest contribution as the prediction model not scaled by baseline working memory performance.

6.5 Discussion

My results demonstrate the utility of multimodal machine learning methods to study the brain mechanisms that underlie individual differences in responsiveness to pharmacotherapy after TBI. As expected, based on past studies, patients showed working memory impairments and widespread cerebral damage. Indeed, abnormalities were evident across all of the imaging modalities examined. However, the accuracy of classification and prediction models varied substantially when trained on these measures individually. More importantly, machine learning models that included multiple types of imaging data had superior prediction accuracy in general when predicting response to pharmacotherapy. This pattern of results accords closely with my central hypothesis, that the behavioural effects of pharmacotherapy are mediated by multiple components of the working memory system.

Previous studies of TBI have primarily focused on relating individual imaging modalities to behavioural deficits and therapeutic responses. The results of those studies show promise insofar as statistically significant relationships were observed between brain metrics and behaviour. However, the strength of those relationships, and the accuracy of prediction, have typically been of small to medium scale. When the complexity of the systems that underlie working memory are considered, it is perhaps unsurprising that our previous study using this cohort, was able to detect treatment effects in a simple reaction time task but not working memory when stratifying patients by DAT (Jenkins et al., 2019). Working memory processes do not map in a simple one-to-one manner onto individual brain regions or dedicated circuits. Instead, they involve the temporary formation of what may be best described as dynamic brain states, where widespread coalitions of brain regions interact in a coordinated manner. In fact, it has been shown that the type of information and manner of processes applied within working memory can be robustly classified based on these states (Soreq et al., 2019). From a mechanistic perspective, this can be considered to reflect the temporary formation and manipulation of information constructs that span multiple brain regions (Hampshire et al., 2012).

TBI can affect the distributed network that underlies working memory at multiple points and does so in a manner that varies across individuals in terms of both severity and spatial pattern. More specifically, the TBI cohort examined here showed significant abnormalities across multiple imaging modalities. Cross-sectional results indicated widespread reductions in both cortical and subcortical volumes for regions associated with working memory such as the striatum, cerebellum, frontal and temporal lobes (Hampshire et al., 2012; Rottschy et al., 2011). They also showed disruption to the integrity of the white matter tracts that connect them (Charlton et al., 2010; Palacios et al., 2012), reduced DaT within striatal areas that modulate those cortical systems, and reflecting this network-wide disruption, reduced cortico-striatal FC connectivity (Tritsch et al., 2012). Furthermore, a proportion of individuals had contusions within the orbitofrontal cortex, a region of the PFC that is crucial for working memory function (Barbey et al., 2011). The multiple points of overlap between the WM network and pattern of TBI damage support the high prevalence of WM deficits observed in this cohort.

More importantly, given that the relationship between patterns of neural damage, behavioural deficit and response to therapy form a many-to-many mapping problem, focusing on any one brain region or imaging modality in isolation is unlikely to provide a good prediction of response to therapy. It is therefore unsurprising that patients differed widely in their baseline deficits and response to therapy. Similar to previous studies (Manktelow et al., 2017; D'Esposito & Postle., 2017), treating patients with methylphenidate led to variable results in patients. Of the 33 patients investigated, only 15 numerically improved on working memory tasks when treated with methylphenidate compared to placebo. Interestingly, a non-linear relationship between baseline working memory performance and response to treatment was observed, whereby patients with moderately low to average baseline scores tended to improve whilst patients with the lowest baseline scores were in contrast found to worsen. This relationship may prove valuable in predicting response to treatment, however the variance between patient's with similar baseline performance and yet vastly different treatment effects, suggests a much more complex relationship associated with patterns of damage within the brain is likely as important to aid prediction.

One of the primary aims of imaging as applied to TBI is to better understand the pathological brain mechanisms that underlie behavioural deficits. A more challenging aim is to provide a method that can be used to predict individual differences in deficits, and ultimately, to predict and individually tailor response to treatment. Given the complexity of the system and variability of neural damage, it is unsurprising that this latter aim has proven difficult to achieve in TBI. This is reflected in my findings, where no single imaging modality could predict treatment effect. However, when combining multiple modalities, several significant models were observed, with the best (as quantified by r, R^2 and MSE) including FA, grey matter and DaT imaging. Importantly, when scaling treatment effect by baseline performance, single modality models remained non-significant and multimodal models demonstrated only incremental gain. This finding supports the notion that a more complex relationship associated with the disruption to the working memory system via damage is central to individual differences in treatment effects, which can be captured using a multimodal machine learning approach.

A useful property of the MKL method is that it enables the features that contribute most to prediction within each data type to be identified. When analysed at this finer grain, weightings within the grey matter and white matter kernels replicated established findings and provided new functional anatomical insights. For example, within the grey matter, multiple subdivisions of the cerebellum and frontal lobes were the most predictive of the response to therapy. This accords particularly well with patient studies using methylphenidate, where altered activation levels within the cerebellum and frontal regions were associated with improved working memory performance after treatment (Manktelow et al., 2017). In the white matter kernel, large tracts such as the uncinate fasciculus, superior longitudinal fasciculus and superior fronto-occipital fasciculus had the strongest weightings. These tracts also are commonly associated with working memory performance, and they connect regions where functional activity has been reported to be modulated by methylphenidate (Palacios et al., 2011; Manktelow et al., 2017). Finally, the ventral striatum had the strongest weighting within the DaT kernel. This is an interesting finding: on the one hand, this region is closely associated with working memory, whilst on the other, it did not show significant patient-control differences in the cross-sectional analysis. In studies of methylphenidate using healthy controls, alterations to receptor availability in the ventral striatum have been

associated with improved performance on spatial working memory tasks (Clatworthy et al., 2009) suggesting an important role of individual differences in this region when predicting treatment response.

A number of potential limitations should be considered. First, multimodal imaging data will by definition have more features and as such may have a higher tendency towards overfitting within multivariate regression models. However, this is unlikely to explain the observed patterns of results as a robust k-fold approach was used. Here a trained model is tested on data to which it is naïve, therefore making it unlikely that a model overfitted to one set of participants would generalise well to others as demonstrated to be the case with high accuracy and significant prediction models. Secondly, it may be more likely to observe a multimodal model as performing better than a unimodal modal because there are more possible combinations. Contrary to this view, only the multimodal models provided a significant prediction of the behavioural response to treatment. Furthermore, the comparison of the grand distributions of model accuracies for the multi- vs unimodal models showed a statistically significant advantage for the former. A further consideration is that the effect of treatment may be due to improvement in a subset of patients due to learning effects. The tasks used here have been shown to demonstrate improvement over time, however when testing for treatment order, no significant effect was observed and patients who improved were not constrained to only those randomised to one treatment order.

More notably, the cohort examined in this study is of medium scale. I note that the primary value of the study is the demonstration of the multimodal approach within this clinical population, which was made possible by the unusual richness of data available for each participant. Future research should apply this approach at a larger population scale. This would have the advantage of allowing the models derived here to be further validated in completely independent datasets (Cawley et al., 2010). Finally, the working memory tasks used within this study are well validated (Hampshire et al., 2012, Daws et al., 2017), yet they are focused within the visuospatial domain. Working memory systems are more complex than this, spanning spatial, object and verbal, and according to the type of process applied to the maintained information. Given that the deficits observed after TBI can vary across cognitive domains according to the underlying pattern of neural damage, interrogating whether similar treatment effects

and predictive models can be derived for other working memory domains would be a sensible future direction.

In summary, this study illustrates the heterogeneity of damage observed across different systems in the brain after TBI and the patterns associated with working memory performance. The application of pattern recognition approaches to individual differences in damage and cognition proved to be particularly beneficial in this clinical population and provide a potentially useful set of imaging markers for the prediction of working memory impairments and the efficacy of its treatment with methylphenidate. Furthermore, the inclusion of multimodal imaging to modelling can improve predictive models, particularly where modulation of working memory is reliant upon multiple systems within the brain. These findings provide a number of potential predictive markers that can be explored further for the stratification of patients during treatment.

Chapter 7

Discussion

In this chapter, I discuss the main findings from my thesis and the potential impact of my research. I discuss a number of interpretations from my results and describe the potential avenues for future research on the basis of my research.

7.1 Summary of findings

In this thesis, I aimed to investigate the structural and functional abnormalities associated with working memory impairment after traumatic brain injury (TBI). I sought to use multimodal imaging with a particular focus on diffusion tensor imaging (DTI) to determine whether patterns of damage associated with working memory impairment could be identified to improve prognosis and treatment in patients.

The main aims of this thesis were:

1. To investigate the impact of white matter damage on working memory after TBI.

2. To identify patterns of white matter damage associated with working memory impairment after TBI.

3. To stratify patients based on cognitive and neuroimaging profiles in order to improve prognosis and tailor interventions.

7.1.1 Chapter 3

In chapter three, I developed and tested a novel diagnostic pipeline that enabled fractional anisotropy measures from individual patients to be compared to a healthy control cohort. The aim of this chapter was to provide a more accurate diagnosis of axonal injury than is currently available clinically. I found that a large proportion of patients in the chronic phase of injury (48%) had evidence of DAI at the individual level using this method. Importantly, I found that over a third of patients with unremarkable MRI's were diagnosed with DAI (DAI+) whilst 40% of patients with visible microbleeds were not diagnosed (DAI-) using this pipeline. When comparing across a range of cognitive and functional outcomes, patients identified as DAI+ were significantly impaired on a number of cognitive domains inclusive of working memory, compared to patients identified as DAI- using this pipeline. These findings suggest that current clinical diagnosis of DAI may be inaccurate and would benefit from the implementation of such a pipeline. Importantly, I demonstrated the utility of this pipeline in subacute

TBI, by demonstrating reliability in diagnosis between subacute to chronic phases in patients. A number of studies support my findings by illustrating cases where chronic cognitive problems in mild TBI patients with unremarkable clinical MRI's are associated with microstructural changes in white matter (Hellstrom et al.,2013; Pall D'Acqua et al., 2017). Furthermore, recent histopathological work in human TBI has demonstrated that traumatic microbleeds are predominantly observed in perivascular spaces in the absence of axonal injury, supporting findings from this chapter that microbleeds are not a definitive marker of DAI (Griffin et al., 2019). Previous literature has demonstrated that dynamic changes in FA can occur drastically within the first years of injury and persist many years afterwards (Kinnunen et al., 2011; Dall'Acqua et al., 2017). This supports my findings, whereby time since injury was an important factor in relation to diagnosis of tract DTI abnormalities.

This work provides a diagnostic pipeline that has been robustly validated against common methodological issues such as age, focal lesions, time since injury and sample size, providing pragmatic guidelines for clinicians to implement in their practice. This work has the potential to change the way in which diagnosis of axonal injury is made clinically, and to ultimately improve the accuracy of diagnosis for improved patient care. The code and example data for this pipeline have been made widely available for use by clinicians and researchers alike in order to support this.

7.1.2 Chapter 4

In chapter four, I investigated whether distinct patterns of white matter damage were associated with working memory impairment. I examined the structural connectomes underpinning working memory and reasoning functional networks (Hampshire et al., 2012) in a large chronic TBI population and compared to healthy individuals using graph theory. I found that altered network topology within both reasoning and working memory networks was present in TBI patients and was associated with impairments. This finding replicated previous work in TBI by demonstrating a move away from small-world topology whereby greater modularity and reduced integration is observed (Pandit et al., 2013). Importantly, I found that alterations to structural connectivity within the reasoning and working memory networks had dissociable effects on

reasoning and working memory processes. Abnormalities in the working memory network were associated with impairments in both working memory and reasoning, whilst abnormalities in the reasoning network were only associated with reasoning impairment. This finding supports previous hierarchical models of working memory (Hampshire et al., 2012; Petrides et al., 1994) that suggest reasoning is reliant upon the ability to maintain information via working memory processes. The findings from this chapter provide for the first time, evidence in support of this from a network neuroscience perspective in TBI. Furthermore, this work provided a discrete set of network nodes that were able to quantify individual differences in working memory impairment after TBI, laying the foundations to explore their prognostic value. My research from this chapter has helped to advance our understanding of the potential mechanisms associated with working memory impairment and the heterogeneity that is observed within this population. This provides a more finer-grained assessment of damage that may be useful for future targeted interventions utilising tools such as TACS and TDCS where structural connectivity is associated to its efficacy (Li et al., 2019).

7.1.3. Chapter 5

In chapter five, I sought to test whether the working memory network nodes defined in chapter four could be used as prognostic markers for the development of working memory impairment after TBI. I found that abnormalities in the working memory network as quantified using graph theory measures defined in chapter four, were also observed in a subacute TBI population. In addition, I found that increases in working memory network modularity (local efficiency) from subacute to chronic timepoints in patients, was associated with higher working memory performance at the chronic phase of injury. In contrast, the presence of lesions in working memory network nodes did not provide any association to working memory performance. This finding suggests that increases in network modularity after damage to the structural network are associated with better outcomes after TBI, providing further mechanistic insights into the heterogeneity of outcomes. This was supported by previous longitudinal studies of cognitive outcomes after TBI (Kuceyeski et al., 2019; Hillary et al., 2014) as well as

evidence of improved working memory in relation to increased local efficiency observed in the subset of patients with longitudinal cognitive and structural data.

Importantly, I found that measures of degree centrality from the working memory network at the subacute phase of injury could predict working memory performance at the chronic phase when using a regression-based machine learning approach. This prediction could not be made when using measures of FA for the same nodes. The role of network topology in supporting cognition has been widely demonstrated (Bassett et al., 2017; Sporns et al., 2018) however, evidence of its utility in the prognosis of outcomes after TBI has been limited. These findings provide a proof of principal that discrete measures of working memory structural connectivity at the subacute phase of injury has prognostic potential that can account for heterogeneity within this population beyond simple measures of FA. My work therefore provides a strong foundation for these measures to be explored further to continue to improve the prognosis of working memory impairments in patients.

7.1.4 Chapter 6

In chapter six, I investigated whether the use of multimodal imaging could predict the efficacy of methylphenidate in treating working memory impairments after TBI. I found that by utilising pattern recognition methods in machine learning with neuroimaging data (PRoNTo, Schrouff et al., 2013) I could improve the accuracy of classification models of patients and controls using multimodal imaging. Critically, when modelling baseline neuroimaging data to predict the impact of methylphenidate on working memory performance in patients, only multimodal imaging could predict treatment effects. The highest performing prediction models included a wide range of imaging modalities inclusive of grey matter volume (T1), white matter integrity (Fractional anisotropy), Dopamine transporter imaging (DaT) and cortico-striatal functional connectivity measures. These findings reflect the multiple systems employed during working memory that can be modulated via methylphenidate (Manktelow et al., 2017; Newsome et al., 2015; McAllister et al., 2004). My findings demonstrate the importance of quantifying damage within the brain from a holistic perspective, particularly when attempting to predict the impact of treatments reliant upon the

intactness of multiple systems in order for effective treatment. This is particularly highlighted by the fact that models from multimodal families, significantly outperformed unimodal models. My research provides clear evidence of the importance of quantifying heterogenous damage across multiple systems implicated in working memory and the potential clinical utility of multimodal machine learning techniques to stratify patients for treatment (Maas et al., 2007; Jenkins et al., 2019). This work provides a methodological framework and evidence in support of the use of multimodal imaging for clinical trials that wish to develop precision medicine in TBI.

7.2 Interpretation

7.2.1 Heterogeneity in working memory impairments after TBI is associated with the distribution of damage across the structural networks that underpin it

It has long been established that structural dysconnectivity after TBI is associated with working memory impairment (Palacios et al., 2012; Kinnunen et al., 2012). However, the variability in deficits observed in patients with white matter damage has suggested this relationship is not simple. Instead, it requires quantification of individual differences in damage within the white matter. Mass univariate tests of axonal injury and its association to working memory impairment have implicated a range of tracts (Meythaler et al., 2001; Vestergaard et. al., 2001; Owens et al., 2016) but has lacked a means to accurately predict which patients are likely to develop working memory impairments from this damage. One reason for this may be that previous research has taken a whole brain approach, using voxelwise measures to explore associations within the white matter with varying signal. For example, the advancement of neuroimaging has demonstrated that cognition does not map to single regions within the brain but instead relies upon dynamic networks of distributed brain regions (Soreq et al., 2019). Therefore, investigating the particular structural architecture that supports these functional networks during working memory will likely be more informative in mapping individual differences in impairment. This was supported by my work where although white matter damage was widespread across the brain, only distinct patterns of damage were associated with working memory impairment and this

was dependent upon where damage was in relation to the working memory structural connectome.

Indeed, dysconnectivity to working memory structural networks demonstrated a hierarchy in cognitive function, whereby other processes are reliant upon the intactness of this network and disruption to hubs within the working memory network had a greater association to working memory impairments in individuals. This supports the notion that nodes within the network may have differential weighting and therefore vary in their impact on working memory when disrupted (Fagerholm et al., 2015; Aerts et al., 2016). Taken together, these findings provide some insight into the co-morbidity of cognitive impairment after TBI and the prevalence of working memory impairment within the constellation of deficits (Fleminger et al., 2005; McAllister et al., 2008; Ponsford et al., 2011). Furthermore, these findings demonstrate that heterogeneity in working memory impairments likely reflect heterogeneity in dysconnectivity to the regions employed within this network, suggesting a more granular quantification of white matter damage may help to predict the development of working memory impairment in individuals.

7.2.2 Identifying the structural connectome of working memory can aid prognosis of impairments

By delineating a specific structural network associated with working memory impairment after TBI, a discrete set of measurements can be investigated that may help to improve prognosis of working memory impairment in individual patients. Heterogeneity in damage has previously impeded the prediction of working memory impairments after TBI (Levin et al., 2002; McAllister et al., 2004) and this likely reflects the lack of specificity contributing to large amounts of noise within prediction models (Barman et al., 2016; Topolovec-Vranic et al., 2011). The identification of specific patterns associated with impairment within this thesis and the quantification of the extent of damage on a continuous scale provides a means to overcome these limitations. I found that by measuring structural dysconnectivity in this network at the subacute phase of injury, I was able to predict working memory performance in the chronic phase in a novel cohort of TBI patients. These findings support the notion that

mapping individual differences in structural dysconnectivity of the working memory network can be valuable in predicting working memory outcomes after TBI.

7.2.3 Network neuroscience provides insights into the potential mechanisms of working memory impairment

The development of network neuroscience and the application of graph theoretical measures to structural connectomes in the brain have helped to elucidate the potential mechanisms of working memory impairment after TBI. In my thesis, I demonstrated that working memory network topology was abnormal after TBI and associated with impairment. Importantly, these findings demonstrated that TBI shifts working memory network topology towards a more modular architecture with less global integration at both the acute and chronic phases of injury. This reduction in integration is associated with less efficiency in the flow of information within the network (Bassett et al., 2006) which is integral for successful maintenance during working memory (D'Esposito & Postle., 2015).

Importantly, the application of graph theory measurements to a longitudinal cohort of subacute TBI patients demonstrated that increases in modularity within the first six months after injury are associated with higher working memory scores. This suggests network reorganisation after injury through hyper-connectivity is beneficial and may reflect network resilience, supporting previous literature (Kuceyeski et al., 2019; Hillary et al., 2014). In contrast, in chronic TBI patients assessed in chapter four, increased modularity (or local efficiency) was associated with poorer working memory performance, with evidence of more widespread dysconnectivity being present (as measured by degree centrality). These findings suggest that increased network modularity may be beneficial for working memory during early recovery but that alterations require an optimal balance to maintain small-world topology to support cognition, much like in healthy brains. These findings also suggest that over time, secondary degeneration within white matter as demonstrated in pathophysiology studies (Schimmel et al., 2017; Scott et al., 2016) may drive aberrant modularity, that ultimately impacts upon working memory. This is supported by evidence that alterations in white matter can span many years (Perez et al., 2014), and that time

since injury was associated with the rates of axonal injury diagnosed in patients using my diagnostic pipeline. Here, network neuroscience, particularly graph theory has demonstrated superior insights into working memory impairment after TBI than standard measures of FA, as further supported by its prognostic accuracy in my thesis.

7.2.4 Broad heuristics in the clinical setting are useful but quantifying white matter damage at the individual level is valuable

In the clinical setting, diagnosis of diffuse axonal injury informs the management of patients by determining a greater risk of poor cognitive and functional outcomes (Vieira et al., 2016). Although a useful heuristic, this method of diagnosis does not accurately predict the development of working memory impairment after injury. My work demonstrates that this is in part due to the lack of diagnostic accuracy for diffuse axonal injury and lack of specificity for markers of working memory impairment. I found that by quantifying fractional anisotropy measures at the individual level I was able to diagnose patients with axonal injury that would not otherwise be diagnosed within a clinical setting. Importantly, when applying DTI measurements within individuals, abnormalities were found to clearly map to cognitive and functional impairments inclusive of working memory, whereas standard clinical markers of microbleeds did not. This work suggests that accurate diagnosis of DAI is required with the use of an individualised DTI assessment as proposed in my pipeline, and that prediction of working memory impairment may be achieved using measurements from the specific structural markers outlined within this thesis.

7.2.5 Working memory impairment is not limited to white matter damage: the case for multimodal imaging and machine learning

Damage to white matter is most commonly associated with working memory impairment after TBI (Lee et al., 2012). I found that quantifying white matter damage was particularly useful in relating to working memory impairment after TBI and in predicting working memory outcomes sub-acutely. Nevertheless, working memory relies upon complex systems that extend beyond the white matter architecture (McAllister. et al., 2004). Although DTI is a valuable measure, it does not provide a

holistic overview of damage to the brain and the complex interactions between systems that can drive working memory impairments.

For example, a key limitation with current pharmacological interventions using methylphenidate to treat working memory is the variability in its efficacy (Jenkins et al., 2016). Previous work has demonstrated that this is in part related to the endogenous dopamine levels present at the point of treatment (Manktelow et al., 2017; Cools & D'Esposito et al., 2011). Providing tailored interventions to treat working memory is a key aim of current research with evidence suggesting the stratification of patients may be valuable (Jenkins et al., 2019). When considering the efficacy of methylphenidate on working memory after TBI, understanding the complex systems this intervention modulates and identifying features associated with its success is important (Mehta et al., 2006).

I found that predicting treatment effects on working memory using methylphenidate was not possible using single modality regression-based machine learning models, demonstrating that white matter damage, although important in the development of working memory impairments, does not provide the full picture. In contrast, when including imaging across multiple systems within the brain inclusive of white matter integrity, grey matter volume, endogenous dopamine levels and cortico-striatal functional connectivity, a significant prediction model was achieved. Furthermore, anatomical regions most informative to the prediction model across imaging modalities reflected similar regions identified in the literature. For example, the ventral striatum was found to be most informative within SPECT imaging. In studies of healthy individuals, performance on working memory tasks after the administration of methylphenidate was associated with DaT within the ventral striatum (Clatworthy et al., 2009). Similarly, in studies of TBI, alterations to functional activation during working memory tasks in the cerebellum were associated with improved working memory performance after the administration of methylphenidate (Manktelow et al., 2017). This too was identified as one of the most informative regions in prediction models. Importantly however, is the fact that previous literature has seldom synthesised these findings across the different systems in the brain. Here, my research demonstrates that by combining information via the use of multimodal imaging in a machine learning

framework, improved patient stratification can be made and ultimately, improved, targeted therapeutic interventions may be possible.

7.3 Future research

7.3.1 Prediction of working memory impairment using structural network measures

This work lays the foundations for future research to test the clinical utility of the structural network measures defined in a chronic TBI population and tested in a subacute cohort. Although I demonstrated significant predictive models of working memory in a longitudinal subacute TBI population, my sample size was small and prediction models may therefore be over-estimated. Applying the same methods and network measures outlined within this thesis to a wider TBI population will help to confirm whether they are effective and generalisable prognostic markers of working memory impairment. Furthermore, my research has demonstrated long term changes in network topology. Future research may also benefit from extending current prediction models into more chronic timepoints to determine whether working memory impairments can be predicted much later after injury. This is a particularly important point in the context of late-term degeneration of working memory which is associated with extended neuroinflammation after TBI (Gorgoraptis et al., 2019).

7.3.2 Targeted modulation of the working memory network and its associated structural connectivity

In addition to defining and testing a discrete set of working memory nodes, my research has illustrated the differential impact of dysconnectivity across nodes within the network. This provides potential insights into the hierarchy of the network, whereby hubs are likely to have greater influence on the network (Fagerholm et al., 2014). Recent work by Li et al., 2019 has also demonstrated that the efficacy of stimulation in modulating functional networks is dependent upon the white matter integrity underlying the stimulation target. Extracting the graph theoretical measures from the working memory network in individual patients defined in this thesis may therefore be

useful in future research to determine optimal stimulation targets for the modulation of working memory networks after TBI.

7.3.3 The use of methylphenidate to treat working memory

My work demonstrates that methylphenidate can treat working memory impairment after TBI but that this is dependent upon the pattern of damage across systems within the brain. I demonstrate that measures utilising T1, DTI, SPECT and rs-fMRI are valuable in the stratification of patients for treatment with methylphenidate. However, I also demonstrate that a range of models including multiple imaging modalities could significantly predict treatment effects in working memory. Future clinical trials may therefore benefit from the employment of similar multimodal machine learning techniques to quantify individual differences in damage and to stratify patients for treatment with methylphenidate. This is a particularly important point as previous clinical trials using this pharmacological intervention have demonstrated highly variable results (Maas et al., 2016; Manktelow et al., 2015; Jenkins et al., 2019) that may reflect their limitations in patient stratification. Future research would therefore benefit from determining whether the improvements observed when using methylphenidate are consistent and clinically useful when better patient stratification is made using multimodal imaging.

7.3.4 Investigating the multiple dimensions of working memory after TBI

Although my thesis has begun to provide ways in which the prognosis and treatment of working memory impairments can be improved, it is currently limited to visuospatial working memory. Working memory is a complex set of processes that spans both visual and verbal domains as well as multiple stages (e.g. encode, maintain, manipulate). My thesis has been limited in fractionating these multiple aspects of working memory and may therefore restrict the generalisability of my findings beyond the visuospatial domain. Future research would therefore benefit from taking the approaches I have detailed in this thesis and applying these to a wider range of working memory dimensions to help a) phenotype the types of working memory

impairments observed after TBI and b) further explore the mechanisms associated with different forms of working memory impairment.

References

Achard, S., Salvador, R., Whitcher, B., Suckling, J. & Bullmore, E. A resilient, low-frequency, small-world human brain functional network with highly connected association cortical hubs. J. Neurosci. **26**, 63–72 (2006).

Adams, J. H., Doyle, D., Ford, I., Gennarelli, T. A., Graham, D. I., & McLellan, D. R. (1989). Diffuse axonal injury in head injury: definition, diagnosis and grading. *Histopathology, 15*(1), 49-59. doi:10.1111/j.1365-2559.1989.tb03040.x

Aerts, H., Fias, W., Caeyenberghs, K., & Marinazzo, D. (2016). Brain networks under attack: robustness properties and the impact of lesions. *Brain, 139*(Pt 12), 3063-3083. doi:10.1093/brain/aww194

Ahn, S., & Lee, S. K. (2011). Diffusion tensor imaging: exploring the motor networks and clinical applications. *Korean J Radiol, 12*(6), 651-661. doi:10.3348/kjr.2011.12.6.651

Andersson, S., Krogstad, J. M., & Finset, A. (1999). Apathy and depressed mood in acquired brain damage: relationship to lesion localization and psychophysiological reactivity. *Psychol Med, 29*(2), 447-456. doi:10.1017/s0033291798008046

Arnsten, A. F. (1998). Catecholamine modulation of prefrontal cortical cognitive function. *Trends Cogn Sci, 2*(11), 436-447. doi:10.1016/s1364-6613(98)01240-6

Arnsten, A. F., Cai, J. X., Murphy, B. L., & Goldman-Rakic, P. S. (1994). Dopamine D1 receptor mechanisms in the cognitive performance of young adult and aged monkeys. *Psychopharmacology (Berl), 116*(2), 143-151. doi:10.1007/bf02245056

Ashburner, J. (2007). A fast diffeomorphic image registration algorithm. *Neuroimage, 38*(1), 95-113. doi:10.1016/j.neuroimage.2007.07.007

Bach, M., Fritzsche, K. H., Stieltjes, B., & Laun, F. B. (2014). Investigation of resolution effects using a specialized diffusion tensor phantom. *Magn Reson Med, 71*(3), 1108-1116. doi:10.1002/mrm.24774

Baddeley, A.D. Hitch G.J. Working memory G.A. Bower (Ed.), Recent Advances in Learning and Motivation, Vol. 8, Academic Press, New York (1974), pp. 47-89

Baddeley, A. (1992). Working Memory: The Interface between Memory and Cognition. *J Cogn Neurosci, 4*(3), 281-288. doi:10.1162/jocn.1992.4.3.281

Baddeley, A. (1998). Recent developments in working memory. *Curr Opin Neurobiol, 8*(2), 234-238. doi:10.1016/s0959-4388(98)80145-1

Baddeley, A. D. (2000). The phonological loop and the irrelevant speech effect: some comments on Neath (2000). *Psychon Bull Rev, 7*(3), 544-549. doi:10.3758/bf03214369

Baddeley, A. (2003). Working memory: looking back and looking forward. Nat Rev Neurosci, 4(10), 829-839

Bales, J. W., Wagner, A. K., Kline, A. E., & Dixon, C. E. (2009). Persistent cognitive dysfunction after traumatic brain injury: A dopamine hypothesis. *Neurosci Biobehav Rev, 33*(7), 981-1003. doi:10.1016/j.neubiorev.2009.03.011

Barbey, A. K., Koenigs, M., & Grafman, J. (2013). Dorsolateral prefrontal contributions to human working memory. *Cortex, 49*(5), 1195-1205. doi:10.1016/j.cortex.2012.05.022

Barton, A. Matthews., B., Farmer E., Belyavin, A. Revealing the basic properties of the visuospatial sketchpad: the use of complete spatial arrays. 1995. Acta Psychological 89(3), 197-216.

Basser, P. J., Mattiello, J., & LeBihan, D. (1994). MR diffusion tensor spectroscopy and imaging. *Biophys J, 66*(1), 259-267. doi:10.1016/S0006-3495(94)80775-1

Basser, P. J., & Pierpaoli, C. (1996). Microstructural and physiological features of tissues elucidated by quantitative-diffusion-tensor MRI. *J Magn Reson B, 111*(3), 209-219.

Bassett, D. S., Meyer-Lindenberg, A., Achard, S., Duke, T., & Bullmore, E. (2006). Adaptive reconfiguration of fractal small-world human brain functional networks. *Proc Natl Acad Sci U S A, 103*(51), 19518-19523. doi:10.1073/pnas.0606005103

Bassett, D. S., & Bullmore, E. (2006). Small-world brain networks. *Neuroscientist, 12*(6), 512-523.

Bassett, D. S., & Bullmore, E. T. (2009). Human brain networks in health and disease. *Curr Opin Neurol, 22*(4), 340-347.

Bassett, D. S., & Bullmore, E. T. (2017). Small-World Brain Networks Revisited. *Neuroscientist, 23*(5), 499-516. doi:10.1177/1073858416667720

Bays, P. M., & Husain, M. (2008). Dynamic shifts of limited working memory resources in human vision. *Science, 321*(5890), 851-854. doi:10.1126/science.1158023

Bazarian, J. J., Cernak, I., Noble-Haeusslein, L., Potolicchio, S., & Temkin, N. (2009). Long-term neurologic outcomes after traumatic brain injury. *J Head Trauma Rehabil, 24*(6), 439-451. doi:10.1097/HTR.0b013e3181c15600

Beckmann, C. F., DeLuca, M., Devlin, J. T., & Smith, S. M. (2005). Investigations into resting-state connectivity using independent component analysis. *Philos Trans R Soc Lond B Biol Sci, 360*(1457), 1001-1013. doi:10.1098/rstb.2005.1634

Behrens, T. E., Woolrich, M. W., Jenkinson, M., Johansen-Berg, H., Nunes, R. G., Clare, S., . . . Smith, S. M. (2003). Characterization and propagation of uncertainty in diffusion-weighted MR imaging. *Magn Reson Med, 50*(5), 1077-1088. doi:10.1002/mrm.10609

Beckmann, C. F., DeLuca, M., Devlin, J. T. & Smith, S. M. *Investigations into resting-state connectivity using independent component analysis*. *Philos. Trans. R. Soc. Lond. B Biol. Sci.* **360**, 1001–1013 (2005).

Benson, R. R., Meda, S. A., Vasudevan, S., Kou, Z., Govindarajan, K. A., Hanks, R. A., . . . Haacke, E. M. (2007). Global white matter analysis of diffusion tensor images is predictive of injury severity in traumatic brain injury. *J Neurotrauma, 24*(3), 446-459. doi:10.1089/neu.2006.0153

Bernat, J. L. (2009). Contemporary controversies in the definition of death. *Prog Brain Res, 177*, 21-31. doi:10.1016/S0079-6123(09)17703-8

Bigler, E. D. (2007). Anterior and middle cranial fossa in traumatic brain injury: relevant neuroanatomy and neuropathology in the study of neuropsychological outcome. *Neuropsychology, 21*(5), 515-531. doi:10.1037/0894-4105.21.5.515

Björklund, A., & Dunnett, S. B. (2007). Dopamine neuron systems in the brain: an update. *Trends Neurosci, 30*(5), 194-202. doi:10.1016/j.tins.2007.03.006

Bonnelle, V., Ham, T. E., Leech, R., Kinnunen, K. M., Mehta, M. A., Greenwood, R. J., & Sharp, D. J. (2012). Salience network integrity predicts default mode network function after traumatic brain injury. *Proc Natl Acad Sci U S A, 109*(12), 4690-4695. doi:10.1073/pnas.1113455109

Bressler, S. L., & Menon, V. (2010). Large-scale brain networks in cognition: emerging methods and principles. *Trends Cogn Sci, 14*(6), 277-290. doi:10.1016/j.tics.2010.04.004

Brozoski, T. J., Brown, R. M., Rosvold, H. E., & Goldman, P. S. (1979). Cognitive deficit caused by regional depletion of dopamine in prefrontal cortex of rhesus monkey. *Science, 205*(4409), 929-932. doi:10.1126/science.112679

Budde, M. D., Janes, L., Gold, E., Turtzo, L. C., & Frank, J. A. (2011). The contribution of gliosis to diffusion tensor anisotropy and tractography following traumatic brain injury: validation in the rat using Fourier analysis of stained tissue sections. *Brain, 134*(Pt 8), 2248-2260. doi:10.1093/brain/awr161

Bullmore, E. & Sporns, O. *Complex brain networks: graph theoretical analysis of structural and functional systems*. *Nat. Rev. Neurosci.* **10**, 186–198 (2009).

Buysse, D. J., Reynolds, C. F., Monk, T. H., Berman, S. R., & Kupfer, D. J. (1989). The Pittsburgh Sleep Quality Index: a new instrument for psychiatric practice and research. *Psychiatry Res, 28*(2), 193-213. doi:10.1016/0165-1781(89)90047-4

Cabeza, R., & Nyberg, L. (2000). Neural bases of learning and memory: functional neuroimaging evidence. *Curr Opin Neurol, 13*(4), 415-421. doi:10.1097/00019052-200008000-00008

Caeyenberghs, K., Leemans, A., Geurts, M., Linden, C. V., Smits-Engelsman, B. C., Sunaert, S., & Swinnen, S. P. (2011). Correlations between white matter integrity and motor function in traumatic brain injury patients. *Neurorehabil Neural Repair, 25*(6), 492-502. doi:10.1177/1545968310394870

Caeyenberghs, K., Leemans, A., Leunissen, I., Gooijers, J., Michiels, K., Sunaert, S., & Swinnen, S. P. (2014). Altered structural networks and executive deficits in traumatic brain injury patients. *Brain Struct Funct, 219*(1), 193-209. doi:10.1007/s00429-012-0494-2

Caeyenberghs, K., Metzler-Baddeley, C., Foley, S., & Jones, D. K. (2016). Dynamics of the Human Structural Connectome Underlying Working Memory Training. *J Neurosci, 36*(14), 4056-4066. doi:10.1523/JNEUROSCI.1973-15.2016

Caplan, D., Rochon, E., & Waters, G. S. (1992). Articulatory and phonological determinants of word length effects in span tasks. *Q J Exp Psychol A, 45*(2), 177-192. doi:10.1080/14640749208401323

Capon, A. Handley, S. & Dennis, I. (2003) Working memory and reasoning: An individual differences perspective, Thinking & Reasoning, 9:3, 203-244.

Cattell R.B. Culture Free Intelligence Test, Scale 1, Handbook. Institute of Personality and Abilit, Champaign, IL; 1949.

Cawley, G.C & Talbot, N. L. C. Over-fitting in model selection and subsequent selection bias in performance evaluation, Journal of Machine Learning Research, (2010) 11, 2079-2107

Charlton, R. A., Barrick, T. R., Lawes, I. N., Markus, H. S., & Morris, R. G. (2010). White matter pathways associated with working memory in normal aging. *Cortex, 46*(4), 474-489. doi:10.1016/j.cortex.2009.07.005

Chen, S. H., & Desmond, J. E. (2005). Cerebrocerebellar networks during articulatory rehearsal and verbal working memory tasks. *Neuroimage, 24*(2), 332-338. doi:10.1016/j.neuroimage.2004.08.032

Cho, H. M., Choi, B. Y., Chang, C. H., Kim, S. H., Lee, J., Chang, M. C., . . . Jang, S. H. (2012). The clinical characteristics of motor function in chronic hemiparetic stroke patients with complete corticospinal tract injury. *NeuroRehabilitation, 31*(2), 207-213. doi:10.3233/NRE-2012-0790

Christensen, B. K., Colella, B., Inness, E., Hebert, D., Monette, G., Bayley, M., & Green, R. E. (2008). Recovery of cognitive function after traumatic brain injury: a multilevel modeling analysis of Canadian outcomes. *Arch Phys Med Rehabil, 89*(12 Suppl), S3-15. doi:10.1016/j.apmr.2008.10.002

Christodoulou, C., DeLuca, J., Ricker, J. H., Madigan, N. K., Bly, B. M., Lange, G., . . . Ni, A. C. (2001). Functional magnetic resonance imaging of working memory impairment after traumatic brain injury. *J Neurol Neurosurg Psychiatry, 71*(2), 161-168. doi:10.1136/jnnp.71.2.161

Christophel, T. B., Klink, P. C., Spitzer, B., Roelfsema, P. R., & Haynes, J. D. (2017). The Distributed Nature of Working Memory. Trends Cogn Sci, 21(2), 111-124.

Cicerone, K., Levin, H., Malec, J., Stuss, D., & Whyte, J. (2006). Cognitive rehabilitation interventions for executive function: moving from bench to bedside in patients with traumatic brain injury. *J Cogn Neurosci, 18*(7), 1212-1222. doi:10.1162/jocn.2006.18.7.1212

Cicerone, K. D., Dahlberg, C., Kalmar, K., Langenbahn, D. M., Malec, J. F., Bergquist, T. F., . . . Morse, P. A. (2000). Evidence-based cognitive rehabilitation: recommendations for clinical practice. *Arch Phys Med Rehabil, 81*(12), 1596-1615. doi:10.1053/apmr.2000.19240

Cicuendez, M., Castaño-León, A., Ramos, A., Hilario, A., Gómez, P. A., & Lagares, A. (2017). [Magnetic resonance in traumatic brain injury: A comparative study of the different conventional magnetic resonance imaging sequences and their diagnostic value in diffuse axonal injury]. *Neurocirugia (Astur), 28*(6), 266-275. doi:10.1016/j.neucir.2017.06.001

Clatworthy, P. L., Lewis, S. J., Brichard, L., Hong, Y. T., Izquierdo, D., Clark, L., . . . Robbins, T. W. (2009). Dopamine release in dissociable striatal subregions predicts the different effects of oral methylphenidate on reversal learning and spatial working memory. *J Neurosci, 29*(15), 4690-4696. doi:10.1523/JNEUROSCI.3266-08.2009

Cloots, R. J., Gervaise, H. M., van Dommelen, J. A., & Geers, M. G. (2008). Biomechanics of traumatic brain injury: influences of the morphologic heterogeneities of the cerebral cortex. *Ann Biomed Eng, 36*(7), 1203-1215. doi:10.1007/s10439-008-9510-3

Cohen, J. D., Perlstein, W. M., Braver, T. S., Nystrom, L. E., Noll, D. C., Jonides, J., & Smith, E. E. (1997). Temporal dynamics of brain activation during a working memory task. *Nature, 386*(6625), 604-608. doi:10.1038/386604a0

Colantonio, A., Ratcliff, G., Chase, S., Kelsey, S., Escobar, M., & Vernich, L. (2004). Long-term outcomes after moderate to severe traumatic brain injury. *Disabil Rehabil, 26*(5), 253-261. doi:10.1080/09638280310001639722

Cole, J. H., Leech, R., Sharp, D. J., & Initiative, A. s. D. N. (2015). Prediction of brain age suggests accelerated atrophy after traumatic brain injury. *Ann Neurol, 77*(4), 571-581. doi:10.1002/ana.24367

Cole, J. H., Jolly, A., de Simoni, S., Bourke, N., Patel, M. C., Scott, G., & Sharp, D. J. (2018). Spatial patterns of progressive brain volume loss after moderate-severe traumatic brain injury. *Brain, 141*(3), 822-836. doi:10.1093/brain/awx354

Coons, E. E., & Miller, N. E. (1960). Conflict versus consolidation of memory traces to explain "retrograde amnesia" produced by ECS. *J Comp Physiol Psychol, 53*, 524-531. doi:10.1037/h0045920

Corbo, J., & Tripathi, P. (2004). Delayed presentation of diffuse axonal injury: a case report. *Ann Emerg Med, 44*(1), 57-60. doi:10.1016/j.annemergmed.2003.11.010

Corkin, S., Rosen, T. J., Sullivan, E. V., & Clegg, R. A. (1989). Penetrating head injury in young adulthood exacerbates cognitive decline in later years. *J Neurosci, 9*(11), 3876-3883.

D'Esposito, M., & Postle, B. R. (2015). The cognitive neuroscience of working memory. *Annu Rev Psychol, 66*, 115-142. doi:10.1146/annurev-psych-010814-015031

D'Esposito, M., Postle, B. R., Ballard., D & Lease., J. (1999). Maintenance versus Manipulation of Information Held in Working Memory: An Event-Related fMRI Study. Brain and Cognition, 41, 66-86

Desikan, R.S., Segonne, F., Fischl, B., Quinn, B.T., Dickerson, B.C., Blacker, D., Buckner, R.L., Dale, A.M., Maguire, P., Hyman, B.T., Albert, M.S., & Killiany, R.J. An automated labelling system for subdividing the human cerebral cortex on MRI scans into gyral based regions of interest. Neuroimage, 31(3), 968-980.

DeSalvo, M.N., Douw, L., Tanaka, N., Reinsberger, C. and Stufflebeam, S.M. (2014). Altered structural connectome in temporal lobe epilepsy. Radiology, 270:3, 842-848.

Dall'Acqua, P., Johannes, S., Mica, L., Simmen, H. P., Glaab, R., Fandino, J., . . . Hänggi, J. (2017). Functional and Structural Network Recovery after Mild Traumatic Brain Injury: A 1-Year Longitudinal Study. *Front Hum Neurosci, 11*, 280. doi:10.3389/fnhum.2017.00280

Daws, R. E., & Hampshire, A. (2017). The Negative Relationship between Reasoning and Religiosity Is Underpinned by a Bias for Intuitive Responses Specifically When Intuition and Logic Are in Conflict. *Front Psychol, 8*, 2191. doi:10.3389/fpsyg.2017.02191

De Simoni, S., Jenkins, P. O., Bourke, N. J., Fleminger, J. J., Hellyer, P. J., Jolly, A. E., . . . Sharp, D. J. (2018). Altered caudate connectivity is associated with executive dysfunction after traumatic brain injury. *Brain, 141*(1), 148-164. doi:10.1093/brain/awx309

De Simoni, S., Grover, P. J., Jenkins, P. O., Honeyfield, L., Quest, R. A., Ross, E., Sharp, D. J. (2016). Disconnection between the default mode network and medial temporal lobes in post-traumatic amnesia. Brain, 139(Pt 12), 3137-3150.

Delis, D. C., Kramer, J. H., Kaplan, E., & Holdnack, J. (2004). Reliability and validity of the Delis-Kaplan Executive Function System: an update. *J Int Neuropsychol Soc, 10*(2), 301-303. doi:10.1017/S1355617704102191

Delis, D.C., Kaplan, E., and Kramer, J.H. (2001). Delis-Kaplan executive function system: technical manual. San Antonio, TX: Harcourt Assessment Company.

Della Sala, S., Gray, C., Baddeley, A., Allamano, N., & Wilson, L. (1999). Pattern span: a tool for unwelding visuo-spatial memory. *Neuropsychologia, 37*(10), 1189-1199. doi:10.1016/s0028-3932(98)00159-6

Desikan, R. S., Ségonne, F., Fischl, B., Quinn, B. T., Dickerson, B. C., Blacker, D., . . . Killiany, R. J. (2006). An automated labeling system for subdividing the human cerebral cortex on MRI scans into gyral based regions of interest. *Neuroimage, 31*(3), 968-980. doi:10.1016/j.neuroimage.2006.01.021

Ding, K., Marquez de la Plata, C., Wang, J. Y., Mumphrey, M., Moore, C., Harper, C., . . . Diaz-Arrastia, R. (2008). Cerebral atrophy after traumatic white matter injury: correlation with acute neuroimaging and outcome. *J Neurotrauma, 25*(12), 1433-1440. doi:10.1089/neu.2008.0683

Dinkel, J., Drier, A., Khalilzadeh, O., Perlbarg, V., Czernecki, V., Gupta, R., . . . Consortium, f. N. N. I. f. C. E. a. R. (2014). Long-term white matter changes after severe traumatic brain injury: a 5-year prospective cohort. *AJNR Am J Neuroradiol, 35*(1), 23-29. doi:10.3174/ajnr.A3616

Donnemiller, E., Brenneis, C., Wissel, J., Scherfler, C., Poewe, W., Riccabona, G., & Wenning, G. K. (2000). Impaired dopaminergic neurotransmission in patients with traumatic brain injury: a SPECT study using 123I-beta-CIT and 123I-IBZM. *Eur J Nucl Med, 27*(9), 1410-1414. doi:10.1007/s002590000308

Draper, K., & Ponsford, J. (2008). Cognitive functioning ten years following traumatic brain injury and rehabilitation. Neuropsychology, 22(5), 618-625.

Duncan, J. (2013). The structure of cognition: attentional episodes in mind and brain. *Neuron, 80*(1), 35-50. doi:10.1016/j.neuron.2013.09.015

Duncan, J., Parr, A., Woolgar, A., Thompson, R., Bright, P., Cox, S., . . . Nimmo-Smith, I. (2008a). Goal neglect and Spearman's g: competing parts of a complex task. *J Exp Psychol Gen, 137*(1), 131-148. doi:10.1037/0096-3445.137.1.131

Duncan, J., Parr, A., Woolgar, A., Thompson, R., Bright, P., Cox, S., . . . Nimmo-Smith, I. (2008b). Goal neglect and Spearman's g: competing parts of a complex task. *J Exp Psychol Gen, 137*(1), 131-148. doi:10.1037/0096-3445.137.1.131

Edlow, B. L., Copen, W. A., Izzy, S., Bakhadirov, K., van der Kouwe, A., Glenn, M. B., . . . Wu, O. (2016). Diffusion tensor imaging in acute-to-subacute traumatic brain injury: a longitudinal analysis. *BMC Neurol, 16*, 2. doi:10.1186/s12883-015-0525-8

Evans, J. S. (2003a). In two minds: dual-process accounts of reasoning. Trends Cogn Sci, 7(10), 454-459.

Fagerholm, E. D., Hellyer, P. J., Scott, G., Leech, R., & Sharp, D. J. (2015). Disconnection of network hubs and cognitive impairment after traumatic brain injury. *Brain, 138*(Pt 6), 1696-1709. doi:10.1093/brain/awv075

Fallon, S. J., Zokaei, N., Norbury, A., Manohar, S. G., & Husain, M. (2017). Dopamine Alters the Fidelity of Working Memory Representations according to Attentional Demands. *J Cogn Neurosci, 29*(4), 728-738. doi:10.1162/jocn_a_01073

Fann, J. R., Katon, W. J., Uomoto, J. M., & Esselman, P. C. (1995). Psychiatric disorders and functional disability in outpatients with traumatic brain injuries. *Am J Psychiatry, 152*(10), 1493-1499. doi:10.1176/ajp.152.10.1493

Fleminger, S., Oliver, D. L., Lovestone, S., Rabe-Hesketh, S., & Giora, A. (2003). Head injury as a risk factor for Alzheimer's disease: the evidence 10 years on; a partial replication. *J Neurol Neurosurg Psychiatry, 74*(7), 857-862. doi:10.1136/jnnp.74.7.857

Fletcher, P. C., & Henson, R. N. (2001). Frontal lobes and human memory: insights from functional neuroimaging. *Brain, 124*(Pt 5), 849-881. doi:10.1093/brain/124.5.849

Gaffan, D. (2005). Neuroscience. Widespread cortical networks underlie memory and attention. *Science, 309*(5744), 2172-2173. doi:10.1126/science.1119445

Gallagher, M. J., Ross, M. A., Raff, G. L., Goldstein, J. A., O'Neill, W. W., & O'Neil, B. (2007). The diagnostic accuracy of 64-slice computed tomography coronary angiography compared with stress nuclear imaging in emergency department low-risk chest pain patients. *Ann Emerg Med, 49*(2), 125-136. doi:10.1016/j.annemergmed.2006.06.043

Gennarelli, T. A. (1993). Mechanisms of brain injury. *J Emerg Med, 11 Suppl 1*, 5-11.

Ghajari, M., Hellyer, P. J., & Sharp, D. J. (2017). Computational modelling of traumatic brain injury predicts the location of chronic traumatic encephalopathy pathology. *Brain, 140*(2), 333-343. doi:10.1093/brain/aww317

Goel, V., Navarrete, G., Noveck, I. A., & Prado, J. (2016). Editorial: The Reasoning Brain: The Interplay between Cognitive Neuroscience and Theories of Reasoning. Front Hum Neurosci, 10, 673

Gorgoraptis, N., Li, L. M., Whittington, A., Zimmerman, K. A., Maclean, L. M., McLeod, C., . . . Sharp, D. J. (2019). In vivo detection of cerebral tau pathology in long-term survivors of traumatic brain injury. *Sci Transl Med, 11*(508). doi:10.1126/scitranslmed.aaw1993

Gorgoraptis, N., Zaw-Linn, J., Feeney, C., Tenorio-Jimenez, C., Niemi, M., Malik, A., . . . Sharp, D. J. (2019). Cognitive impairment and health-related quality of life following traumatic brain injury. *NeuroRehabilitation, 44*(3), 321-331. doi:10.3233/NRE-182618

Göttlich, M., Münte, T. F., Heldmann, M., Kasten, M., Hagenah, J., & Krämer, U. M. (2013). Altered resting state brain networks in Parkinson's disease. *PLoS One, 8*(10), e77336. doi:10.1371/journal.pone.0077336

Gould S.J. The Mismeasure of Man. Norton, New York; 1981

Graham, N. S. N & Sharp, D. J. (2019). Understanding neurodegeneration after traumatic brain injury: from mechanisms to clinical trials in dementia. J Neurol Neurosurg Psychiatry, 90(11), 1221-1233.

Grossman, E. J., Jensen, J. H., Babb, J. S., Chen, Q., Tabesh, A., Fieremans, E., . . . Grossman, R. I. (2013). Cognitive impairment in mild traumatic brain injury: a longitudinal diffusional kurtosis and perfusion imaging study. *AJNR Am J Neuroradiol, 34*(5), 951-957, S951-953. doi:10.3174/ajnr.A3358

Gurdjian, E. S. (1975). Re-evaluation of the biomechanics of blunt impact injury of the head. *Surg Gynecol Obstet, 140*(6), 845-850.

Haier, R.J., Karama, S., Colom, R., Jung, R., & Johnson, W. (2014). A comment on “Fractionating Human Intelligence” and the peer review process. Intelligence, 46, 323-332.

Hampshire, A., Highfield, R. R., Parkin, B. L., & Owen, A. M. (2012). Fractionating human intelligence. *Neuron, 76*(6), 1225-1237. doi:10.1016/j.neuron.2012.06.022

Hampshire, A., Sandrone, S., & Hellyer, P.J. (2019). A large-scale, cross-sectional investigation into the efficacy of brain training. Front. Hum. Neurosci, 13, 221.

Hampshire, A., Hellyer, P. J., Parkin, B., Hiebert, N., MacDonald, P., Owen, A. M., . . . Rowe, J. (2016). Network mechanisms of intentional learning. Neuroimage, 127, 123-134.

Hampshire, A., & Sharp, D. (2015). Inferior PFC Subregions Have Broad Cognitive Roles. *Trends Cogn Sci, 19*(12), 712-713.

Hashim, E., Caverzasi, E., Papinutto, N., Lewis, C. E., Jing, R., Charles, O., . . . Cusimano, M. D. (2017). Investigating Microstructural Abnormalities and Neurocognition in Sub-Acute and Chronic Traumatic Brain Injury Patients with Normal-Appearing White Matter: A Preliminary Diffusion Tensor Imaging Study. *Front Neurol, 8*, 97. doi:10.3389/fneur.2017.00097

Hayes, J. P., Bigler, E. D., & Verfaellie, M. (2016). Traumatic Brain Injury as a Disorder of Brain Connectivity. *J Int Neuropsychol Soc, 22*(2), 120-137. doi:10.1017/S1355617715000740

Hellyer, P. J., Leech, R., Ham, T. E., Bonnelle, V., & Sharp, D. J. (2013). Individual prediction of white matter injury following traumatic brain injury. *Ann Neurol, 73*(4), 489-499. doi:10.1002/ana.23824

Hellstrøm, T., Westlye, L. T., Kaufmann, T., Trung Doan, N., Søberg, H. L., Sigurdardottir, S., . . . Andelic, N. (2017). White matter microstructure is associated with functional, cognitive and emotional symptoms 12 months after mild traumatic brain injury. *Sci Rep, 7*(1), 13795. doi:10.1038/s41598-017-13628-1

Hill, C. S., Coleman, M. P., & Menon, D. K. (2016). Traumatic Axonal Injury: Mechanisms and Translational Opportunities. *Trends Neurosci, 39*(5), 311-324. doi:10.1016/j.tins.2016.03.002

Hillary, F. G., & Grafman, J. H. (2017). Injured Brains and Adaptive Networks: The Benefits and Costs of Hyperconnectivity. *Trends Cogn Sci, 21*(5), 385-401. doi:10.1016/j.tics.2017.03.003

Hillary, F. G., Medaglia, J. D., Gates, K. M., Molenaar, P. C., & Good, D. C. (2014). Examining network dynamics after traumatic brain injury using the extended unified SEM approach. *Brain Imaging Behav, 8*(3), 435-445. doi:10.1007/s11682-012-9205-0

Humphreys, I., Wood, R. L., Phillips, C. J., & Macey, S. (2013). The costs of traumatic brain injury: a literature review. *Clinicoecon Outcomes Res, 5*, 281-287. doi:10.2147/CEOR.S44625

Hyder, A. A., Wunderlich, C. A., Puvanachandra, P., Gururaj, G., & Kobusingye, O. C. (2007). The impact of traumatic brain injuries: a global perspective. *NeuroRehabilitation, 22*(5), 341-353.

Imms, P., Clemente, A., Cook, M., D'Souza, W., Wilson, P. H., Jones, D. K., & Caeyenberghs, K. (2019). The structural connectome in traumatic brain injury:

A meta-analysis of graph metrics. *Neurosci Biobehav Rev, 99*, 128-137. doi:10.1016/j.neubiorev.2019.01.002

Irimia, A., Wang, B., Aylward, S. R., Prastawa, M. W., Pace, D. F., Gerig, G., . . . Van Horn, J. D. (2012). Neuroimaging of structural pathology and connectomics in traumatic brain injury: Toward personalized outcome prediction. *Neuroimage Clin, 1*(1), 1-17. doi:10.1016/j.nicl.2012.08.002

Jacobs, H. E. (1988). The Los Angeles Head Injury Survey: procedures and initial findings. *Arch Phys Med Rehabil, 69*(6), 425-431.

Jenkins, P. O., De Simoni, S., Bourke, N. J., Fleminger, J., Scott, G., Towey, D. J., . . . Sharp, D. J. (2018). Dopaminergic abnormalities following traumatic brain injury. *Brain, 141*(3), 797-810. doi:10.1093/brain/awx357

Jenkins, P. O., De Simoni, S., Bourke, N. J., Fleminger, J., Scott, G., Towey, D. J., . . . Sharp, D. J. (2019). Stratifying drug treatment of cognitive impairments after traumatic brain injury using neuroimaging. *Brain, 142*(8), 2367-2379. doi:10.1093/brain/awz149

Jenkins, P. O., Mehta, M. A., & Sharp, D. J. (2016). Catecholamines and cognition after traumatic brain injury. *Brain, 139*(Pt 9), 2345-2371. doi:10.1093/brain/aww128

Jenkinson, M., Bannister, P., Brady, M., & Smith, S. (2002). Improved optimization for the robust and accurate linear registration and motion correction of brain images. *Neuroimage, 17*(2), 825-841. doi:10.1016/s1053-8119(02)91132-8

Jenkinson, M., & Smith, S. (2001). A global optimisation method for robust affine registration of brain images. *Med Image Anal, 5*(2), 143-156. doi:10.1016/s1361-8415(01)00036-6

Jennett, B., Snoek, J., Bond, M. R., & Brooks, N. (1981). Disability after severe head injury: observations on the use of the Glasgow Outcome Scale. *J Neurol Neurosurg Psychiatry, 44*(4), 285-293. doi:10.1136/jnnp.44.4.285

Jilka, S. R., Scott, G., Ham, T., Pickering, A., Bonnelle, V., Braga, R. M., . . . Sharp, D. J. (2014). Damage to the Salience Network and interactions with the Default Mode Network. *J Neurosci, 34*(33), 10798-10807. doi:10.1523/JNEUROSCI.0518-14.2014

Jolly, A. E., Raymont, V., Cole, J. H., Whittington, A., Scott, G., De Simoni, S., . . . Sharp, D. J. (2019). Dopamine D2/D3 receptor abnormalities after traumatic brain injury and their relationship to post-traumatic depression. *Neuroimage Clin, 24*, 101950. doi:10.1016/j.nicl.2019.101950

Jolly A.E., Scott G., Sharp D., Hampshire A. Distinct patterns of structural damage underlie working memory and reasoning deficits after traumatic brain injury, *Brain*, Volume 143, Issue 4, April 2020, Pages 1158–1176.

Kane, M. J., & Engle, R. W. (2002). The role of prefrontal cortex in working-memory capacity, executive attention, and general fluid intelligence: an individual-differences perspective. *Psychon Bull Rev, 9*(4), 637-671. doi:10.3758/bf03196323

Katkov, M., Romani, S., & Tsodyks, M. (2014). Word length effect in free recall of randomly assembled word lists. *Front Comput Neurosci, 8*, 129. doi:10.3389/fncom.2014.00129

Khemlani, S., & Johnson-Laird, P. N. (2012). Theories of the syllogism: A meta-analysis. Psychol Bull, 138(3), 427-457.

Kim, Y. H. *et al*. *Plasticity of the attentional network after brain injury and cognitive rehabilitation*. *Neurorehabil. Neural Repair* **23**, 468–477 (2009).

Kinnunen, K. M., Greenwood, R., Powell, J. H., Leech, R., Hawkins, P. C., Bonnelle, V., . . . Sharp, D. J. (2011). White matter damage and cognitive impairment after traumatic brain injury. *Brain, 134*(Pt 2), 449-463. doi:10.1093/brain/awq347

Klados, M. A., Kanatsouli, K., Antoniou, I., Babiloni, F., Tsirka, V., Bamidis, P. D., & Micheloyannis, S. (2013). A Graph theoretical approach to study the organization of the cortical networks during different mathematical tasks. *PLoS One, 8*(8), e71800. doi:10.1371/journal.pone.0071800

Kochunov, P., Williamson, D.E., Lancaster, J., Fox, P, Cornell, J., Blangero, J., & Glahn, D.C. Fractional anisotropy of water diffusion in cerebral white matter across the lifespan. Neurobiology of Ageing., 33(1): 9-20. (2012).

Krueger, F., Pardini, M., Huey, E. D., Raymont, V., Solomon, J., Lipsky, R. H., . . . Grafman, J. (2011). The role of the Met66 brain-derived neurotrophic factor allele in the recovery of executive functioning after combat-related traumatic brain injury. *J Neurosci, 31*(2), 598-606. doi:10.1523/JNEUROSCI.1399-10.2011

Kuceyeski, A., Jamison, K., Owen, J., Raj, A. and Mukherjee, P. (2019) Longitudinal increases in structural connectome segregation and functional connectome integration are associated with better recovery after mild TBI. Human Brain Mapping. 40(15): 4441-4456.

Kumar, R., Gupta, R. K., Husain, M., Chaudhry, C., Srivastava, A., Saksena, S., & Rathore, R. K. (2009). Comparative evaluation of corpus callosum DTI metrics in acute mild and moderate traumatic brain injury: its correlation with neuropsychometric tests. *Brain Inj, 23*(7), 675-685. doi:10.1080/02699050903014915

Kyllonen, P.C and Christal, R.E. Reasoning ability is (little more than) working memory capacity?!,Intelligence, Volume 14, Issue 4,1990, Pages 389-433,ISSN 0160-2896.

Laitinen, T., Sierra, A., Bolkvadze, T., Pitkänen, A., & Gröhn, O. (2015). Diffusion tensor imaging detects chronic microstructural changes in white and gray matter after traumatic brain injury in rat. *Frontiers in neuroscience*, *9*, 128. doi:10.3389/fnins.2015.00128

Lara, A. H., & Wallis, J. D. (2015). The Role of Prefrontal Cortex in Working Memory: A Mini Review. *Front Syst Neurosci, 9*, 173. doi:10.3389/fnsys.2015.00173

Latora, V., & Marchiori, M. (2001). Efficient behavior of small-world networks. *Phys Rev Lett, 87*(19), 198701. doi:10.1103/PhysRevLett.87.198701

Lawrence, T., Helmy, A., Bouamra, O., Woodford, M., Lecky, F., & Hutchinson, P. J. (2016). Traumatic brain injury in England and Wales: prospective audit of epidemiology, complications and standardised mortality. *BMJ Open, 6*(11), e012197. doi:10.1136/bmjopen-2016-012197

Leclercq, M., Couillet, J., Azouvi, P., Marlier, N., Martin, Y., Strypstein, E., & Rousseaux, M. (2000). Dual task performance after severe diffuse traumatic brain injury or vascular prefrontal damage. *J Clin Exp Neuropsychol, 22*(3), 339-350. doi:10.1076/1380-3395(200006)22:3;1-V;FT339

Lee, S. Y., Kim, S. S., Kim, C. H., Park, S. W., Park, J. H., & Yeo, M. (2012). Prediction of outcome after traumatic brain injury using clinical and neuroimaging variables. *J Clin Neurol, 8*(3), 224-229. doi:10.3988/jcn.2012.8.3.224

Leergaard, T. B., White, N. S., de Crespigny, A., Bolstad, I., D'Arceuil, H., Bjaalie, J. G., & Dale, A. M. (2010). Quantitative histological validation of diffusion MRI fiber orientation distributions in the rat brain. *PLoS One, 5*(1), e8595. doi:10.1371/journal.pone.0008595

Lewis-Peacock, J. A., & Postle, B. R. (2008). Temporary activation of long-term memory supports working memory. *J Neurosci, 28*(35), 8765-8771. doi:10.1523/JNEUROSCI.1953-08.2008

Li, L. M., Violante, I. R., Zimmerman, K., Leech, R., Hampshire, A., Patel, M., . . . Sharp, D. J. (2019). Traumatic axonal injury influences the cognitive effect of non-invasive brain stimulation. *Brain, 142*(10), 3280-3293. doi:10.1093/brain/awz252

Li, J., Li, X. Y., Feng, D. F., & Gu, L. (2011). Quantitative evaluation of microscopic injury with diffusion tensor imaging in a rat model of diffuse axonal injury. *Eur J Neurosci, 33*(5), 933-945. doi:10.1111/j.1460-9568.2010.07573.x

Li, L. M., Violante, I. R., Leech, R., Ross, E., Hampshire, A., Opitz, A., . . . Sharp, D. J. (2019). Brain state and polarity dependent modulation of brain networks by transcranial direct current stimulation. *Hum Brain Mapp, 40*(3), 904-915.

Lo, C., Shifteh, K., Gold, T., Bello, J. A., & Lipton, M. L. (2009). Diffusion tensor imaging abnormalities in patients with mild traumatic brain injury and

neurocognitive impairment. *J Comput Assist Tomogr, 33*(2), 293-297. doi:10.1097/RCT.0b013e31817579d1

Lorenz, R., Violante, I. R., Monti, R. P., Montana, G., Hampshire, A., & Leech, R. (2018). Dissociating frontoparietal brain networks with neuroadaptive Bayesian optimization. *Nat Commun, 9*(1), 1227.

Ma, W. J., Husain, M., & Bays, P. M. (2014). Changing concepts of working memory. *Nat Neurosci, 17*(3), 347-356. doi:10.1038/nn.3655

Makris N, Goldstein JM, Kennedy D, Hodge SM, Caviness VS, Faraone SV, Tsuang MT, Seidman LJ. Decreased volume of left and total anterior insular lobule in schizophrenia. Schizophr Res. 2006 Apr;83(2-3):155-71

Maas, A. I., Murray, G. D., Roozenbeek, B., Lingsma, H. F., Butcher, I., McHugh, G. S., . . . Group, I. M. o. P. A. o. C. T. i. T. B. I. I. S. (2013). Advancing care for traumatic brain injury: findings from the IMPACT studies and perspectives on future research. *Lancet Neurol, 12*(12), 1200-1210. doi:10.1016/S1474-4422(13)70234-5

Mac Donald, C. L., Dikranian, K., Bayly, P., Holtzman, D., & Brody, D. (2007). Diffusion tensor imaging reliably detects experimental traumatic axonal injury and indicates approximate time of injury. *J Neurosci, 27*(44), 11869-11876. doi:10.1523/JNEUROSCI.3647-07.2007

Mac Donald, C. L., Dikranian, K., Song, S. K., Bayly, P. V., Holtzman, D. M., & Brody, D. L. (2007). Detection of traumatic axonal injury with diffusion tensor imaging in a mouse model of traumatic brain injury. *Exp Neurol, 205*(1), 116-131. doi:10.1016/j.expneurol.2007.01.035

Mac Donald, C. L., Johnson, A. M., Cooper, D., Nelson, E. C., Werner, N. J., Shimony, J. S., . . . Brody, D. L. (2011). Detection of blast-related traumatic brain injury in U.S. military personnel. *N Engl J Med, 364*(22), 2091-2100. doi:10.1056/NEJMoa1008069

Magnussen, S. (2000). Low-level memory processes in vision. *Trends Neurosci, 23*(6), 247-251. doi:10.1016/s0166-2236(00)01569-1

Malec, J. F., Brown, A. W., Leibson, C. L., Flaada, J. T., Mandrekar, J. N., Diehl, N. N., & Perkins, P. K. (2007). The mayo classification system for traumatic brain injury severity. *J Neurotrauma, 24*(9), 1417-1424. doi:10.1089/neu.2006.0245

Manktelow, A. E., Menon, D. K., Sahakian, B. J., & Stamatakis, E. A. (2017). Working Memory after Traumatic Brain Injury: The Neural Basis of Improved Performance with Methylphenidate. *Front Behav Neurosci, 11*, 58. doi:10.3389/fnbeh.2017.00058

Markovits, H., Doyon, C. & Simoneau, M. (2002). Individual differences in working memory and conditional reasoning with concrete and abstract content, Thinking & Reasoning, 8:2, 97-107.

Marshall L.F.Marshall S.B.Klauber M.R.et al.1991A new classification of head injury based on computerized tomography**J. Neurosurg.**75S14S20.Marshall, L.F., Marshall, S.B., Klauber, M.R., et al. (1991). A new classification of head injury based on computerized tomography. J. Neurosurg. 75, S14–S20.

Matthews, P. M., & Hampshire, A. (2016). Clinical Concepts Emerging from fMRI Functional Connectomics. *Neuron, 91*(3), 511-528.

McAllister, T. W. *et al*. *Brain activation during working memory 1 month after mild traumatic brain injury: a functional MRI study*. *Neurology* **53**, 1300–1308 (1999).

McAllister, T. W., Flashman, L. A., Sparling, M. B., & Saykin, A. J. (2004). Working memory deficits after traumatic brain injury: catecholaminergic mechanisms and prospects for treatment -- a review. *Brain Inj, 18*(4), 331-350. doi:10.1080/02699050310001617370

McDowell, S., Whyte, J., & D'Esposito, M. (1997a). Working memory impairments in traumatic brain injury: evidence from a dual-task paradigm. *Neuropsychologia, 35*(10), 1341-1353. doi:10.1016/s0028-3932(97)00082-1

McDowell, S., Whyte, J., & D'Esposito, M. (1997b). Working memory impairments in traumatic brain injury: evidence from a dual-task paradigm. *Neuropsychologia, 35*(10), 1341-1353. doi:10.1016/s0028-3932(97)00082-1

Mckee, A. C., & Daneshvar, D. H. (2015). The neuropathology of traumatic brain injury. *Handb Clin Neurol, 127*, 45-66. doi:10.1016/B978-0-444-52892-6.00004-0

McMillan, T. M., & Glucksman, E. E. (1987). The neuropsychology of moderate head injury. *J Neurol Neurosurg Psychiatry, 50*(4), 393-397. doi:10.1136/jnnp.50.4.393

McDowell, S., Whyte, J., & D'Esposito, M. (1997a). Working memory impairments in traumatic brain injury: evidence from a dual-task paradigm. *Neuropsychologia, 35*(10), 1341-1353. doi:10.1016/s0028-3932(97)00082-1

McDowell, S., Whyte, J., & D'Esposito, M. (1997b). Working memory impairments in traumatic brain injury: evidence from a dual-task paradigm. *Neuropsychologia, 35*(10), 1341-1353. doi:10.1016/s0028-3932(97)00082-1

Mehta, M. A., & Riedel, W. J. (2006). Dopaminergic enhancement of cognitive function. *Curr Pharm Des, 12*(20), 2487-2500. doi:10.2174/138161206777698891

Menon, D. K., Schwab, K., Wright, D. W., Maas, A. I., & Health, (2010). Position statement: definition of traumatic brain injury. *Arch Phys Med Rehabil, 91*(11), 1637-1640. doi:10.1016/j.apmr.2010.05.017

Menon, D. K., & Zahed, C. (2009). Prediction of outcome in severe traumatic brain injury. *Curr Opin Crit Care, 15*(5), 437-441. doi:10.1097/MCC.0b013e3283307a26

Meythaler, J. M., Peduzzi, J. D., Eleftheriou, E., & Novack, T. A. (2001). Current concepts: diffuse axonal injury-associated traumatic brain injury. *Arch Phys Med Rehabil, 82*(10), 1461-1471. doi:10.1053/apmr.2001.25137

Mitra, J., Shen, K. K., Ghose, S., Bourgeat, P., Fripp, J., Salvado, O., . . . Rose, S. (2016). Statistical machine learning to identify traumatic brain injury (TBI) from structural disconnections of white matter networks. *Neuroimage, 129*, 247-259. doi:10.1016/j.neuroimage.2016.01.056

Mollayeva, T., Mollayeva, S., Pacheco, N., D'Souza, A., & Colantonio, A. (2019). The course and prognostic factors of cognitive outcomes after traumatic brain injury: A systematic review and meta-analysis. *Neurosci Biobehav Rev, 99*, 198-250. doi:10.1016/j.neubiorev.2019.01.011

Mori, S., & Zhang, J. (2006). Principles of diffusion tensor imaging and its applications to basic neuroscience research. *Neuron, 51*(5), 527-539. doi:10.1016/j.neuron.2006.08.012

Mori, S., Oishi, K., Jiang, H., Jiang, L., Li, X., Akhter, K., . . . Mazziotta, J. (2008). Stereotaxic white matter atlas based on diffusion tensor imaging in an ICBM template. *Neuroimage, 40*(2), 570-582. doi:10.1016/j.neuroimage.2007.12.035

Newcombe, V., Chatfield, D., Outtrim, J., Vowler, S., Manktelow, A., Cross, J., . . . Menon, D. (2011). Mapping traumatic axonal injury using diffusion tensor imaging: correlations with functional outcome. *PLoS One, 6*(5), e19214. doi:10.1371/journal.pone.0019214

Newsome, M. R., Durgerian, S., Mourany, L., Scheibel, R. S., Lowe, M. J., Beall, E. B., . . . Rao, S. M. (2015). Disruption of caudate working memory activation in chronic blast-related traumatic brain injury. *Neuroimage Clin, 8*, 543-553. doi:10.1016/j.nicl.2015.04.024

Oberauer, K. (2001). Removing irrelevant information from working memory: a cognitive aging study with the modified Sternberg task. *J Exp Psychol Learn Mem Cogn, 27*(4), 948-957.

Oberauer, K. (2002). Access to information in working memory: exploring the focus of attention. *J Exp Psychol Learn Mem Cogn, 28*(3), 411-421.

Oberauer, K. (2005). Control of the contents of working memory--a comparison of two paradigms and two age groups. *J Exp Psychol Learn Mem Cogn, 31*(4), 714-728. doi:10.1037/0278-7393.31.4.714

Oishi, K., Zilles, K., Amunts, K., Faria, A., Jiang, H., Li, X., . . . Mori, S. (2008). Human brain white matter atlas: identification and assignment of common anatomical structures in superficial white matter. *Neuroimage, 43*(3), 447-457. doi:10.1016/j.neuroimage.2008.07.009

Onnela, J. P., Saramäki, J., Kertész, J., & Kaski, K. (2005). Intensity and coherence of motifs in weighted complex networks. *Phys Rev E Stat Nonlin Soft Matter Phys, 71*(6 Pt 2), 065103. doi:10.1103/PhysRevE.71.065103

Osaka, N., Osaka, M., Kondo, H., Morishita, M., Fukuyama, H., & Shibasaki, H. (2004). The neural basis of executive function in working memory: an fMRI study based on individual differences. *Neuroimage, 21*(2), 623-631. doi:10.1016/j.neuroimage.2003.09.069

Ott, T., & Nieder, A. (2019). Dopamine and Cognitive Control in Prefrontal Cortex. *Trends Cogn Sci, 23*(3), 213-234. doi:10.1016/j.tics.2018.12.006

Owen, A. M., Doyon, J., Petrides, M., & Evans, A. C. (1996). Planning and spatial working memory: a positron emission tomography study in humans. *Eur J Neurosci, 8*(2), 353-364. doi:10.1111/j.1460-9568.1996.tb01219.x

Owen, A. M., Herrod, N. J., Menon, D. K., Clark, J. C., Downey, S. P., Carpenter, T. A., . . . Pickard, J. D. (1999). Redefining the functional organization of working memory processes within human lateral prefrontal cortex. *Eur J Neurosci, 11*(2), 567-574. doi:10.1046/j.1460-9568.1999.00449.x

Owens, J. A., Spitz, G., Ponsford, J. L., Dymowski, A. R., Ferris, N., & Willmott, C. (2017). White matter integrity of the medial forebrain bundle and attention and working memory deficits following traumatic brain injury. *Brain Behav, 7*(2), e00608. doi:10.1002/brb3.608

Palacios, E. M., Sala-Llonch, R., Junque, C., Roig, T., Tormos, J. M., Bargallo, N., & Vendrell, P. (2012). White matter integrity related to functional working memory networks in traumatic brain injury. *Neurology, 78*(12), 852-860. doi:10.1212/WNL.0b013e31824c465a

Palacios, E. M., Fernandez-Espejo, D., Junque, C., Sanchez-Carrion, R., Roig, T., Tormos, J. M., Vendrell, P. (2011). Diffusion tensor imaging differences relate to memory deficits in diffuse traumatic brain injury. BMC Neurol, 11, 24.

Pandit, A. S., Expert, P., Lambiotte, R., Bonnelle, V., Leech, R., Turkheimer, F. E., & Sharp, D. J. (2013). Traumatic brain injury impairs small-world topology. *Neurology, 80*(20), 1826-1833. doi:10.1212/WNL.0b013e3182929f38

Parizel, P. M., Ozsarlak, Van Goethem, J. W., van den Hauwe, L., Dillen, C., Verlooy, J., . . . De Schepper, A. M. (1998). Imaging findings in diffuse axonal injury after closed head trauma. *Eur Radiol, 8*(6), 960-965.

Paulesu, E., Frith, C. D., & Frackowiak, R. S. (1993). The neural correlates of the verbal component of working memory. *Nature, 362*(6418), 342-345. doi:10.1038/362342a0

Peeters, W., van den Brande, R., Polinder, S., Brazinova, A., Steyerberg, E. W., Lingsma, H. F., & Maas, A. I. (2015). Epidemiology of traumatic brain injury in Europe. *Acta Neurochir (Wien), 157*(10), 1683-1696. doi:10.1007/s00701-015-2512-7

Petrides, M. (1995). Impairments on nonspatial self-ordered and externally ordered working memory tasks after lesions of the mid-dorsal part of the lateral frontal cortex in the monkey. *J Neurosci, 15*(1 Pt 1), 359-375.

Petrides, M., Alivisatos, B., Meyer, E., & Evans, A. C. (1993). Functional activation of the human frontal cortex during the performance of verbal working memory tasks. *Proc Natl Acad Sci U S A, 90*(3), 878-882. doi:10.1073/pnas.90.3.878

Petrides, M., & Milner, B. (1982). Deficits on subject-ordered tasks after frontal- and temporal-lobe lesions in man. *Neuropsychologia, 20*(3), 249-262. doi:10.1016/0028-3932(82)90100-2

Petrides, M. 1989. Frontal lobes and memory. In F. Boller & J. Grafman (Eds.), *Handbook of neuropsychology* (Vol. 3, pp. 75–90). New York: Elsevier.

Petrides, M. (1994). Frontal lobes and behaviour. *Curr Opin Neurobiol, 4*(2), 207-211.

Pfefferbaum, A., Sullivan, E. V., Hedehus, M., Lim, K. O., Adalsteinsson, E., & Moseley, M. (2000). Age-related decline in brain white matter anisotropy measured with spatially corrected echo-planar diffusion tensor imaging. *Magn Reson Med, 44*(2), 259-268. doi:10.1002/1522-2594(200008)44:2

Ponsford, J. L., Downing, M. G., Olver, J., Ponsford, M., Acher, R., Carty, M., & Spitz, G. (2014). Longitudinal follow-up of patients with traumatic brain injury: outcome at two, five, and ten years post-injury. J Neurotrauma, 31(1), 64-77.

Postle, B. R., Idzikowski, C., Sala, S. D., Logie, R. H., & Baddeley, A. D. (2006). The selective disruption of spatial working memory by eye movements. *Q J Exp Psychol (Hove), 59*(1), 100-120. doi:10.1080/17470210500151410

Rabinowitz, A. R., & Levin, H. S. (2014). Cognitive sequelae of traumatic brain injury. *Psychiatr Clin North Am, 37*(1), 1-11. doi:10.1016/j.psc.2013.11.004

Rabinowitz, A. R., Li, X., McCauley, S. R., Wilde, E. A., Barnes, A., Hanten, G., . . . Levin, H. S. (2015). Prevalence and Predictors of Poor Recovery from Mild Traumatic Brain Injury. *J Neurotrauma, 32*(19), 1488-1496. doi:10.1089/neu.2014.3555

Ramlackhansingh, A. F., Brooks, D. J., Greenwood, R. J., Bose, S. K., Turkheimer, F. E., Kinnunen, K. M., . . . Sharp, D. J. (2011). Inflammation after trauma: microglial activation and traumatic brain injury. *Ann Neurol, 70*(3), 374-383. doi:10.1002/ana.22455

Randolph, C., Tierney, M. C., Mohr, E., & Chase, T. N. (1998). The Repeatable Battery for the Assessment of Neuropsychological Status (RBANS): preliminary clinical validity. *J Clin Exp Neuropsychol, 20*(3), 310-319. doi:10.1076/jcen.20.3.310.823

Roozenbeek, B., Chiu, Y. L., Lingsma, H. F., Gerber, L. M., Steyerberg, E. W., Ghajar, J., & Maas, A. I. (2012). Predicting 14-day mortality after severe traumatic brain injury: application of the IMPACT models in the brain trauma foundation TBI-trac® New York State database. *J Neurotrauma, 29*(7), 1306-1312. doi:10.1089/neu.2011.1988

Ross, D. E. (2011). Review of longitudinal studies of MRI brain volumetry in patients with traumatic brain injury. *Brain Inj, 25*(13-14), 1271-1278. doi:10.3109/02699052.2011.624568

Rottschy, C., Langner, R., Dogan, I., Reetz, K., Laird, A. R., Schulz, J. B., . . . Eickhoff, S. B. (2012). Modelling neural correlates of working memory: a coordinate-based meta-analysis. *Neuroimage, 60*(1), 830-846. doi:10.1016/j.neuroimage.2011.11.050

Ruan, Y. and Li, A. (2015). Influence of Dynamical Change of Edges on Clustering Coefficients. Discrete Dynamics in Nature and Society, vol. 2015, 5, 2015.

Rubinov, M., & Sporns, O. (2010). Complex network measures of brain connectivity: uses and interpretations. Neuroimage, 52(3), 1059-1069.

Rutgers, D. R., Fillard, P., Paradot, G., Tadié, M., Lasjaunias, P., & Ducreux, D. (2008). Diffusion tensor imaging characteristics of the corpus callosum in mild, moderate, and severe traumatic brain injury. *AJNR Am J Neuroradiol, 29*(9), 1730-1735. doi:10.3174/ajnr.A1213

Sairanen, V., Kuusela, L., Sipilä, O., Savolainen, S., & Vanhatalo, S. (2017). A novel measure of reliability in Diffusion Tensor Imaging after data rejections due to subject motion. *Neuroimage, 147*, 57-65. doi:10.1016/j.neuroimage.2016.11.061

Salmon, E., Van der Linden, M., Collette, F., Delfiore, G., Maquet, P., Degueldre, C., . . . Franck, G. (1996). Regional brain activity during working memory tasks. *Brain, 119 (Pt 5)*, 1617-1625. doi:10.1093/brain/119.5.1617

Schnyer, D. M., Clasen, P. C., Gonzalez, C., & Beevers, C. G. (2017). Evaluating the diagnostic utility of applying a machine learning algorithm to diffusion tensor MRI measures in individuals with major depressive disorder. *Psychiatry Res Neuroimaging, 264*, 1-9. doi:10.1016/j.pscychresns.2017.03.003

Sidaros, A., Engberg, A. W., Sidaros, K., Liptrot, M. G., Herning, M., Petersen, P., . . . Rostrup, E. (2008). Diffusion tensor imaging during recovery from severe traumatic brain injury and relation to clinical outcome: a longitudinal study. *Brain, 131*(Pt 2), 559-572. doi:10.1093/brain/awm294

Schimmel, S. J., Acosta, S., & Lozano, D. (2017). Neuroinflammation in traumatic brain injury: A chronic response to an acute injury. *Brain Circ, 3*(3), 135-142. doi:10.4103/bc.bc_18_17

Schrouff, J., Rosa, M. J., Rondina, J. M., Marquand, A. F., Chu, C., Ashburner, J., . . . Mourão-Miranda, J. (2013). PRoNTo: pattern recognition for neuroimaging toolbox. *Neuroinformatics, 11*(3), 319-337. doi:10.1007/s12021-013-9178-1

Scott, G., Zetterberg, H., Jolly, A., Cole, J. H., De Simoni, S., Jenkins, P. O., . . . Sharp, D. J. (2018). Minocycline reduces chronic microglial activation after brain trauma but increases neurodegeneration. *Brain, 141*(2), 459-471. doi:10.1093/brain/awx339

Seehaus, A. K., Roebroeck, A., Chiry, O., Kim, D. S., Ronen, I., Bratzke, H., . . . Galuske, R. A. (2013). Histological validation of DW-MRI tractography in human postmortem tissue. *Cereb Cortex, 23*(2), 442-450. doi:10.1093/cercor/bhs036

Shallice, T. (1982). Specific impairments of planning. Philos Trans R Soc Lond B Biol Sci, 298(1089), 199-209

Sharp, D. J., Scott, G., & Leech, R. (2014). Network dysfunction after traumatic brain injury. *Nat Rev Neurol, 10*(3), 156-166. doi:10.1038/nrneurol.2014.15

Sharp, D. J., Beckmann, C. F., Greenwood, R., Kinnunen, K. M., Bonnelle, V., De Boissezon, X., . . . Leech, R. (2011). Default mode network functional and structural connectivity after traumatic brain injury. *Brain, 134*(Pt 8), 2233-2247. doi:10.1093/brain/awr175

Sidaros, A., Skimminge, A., Liptrot, M. G., Sidaros, K., Engberg, A. W., Herning, M., . . . Rostrup, E. (2009). Long-term global and regional brain volume changes following severe traumatic brain injury: a longitudinal study with clinical correlates. *Neuroimage, 44*(1), 1-8. doi:10.1016/j.neuroimage.2008.08.030

Skandsen, T., Kvistad, K. A., Solheim, O., Strand, I. H., Folvik, M., & Vik, A. (2010). Prevalence and impact of diffuse axonal injury in patients with moderate and severe head injury: a cohort study of early magnetic resonance imaging findings and 1-year outcome. *J Neurosurg, 113*(3), 556-563. doi:10.3171/2009.9.JNS09626

Smith, S. M., Jenkinson, M., Johansen-Berg, H., Rueckert, D., Nichols, T. E., Mackay, C. E., . . . Behrens, T. E. (2006). Tract-based spatial statistics: voxelwise analysis of multi-subject diffusion data. *Neuroimage, 31*(4), 1487-1505. doi:10.1016/j.neuroimage.2006.02.024

Smith, D. H., Chen, X. H., Iwata, A., & Graham, D. I. (2003). Amyloid beta accumulation in axons after traumatic brain injury in humans. *J Neurosurg, 98*(5), 1072-1077. doi:10.3171/jns.2003.98.5.1072

Snaith, R. P. (2003). The Hospital Anxiety And Depression Scale. *Health Qual Life Outcomes, 1*, 29. doi:10.1186/1477-7525-1-29

Smith, S. M. *et al*. *Correspondence of the brain's functional architecture during activation and rest*. *Proc. Natl Acad. Sci. USA* **106**, 13040–13045 (2009).

Soreq, E., Leech, R., & Hampshire, A. (2019). Dynamic network coding of working-memory domains and working-memory processes. *Nat Commun, 10*(1), 936. doi:10.1038/s41467-019-08840-8

Spikman, J. M., & van der Naalt, J. (2010). Indices of impaired self-awareness in traumatic brain injury patients with focal frontal lesions and executive deficits: implications for outcome measurement. *J Neurotrauma, 27*(7), 1195-1202. doi:10.1089/neu.2010.1277

Sporns, O., & Honey, C. J. (2006). Small worlds inside big brains. *Proc Natl Acad Sci U S A, 103*(51), 19219-19220. doi:10.1073/pnas.0609523103

Stein, S. C., Georgoff, P., Meghan, S., Mizra, K., & Sonnad, S. S. (2010). 150 years of treating severe traumatic brain injury: a systematic review of progress in mortality. *J Neurotrauma, 27*(7), 1343-1353. doi:10.1089/neu.2009.120

Stocchetti, N., & Zanier, E. R. (2016). Chronic impact of traumatic brain injury on outcome and quality of life: a narrative review. *Crit Care, 20*(1), 148. doi:10.1186/s13054-016-1318-1

Stuss, D. T. (2011). Traumatic brain injury: relation to executive dysfunction and the frontal lobes. *Curr Opin Neurol, 24*(6), 584-589. doi:10.1097/WCO.0b013e32834c7eb9

Thornhill, S., Teasdale, G. M., Murray, G. D., McEwen, J., Roy, C. W., & Penny, K. I. (2000). Disability in young people and adults one year after head injury: prospective cohort study. *BMJ, 320*(7250), 1631-1635. doi:10.1136/bmj.320.7250.1631

Tononi, G., & Sporns, O. (2003). Measuring information integration. *BMC Neurosci, 4*, 31. doi:10.1186/1471-2202-4-31

Tritsch, N. X., & Sabatini, B. L. (2012). Dopaminergic modulation of synaptic transmission in cortex and striatum. *Neuron, 76*(1), 33-50. doi:10.1016/j.neuron.2012.09.023

Tzourio-Mazoyer, N., Landeau, B., Papathanassiou, D., Crivello, F., Etard, O., Delcroix, N., et al. (2002). Automated anatomical labeling of activations in SPM using a macroscopic anatomical parcellation of the MNI MRI single-subject brain., *15*(1), 273–289. http://doi.org/10.1006/nimg.2001.0978

Vallar, G., Di Betta, A. M., & Silveri, M. C. (1997). The phonological short-term store-rehearsal system: patterns of impairment and neural correlates. *Neuropsychologia, 35*(6), 795-812. doi:10.1016/s0028-3932(96)00127-3

van den Heuvel, M. P., Mandl, R. C., Kahn, R. S., & Hulshoff Pol, H. E. (2009). Functionally linked resting-state networks reflect the underlying structural connectivity architecture of the human brain. *Hum Brain Mapp, 30*(10), 3127-3141. doi:10.1002/hbm.20737

Violante, I. R., Li, L. M., Carmichael, D. W., Lorenz, R., Leech, R., Hampshire, A., . . . Sharp, D. J. (2017). Externally induced frontoparietal synchronization modulates network dynamics and enhances working memory performance. *Elife, 6*.

Vella, M. A., Crandall, M. L., & Patel, M. B. (2017). Acute Management of Traumatic Brain Injury. *Surg Clin North Am, 97*(5), 1015-1030. doi:10.1016/j.suc.2017.06.003

Vergara, V. M., Mayer, A. R., Kiehl, K. A., & Calhoun, V. D. (2018). Dynamic functional network connectivity discriminates mild traumatic brain injury through machine learning. *Neuroimage Clin, 19*, 30-37. doi:10.1016/j.nicl.2018.03.017

Vespa, P., Tubi, M., Claassen, J., Buitrago-Blanco, M., McArthur, D., Velazquez, A. G., . . . Nuwer, M. (2016). Metabolic crisis occurs with seizures and periodic discharges after brain trauma. *Ann Neurol, 79*(4), 579-590. doi:10.1002/ana.24606

Vestergaard, M., Madsen, K. S., Baaré, W. F., Skimminge, A., Ejersbo, L. R., Ramsøy, T. Z., . . . Jernigan, T. L. (2011). White matter microstructure in superior longitudinal fasciculus associated with spatial working memory performance in children. *J Cogn Neurosci, 23*(9), 2135-2146. doi:10.1162/jocn.2010.21592

Vollmar C, O'Muircheartaigh J, Symms MR et al. Altered microstructural connectivity in juvenile myoclonic epilepsy: the missing link. Neurology 2012;78(20):1555–1559.

Vukic, M., Negovetic, L., Kovac, D., Ghajar, J., Glavic, Z., & Gopcevic, A. (1999). The effect of implementation of guidelines for the management of severe head injury on patient treatment and outcome. *Acta Neurochir (Wien), 141*(11), 1203-1208. doi:10.1007/s007010050419

Wagner, A. K., Scanlon, J. M., Becker, C. R., Ritter, A. C., Niyonkuru, C., Dixon, C. E., . . . Price, J. C. (2014). The influence of genetic variants on striatal dopamine transporter and D2 receptor binding after TBI. *J Cereb Blood Flow Metab, 34*(8), 1328-1339. doi:10.1038/jcbfm.2014.87

Wagner, A. K., Sokoloski, J. E., Ren, D., Chen, X., Khan, A. S., Zafonte, R. D., . . . Dixon, C. E. (2005). Controlled cortical impact injury affects dopaminergic transmission in the rat striatum. *J Neurochem, 95*(2), 457-465. doi:10.1111/j.1471-4159.2005.03382.x

Wang, J. Y., Bakhadirov, K., Abdi, H., Devous, M. D., Marquez de la Plata, C. D., Moore, C., . . . Diaz-Arrastia, R. (2011). Longitudinal changes of structural connectivity in traumatic axonal injury. *Neurology, 77*(9), 818-826. doi:10.1212/WNL.0b013e31822c61d7

Watanabe, A., Inoue, Y., Asano, Y., Kikuchi, K., Miyatake, H., & Tokushige, T. (2017). Examination of a Method to Determine the Reference Region for Calculating the Specific Binding Ratio in Dopamine Transporter Imaging. *Nihon Hoshasen Gijutsu Gakkai Zasshi, 73*(4), 291-297. doi:10.6009

Watts, D. J., & Strogatz, S. H. (1998). Collective dynamics of 'small-world' networks. *Nature, 393*(6684), 440-442. doi:10.1038/30918

Weschler., D. A standardized memory scale for clinical use. J Psychol 1945;19: 87-95.

Werner, C., & Engelhard, K. (2007). Pathophysiology of traumatic brain injury. *Br J Anaesth, 99*(1), 4-9. doi:10.1093/bja/aem131

Wheeler, M. E., & Treisman, A. M. (2002). Binding in short-term visual memory. *J Exp Psychol Gen, 131*(1), 48-64. doi:10.1037//0096-3445.131.1.48

Wilde, E. A., McCauley, S. R., Hunter, J. V., Bigler, E. D., Chu, Z., Wang, Z. J., . . . Levin, H. S. (2008). Diffusion tensor imaging of acute mild traumatic brain injury in adolescents. *Neurology, 70*(12), 948-955. doi:10.1212/01.wnl.0000305961.68029.54

Williams, S. M., & Goldman-Rakic, P. S. (1998). Widespread origin of the primate mesofrontal dopamine system. *Cereb Cortex, 8*(4), 321-345. doi:10.1093/cercor/8.4.321

Yin, B., Li, D. D., Huang, H., Gu, C. H., Bai, G. H., Hu, L. X., . . . Zhang, M. (2019). Longitudinal Changes in Diffusion Tensor Imaging Following Mild Traumatic Brain Injury and Correlation With Outcome. *Front Neural Circuits, 13*, 28. doi:10.3389/fncir.2019.00028

Zaksas, D., Bisley, J. W., & Pasternak, T. (2001). Motion information is spatially localized in a visual working-memory task. *J Neurophysiol, 86*(2), 912-921. doi:10.1152/jn.2001.86.2.912

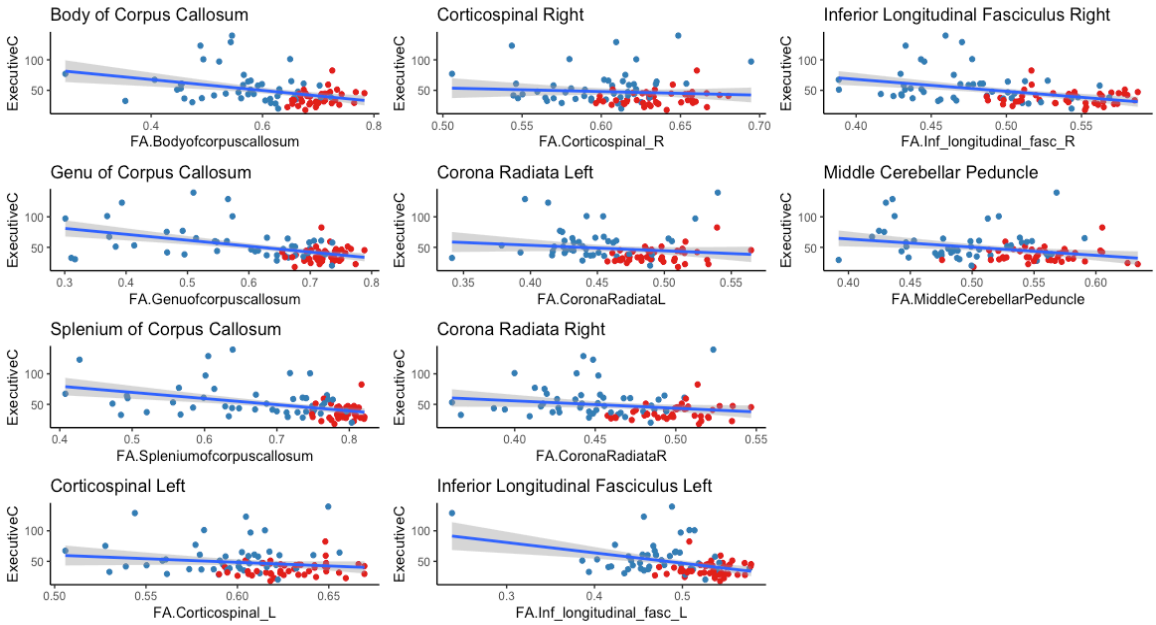
Zappala, G., Thiebaut de Schotten, M., & Eslinger, P. J. (2012). Traumatic brain injury and the frontal lobes: what can we gain with diffusion tensor imaging? Cortex, 48(2), 156-165.

Zhang S, Arfanakis K. Evaluation of standardized and study-specific diffusion tensor imaging templates of the adult human brain: Template characteristics, spatial normalization accuracy, and detection of small inter-group FA differences. Neuroimage 2018;172:40-50.

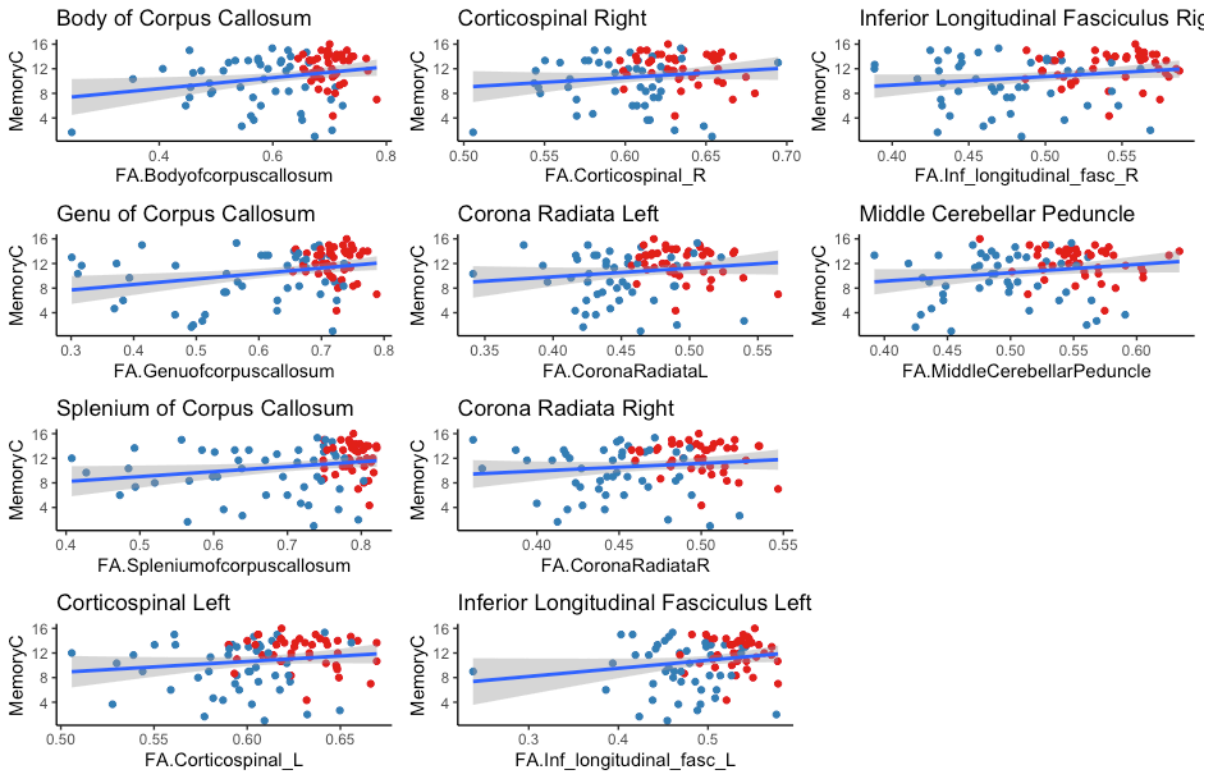
Appendix

Figures

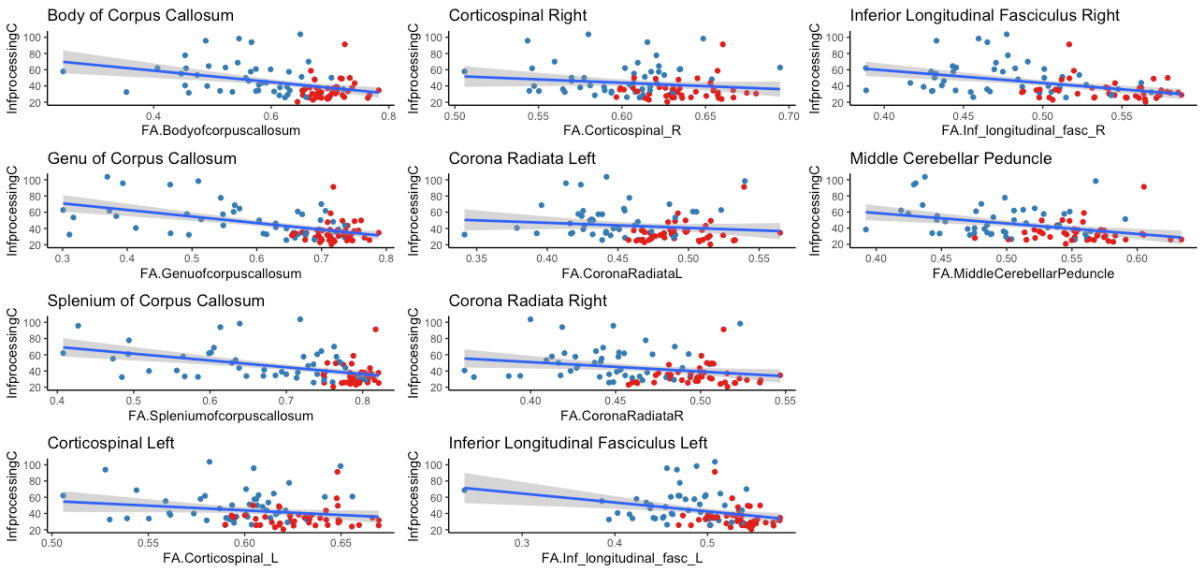
Chapter 3



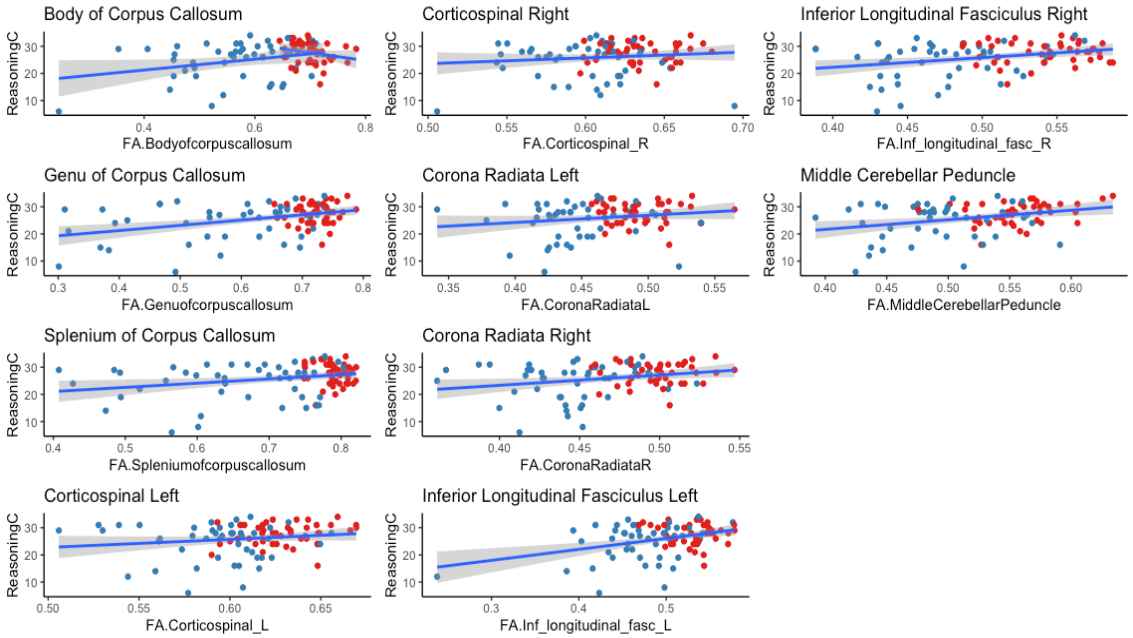
Appendix figure 1.1: Correlation between mean tract FA and composite executive function neuropsychological scores for all TBI patients (n=92). Red dots denote patients identified as having normal DTI. Blue dots denote patients identified as having abnormal DTI using the tool. Results are from chapter 3 (section 3.5.11).



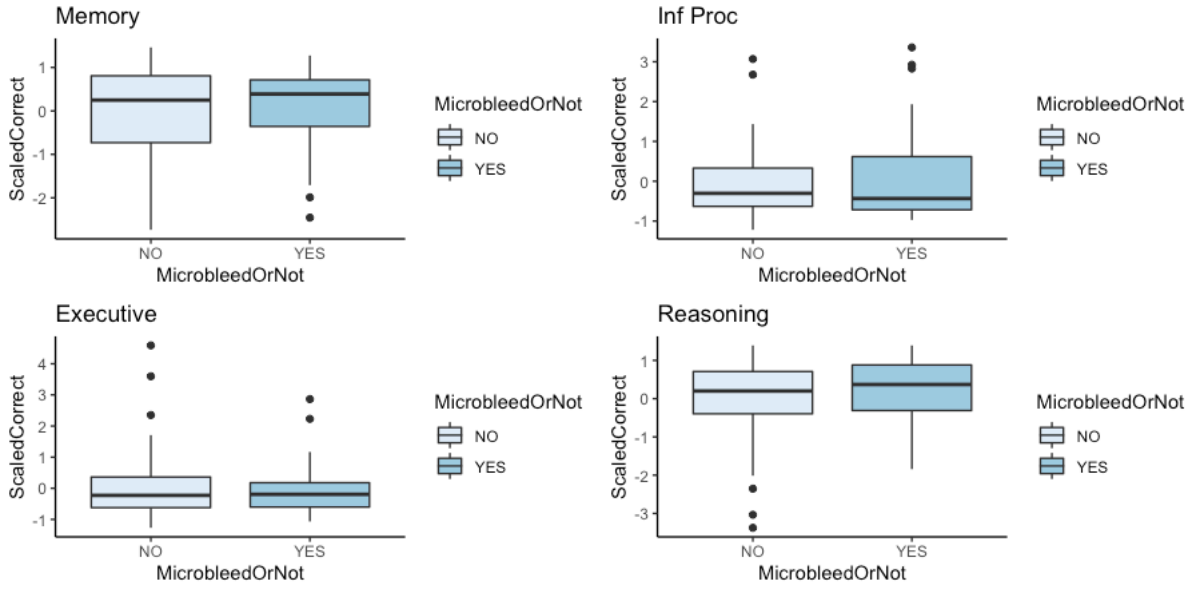
Appendix figure 1.2: Correlation between mean tract FA and composite memory neuropsychological scores for all TBI patients (n=92). Red dots denote patients identified as having normal DTI. Blue dots denote patients identified as having abnormal DTI using the tool.



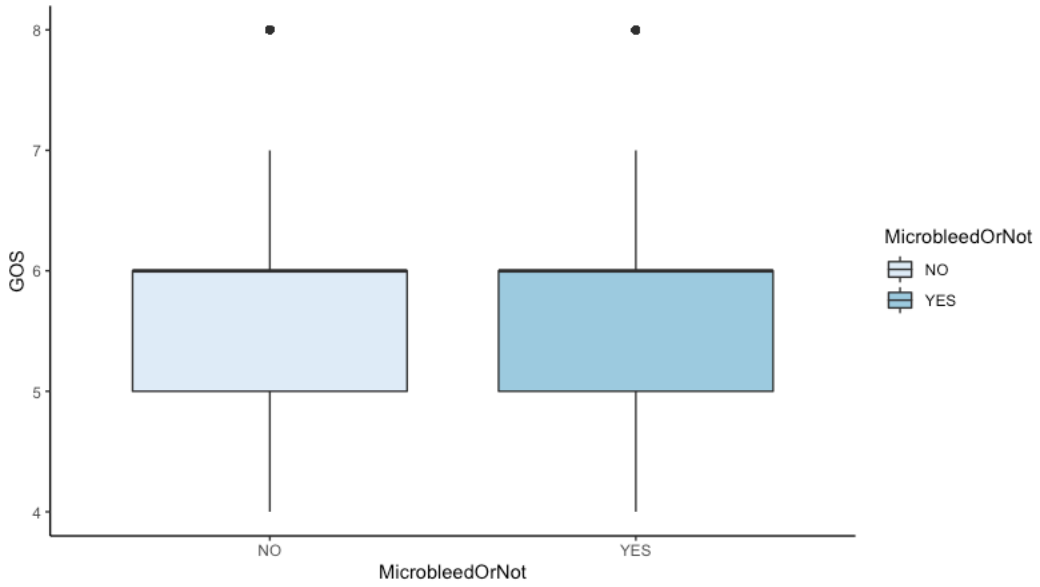
Appendix figure 1.3: Correlation between mean tract FA and composite information processing neuropsychological scores for all TBI patients (n=92). Red dots denote patients identified as having normal DTI. Blue dots denote patients identified as having abnormal DTI using the tool.



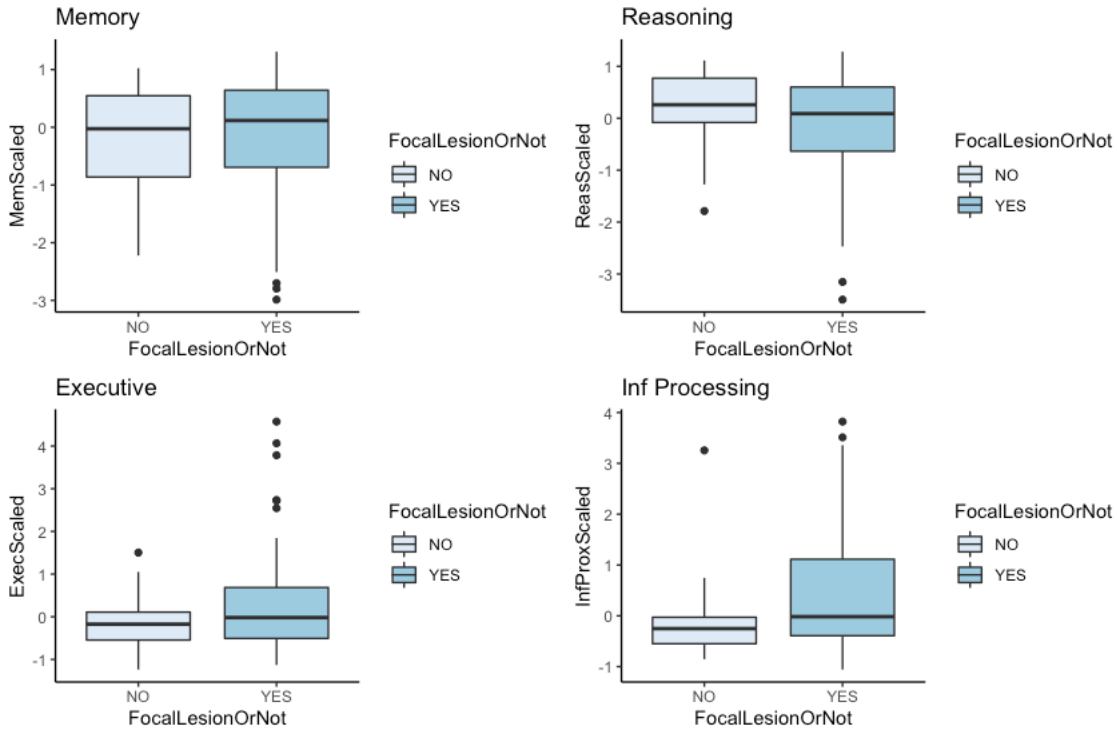
Appendix figure 1.4: Correlation between mean tract FA and reasoning neuropsychological scores for all TBI patients (n=92). Red dots denote patients identified as having normal DTI. Blue dots denote patients identified as having abnormal DTI using the tool.



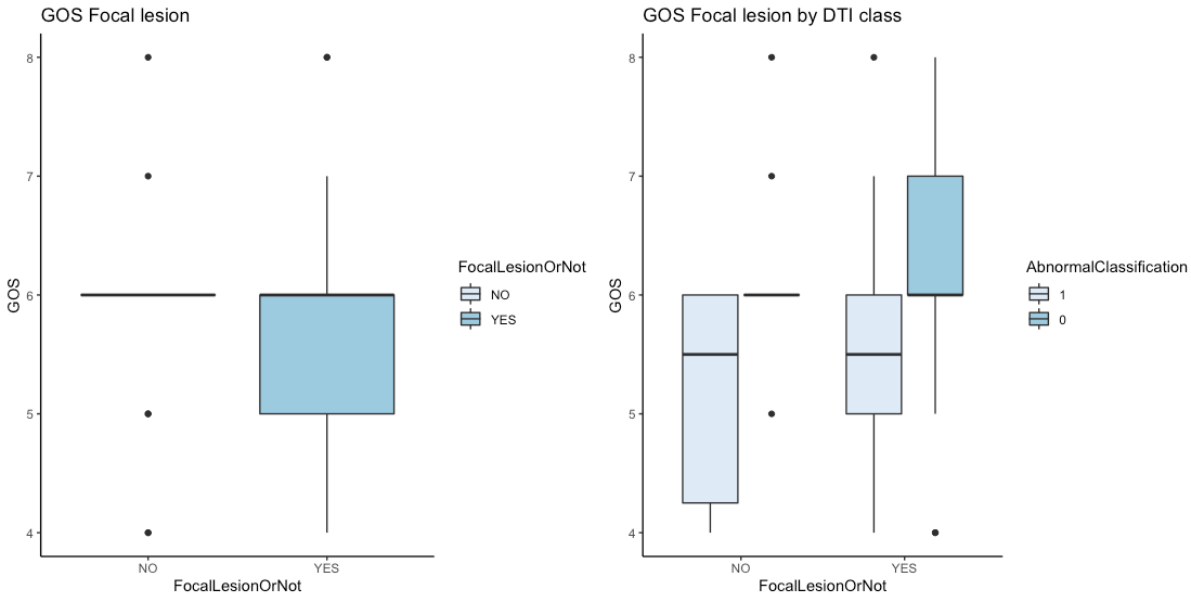
Appendix figure 1.5: Comparison of cognitive performance between patients with (n=40) or without (n=52) microbleeds.



Appendix figure 1.6 : Comparison of cognitive performance across the four cognitive domains. B. Comparison of functional outcome (GOSE) between patients.

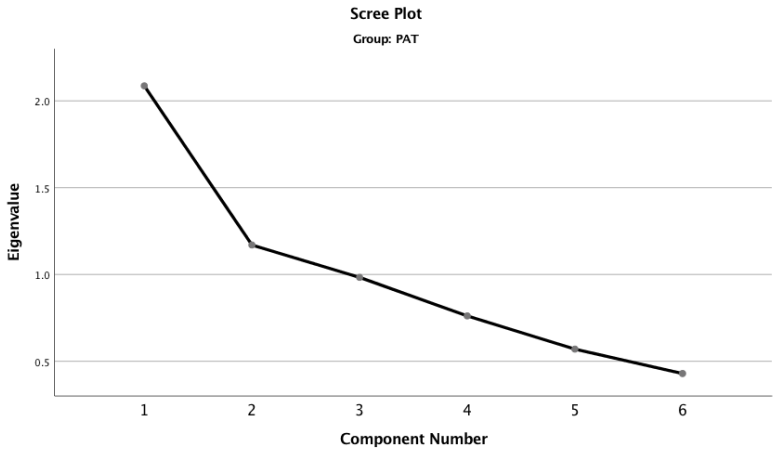


Appendix figure 1.7: Comparison of cognitive and functional outcomes between patients with (n=27) or without (n=65) focal lesions. A. Comparison of cognitive performance across the four cognitive domains.



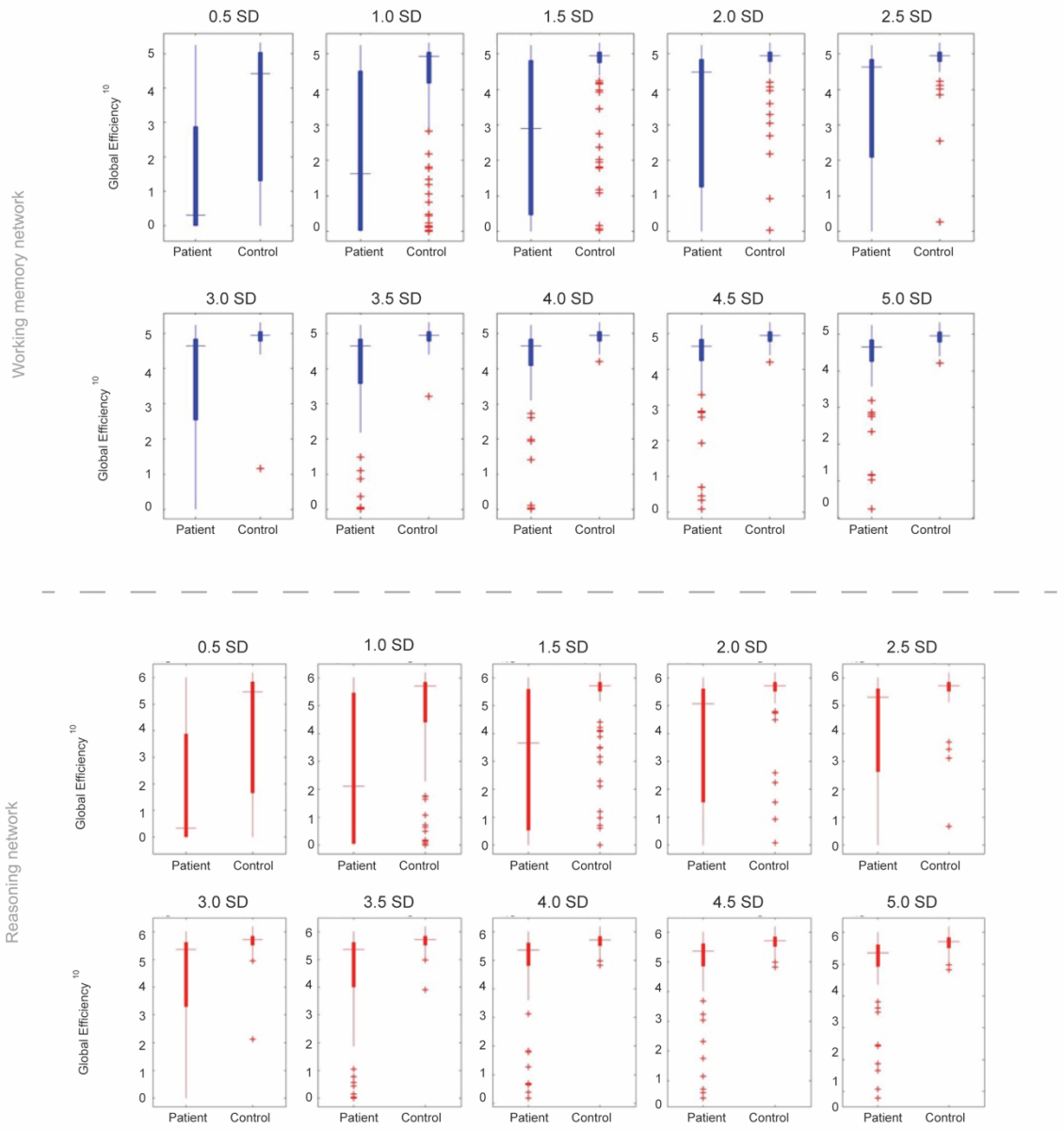
Appendix figure 1.8 : Comparison of functional outcome (GOSE) between patients.

Chapter 4



Task	MKL	PAL	SOS	FTM	OOO	HTT
MKL	1	0.371	0.306	0.17	0.161	0.224
PAL	0.371	1	0.251	0.119	0.267	0.047
SOS	0.306	0.251	1	0.134	0.178	0.061
FTM	0.17	0.119	0.134	1	0.52	0.262
OOO	0.161	0.267	0.178	0.52	1	0.096
HTT	0.224	0.047	0.061	0.262	0.096	1

Appendix figure 1.9: Scree plot and cross-correlation table of patient cognitive components from PCA analysis with orthogonal rotation.



Appendix figure 1.10: Results from global cross sectional analysis of working memory and reasoning network graph theory properties across threshold iterations. Blue figures represent working memory global network properties, red figures represent reasoning global network properties. Threshold iterations from 0.5-5 SD in 10 increments of 0.5 from left to right, top to bottom. 0=Patients, 1=Controls.

Tables

Chapter 3

Patient	No. Abnormal tracts including lesion	No. Abnormal tracts excluding lesion
1	6	6
2	3	3
3	0	0
4	0	0
5	0	0
6	9	9
7	1	1
8	5	5
9	5	5
10	9	8
11	7	5
12	9	9
13	0	0
14	3	0
15	0	0
16	7	6
17	0	0
18	8	8
19	6	6
20	1	1
21	0	0
22	5	4
23	6	6
24	0	0
25	0	0
26	0	0
27	0	0
28	4	3
29	0	0
30	9	9
31	0	0

32	0	0
33	6	6
34	0	0
35	5	5
36	5	3
37	0	0
38	8	6
39	0	0
40	2	0
41	0	0
42	0	0
43	0	0
44	5	4
45	0	0
46	0	0
47	6	5
48	9	9
49	9	8
50	9	9
51	5	3
52	4	4
53	9	9
54	9	8
55	10	10
56	0	0
57	1	1
58	1	1
59	3	2
60	1	0
61	0	0
62	0	0
63	0	0
64	6	5

Appendix table 2.1: Diagnostic results of the 64 patients with focal lesions when including or excluding lesions.

Working memory network									
	Local Efficiency			Degree			Clustering coefficient		
Node	Con	Pat	P(FDR)	Con	Pat	P(FDR)	Con	PAT	P(FDR)
Caudate.L†	16815.549	20236.534	0.000***	29.434	26.478	0.000***	12666.228	15931.769	0.000***
Pallidum.L	16007.302	17985.204	0.000***	28.660	26.261	0.000***	11149.220	12062.893	0.001**
Hippocampus.L	8747.993	9842.603	0.000***	26.698	24.837	0.000***	6290.153	7392.492	0.000***
Caudate.R	21100.774	25168.573	0.000***	29.736	27.000	0.000***	15984.150	20201.510	0.000***
Pallidum.R†	24084.156	26877.096	0.000***	29.604	27.315	0.000***	17604.054	19070.478	0.000***
Hippocampus.R	6149.067	6568.627	0.000***	26.698	25.337	0.000***	4062.609	4388.791	0.001**
CaudAntCing.L	6859.146	6793.239	0.579	25.717	23.609	0.000***	5603.492	5700.563	0.551
LatOrbitoFront.L	13498.172	15146.114	0.000***	27.717	25.065	0.000***	10111.978	11650.011	0.000***
Paracentral.L	31543.029	34137.437	0.000***	26.585	23.315	0.000***	22102.203	23919.350	0.023*
PostCentral.L	23411.077	26636.278	0.000***	26.689	23.804	0.000***	16277.600	19546.049	0.000***
PostCingulate.L	10519.887	11387.525	0.000***	24.670	22.076	0.000***	6651.602	7963.272	0.000***
Precentral.L	40576.919	43968.222	0.000***	26.679	23.424	0.000***	28909.212	28470.366	0.583
Precuneus.L	25475.842	28309.738	0.000***	27.679	24.500	0.000***	17723.149	20382.424	0.002**
RosAntCing.L	4499.403	4032.585	0.000***	22.858	21.783	0.000***	4836.203	4727.655	0.487
RosMidFront.L	34091.968	37622.774	0.000***	29.519	26.228	0.000***	24219.030	27691.741	0.002**
SupFront.L	52953.337	55941.815	0.000***	29.623	25.935	0.000***	37634.545	38086.021	0.647
Insula.L†	27615.340	30807.954	0.000***	28.623	26.500	0.000***	20551.918	22759.488	0.000***
CaudaAntCing.R	6179.156	6248.551	0.574	24.736	23.891	0.000***	5551.114	7569.185	0.004**
CaudMidFront.R	20421.489	20600.807	0.352	24.689	22.870	0.000***	13967.221	13694.287	0.402
LatOrbitoFront.R	11702.886	12391.604	0.000***	29.764	27.250	0.000***	9890.857	11310.579	0.000***
Paracentral.R	36704.269	42028.098	0.000***	27.660	24.489	0.000***	27810.266	33244.109	0.012*
PostCentral.R	30942.906	35907.345	0.000***	27.708	24.804	0.000***	23980.939	26897.134	0.001**
PostCingulate.R	9346.930	10073.217	0.000***	27.774	25.902	0.000***	7753.104	15332.966	0.054
Precentral.R	44466.331	47485.613	0.000***	26.604	24.011	0.000***	31718.234	31602.625	0.854
Precuneus.R†	25194.630	25889.898	0.003**	28.689	26.989	0.000***	17485.324	18971.761	0.005**
RosAntCing.R	4610.147	4444.214	0.000***	20.868	19.891	0.000***	3755.706	3702.175	0.504
RosMidFront.R	23123.279	26133.465	0.000***	29.679	26.283	0.000***	16973.678	20494.366	0.006**
SupFront.R	48482.950	50489.749	0.000***	29.679	26.326	0.000***	34139.131	36110.027	0.158
SupParietal.R†	29222.546	30795.403	0.000***	27.594	25.446	0.000***	20701.982	21328.062	0.087
SupraMarg.R	25978.043	28959.918	0.000***	28.660	25.880	0.000***	19039.778	20240.209	0.005**
Insula.R†	21363.536	23795.822	0.000***	29.660	27.304	0.000***	16754.316	18462.856	0.002**

Appendix table 2.2: Local/nodal network properties of patients and controls in the working memory network. †Network hubs as classified by determining top 20% of nodes with highest degree across healthy population at threshold of 2.5 S.D.

Reasoning network									
	Local Efficiency			Degree			Clustering Coefficient		
Node	Con	Pat	FDR	Con	Pat	FDR	Con	Pat	FDR

CaudMidFront.L	45143.064	44334.101	0.008**	21.792	20.641	0.000***	39036.915	37322.438	0.004**
Cuneus.L	8098.240	8464.496	0.008**	19.896	19.033	0.000***	5960.671	6481.295	0.005**
Fusiform.L	17083.379	18696.326	0.000***	24.708	23.793	0.000***	15571.427	18407.135	0.001**
InfParietal.L	29577.958	33073.872	0.000***	24.736	23.098	0.000***	24823.057	27423.823	0.003**
InfTemporal.L	24712.372	28086.847	0.000***	24.689	23.478	0.000***	21018.432	26710.216	0.003**
LatOcc.L	20438.961	22437.616	0.001**	24.868	23.739	0.000***	18094.638	20881.697	0.002**
LatOrbFront.L	11029.768	11370.555	0.000***	24.679	23.554	0.000***	9940.590	10759.964	0.001**
ParsOperc.L	37997.545	38808.974	0.022*	19.745	18.185	0.000***	30469.375	29968.675	0.245
Pericalcarine.L	9011.637	9705.834	0.001**	20.868	20.033	0.000***	7766.978	8751.377	0.000***
Precentral.L	44359.494	45466.625	0.079	21.849	20.620	0.000***	36580.574	37157.042	0.567
RosMidFront.L†	41476.861	42062.625	0.191	23.745	22.326	0.000***	35885.362	37641.653	0.068
SupFront.L†	53626.504	50157.573	0.000***	22.679	21.337	0.000***	42650.488	39598.898	0.001**
SupParietal.L†	32088.953	35690.365	0.000***	24.736	22.880	0.000***	23379.730	27864.039	0.001**
CaudMidFront.R	28904.806	27657.205	0.010*	22.689	21.174	0.000***	24191.172	22219.897	0.000***
Cuneus.R	12546.965	13544.679	0.001**	17.877	16.880	0.000***	9455.167	10563.770	0.009**
Fusiform.R	22244.117	24520.766	0.000***	23.783	22.457	0.000***	18225.608	20160.950	0.002**
InfParietal.R†	21473.320	21728.667	0.251	24.575	23.065	0.000***	16235.403	15821.861	0.070
InfTemporal.R	16802.134	17683.229	0.022*	23.613	21.978	0.000***	12770.564	12973.215	0.567
LateralOcc.R	19040.846	21358.076	0.000***	20.811	19.500	0.000***	13784.563	15711.671	0.000***
Lingual.R	16853.564	19239.613	0.000***	21.849	20.609	0.000***	14119.562	17048.882	0.000***
ParsOperc.R	23408.375	22493.908	0.035*	20.755	19.467	0.000***	19797.425	18565.069	0.002**
Paricalcarine.R	20198.020	22761.774	0.000***	20.858	19.826	0.000***	17317.791	21352.841	0.001**
Precentral.R	28421.789	27105.584	0.001**	22.736	21.261	0.000***	24187.744	22030.213	0.000***
RosMidFront.R	24968.764	24514.426	0.204	19.660	18.239	0.000***	17455.188	17226.701	0.567
SupFront.R	45786.966	42725.445	0.002**	22.726	20.837	0.000***	35565.529	34430.753	0.310
SupParietal.R†	20924.338	21746.199	0.002**	24.726	23.054	0.000***	14784.840	15235.855	0.096

Appendi table 2.3: Local/nodal network properties of patients and controls in the working memory network. †Network hubs as classified by determining top 20% of nodes with highest degree across healthy population at threshold of 2.5 S.D.

Working memory network correlations to cognitive components across all structural connectome threshold iterations (see supplementary figure 9 for graphical illustration of results)

0.5 SD units

GT Metrics	Degree centrality				Local Efficiency				Clustering coefficient			
Node	Reasoning R.	p(FDR)	Working mem R.	p(FDR)	Reasoning R.	p(FDR)	Working mem R.	p(FDR)	Reasoning R.	p(FDR)	Working mem. R.	p(FDR)
Caudate.L†	0.081	0.839	0.116	0.761	-0.322	0.018*	-0.214	0.238	-0.247	0.068	-0.190	0.258
Pallidum.L	0.056	0.839	0.109	0.774	-0.308	0.022*	-0.139	0.388	-0.246	0.068	-0.177	0.294

Hippocampus.L	0.013	0.963	-0.071	0.958	-0.268	0.032*	-0.246	0.158	-0.379	0.005*	-0.242	0.203
Caudate.R	0.116	0.794	0.020	0.997	-0.209	0.075	-0.241	0.158	-0.191	0.160	-0.214	0.203
Pallidum.R†	0.051	0.845	0.086	0.865	-0.232	0.051	-0.251	0.158	-0.156	0.267	-0.258	0.203
Hippocampus.R	0.025	0.925	-0.064	0.958	-0.269	0.032*	-0.179	0.271	-0.299	0.028*	-0.160	0.334
CaudAntCing.L	0.073	0.839	0.143	0.594	-0.035	0.789	0.182	0.271	NaN	NaN	NaN	NaN
LatOrbitoFront.L	-0.062	0.839	0.003	0.997	-0.289	0.026*	-0.254	0.158	-0.024	0.857	-0.172	0.294
Paracentral.L	0.083	0.839	0.001	0.997	-0.231	0.051	-0.078	0.559	NaN	NaN	NaN	NaN
PostCentral.L	0.056	0.839	-0.012	0.997	-0.285	0.026*	-0.097	0.559	-0.295	0.028*	-0.208	0.203
PostCingulate.L	0.090	0.839	0.096	0.865	-0.108	0.377	-0.038	0.746	-0.126	0.376	-0.098	0.708
Precentral.L	0.005	0.989	-0.001	0.997	-0.245	0.044*	-0.087	0.559	-0.144	0.295	-0.116	0.583
Precuneus.L	0.114	0.794	0.154	0.550	-0.200	0.082	-0.153	0.319	-0.228	0.093	-0.214	0.203
RosAntCing.L	-0.141	0.794	0.062	0.958	0.008	0.943	0.084	0.559	-0.029	0.852	-0.011	0.974
RosMidFront.L	0.089	0.839	0.132	0.652	-0.172	0.136	-0.072	0.571	0.000	0.998	-0.043	0.893
SupFront.L	0.113	0.794	0.190	0.433	-0.332	0.018*	-0.096	0.559	-0.182	0.177	-0.006	0.974
Insula.L	-0.064	0.839	0.205	0.383	-0.251	0.040*	-0.120	0.491	-0.222	0.098	0.008	0.974
CaudaAntCing.R	0.085	0.839	0.209	0.383	-0.027	0.827	0.066	0.571	-0.091	0.536	0.074	0.828
CaudMidFront.R	-0.024	0.925	0.000	0.997	-0.105	0.379	-0.110	0.540	-0.090	0.536	0.007	0.974
LatOrbitoFront.R	0.028	0.925	0.226	0.383	-0.159	0.167	-0.160	0.311	0.097	0.536	-0.079	0.828
Paracentral.R	0.147	0.794	0.045	0.997	-0.211	0.075	-0.159	0.311	NaN	NaN	NaN	NaN
PostCentral.R	0.152	0.794	0.053	0.997	-0.258	0.036*	-0.196	0.238	-0.198	0.153	-0.131	0.502
PostCingulate.R	0.058	0.839	-0.085	0.865	-0.198	0.083	-0.076	0.559	NaN	NaN	NaN	NaN
Precentral.R	0.027	0.925	-0.027	0.997	-0.067	0.596	-0.089	0.559	0.062	0.684	-0.061	0.863
Precuneus.R	0.137	0.794	0.030	0.997	-0.266	0.032*	-0.067	0.571	-0.154	0.267	-0.045	0.893
RosAntCing.R	-0.124	0.794	0.240	0.383	0.065	0.596	0.026	0.804	0.036	0.826	-0.070	0.828
RosMidFront.R	0.127	0.794	0.001	0.997	-0.203	0.081	-0.078	0.559	-0.263	0.059	-0.003	0.974
SupFront.R	0.022	0.925	0.019	0.997	-0.242	0.045*	-0.086	0.559	NaN	NaN	NaN	NaN
SupParietal.R	0.001	0.989	-0.040	0.997	-0.229	0.051	-0.167	0.311	-0.059	0.684	-0.045	0.893
SupraMarg.R	0.173	0.794	0.172	0.525	-0.295	0.026*	-0.196	0.238	-0.320	0.025*	-0.223	0.203
Insula.R	0.131	0.794	0.155	0.550	-0.350	0.018*	-0.204	0.238	-0.076	0.615	-0.006	0.974

Appendix table 2.4: Correlation coefficients and p-values for the relationship between cognitive components and graph theory metrics of a given node within the working memory network constructed using a 0.5 SD thresholding approach. R=Pearson's r, p(FDR)=p-value with FDR correction applied across nodes.

1.0 SD units

GT Metrics	Degree				Local Efficiency				Clustering coefficient			
Node	Reasoning		Working mem		Reasoning		Working mem.		Reasoning		Working mem.	
	R.	p(FDR)	R.	p(FDR)	R.	p(FDR)	R.	p(FDR)	R.	p(FDR)	R.	p(FDR)
Caudate.L	0.126	0.472	0.186	0.172	-0.300	0.020*	-0.258	0.067	-0.283	0.032*	-0.231	0.124
Pallidum.L	0.076	0.586	0.214	0.172	-0.270	0.032*	-0.183	0.192	-0.314	0.016*	-0.162	0.310
Hippocampus.L	0.062	0.663	0.041	0.772	-0.264	0.032	-0.230	0.105	-0.362	0.011*	-0.245	0.124
Caudate.R	0.110	0.472	0.122	0.391	-0.198	0.100	-0.272	0.067	-0.137	0.330	-0.267	0.124
Pallidum.R	0.138	0.454	0.185	0.172	-0.190	0.102	-0.261	0.067	-0.159	0.306	-0.293	0.124
Hippocampus.R	0.085	0.544	0.041	0.772	-0.299	0.020*	-0.206	0.162	-0.334	0.016*	-0.157	0.315
CaudAntCing.L	0.217	0.223	0.188	0.172	-0.001	0.992	0.157	0.234	-0.205	0.141	0.094	0.653
LatOrbitoFront.L	0.028	0.876	0.171	0.215	-0.354	0.010*	-0.290	0.067	-0.056	0.727	-0.217	0.131

Paracentral.L	0.105	0.472	0.114	0.396	-0.280	0.027*	-0.098	0.419	NaN	NaN	NaN	NaN
PostCentral.L	0.111	0.472	0.020	0.912	-0.256	0.035*	-0.126	0.313	-0.316	0.016*	-0.246	0.124
PostCingulate.L	0.136	0.454	0.207	0.172	-0.109	0.373	0.025	0.837	-0.129	0.330	-0.012	0.911
Precentral.L	0.057	0.673	0.117	0.396	-0.179	0.118	-0.165	0.234	-0.131	0.330	-0.171	0.310
Precuneus.L	0.133	0.454	0.189	0.172	-0.234	0.048*	-0.143	0.256	-0.119	0.361	-0.101	0.634
RosAntCing.L	0.004	0.967	0.085	0.522	0.057	0.640	0.067	0.580	-0.030	0.863	-0.027	0.911
RosMidFront.L	0.212	0.223	0.158	0.259	-0.186	0.108	-0.119	0.332	0.011	0.918	-0.143	0.372
SupFront.L	0.153	0.448	0.208	0.172	-0.300	0.020*	-0.200	0.162	-0.222	0.104	-0.041	0.911
Insula.L	0.111	0.472	0.206	0.172	-0.262	0.032*	-0.179	0.196	-0.255	0.050	-0.082	0.722
CaudaAntCing.R	0.106	0.472	0.263	0.172	0.079	0.521	0.059	0.613	-0.027	0.863	0.052	0.911
CaudMidFront.R	0.122	0.472	0.188	0.172	-0.114	0.361	-0.199	0.162	-0.128	0.330	-0.047	0.911
LatOrbitoFront.R	0.024	0.876	0.200	0.172	-0.249	0.039*	-0.126	0.313	-0.079	0.602	-0.038	0.911
Paracentral.R	0.211	0.223	0.073	0.585	-0.193	0.100	-0.154	0.234	NaN	NaN	NaN	NaN
PostCentral.R	0.226	0.223	0.130	0.375	-0.247	0.039*	-0.244	0.083	-0.158	0.306	-0.234	0.124
PostCingulate.R	0.176	0.319	0.013	0.915	-0.047	0.677	-0.160	0.234	NaN	NaN	NaN	NaN
Precentral.R	0.094	0.523	-0.011	0.915	-0.056	0.640	-0.081	0.506	0.030	0.863	-0.016	0.911
Precuneus.R	0.268	0.223	0.088	0.519	-0.196	0.100	-0.149	0.242	0.017	0.907	-0.065	0.841
RosAntCing.R	0.009	0.962	0.244	0.172	0.099	0.414	-0.006	0.958	0.076	0.602	-0.017	0.911
RosMidFront.R	0.187	0.289	0.139	0.338	-0.244	0.040*	-0.117	0.332	-0.268	0.039*	-0.014	0.911
SupFront.R	0.088	0.544	0.121	0.391	-0.196	0.100	-0.156	0.234	-0.140	0.330	0.012	0.911
SupParietal.R	0.145	0.454	0.095	0.498	-0.280	0.027*	-0.193	0.168	-0.145	0.330	-0.135	0.398
SupraMarg.R	0.188	0.289	0.210	0.172	-0.300	0.020*	-0.266	0.067	-0.280	0.032*	-0.217	0.131
Insula.R	0.229	0.223	0.285	0.172	-0.350	0.010*	-0.278	0.067	-0.139	0.330	-0.164	0.310

Appendix table 2.5: Correlation coefficients and p-values for the relationship between cognitive components and graph theory metrics of a given node within the working memory network constructed using a 1.0 SD thresholding approach. R=Pearson's r, p(FDR)=p-value with FDR correction applied across nodes.

1.5 SD units

GT Metrics	Degree				Local Efficiency				Clustering coefficient			
Node	Reasoning		Working mem.		Reasoning		Working mem.		Reasoning		Working mem.	
	R.	p(FDR)	R.	p(FDR)	R.	p(FDR)	R.	p(FDR)	R.	p(FDR)	R.	p(FDR)
Caudate.L	0.173	0.175	0.270	0.067	-0.324	0.012*	-0.297	0.051	-0.318	0.016*	-0.213	0.109
Palidum.L	0.169	0.175	0.219	0.80	-0.314	0.012*	-0.266	0.065	-0.322	0.016*	-0.236	0.083
Hippocampus.L	0.140	0.240	0.192	0.104	-0.232	0.048*	-0.275	0.063	-0.359	0.013*	-0.254	0.083
Caudate.R	0.134	0.240	0.253	0.067	-0.241	0.043*	-0.241	0.079	-0.248	0.045*	-0.248	0.083
Pallidum.R	0.208	0.104	0.255	0.067	-0.202	0.085	-0.232	0.089	-0.133	0.338	-0.228	0.083
Hippocampus.R	0.240	0.071	0.111	0.300	-0.288	0.021*	-0.157	0.233	-0.297	0.020*	-0.139	0.324
CaudAntCing.L	0.244	0.071	0.241	0.068	-0.023	0.882	0.110	0.385	-0.206	0.095	0.092	0.586
LatOrbitoFront.L	0.098	0.393	0.242	0.068	-0.327	0.012*	-0.308	0.051	-0.245	0.045*	-0.242	0.083
Paracentral.L	0.162	0.189	0.173	0.133	-0.265	0.027*	-0.158	0.233	-0.074	0.581	-0.176	0.208
PostCentral.L	0.113	0.325	0.120	0.274	-0.278	0.023*	-0.189	0.157	-0.316	0.016*	-0.259	0.083
PostCingulate.L	0.191	0.142	0.210	0.080	-0.084	0.482	-0.121	0.370	-0.064	0.628	-0.168	0.226
Precentral.L	0.145	0.235	0.141	0.225	-0.164	0.160	-0.243	0.079	-0.102	0.461	-0.240	0.083

Precuneus.L	0.156	0.204	0.185	0.115	-0.150	0.199	-0.190	0.157	-0.233	0.053	-0.244	0.083
RosAntCing.L	0.074	0.484	0.133	0.239	0.099	0.415	0.068	0.555	0.049	0.710	0.009	0.979
RosMidFront.L	0.232	0.071	0.226	0.072	-0.281	0.023*	-0.157	0.233	-0.132	0.338	-0.140	0.324
SupFront.L	0.217	0.091	0.232	0.068	-0.320	0.012*	-0.149	0.255	-0.249	0.045*	-0.009	0.979
Insula.L	0.135	0.240	0.232	0.068	-0.262	0.027*	-0.200	0.145	-0.292	0.020*	-0.101	0.545
CaudaAntCing.R	0.231	0.071	0.239	0.068	-0.013	0.934	0.042	0.702	-0.293	0.020*	-0.037	0.913
CaudMidFront.R	0.171	0.175	0.211	0.080	-0.082	0.482	-0.040	0.702	-0.093	0.496	0.060	0.786
LatOrbitoFront.R	0.177	0.175	0.265	0.067	-0.310	0.012*	-0.129	0.341	-0.109	0.438	-0.065	0.778
Paracentral.R	0.243	0.071	0.163	0.155	-0.168	0.156	-0.165	0.233	NaN	NaN	NaN	NaN
PostCentral.R	0.266	0.065	0.192	0.104	-0.244	0.042*	-0.225	0.097	-0.116	0.413	-0.231	0.083
PostCingulate.R	0.286	0.054	0.122	0.271	-0.100	0.415	-0.110	0.385	NaN	NaN	NaN	NaN
Precentral.R	0.089	0.427	0.095	0.366	0.002	0.982	-0.084	0.526	0.043	0.710	-0.047	0.866
Precuneus.R	0.320	0.040*	0.174	0.133	-0.232	0.048*	-0.110	0.385	0.046	0.710	-0.020	0.979
RosAntCing.R	0.082	0.449	0.265	0.067	0.201	0.085	0.071	0.554	0.090	0.496	-0.003	0.979
RosMidFront.R	0.230	0.071	0.211	0.080	-0.268	0.027*	-0.071	0.554	-0.281	0.024*	0.005	0.979
SupFront.R	0.136	0.240	0.192	0.104	-0.199	0.085	-0.078	0.551	-0.240	0.047*	0.026	0.976
SupParietal.R	0.249	0.071	0.133	0.239	-0.225	0.053	-0.202	0.145	0.008	0.939	-0.138	0.324
SupraMarg.R	0.280	0.054	0.270	0.067	-0.349	0.010*	-0.247	0.079	-0.274	0.026*	-0.178	0.208
Insula.R	0.311	0.040*	0.277	0.067	-0.349	0.010*	-0.290	0.051	-0.161	0.228	-0.235	0.083

Appendix table 2.6: Correlation coefficients and p-values for the relationship between cognitive components and graph theory metrics of a given node within the working memory network constructed using a 1.5 SD thresholding approach. R=Pearson's r, p(FDR)=p-value with FDR correction applied across nodes.

2.0 SD units

GT Metrics	Degree				Local Efficiency				Clustering coefficient			
Node	Reasoning		Working mem.		Reasoning		Working mem.		Reasoning		Working mem.	
	R.	p(FDR)	R.	p(FDR)	R.	p(FDR)	R.	p(FDR)	R.	p(FDR)	R.	p(FDR)
Caudate.L	0.188	0.087	0.293	0.037*	-0.291	0.020*	-0.294	0.048*	-0.327	0.019*	-0.213	0.125
Pallidum.L	0.179	0.100	0.238	0.055	-0.245	0.041*	-0.250	0.056	-0.270	0.039*	-0.212	0.125
Hippocampus.L	0.204	0.084	0.211	0.064	-0.258	0.031*	-0.264	0.048*	-0.357	0.015*	-0.294	0.053
Caudate.R	0.190	0.087	0.298	0.037*	-0.260	0.031*	-0.260	0.048*	-0.280	0.039*	-0.258	0.081
Pallidum.R	0.221	0.076	0.279	0.037*	-0.216	0.063	-0.270	0.048*	-0.184	0.134	-0.261	0.081
Hippocampus.R	0.324	0.025*	0.173	0.116	-0.242	0.041*	-0.180	0.147	-0.260	0.040*	-0.167	0.229
CaudAntCing.L	0.292	0.029*	0.227	0.055	-0.082	0.466	0.081	0.474	-0.255	0.040*	0.041	0.864
LatOrbitoFront.L	0.189	0.087	0.223	0.056	-0.290	0.020*	-0.276	0.048*	-0.200	0.102	-0.238	0.114
Paracentral.L	0.191	0.087	0.182	0.108	-0.229	0.051	-0.185	0.141	-0.089	0.492	-0.179	0.195
PostCentral.L	0.189	0.087	0.172	0.116	-0.283	0.022*	-0.189	0.138	-0.272	0.039*	-0.218	0.125
PostCingulate.L	0.205	0.084	0.234	0.055	-0.154	0.176	-0.240	0.060	-0.110	0.440	-0.203	0.125
Precentral.L	0.168	0.121	0.167	0.120	-0.148	0.190	-0.220	0.083	-0.043	0.787	-0.206	0.125
Precuneus.L	0.209	0.084	0.191	0.092	-0.181	0.113	-0.192	0.138	-0.231	0.060	-0.289	0.053
RosAntCing.L	0.129	0.235	0.152	0.149	0.124	0.273	0.095	0.406	0.027	0.829	0.017	0.934
RosMidFront.L	0.246	0.047*	0.234	0.055	-0.273	0.026*	-0.134	0.273	-0.182	0.134	-0.085	0.726
SupFront.L	0.254	0.045*	0.271	0.040*	-0.325	0.016*	-0.158	0.217	-0.267	0.039*	0.005	0.966
Insula.L	0.199	0.087	0.289	0.037*	-0.311	0.016*	-0.265	0.048*	-0.320	0.019*	-0.144	0.329
CaudaAntCing.R	0.251	0.045*	0.252	0.053	-0.076	0.485	0.013	0.903	-0.231	0.060	-0.069	0.754

CaudMidFront.R	0.214	0.083	0.226	0.055	-0.085	0.463	-0.111	0.376	-0.092	0.492	0.073	0.754
LatOrbitoFront.R	0.204	0.084	0.326	0.037*	-0.304	0.016*	-0.223	0.083	-0.156	0.213	-0.078	0.750
Paracentral.R	0.276	0.029*	0.219	0.059	-0.155	0.176	-0.143	0.244	0.026	0.829	0.044	0.864
PostCentral.R	0.226	0.073	0.248	0.054	-0.219	0.062	-0.242	0.060	-0.103	0.464	-0.206	0.125
PostCingulate.R	0.306	0.029*	0.167	0.120	-0.239	0.042*	-0.145	0.244	-0.005	0.964	0.025	0.934
Precentral.R	0.120	0.255	0.157	0.138	-0.010	0.927	-0.098	0.403	0.038	0.796	-0.049	0.862
Precuneus.R	0.360	0.013*	0.195	0.089	-0.203	0.078	-0.150	0.238	0.093	0.492	-0.055	0.846
RosAntCing.R	0.122	0.255	0.227	0.055	0.311	0.016*	0.101	0.403	0.255	0.040*	-0.014	0.934
RosMidFront.R	0.273	0.029*	0.213	0.064	-0.263	0.031*	-0.101	0.403	-0.279	0.039*	-0.013	0.934
SupFront.R	0.195	0.087	0.231	0.055	-0.203	0.078	-0.023	0.857	-0.238	0.058	0.036	0.876
SupParietal.R	0.274	0.029*	0.173	0.116	-0.197	0.084	-0.217	0.083	0.054	0.727	-0.093	0.692
SupraMarg.R	0.281	0.029*	0.252	0.053	-0.329	0.016*	-0.302	0.048*	-0.226	0.062	-0.305	0.053
Insula.R	0.279	0.029*	0.279	0.037*	-0.338	0.016*	-0.284	0.048*	-0.223	0.064	-0.222	0.125

Appendix table 2.7: Correlation coefficients and p-values for the relationship between cognitive components and graph theory metrics of a given node within the working memory network constructed using a 2.0 SD thresholding approach. R=Pearson's r, p(FDR)=p-value with FDR correction applied across nodes.

2.5 SD Units

Working memory network												
GT metrics	**Degree**				**Local Efficiency**				**Clustering coefficient**			
Node	**Reasoning C**		**Work mem C**		**Reasoning C**		**Work mem C**		**Reasoning C**		**Work mem C**	
	R.	p(FDR)	R.	p(FDR)	R.	p(FDR)	R.	p(FDR)	R.	p(FDR)	R.	p(FDR)
Caudate.L†	0.231	0.041*	0.312	0.032*	-0.321	0.029*	-0.297	0.042*	-0.369	0.005*	-0.217	0.118
Pallidum.L	0.236	0.038*	0.225	0.054	-0.281	0.029*	-0.247	0.055	-0.258	0.045*	-0.218	0.118
Hippocampus.L	0.188	0.083	0.222	0.054	-0.273	0.029*	-0.269	0.046*	-0.377	0.005*	-0.321	0.028*
Caudate.R	0.244	0.036*	0.294	0.032*	-0.273	0.029*	-0.266	0.046*	-0.309	0.028*	-0.262	0.073
Pallidum.R†	0.266	0.029*	0.333	0.032*	-0.237	0.051	-0.283	0.044*	-0.202	0.105	-0.241	0.093
Hippocampus.R	0.288	0.025*	0.217	0.054	-0.241	0.049*	-0.189	0.146	-0.257	0.045*	-0.173	0.235
CaudAntCing.L	0.346	0.011*	0.217	0.054	-0.117	0.294	0.093	0.428	-0.272	0.045*	0.067	0.813
LatOrbitoFront.L	0.212	0.053	0.216	0.054	-0.284	0.029*	-0.279	0.044*	-0.251	0.045*	-0.275	0.063
Paracentral.L	0.210	0.053	0.174	0.101	-0.218	0.071	-0.162	0.183	-0.051	0.722	-0.163	0.245
PostCentral.L	0.212	0.053	0.199	0.068	-0.266	0.029*	-0.181	0.153	-0.264	0.045*	-0.199	0.162
PostCingulate.L	0.237	0.038*	0.223	0.054	-0.153	0.195	-0.233	0.062	-0.075	0.567	-0.222	0.118
Precentral.L	0.171	0.110	0.205	0.063	-0.151	0.195	-0.234	0.062	-0.025	0.841	-0.188	0.187
Precuneus.L	0.210	0.053	0.178	0.096	-0.160	0.181	-0.173	0.171	-0.214	0.083	-0.274	0.063
RosAntCing.L	0.175	0.106	0.170	0.105	0.146	0.204	0.143	0.239	0.043	0.728	0.051	0.837
RosMidFront.L	0.269	0.029*	0.235	0.054	-0.245	0.048*	-0.162	0.183	-0.156	0.237	-0.125	0.405
SupFront.L	0.251	0.036*	0.265	0.033*	-0.224	0.065	-0.184	0.152	-0.222	0.075	-0.032	0.878
Insula.L†	0.249	0.036*	0.267	0.033*	-0.301	0.029*	-0.252	0.055	-0.275	0.045*	-0.170	0.235
CaudaAntCing.R	0.242	0.036*	0.276	0.033*	-0.053	0.642	0.027	0.799	-0.254	0.045*	-0.042	0.837
CaudMidFront.R	0.222	0.047*	0.185	0.086	-0.052	0.642	-0.030	0.799	-0.097	0.459	0.101	0.555
LatOrbitoFront.R	0.247	0.036*	0.290	0.032*	-0.268	0.029*	-0.248	0.055	-0.136	0.321	-0.146	0.300
Paracentral.R	0.294	0.025*	0.248	0.049*	-0.136	0.226	-0.120	0.315	0.046	0.728	0.028	0.878

PostCentral.R	0.225	0.045*	0.270	0.033*	-0.198	0.095	-0.232	0.062	-0.086	0.517	-0.160	0.245
PostCingulate.R	0.287	0.025*	0.215	0.054	-0.204	0.087	-0.166	0.183	-0.014	0.897	0.010	0.936
Precentral.R	0.106	0.327	0.194	0.074	0.031	0.773	-0.127	0.295	0.120	0.386	-0.043	0.837
Precuneus.R†	0.353	0.011*	0.228	0.054	-0.164	0.176	-0.142	0.239	0.100	0.459	-0.013	0.936
RosAntCing.R	0.101	0.339	0.298	0.032*	0.216	0.071	0.097	0.424	0.102	0.459	0.044	0.837
RosMidFront.R	0.277	0.026*	0.219	0.054	-0.287	0.029*	-0.091	0.428	-0.281	0.045*	0.009	0.936
SupFront.R	0.249	0.036*	0.233	0.054	-0.144	0.204	-0.054	0.652	-0.237	0.059	0.040	0.837
SupParietal.R†	0.304	0.025*	0.205	0.063	-0.185	0.120	-0.208	0.103	0.118	0.386	-0.063	0.816
SupraMarg.R	0.294	0.025*	0.242	0.053	-0.319	0.029*	-0.299	0.042*	-0.231	0.064	-0.336	0.028*
Insula.R†	0.277	0.026*	0.276	0.033*	-0.292	0.029*	-0.300	0.042*	-0.185	0.141	-0.241	0.093

Appendix table 2.8: Correlation coefficients and p-values for the relationship between cognitive components and graph theory metrics of a given node within the working memory network constructed using a 2.5 SD thresholding approach. R=Pearson's r, p(FDR)=p-value with FDR correction applied across nodes.

3.0 SD units

GT Metrics	Degree				Local Efficiency				Clustering coefficient			
Node	Reasoning		Working mem.		Reasoning		Working mem.		Reasoning		Working mem.	
	R.	p(FDR)	R.	p(FDR)	R.	p(FDR)	R.	p(FDR)	R.	p(FDR)	R.	p(FDR)
Caudate.L	0.259	0.022*	0.314	0.036*	-0.329	0.015*	-0.294	0.047*	-0.372	0.006*	-0.210	0.143
Pallidum.L	0.264	0.020*	0.227	0.043*	-0.287	0.022*	-0.254	0.056	-0.233	0.071	-0.209	0.143
Hippocampus.L	0.208	0.052	0.231	0.043*	-0.282	0.022*	-0.251	0.056	-0.363	0.006*	-0.283	0.064
Caudate.R	0.307	0.013*	0.251	0.043*	-0.315	0.015*	-0.231	0.056	-0.354	0.006*	-0.242	0.090
Pallidum.R	0.318	0.013*	0.318	0.036*	-0.251	0.040*	-0.277	0.047*	-0.163	0.207	-0.208	0.143
Hippocampus.R	0.342	0.009*	0.273	0.043*	-0.224	0.066	-0.178	0.153	-0.212	0.100	-0.174	0.217
CaudAntCing.L	0.354	0.008*	0.223	0.046*	-0.142	0.230	0.069	0.567	-0.313	0.019*	0.045	0.828
LatOrbitoFront.L	0.234	0.033*	0.234	0.043*	-0.310	0.015*	-0.288	0.047*	-0.288	0.028*	-0.268	0.077
Paracentral.L	0.208	0.052	0.196	0.068	-0.190	0.114	-0.231	0.056	-0.043	0.733	-0.204	0.143
PostCentral.L	0.232	0.033*	0.194	0.068	-0.276	0.024*	-0.217	0.073	-0.246	0.056	-0.255	0.089
PostCingulate.L	0.216	0.046*	0.232	0.043*	-0.167	0.157	-0.233	0.056	-0.068	0.577	-0.191	0.161
Precentral.L	0.192	0.071	0.194	0.068	-0.143	0.230	-0.241	0.056	0.025	0.840	-0.197	0.156
Precuneus.L	0.232	0.033*	0.168	0.109	-0.126	0.265	-0.192	0.122	-0.196	0.135	-0.315	0.035*
RosAntCing.L	0.251	0.025*	0.207	0.059	0.202	0.093	0.158	0.178	0.120	0.375	0.047	0.828
RosMidFront.L	0.306	0.013*	0.229	0.043*	-0.245	0.045*	-0.171	0.160	-0.153	0.226	-0.140	0.330
SupFront.L	0.277	0.017*	0.239	0.043*	-0.209	0.083	-0.132	0.262	-0.172	0.183	0.010	0.965
Insula.L	0.242	0.030*	0.267	0.043*	-0.291	0.021*	-0.232	0.056	-0.295	0.027*	-0.144	0.330
CaudaAntCing.R	0.326	0.012*	0.191	0.070	-0.134	0.243	0.009	0.932	-0.253	0.051	-0.055	0.813
CaudMidFront.R	0.256	0.023*	0.195	0.068	-0.019	0.859	-0.037	0.749	-0.084	0.507	0.092	0.622
LatOrbitoFront.R	0.271	0.017*	0.289	0.043*	-0.237	0.051	-0.246	0.056	-0.105	0.412	-0.137	0.330
Paracentral.R	0.293	0.014*	0.245	0.043*	-0.139	0.233	-0.169	0.160	0.076	0.542	-0.071	0.779
PostCentral.R	0.231	0.033*	0.265	0.043*	-0.217	0.073	-0.244	0.056	-0.105	0.412	-0.168	0.226
PostCingulate.R	0.272	0.017*	0.256	0.043*	-0.167	0.157	-0.169	0.160	-0.009	0.932	0.032	0.857
Precentral.R	0.151	0.156	0.211	0.056	0.038	0.741	-0.162	0.174	0.177	0.177	-0.062	0.785
Precuneus.R	0.370	0.008*	0.230	0.043*	-0.089	0.428	-0.153	0.188	0.114	0.396	-0.041	0.828

RosAntCing.R	0.147	0.161	0.248	0.043*	0.348	0.015*	0.062	0.592	0.159	0.210	-0.009	0.965
RosMidFront.R	0.299	0.013*	0.217	0.051	-0.307	0.015*	-0.110	0.353	-0.278	0.032*	0.003	0.978
SupFront.R	0.285	0.017*	0.263	0.043*	-0.118	0.291	-0.084	0.488	-0.271	0.035*	0.030	0.857
SupParietal.R	0.279	0.017*	0.241	0.043*	-0.176	0.146	-0.248	0.056	0.087	0.505	-0.064	0.785
SupraMarg.R	0.304	0.013*	0.242	0.043*	-0.309	0.015*	-0.284	0.047*	-0.216	0.099	-0.330	0.035*
Insula.R	0.281	0.017*	0.280	0.043*	-0.273	0.024*	-0.295	0.047*	-0.190	0.144	-0.245	0.090

Appendix table 2.9: Correlation coefficients and p-values for the relationship between cognitive components and graph theory metrics of a given node within the working memory network constructed using a 3.0 SD thresholding approach. R=Pearson's r, p(FDR)=p-value with FDR correction applied across nodes.

3.5 SD Units

GT Metrics	Degree				Local Efficiency				Clustering coefficient			
Node	Reasoning		Working mem.		Reasoning		Working mem.		Reasoning		Working mem.	
	R.	p(FDR)	R.	p(FDR)	R.	p(FDR)	R.	p(FDR)	R.	p(FDR)	R.	p(FDR)
Caudate.L	0.290	0.015*	0.304	0.032*	-0.304	0.019*	-0.280	0.051	-0.324	0.013*	-0.203	0.175
Pallidum.L	0.248	0.026*	0.223	0.048*	-0.258	0.037*	-0.240	0.058	-0.207	0.122	-0.195	0.175
Hippocampus.L	0.214	0.047*	0.269	0.032*	-0.296	0.019*	-0.248	0.058	-0.368	0.006*	-0.232	0.134
Caudate.R	0.340	0.006*	0.257	0.034*	-0.338	0.019*	-0.238	0.058	-0.362	0.006*	-0.243	0.123
Pallidum.R	0.348	0.006*	0.298	0.032*	-0.297	0.019*	-0.258	0.058	-0.210	0.122	-0.183	0.205
Hippocampus.R	0.342	0.006*	0.273	0.032*	-0.213	0.072	-0.149	0.221	-0.174	0.216	-0.142	0.324
CaudAntCing.L	0.375	0.006*	0.211	0.059	-0.143	0.226	0.068	0.552	-0.292	0.024*	0.062	0.720
LatOrbitoFront.L	0.232	0.033*	0.270	0.032*	-0.313	0.019*	-0.340	0.028*	-0.301	0.022*	-0.324	0.025*
Paracentral.L	0.239	0.030*	0.179	0.097	-0.190	0.103	-0.182	0.134	-0.013	0.899	-0.204	0.175
PostCentral.L	0.220	0.042*	0.176	0.100	-0.251	0.037*	-0.206	0.101	-0.233	0.078	-0.244	0.123
PostCingulate.L	0.210	0.049*	0.226	0.047*	-0.153	0.197	-0.232	0.062	-0.049	0.684	-0.196	0.175
Precentral.L	0.184	0.085	0.183	0.092	-0.153	0.197	-0.239	0.058	0.026	0.834	-0.202	0.175
Precuneus.L	0.256	0.023*	0.184	0.092	-0.127	0.262	-0.197	0.117	-0.149	0.242	-0.292	0.049*
RosAntCing.L	0.258	0.023*	0.157	0.139	0.241	0.046*	0.141	0.242	0.162	0.237	-0.021	0.958
RosMidFront.L	0.299	0.013*	0.229	0.045*	-0.208	0.072	-0.190	0.119	-0.152	0.240	-0.115	0.446
SupFront.L	0.280	0.015*	0.230	0.045*	-0.208	0.072	-0.111	0.350	-0.144	0.254	0.009	0.993
Insula.L	0.257	0.023*	0.245	0.040*	-0.307	0.019*	-0.222	0.075	-0.322	0.013*	-0.165	0.240
CaudaAntCing.R	0.317	0.009*	0.103	0.328	-0.213	0.072	-0.044	0.680	-0.265	0.048*	-0.055	0.751
CaudMidFront.R	0.239	0.030*	0.232	0.045*	-0.019	0.862	-0.052	0.644	-0.073	0.579	0.092	0.590
LatOrbitoFront.R	0.286	0.015*	0.296	0.032*	-0.254	0.037*	-0.253	0.058	-0.132	0.294	-0.145	0.323
Paracentral.R	0.270	0.018*	0.203	0.068	-0.127	0.262	-0.164	0.184	0.092	0.472	-0.129	0.378
PostCentral.R	0.232	0.033*	0.238	0.043*	-0.226	0.059	-0.238	0.058	-0.095	0.472	-0.174	0.217
PostCingulate.R	0.240	0.030*	0.282	0.032*	-0.231	0.056	-0.193	0.118	-0.071	0.579	-0.062	0.720
Precentral.R	0.171	0.106	0.215	0.056	-0.018	0.862	-0.132	0.260	0.165	0.237	-0.004	0.993
Precuneus.R	0.347	0.006*	0.258	0.034*	-0.056	0.638	-0.157	0.198	0.123	0.325	-0.019	0.958
RosAntCing.R	0.133	0.208	0.266	0.032*	0.317	0.019*	-0.074	0.538	0.061	0.624	-0.063	0.720

RosMidFront.R	0.319	0.009*	0.191	0.085	-0.276	0.027*	-0.091	0.447	-0.253	0.054	0.001	0.993
SupFront.R	0.277	0.015*	0.282	0.032*	-0.099	0.384	-0.136	0.252	-0.251	0.054	0.018	0.958
SupParietal.R	0.287	0.015*	0.244	0.040*	-0.138	0.237	-0.279	0.051	0.154	0.240	-0.069	0.720
SupraMarg.R	0.304	0.012*	0.251	0.038*	-0.283	0.024*	-0.311	0.039*	-0.157	0.240	-0.335	0.025*
Insula.R	0.281	0.015*	0.289	0.032*	-0.266	0.032*	-0.274	0.051	-0.202	0.128	-0.180	0.205

Appendix table 2.10: Correlation coefficients and p-values for the relationship between cognitive components and graph theory metrics of a given node within the working memory network constructed using a 3.5 SD thresholding approach. R=Pearson's r, p(FDR)=p-value with FDR correction applied across nodes.

4.0 SD Units

GT Metrics	Degree				Local Efficiency				Clustering coefficient			
Node	Reasoning		Working mem.		Reasoning		Working mem.		Reasoning		Working mem.	
	R.	p(FDR)	R.	p(FDR)	R.	p(FDR)	R.	p(FDR)	R.	p(FDR)	R.	p(FDR)
Caudate.L	0.286	0.013*	0.315	0.023*	-0.306	0.016*	-0.302	0.035*	-0.331	0.010*	-0.244	0.075
Pallidum.L	0.210	0.049*	0.252	0.034*	-0.241	0.047*	-0.292	0.037*	-0.228	0.086	-0.249	0.075
Hippocampus.L	0.242	0.030*	0.262	0.033*	-0.310	0.016*	-0.233	0.065	-0.383	0.004*	-0.248	0.075
Caudate.R	0.351	0.008*	0.257	0.034*	-0.345	0.012*	-0.227	0.069	-0.367	0.004*	-0.247	0.075
Pallidum.R	0.327	0.008*	0.308	0.023*	-0.291	0.019*	-0.250	0.055	-0.221	0.089	-0.151	0.311
Hippocampus.R	0.330	0.008*	0.280	0.023*	-0.237	0.047*	-0.170	0.137	-0.225	0.086	-0.168	0.240
CaudAntCing.L	0.370	0.008*	0.178	0.098	-0.195	0.091	0.013	0.900	-0.365	0.004*	-0.014	0.893
LatOrbitoFront.L	0.214	0.048*	0.283	0.023*	-0.264	0.038*	-0.325	0.025*	-0.253	0.066	-0.280	0.075
Paracentral.L	0.227	0.038*	0.177	0.098	-0.171	0.146	-0.215	0.077	-0.003	0.980	-0.204	0.143
PostCentral.L	0.211	0.049*	0.180	0.098	-0.225	0.056	-0.222	0.069	-0.207	0.114	-0.261	0.075
PostCingulate.L	0.226	0.038*	0.211	0.061	-0.127	0.271	-0.205	0.086	-0.022	0.891	-0.190	0.165
Precentral.L	0.147	0.162	0.159	0.134	-0.115	0.307	-0.244	0.055	-0.015	0.920	-0.238	0.076
Precuneus.L	0.257	0.022*	0.190	0.087	-0.137	0.250	-0.185	0.120	-0.161	0.217	-0.266	0.075
RosAntCing.L	0.281	0.013*	0.183	0.095	0.216	0.063	0.153	0.179	0.108	0.428	0.027	0.869
RosMidFront.L	0.321	0.008*	0.241	0.036*	-0.235	0.047*	-0.224	0.069	-0.145	0.259	-0.117	0.435
SupFront.L	0.281	0.013*	0.239	0.036*	-0.223	0.056	-0.183	0.120	-0.170	0.215	-0.017	0.893
Insula.L	0.283	0.013*	0.255	0.034*	-0.317	0.016*	-0.256	0.055	-0.303	0.017*	-0.205	0.143
CaudaAntCing.R	0.276	0.014*	0.118	0.265	-0.298	0.017*	-0.077	0.481	-0.308	0.017*	-0.084	0.591
CaudMidFront.R	0.230	0.038*	0.243	0.036*	-0.043	0.708	-0.082	0.465	-0.038	0.795	0.082	0.591
LatOrbitoFront.R	0.261	0.020*	0.287	0.023*	-0.237	0.047*	-0.205	0.086	-0.164	0.215	-0.147	0.312
Paracentral.R	0.284	0.013*	0.195	0.081	-0.133	0.257	-0.178	0.125	0.105	0.428	-0.139	0.342
PostCentral.R	0.252	0.024*	0.239	0.036*	-0.210	0.069	-0.255	0.055	-0.075	0.547	-0.192	0.165
PostCingulate.R	0.229	0.038*	0.289	0.023*	-0.244	0.047*	-0.243	0.055	-0.099	0.451	-0.098	0.547
Precentral.R	0.159	0.135	0.207	0.065	-0.011	0.921	-0.127	0.265	0.170	0.215	0.025	0.869
Precuneus.R	0.334	0.008*	0.247	0.036*	-0.082	0.465	-0.176	0.125	0.106	0.428	-0.057	0.734
RosAntCing.R	0.197	0.063	0.284	0.023*	0.421	0.001*	-0.126	0.265	0.076	0.547	-0.066	0.686
RosMidFront.R	0.337	0.008*	0.222	0.049*	-0.312	0.016*	-0.092	0.425	-0.238	0.086	0.037	0.863
SupFront.R	0.302	0.012*	0.283	0.023*	-0.146	0.221	-0.186	0.120	-0.232	0.086	0.028	0.869
SupParietal.R	0.291	0.013*	0.235	0.037*	-0.125	0.271	-0.259	0.055	0.153	0.235	-0.089	0.590
SupraMarg.R	0.289	0.013*	0.272	0.027*	-0.239	0.047*	-0.340	0.025*	-0.086	0.516	-0.312	0.075
Insula.R	0.304	0.012*	0.307	0.023*	-0.259	0.040*	-0.258	0.055	-0.164	0.215	-0.118	0.435

Appendix table 2.11: Correlation coefficients and p-values for the relationship between cognitive components and graph theory metrics of a given node within the working memory network constructed using a 4.0 SD thresholding approach. R=Pearson's r, p(FDR)=p-value with FDR correction applied across nodes.

4.5 SD Units

GT Metrics	Degree				Local Efficiency				Clustering coefficient			
Node	Reasoning		Working mem.		Reasoning		Working mem,		Reasoning		Working mem.	
	R.	p(FDR)	R.	p(FDR)	R.	p(FDR)	R.	p(FDR)	R.	p(FDR)	R.	p(FDR)
Caudate.L	0.294	0.011*	0.303	0.015*	-0.337	0.011*	-0.305	0.027*	-0.365	0.003*	-0.246	0.071
Pallidum.L	0.222	0.041*	0.247	0.029*	-0.246	0.033*	-0.286	0.035*	-0.213	0.120	-0.249	0.071
Hippocampus.L	0.261	0.018*	0.257	0.027*	-0.325	0.012*	-0.216	0.067	-0.385	0.003*	-0.226	0.104
Caudate.R	0.356	0.007*	0.269	0.027*	-0.369	0.005*	-0.256	0.039*	-0.382	0.003*	-0.261	0.071
Pallidum.R	0.314	0.009*	0.307	0.015*	-0.300	0.017*	-0.247	0.045*	-0.249	0.058	-0.140	0.358
Hippocampus.R	0.314	0.009*	0.268	0.027*	-0.272	0.024*	-0.228	0.060	-0.268	0.043*	-0.218	0.104
CaudAntCing.L	0.363	0.007*	0.169	0.114	-0.269	0.025*	-0.013	0.899	-0.371	0.003*	-0.037	0.840
LatOrbitoFront.L	0.228	0.037*	0.309	0.015*	-0.279	0.022*	-0.350	0.015*	-0.263	0.043*	-0.324	0.040*
Paracentral.L	0.214	0.049*	0.180	0.099*	-0.180	0.120	-0.209	0.070	-0.035	0.791	-0.189	0.157
PostCentral.L	0.191	0.073	0.170	0.114	-0.214	0.067	-0.228	0.060	-0.190	0.154	-0.260	0.071
PostCingulate.L	0.209	0.053	0.227	0.042*	-0.112	0.319	-0.222	0.061	-0.024	0.824	-0.198	0.151
Precentral.L	0.155	0.145	0.184	0.098	-0.134	0.243	-0.256	0.039*	-0.027	0.821	-0.219	0.104
Precuneus.L	0.258	0.019*	0.180	0.099	-0.157	0.183	-0.203	0.074	-0.166	0.206	-0.278	0.071
RosAntCing.L	0.321	0.009*	0.131	0.213	0.250	0.033*	0.153	0.181	0.128	0.321	0.017	0.891
RosMidFront.L	0.324	0.009*	0.259	0.027*	-0.257	0.030*	-0.266	0.039*	-0.119	0.346	-0.122	0.426
SupFront.L	0.275	0.014*	0.263	0.027*	-0.218	0.063	-0.223	0.061	-0.134	0.316	-0.026	0.857
Insula.L	0.277	0.014*	0.266	0.027*	-0.316	0.013*	-0.301	0.027*	-0.302	0.018*	-0.249	0.071
CaudaAntCing.R	0.331	0.009*	0.150	0.159	-0.298	0.017*	-0.106	0.347	-0.320	0.011*	-0.101	0.555
CaudMidFront.R	0.205	0.055	0.256	0.027*	-0.020	0.880	-0.099	0.369	-0.054	0.724	0.055	0.839
LatOrbitoFront.R	0.262	0.018*	0.324	0.015*	-0.207	0.071	-0.188	0.095	-0.134	0.316	-0.122	0.426
Paracentral.R	0.300	0.011*	0.215	0.054	-0.129	0.252	-0.206	0.072	0.127	0.321	-0.180	0.177
PostCentral.R	0.278	0.014*	0.252	0.028*	-0.209	0.071	-0.271	0.039*	-0.036	0.791	-0.194	0.151
PostCingulate.R	0.244	0.025*	0.261	0.027*	-0.261	0.028*	-0.236	0.056	-0.083	0.535	-0.048	0.839
Precentral.R	0.145	0.167	0.209	0.059	-0.012	0.906	-0.119	0.296	0.153	0.248	0.051	0.839
Precuneus.R	0.303	0.011*	0.247	0.029*	-0.056	0.634	-0.212	0.069	0.171	0.206	-0.015	0.891
RosAntCing.R	0.263	0.018*	0.304	0.015*	0.380	0.005*	-0.086	0.428	0.040	0.791	-0.030	0.857
RosMidFront.R	0.348	0.007*	0.233	0.039*	-0.290	0.020*	-0.125	0.279	-0.209	0.120	0.040	0.840
SupFront.R	0.295	0.011*	0.303	0.015*	-0.150	0.192	-0.193	0.088	-0.208	0.120	0.036	0.840
SupParietal.R	0.292	0.011*	0.232	0.039*	-0.150	0.192	-0.280	0.035*	0.168	0.206	-0.067	0.777
SupraMarg.R	0.289	0.011*	0.276	0.027*	-0.246	0.033*	-0.338	0.015*	-0.102	0.429	-0.310	0.040*
Insula.R	0.281	0.014*	0.320	0.015*	-0.281	0.022*	-0.261	0.039*	-0.191	0.154	-0.085	0.648

Appendix table 2.12: Correlation coefficients and p-values for the relationship between cognitive components and graph theory metrics of a given node within the working memory network constructed using a 4.5 SD thresholding approach. R=Pearson's r, p(FDR)=p-value with FDR correction applied across nodes.

5.0 SD Units

GT Metrics	Degree				Local Efficiency				Clustering coefficient			
Node	Reasoning		Working mem.		Reasoning		Working mem.		Reasoning		Working mem.	
	R.	p(FDR)	R.	p(FDR)	R.	p(FDR)	R.	p(FDR)	R.	p(FDR)	R.	p(FDR)
Caudate.L	0.301	0.015*	0.307	0.023*	-0.335	0.014*	-0.304	0.017*	-0.354	0.004*	-0.228	0.091
Pallidum.L	0.190	0.077	0.261	0.025*	-0.208	0.077	-0.311	0.016*	-0.202	0.126	-0.282	0.050
Hippocampus.L	0.277	0.016*	0.239	0.035*	-0.321	0.014*	-0.200	0.075	-0.354	0.004*	-0.225	0.091
Caudate.R	0.345	0.008*	0.282	0.023*	-0.355	0.014*	-0.252	0.046*	-0.365	0.004*	-0.238	0.091
Pallidum.R	0.302	0.015*	0.271	0.023*	-0.294	0.020*	-0.247	0.046*	-0.261	0.042*	-0.169	0.208
Hippocampus.R	0.287	0.015*	0.275	0.023*	-0.293	0.020*	-0.240	0.050	-0.289	0.027*	-0.236	0.091
CaudAntCing.L	0.355	0.008*	0.167	0.122	-0.313	0.015*	0.009	0.930	-0.410	0.002*	-0.036	0.864
LatOrbitoFront.L	0.252	0.021*	0.338	0.023*	-0.284	0.021*	-0.343	0.016*	-0.262	0.042*	-0.288	0.050
Paracentral.L	0.207	0.059	0.178	0.102	-0.165	0.163	-0.210	0.065	-0.006	0.981	-0.220	0.091
PostCentral.L	0.194	0.073	0.166	0.122	-0.208	0.077	-0.227	0.056	-0.175	0.196	-0.263	0.058
PostCingulate.L	0.219	0.046*	0.208	0.062	-0.128	0.265	-0.215	0.062	-0.047	0.785	-0.201	0.126
Precentral.L	0.150	0.155	0.181	0.101	-0.110	0.338	-0.252	0.046*	0.024	0.907	-0.220	0.091
Precuneus.L	0.263	0.018*	0.188	0.092	-0.138	0.236	-0.226	0.056	-0.124	0.389	-0.269	0.058
RosAntCing.L	0.313	0.015*	0.109	0.302	0.227	0.071	0.190	0.089	0.078	0.592	0.024	0.864
RosMidFront.L	0.282	0.015*	0.252	0.027*	-0.179	0.129	-0.310	0.016*	0.003	0.981	-0.114	0.456
SupFront.L	0.279	0.016*	0.272	0.023*	-0.213	0.077	-0.222	0.058	-0.068	0.642	-0.002	0.982
Insula.L	0.255	0.021*	0.265	0.024*	-0.289	0.020*	-0.315	0.016*	-0.290	0.027*	-0.292	0.050
CaudaAntCing.R	0.345	0.008*	0.162	0.126	-0.274	0.023*	-0.157	0.161	-0.261	0.042*	-0.124	0.412
CaudMidFront.R	0.182	0.089	0.227	0.043*	-0.088	0.430	-0.130	0.242	-0.112	0.412	0.022	0.864
LatOrbitoFront.R	0.253	0.021*	0.299	0.023*	-0.188	0.112	-0.208	0.066	-0.111	0.412	-0.160	0.233
Paracentral.R	0.294	0.015*	0.220	0.050	-0.144	0.222	-0.217	0.061	0.118	0.406	-0.187	0.154
PostCentral.R	0.284	0.015*	0.273	0.023*	-0.211	0.077	-0.293	0.020*	-0.014	0.952	-0.199	0.126
PostCingulate.R	0.195	0.073	0.302	0.023*	-0.212	0.077	-0.235	0.053	-0.124	0.389	-0.092	0.565
Precentral.R	0.150	0.155	0.187	0.092	-0.031	0.772	-0.073	0.508	0.158	0.254	0.093	0.565
Precuneus.R	0.271	0.016*	0.256	0.025*	-0.058	0.602	-0.229	0.056	0.127	0.389	-0.057	0.761
RosAntCing.R	0.262	0.018*	0.288	0.023*	0.329	0.014*	-0.117	0.287	0.040	0.806	-0.067	0.706
RosMidFront.R	0.317	0.015*	0.258	0.025*	-0.255	0.036*	-0.145	0.194	-0.213	0.121	0.038	0.864
SupFront.R	0.297	0.015*	0.292	0.023*	-0.144	0.222	-0.179	0.108	-0.208	0.121	0.028	0.864
SupParietal.R	0.263	0.018*	0.238	0.035*	-0.093	0.418	-0.266	0.041*	0.208	0.121	-0.025	0.864
SupraMarg.R	0.273	0.016*	0.269	0.023*	-0.218	0.077	-0.332	0.016*	-0.093	0.506	-0.323	0.050
Insula.R	0.283	0.015*	0.321	0.023*	-0.276	0.023*	-0.246	0.046*	-0.179	0.193	-0.068	0.706

Appendix table 2.13: Correlation coefficients and p-values for the relationship between cognitive components and graph theory metrics of a given node within the working memory network constructed using a 5.0 SD thresholding approach. R=Pearson's r, p(FDR)=p-value with FDR correction applied across nodes.

Reasoning network correlations to cognitive components across all structural connectome threshold iterations (see supplementary figure 10 for graphical illustration of results)

0.5 SD Units

GT Metrics	Degree				Local Eff				Clustering Coeff			
Node	Reasoning		Working mem.		Reasoning		Working mem.		Reasoning		Working mem.	
	R.	p(FDR)	R.	p(FDR)	R.	p(FDR)	R.	p(FDR)	R.	p(FDR)	R.	p(FDR)
CaudMidFront.L	0.015	0.884	0.148	0.459	-0.067	0.704	0.101	0.835	-0.080	0.765	-0.054	0.899
Cuneus.L	0.060	0.647	-0.098	0.555	-0.123	0.445	-0.036	0.952	-0.126	0.639	-0.023	0.899
Fusiform.L	0.149	0.389	0.054	0.757	-0.077	0.681	-0.077	0.866	-0.068	0.765	-0.062	0.899
InfParietal.L	0.263	0.097	0.046	0.781	-0.278	0.067	-0.032	0.952	-0.240	0.154	-0.190	0.381
InfTemporal.L	0.187	0.244	0.003	0.979	-0.170	0.345	-0.031	0.952	-0.078	0.765	0.005	0.962
LatOcc.L	0.174	0.283	0.155	0.459	-0.137	0.415	-0.017	0.970	-0.184	0.440	-0.038	0.899
LatOrbFront.L	0.135	0.389	0.026	0.839	-0.292	0.067	-0.101	0.835	NaN	NaN	NaN	NaN
ParsOperc.L	-0.099	0.503	-0.056	0.757	-0.193	0.282	-0.005	0.972	-0.314	0.051	-0.100	0.815
Pericalcarine.L	0.133	0.389	0.032	0.826	-0.145	0.412	-0.112	0.835	-0.018	0.897	0.118	0.723
Precentral.L	-0.085	0.548	0.192	0.388	-0.081	0.681	-0.052	0.952	-0.104	0.765	-0.156	0.506
RosMidFront.L	0.107	0.480	0.105	0.553	-0.025	0.884	0.150	0.835	NaN	NaN	NaN	NaN
SupFront.L	0.040	0.767	0.127	0.484	0.015	0.923	0.143	0.835	0.045	0.889	0.252	0.169
SupParietal.L	0.141	0.389	0.191	0.388	-0.276	0.067	-0.104	0.835	-0.245	0.154	-0.260	0.169
CaudMidFront.R	-0.026	0.837	0.183	0.388	0.076	0.681	-0.015	0.970	NaN	NaN	NaN	NaN
Cuneus.R	0.197	0.222	0.178	0.388	-0.151	0.412	-0.036	0.952	0.093	0.765	0.040	0.899
Fusiform.R	0.225	0.133	0.068	0.710	-0.183	0.302	-0.100	0.835	-0.070	0.765	-0.170	0.464
InfParietal.R	0.387	0.004*	0.096	0.555	-0.219	0.234	0.004	0.972	-0.026	0.889	-0.020	0.899
InfTemporal.R	0.252	0.100	0.150	0.459	-0.119	0.445	-0.081	0.866	-0.014	0.897	0.034	0.899
LateralOcc.R	0.132	0.389	0.187	0.388	-0.063	0.704	-0.111	0.835	0.042	0.889	-0.094	0.815
Lingual.R	0.121	0.436	0.038	0.812	-0.143	0.412	-0.052	0.952	-0.172	0.448	-0.206	0.362
ParsOperc.R	0.077	0.578	0.126	0.484	-0.031	0.872	-0.014	0.970	-0.133	0.639	0.029	0.899
Paricalcarine.R	0.232	0.133	0.117	0.493	-0.196	0.282	-0.098	0.835	-0.136	0.639	-0.042	0.899
Precentral.R	0.072	0.587	0.303	0.086	-0.048	0.765	-0.174	0.835	0.031	0.889	-0.019	0.899
RosMidFront.R	0.087	0.548	0.086	0.603	0.060	0.704	0.068	0.905	0.088	0.765	0.145	0.525
SupFront.R	0.106	0.480	0.133	0.484	0.010	0.926	0.109	0.835	NaN	NaN	NaN	NaN
SupParietal.R	0.335	0.014*	0.123	0.484	-0.125	0.445	0.084	0.866	0.029	0.889	0.033	0.899

Appendix table 2.14: Correlation coefficients and p-values for the relationship between cognitive components and graph theory metrics of a given node within the reasoning network constructed using a 0.5 SD thresholding approach. R=Pearson's r, p(FDR)=p-value with FDR correction applied across nodes.

1.0 SD Units

GT Metrics	Degree		Local Eff		Clustering Coeff	
Node	Reasoning	Working mem.	Reasoning	Working mem.	Reasoning	Working mem.

	R.	p(FDR)	R.	p(FDR)	R.	p(FDR)	R.	p(FDR)	R.	p(FDR)	R.	p(FDR)
CaudMidFront.L	0.005	0.959	0.044	0.768	0.013	0.971	0.119	0.727	-0.105	0.566	0.007	0.949
Cuneus.L	0.161	0.181	-0.050	0.751	-0.108	0.395	0.032	0.849	-0.154	0.443	-0.046	0.787
Fusiform.L	0.176	0.162	0.027	0.802	-0.132	0.338	-0.092	0.765	-0.143	0.451	-0.170	0.478
InfParietal.L	0.321	0.009*	0.080	0.599	-0.334	0.024*	-0.070	0.829	-0.314	0.035*	-0.166	0.478
InfTemporal.L	0.305	0.013*	-0.034	0.775	-0.299	0.024*	-0.034	0.849	-0.277	0.047*	-0.179	0.478
LatOcc.L	0.259	0.033*	0.106	0.588	-0.277	0.028*	-0.054	0.849	-0.308	0.035*	-0.056	0.787
LatOrbFront.L	0.173	0.162	0.154	0.373	-0.303	0.024*	-0.175	0.727	-0.042	0.806	-0.020	0.920
ParsOperc.L	-0.035	0.835	0.039	0.771	-0.186	0.179	-0.108	0.727	-0.288	0.045*	-0.109	0.758
Pericalcarine.L	0.188	0.134	0.055	0.745	-0.186	0.179	-0.029	0.849	-0.119	0.547	0.059	0.787
Precentral.L	0.016	0.915	0.126	0.541	-0.019	0.971	-0.109	0.727	-0.043	0.806	-0.176	0.478
RosMidFront.L	0.255	0.033*	0.083	0.599	0.009	0.971	0.168	0.727	0.118	0.547	0.061	0.787
SupFront.L	0.024	0.885	0.200	0.214	0.118	0.373	0.094	0.765	0.070	0.745	0.191	0.478
SupParietal.L	0.327	0.009*	0.243	0.214	-0.309	0.024*	-0.144	0.727	-0.218	0.182	-0.266	0.260
CaudMidFront.R	0.067	0.621	0.199	0.214	0.116	0.373	-0.048	0.849	-0.046	0.806	0.042	0.787
Cuneus.R	0.296	0.016*	0.204	0.214	-0.179	0.190	0.007	0.950	0.034	0.806	0.092	0.787
Fusiform.R	0.247	0.036*	0.089	0.599	-0.232	0.084	-0.136	0.727	-0.174	0.346	-0.128	0.701
InfParietal.R	0.404	0.001*	0.078	0.599	-0.210	0.128	-0.039	0.849	-0.011	0.918	-0.059	0.787
InfTemporal.R	0.267	0.029*	0.121	0.541	-0.146	0.305	-0.133	0.727	-0.030	0.806	-0.045	0.787
LateralOcc.R	0.289	0.017*	0.183	0.263	-0.136	0.338	-0.143	0.727	0.032	0.806	-0.043	0.787
Lingual.R	0.246	0.036*	0.094	0.599	-0.284	0.026*	-0.078	0.799	-0.191	0.286	-0.112	0.758
ParsOperc.R	0.119	0.338	0.206	0.214	-0.011	0.971	0.008	0.950	-0.108	0.566	0.059	0.787
Paricalcarine.R	0.322	0.009*	0.217	0.214	-0.284	0.026*	-0.108	0.727	-0.141	0.451	0.054	0.787
Precentral.R	0.161	0.181	0.223	0.214	-0.002	0.986	-0.142	0.727	0.064	0.755	-0.016	0.920
RosMidFront.R	0.086	0.511	0.085	0.599	0.154	0.287	0.083	0.797	0.076	0.733	0.149	0.555
SupFront.R	0.153	0.200	0.116	0.543	0.091	0.480	0.060	0.849	NaN	NaN	NaN	NaN
SupParietal.R	0.413	0.001*	0.173	0.288	-0.128	0.340	-0.042	0.849	0.081	0.733	-0.054	0.787

Appendix table 2.15: Correlation coefficients and p-values for the relationship between cognitive components and graph theory metrics of a given node within the reasoning network constructed using a 1.0 SD thresholding approach. R=Pearson's r, p(FDR)=p-value with FDR correction applied across nodes.

1.5 SD Units

GT Metrics	Degree				Local Eff				Clustering Coeff			
Node	Reasoning		Working mem.		Reasoning		Working mem.		Reasoning		Working mem.	
	R.	p(FDR)	R.	P(FDR)	R.	p(FDR)	R.	p(FDR)	R.	p(FDR)	R.	p(FDR)
CaudMidFron.L	0.137	0.200	-0.015	0.884	-0.020	0.854	0.148	0.458	-0.082	0.648	-0.033	0.899
Cuneus.L	0.242	0.032*	0.148	0.318	-0.124	0.326	-0.040	0.829	-0.150	0.386	-0.021	0.914
Fusiform.L	0.200	0.076	0.077	0.502	-0.202	0.083	-0.144	0.458	-0.222	0.106	-0.195	0.223
InfParietal.L	0.350	0.003*	0.117	0.364	-0.341	0.011*	-0.114	0.556	-0.288	0.033*	-0.196	0.223
InfTemporal.L	0.377	0.001*	-0.047	0.685	-0.342	0.011*	-0.050	0.789	-0.334	0.014*	-0.288	0.045
LatOcc.L	0.335	0.004*	0.101	0.442	-0.287	0.018*	-0.086	0.677	-0.308	0.023*	-0.082	0.867
LatOrbFront.L	0.207	0.073	0.209	0.260	-0.295	0.016*	-0.160	0.458	-0.048	0.772	-0.012	0.947
ParsOperc.L	0.162	0.153	0.173	0.260	-0.253	0.036*	-0.137	0.458	-0.340	0.014*	-0.038	0.899
Pericalcarine.L	0.266	0.019*	0.162	0.289	-0.258	0.034*	-0.061	0.730	-0.226	0.106	0.048	0.867
Precentral.L	0.143	0.190	0.092	0.455	-0.019	0.854	-0.142	0.458	-0.010	0.961	-0.202	0.223

RosMidFront.L	0.290	0.011*	0.120	0.364	-0.102	0.393	0.149	0.458	-0.005	0.961	0.047	0.867
SupFront.L	0.152	0.168	0.219	0.260	0.149	0.225	0.219	0.458	0.083	0.648	0.299	0.045
SupParietal.L	0.344	0.003*	0.225	0.260	-0.310	0.012*	-0.174	0.458	-0.275	0.040*	-0.290	0.045
CaudMidFront.R	0.152	0.168	0.173	0.260	0.117	0.344	0.024	0.886	0.023	0.903	0.053	0.867
Cuneus.R	0.356	0.003*	0.138	0.325	-0.247	0.038*	-0.002	0.985	-0.061	0.706	0.069	0.867
Fusiform.R	0.303	0.008*	0.096	0.452	-0.277	0.022*	-0.139	0.458	-0.175	0.264	-0.131	0.588
InfParietal.R	0.377	0.001*	0.086	0.472	-0.309	0.012*	-0.099	0.649	-0.139	0.420	-0.148	0.500
InfTemporal.R	0.272	0.017*	0.131	0.325	-0.202	0.083	-0.199	0.458	-0.070	0.665	-0.100	0.860
LateralOcc.R	0.320	0.005*	0.134	0.325	-0.220	0.065	-0.085	0.677	-0.104	0.577	0.001	0.992
Lingual.R	0.329	0.004*	0.136	0.325	-0.331	0.011*	-0.077	0.677	-0.266	0.044*	-0.061	0.867
ParsOperc.R	0.196	0.079	0.194	0.260	0.049	0.694	0.003	0.985	-0.076	0.656	0.050	0.867
Paricalcarine.R	0.391	0.001*	0.178	0.260	-0.318	0.012*	-0.078	0.677	-0.081	0.648	0.067	0.867
Precentral.R	0.245	0.032*	0.189	0.260	0.053	0.694	-0.032	0.862	0.124	0.494	0.059	0.867
RosMidFront.R	0.094	0.372	0.154	0.310	0.222	0.065	0.213	0.458	0.114	0.536	0.252	0.097
SupFront.R	0.201	0.076	0.173	0.260	0.104	0.393	0.121	0.547	NaN	NaN	NaN	NaN
SupParietal.R	0.411	0.001*	0.202	0.260	-0.204	0.083	-0.067	0.716	0.043	0.780	-0.022	0.914

Appendix table 2.16: Correlation coefficients and p-values for the relationship between cognitive components and graph theory metrics of a given node within the reasoning network constructed using a 1.5 SD thresholding approach. R=Pearson's r, p(FDR)=p-value with FDR correction applied across nodes.

2.0 SD Units

GT Metrics	Degree				Local Eff				Clustering Coeff			
Node	Reasoning		Working mem.		Reasoning		Working mem.		Reasoning		Working mem	
	R.	p(FDR)	R.	p(FDR)	R.	p(FDR)	R.	p(FDR)	R.	p(FDR)	R.	p(FDR)
Cuneus.L	0.327	0.003*	0.120	0.329	-0.174	0.127	-0.068	0.713	-0.202	0.138	-0.084	0.719
Fusiform.L	0.249	0.024*	0.131	0.317	-0.273	0.018*	-0.201	0.472	-0.268	0.037*	-0.237	0.149
InfParietal.L	0.352	0.002*	0.129	0.317	-0.360	0.006*	-0.111	0.472	-0.328	0.027*	-0.169	0.350
InfTemporal.L	0.336	0.002*	-0.007	0.946	-0.351	0.006*	-0.127	0.472	-0.288	0.029*	-0.304	0.058
LatOcc.L	0.366	0.001*	0.125	0.322	-0.339	0.006*	-0.133	0.472	-0.317	0.027*	-0.143	0.496
LatOrbFront.L	0.252	0.024*	0.255	0.179	-0.284	0.014*	-0.150	0.472	-0.103	0.475	-0.012	0.922
ParsOperc.L	0.229	0.036*	0.208	0.179	-0.215	0.060	-0.118	0.472	-0.287	0.029*	-0.011	0.922
Pericalcarine.L	0.338	0.002*	0.228	0.179	-0.299	0.010*	-0.139	0.472	-0.303	0.029*	-0.034	0.887
Precentral.L	0.095	0.367	0.060	0.594	0.016	0.880	-0.117	0.472	0.008	0.938	-0.198	0.272
RosMidFront.L	0.281	0.011*	0.186	0.204	-0.077	0.549	0.093	0.547	-0.084	0.525	0.059	0.788
SupFront.L	0.160	0.145	0.255	0.179	0.213	0.060	0.185	0.472	0.155	0.260	0.253	0.128
SupParietal.L	0.337	0.002*	0.147	0.280	-0.314	0.007*	-0.168	0.472	-0.281	0.029*	-0.294	0.058
CaudMidFront.R	0.189	0.085	0.179	0.204	0.158	0.163	0.024	0.890	0.122	0.379	0.114	0.528
Cuneus.R	0.388	0.001*	0.179	0.204	-0.241	0.038*	-0.033	0.854	-0.061	0.668	0.070	0.733
Fusiform.R	0.342	0.002*	0.102	0.393	-0.326	0.006*	-0.143	0.472	-0.219	0.103	-0.122	0.528
InfParietal.R	0.379	0.001*	0.113	0.350	-0.333	0.006*	-0.114	0.472	-0.127	0.372	-0.132	0.496
InfTemporal.R	0.285	0.011*	0.175	0.204	-0.265	0.021*	-0.186	0.472	-0.085	0.525	-0.081	0.719
LateralOcc.R	0.372	0.001*	0.141	0.293	-0.298	0.010*	-0.006	0.991	-0.153	0.260	0.074	0.733
Lingual.R	0.333	0.003*	0.162	0.244	-0.341	0.006*	-0.123	0.472	-0.262	0.038*	-0.113	0.528
ParsOperc.R	0.230	0.036*	0.157	0.252	0.072	0.562	-0.001	0.992	-0.019	0.888	0.018	0.922
Paricalcarine.R	0.412	0.001*	0.206	0.179	-0.322	0.006*	-0.054	0.732	-0.178	0.210	0.046	0.817

Precentral.R	0.261	0.019*	0.229	0.179	0.058	0.629	0.053	0.732	0.151	0.260	0.132	0.496
RosMidFront.R	0.151	0.164	0.099	0.393	0.219	0.059	0.209	0.472	0.050	0.722	0.195	0.272
SupFront.R	0.219	0.044*	0.214	0.179	0.174	0.127	0.164	0.472	-0.160	0.260	0.171	0.350
SupParietal.R	0.411	0.001*	0.197	0.197	-0.235	0.042*	-0.098	0.537	0.032	0.825	-0.054	0.789

Appendix table 2.17: Correlation coefficients and p-values for the relationship between cognitive components and graph theory metrics of a given node within the reasoning network constructed using a 2.0 SD thresholding approach. R=Pearson's r, p(FDR)=p-value with FDR correction applied across nodes.

2.5 SD Units

Reasoning network												
	Degree				Local Efficiency				Clustering coefficient			
Node	Reasoning		Work mem		Reasoning		Work mem		Reasoning		Work mem	
	R.	FDR	R	FDR	R	FDR	R	FDR	R	FDR	R	FDR
CaudMidFront.L	0.141	0.193	0.095	0.398	0.035	0.800	-0.078	0.665	-0.022	0.838	-0.060	0.752
Cuneus.L	0.331	0.003**	0.107	0.366	-0.334	0.004**	-0.036	0.829	-0.332	0.010*	-0.059	0.752
Fusiform.L	0.299	0.007**	0.164	0.219	-0.334	0.004**	-0.251	0.207	-0.321	0.010*	-0.258	0.112
InfParietal.L	0.338	0.003**	0.120	0.329	-0.347	0.004**	-0.123	0.444	-0.317	0.010*	-0.177	0.328
InfTemporal.L	0.288	0.009**	0.070	0.526	-0.337	0.004**	-0.176	0.444	-0.339	0.010*	-0.310	0.068
LatOcc.L	0.369	0.002**	0.122	0.329	-0.331	0.004**	-0.142	0.444	-0.314	0.010*	-0.177	0.328
LatOrbFront.L	0.245	0.024*	0.238	0.136	-0.208	0.064	-0.158	0.444	-0.087	0.534	-0.006	0.958
ParsOperc.L	0.308	0.005**	0.187	0.160	-0.236	0.034*	-0.116	0.444	-0.286	0.019*	-0.042	0.812
Pericalcarine.L	0.355	0.002**	0.211	0.142	-0.367	0.004**	-0.111	0.444	-0.322	0.010*	-0.038	0.812
Precentral.L	0.085	0.420	0.066	0.534	0.005	0.959	-0.113	0.444	0.025	0.838	-0.172	0.328
RosMidFront.L†	0.280	0.010*	0.198	0.151	-0.020	0.885	0.032	0.829	-0.022	0.838	-0.076	0.718
SupFront.L†	0.195	0.071	0.256	0.136	0.284	0.012*	0.136	0.444	0.242	0.058	0.193	0.328
SupParietal.L†	0.345	0.002**	0.130	0.311	-0.338	0.004**	-0.141	0.444	-0.300	0.014*	-0.261	0.112
CaudMidFront.R	0.230	0.032*	0.224	0.136	0.134	0.240	0.011	0.941	0.112	0.495	0.160	0.337
Cuneus.R	0.439	0.000***	0.180	0.174	-0.305	0.007**	-0.038	0.829	-0.081	0.547	0.061	0.752
Fusiform.R	0.347	0.002**	0.151	0.250	-0.321	0.005**	-0.159	0.444	-0.214	0.087	-0.109	0.558
InfParietal.R†	0.366	0.002**	0.139	0.285	-0.329	0.004**	-0.160	0.444	-0.094	0.534	-0.137	0.387
InfTemporal.R	0.331	0.003**	0.191	0.160	-0.272	0.014*	-0.253	0.207	-0.087	0.534	-0.148	0.346
LateralOcc.R	0.327	0.003**	0.113	0.354	-0.278	0.013*	-0.034	0.829	-0.139	0.344	0.025	0.881
Lingual.R	0.358	0.002**	0.203	0.151	-0.311	0.006**	-0.155	0.444	-0.219	0.085	-0.099	0.605
ParsOperc.R	0.257	0.018*	0.230	0.136	0.136	0.240	0.008	0.941	0.108	0.495	0.078	0.718
Paricalcarine.R	0.419	0.000***	0.150	0.250	-0.314	0.006**	-0.055	0.787	-0.159	0.262	0.013	0.939
Precentral.R	0.233	0.032*	0.250	0.136	0.085	0.476	0.061	0.769	0.230	0.072	0.155	0.337
RosMidFront.R	0.137	0.202	0.095	0.398	0.252	0.024*	0.215	0.344	0.074	0.568	0.179	0.328
SupFront.R	0.259	0.018*	0.269	0.136	0.204	0.067	0.114	0.444	-0.095	0.534	0.154	0.337
SupParietal.R†	0.436	0.000***	0.212	0.142	-0.277	0.013*	-0.121	0.444	0.030	0.838	-0.041	0.812

Appendix table 2.18: Correlation coefficients and p-values for the relationship between cognitive components and graph theory metrics of a given node within the reasoning network constructed using a 2.5 SD thresholding approach. R=Pearson's r, p(FDR)=p-value with FDR correction applied across nodes.

3.0 SD Units

GT Metrics	Degree				Local Eff				Clustering Coeff			
Node	Reasoning		Working mem.		Reasoning		Working mem.		Reasoning		Working mem.	
	R.	p(FDR)	R.	p(FDR)	R.	p(FDR)	R.	p(FDR)	R.	p(FDR)	R.	p(FDR)
CaudMidFront.L	0.208	0.050	0.113	0.337	0.120	0.301	-0.034	0.806	0.057	0.641	-0.074	0.702
Cuneus.L	0.336	0.002*	0.107	0.348	-0.337	0.003*	-0.064	0.746	-0.330	0.006*	-0.064	0.740
Fusiform.L	0.342	0.002*	0.194	0.187	-0.371	0.003*	-0.221	0.383	-0.343	0.006*	-0.221	0.315
InfParietal.L	0.350	0.002*	0.141	0.236	-0.351	0.003*	-0.125	0.383	-0.333	0.006*	-0.154	0.449
InfTemporal.L	0.302	0.005*	0.075	0.477	-0.374	0.003*	-0.204	0.383	-0.336	0.006*	-0.296	0.108
LatOcc.L	0.356	0.001*	0.146	0.236	-0.342	0.003*	-0.128	0.383	-0.344	0.006*	-0.124	0.515
LatOrbFront.L	0.259	0.014*	0.269	0.100	-0.171	0.128	-0.143	0.383	-0.047	0.685	0.040	0.767
ParsOperc.L	0.265	0.013*	0.142	0.236	-0.089	0.431	-0.168	0.383	-0.179	0.152	-0.079	0.697
Pericalcarine.L	0.332	0.002*	0.169	0.206	-0.368	0.003*	-0.100	0.524	-0.346	0.006*	-0.047	0.740
Precentral.L	0.103	0.331	0.090	0.410	0.036	0.760	-0.132	0.383	0.074	0.546	-0.166	0.426
RosMidFront.L	0.279	0.010*	0.184	0.187	-0.017	0.875	0.069	0.746	-0.129	0.318	-0.050	0.740
SupFront.L	0.202	0.056	0.251	0.100	0.320	0.005*	0.137	0.383	0.274	0.021*	0.192	0.315
SupParietal.L	0.366	0.001*	0.151	0.236	-0.359	0.003*	-0.156	0.383	-0.285	0.017*	-0.214	0.315
CaudMidFront.R	0.276	0.010*	0.245	0.100	0.200	0.077	0.038	0.806	0.201	0.110	0.149	0.449
Cuneus.R	0.396	0.001*	0.147	0.236	-0.280	0.013*	-0.028	0.825	-0.080	0.546	0.050	0.740
Fusiform.R	0.405	0.001*	0.184	0.187	-0.316	0.005*	-0.145	0.383	-0.204	0.110	-0.109	0.525
InfParietal.R	0.369	0.001*	0.126	0.285	-0.294	0.009*	-0.155	0.383	-0.005	0.965	-0.132	0.515
InfTemporal.R	0.335	0.002*	0.167	0.206	-0.270	0.016*	-0.244	0.383	-0.076	0.546	-0.126	0.515
LateralOcc.R	0.345	0.002*	0.094	0.406	-0.314	0.005*	-0.023	0.825	-0.221	0.082	0.028	0.821
Lingual.R	0.358	0.001*	0.192	0.187	-0.356	0.003*	-0.155	0.383	-0.296	0.014*	-0.109	0.525
ParsOperc.R	0.306	0.005*	0.228	0.126	0.186	0.098	0.057	0.765	0.176	0.152	0.084	0.689
Paricalcarine.R	0.413	0.001*	0.156	0.236	-0.307	0.006*	-0.045	0.806	-0.170	0.160	0.016	0.876
Precentral.R	0.280	0.010*	0.256	0.100	0.116	0.306	0.039	0.806	0.307	0.011*	0.114	0.525
RosMidFront.R	0.268	0.012*	0.179	0.190	0.243	0.032*	0.158	0.383	0.183	0.150	0.192	0.315
SupFront.R	0.355	0.001*	0.244	0.100	0.222	0.048*	0.126	0.383	0.081	0.546	0.188	0.315
SupParietal.R	0.423	0.001*	0.220	0.129	-0.233	0.039*	-0.151	0.383	0.101	0.463	-0.050	0.740

Appendix table 2.19: Correlation coefficients and p-values for the relationship between cognitive components and graph theory metrics of a given node within the reasoning network constructed using a 3.0 SD thresholding approach. R=Pearson's r, p(FDR)=p-value with FDR correction applied across nodes.

3.5 SD Units

GT Metrics	Degree				Local Eff				Clustering Coeff			
Node	Reasoning		Working mem.		Reasoning		Working mem.		Reasoning		Working mem.	
	R.	p(FDR)	R.	p(FDR)	R.	p(FDR)	R.	p(FDR)	R.	p(FDR)	R.	p(FDR)
CaudMidFront.L	0.219	0.040*	0.141	0.262	0.135	0.236	0.077	0.595	0.118	0.326	0.040	0.837
Cuneus.L	0.330	0.003*	0.092	0.394	-0.340	0.002*	-0.074	0.595	-0.354	0.005*	-0.061	0.771
Fusiform.L	0.325	0.003*	0.208	0.157	-0.378	0.002*	-0.225	0.405	-0.365	0.005*	-0.224	0.279
InfParietal.L	0.312	0.004*	0.104	0.373	-0.328	0.003*	-0.096	0.554	-0.329	0.006*	-0.137	0.454
InfTemporal.L	0.306	0.004*	0.100	0.373	-0.346	0.002*	-0.202	0.405	-0.315	0.007*	-0.292	0.123
LatOcc.L	0.337	0.003*	0.142	0.262	-0.330	0.003*	-0.108	0.528	-0.344	0.005*	-0.072	0.715
LatOrbFront.L	0.214	0.044*	0.267	0.052	-0.012	0.908	-0.113	0.528	0.108	0.360	0.045	0.834
ParsOperc.L	0.306	0.004*	0.189	0.186	-0.038	0.782	-0.180	0.405	-0.169	0.171	-0.110	0.511
Pericalcarine.L	0.332	0.003*	0.182	0.196	-0.364	0.002*	-0.099	0.554	-0.347	0.005*	-0.021	0.876
Precentral.L	0.089	0.401	0.090	0.394	0.018	0.897	-0.130	0.473	0.074	0.526	-0.169	0.319
RosMidFront.L	0.267	0.013*	0.152	0.258	0.138	0.234	0.023	0.825	0.085	0.478	-0.055	0.781
SupFront.L	0.204	0.053	0.233	0.111	0.350	0.002*	0.163	0.405	0.315	0.007*	0.168	0.319
SupParietal.L	0.372	0.001*	0.148	0.258	-0.376	0.002*	-0.164	0.405	-0.312	0.007*	-0.224	0.279
CaudMidFront.R	0.264	0.013*	0.288	0.047*	0.207	0.065	0.063	0.618	0.220	0.066	0.191	0.304
Cuneus.R	0.392	0.001*	0.133	0.280	-0.280	0.013*	-0.039	0.743	-0.122	0.319	0.026	0.875
Fusiform.R	0.434	0.000*	0.206	0.157	-0.365	0.002*	-0.173	0.405	-0.246	0.036*	-0.128	0.473
InfParietal.R	0.363	0.001*	0.149	0.258	-0.272	0.015*	-0.152	0.405	0.011	0.918	-0.106	0.511
InfTemporal.R	0.336	0.003*	0.165	0.252	-0.305	0.006*	-0.275	0.208	-0.123	0.319	-0.182	0.304
LateralOcc.R	0.358	0.001*	0.100	0.373	-0.357	0.002*	-0.060	0.618	-0.300	0.009*	-0.012	0.908
Lingual.R	0.335	0.003*	0.130	0.280	-0.356	0.002*	-0.144	0.405	-0.311	0.007*	-0.120	0.473
ParsOperc.R	0.290	0.007*	0.267	0.052	0.246	0.029*	0.077	0.595	0.200	0.098	0.123	0.473
Paricalcarine.R	0.390	0.001*	0.124	0.298	-0.348	0.002*	-0.073	0.595	-0.262	0.025*	-0.032	0.860
Precentral.R	0.242	0.024*	0.289	0.047*	0.125	0.268	0.071	0.595	0.335	0.006*	0.146	0.426
RosMidFront.R	0.308	0.004*	0.151	0.258	0.223	0.050	0.145	0.405	0.130	0.311	0.185	0.304
SupFront.R	0.389	0.001*	0.292	0.047*	0.210	0.065	0.110	0.528	0.059	0.597	0.205	0.304
SupParietal.R	0.419	0.000*	0.189	0.186	-0.166	0.147	-0.158	0.405	0.167	0.171	-0.078	0.699

Appendix table 2.20: Correlation coefficients and p-values for the relationship between cognitive components and graph theory metrics of a given node within the reasoning network constructed using a 3.5 SD thresholding approach. R=Pearson's r, p(FDR)=p-value with FDR correction applied across nodes.

4.0 SD Units

GT Metrics	Degree				Local Eff				Clustering Coeff			
Node	Reasoning		Working mem.		Reasoning		Working mem.		Reasoning		Working mem.	
	R.	p(FDR)	R.	p(FDR)	R.	p(FDR)	R.	p(FDR)	R.	p(FDR)	R.	p(FDR)
CaudMidFront.L	0.250	0.019*	0.130	0.331	0.170	0.125	0.066	0.670	0.193	0.099	0.040	0.877
Cuneus.L	0.316	0.004*	0.083	0.491	-0.341	0.003*	-0.063	0.670	-0.341	0.004*	-0.029	0.878
Fusiform.L	0.361	0.002*	0.178	0.212	-0.407	0.001*	-0.233	0.333	-0.357	0.004*	-0.245	0.314
InfParietal.L	0.325	0.003*	0.100	0.448	-0.291	0.009*	-0.103	0.646	-0.255	0.034*	-0.158	0.360

InfTemporal.L	0.292	0.007*	0.082	0.491	-0.345	0.002*	-0.164	0.512	-0.337	0.004*	-0.235	0.314
LatOcc.L	0.303	0.006*	0.089	0.491	-0.326	0.004*	-0.088	0.670	-0.347	0.004*	-0.059	0.805
LatOrbFront.L	0.238	0.025*	0.288	0.061	0.049	0.698	-0.155	0.512	0.161	0.162	0.040	0.877
ParsOperc.L	0.288	0.007*	0.172	0.218	-0.013	0.903	-0.166	0.512	-0.159	0.162	-0.156	0.360
Pericalcarine.L	0.329	0.003*	0.135	0.321	-0.366	0.002*	-0.074	0.670	-0.369	0.004*	-0.030	0.878
Precentral.L	0.128	0.226	0.074	0.506	0.041	0.724	-0.099	0.646	0.113	0.322	-0.144	0.404
RosMidFront.L	0.290	0.007*	0.202	0.181	0.082	0.493	-0.004	0.972	0.028	0.790	0.011	0.917
SupFront.L	0.173	0.103	0.195	0.181	0.396	0.001*	0.130	0.564	0.305	0.009*	0.160	0.360
SupParietal.L	0.343	0.002*	0.159	0.240	-0.365	0.002*	-0.171	0.512	-0.318	0.007*	-0.200	0.335
CaudMidFront.R	0.258	0.016*	0.303	0.061	0.205	0.069	0.069	0.670	0.208	0.076	0.194	0.335
Cuneus.R	0.376	0.001*	0.123	0.334	-0.316	0.004*	-0.044	0.729	-0.176	0.126	0.025	0.878
Fusiform.R	0.448	0.000*	0.203	0.181	-0.369	0.002*	-0.157	0.512	-0.241	0.040*	-0.107	0.539
InfParietal.R	0.347	0.002*	0.137	0.321	-0.234	0.038*	-0.115	0.646	0.034	0.780	-0.093	0.613
InfTemporal.R	0.353	0.002*	0.164	0.235	-0.334	0.003*	-0.249	0.333	-0.181	0.122	-0.162	0.360
LateralOcc.R	0.337	0.002*	0.061	0.560	-0.346	0.002*	-0.066	0.670	-0.310	0.009*	-0.057	0.805
Lingual.R	0.377	0.001*	0.124	0.334	-0.381	0.002*	-0.142	0.512	-0.301	0.009*	-0.121	0.524
ParsOperc.R	0.295	0.007*	0.270	0.061	0.272	0.015*	0.057	0.670	0.239	0.040*	0.109	0.539
Paricalcarine.R	0.347	0.002*	0.079	0.491	-0.320	0.004*	-0.041	0.729	-0.251	0.034*	-0.018	0.896
Precentral.R	0.220	0.038*	0.266	0.061	0.179	0.114	0.057	0.670	0.339	0.004*	0.118	0.524
RosMidFront.R	0.282	0.008*	0.184	0.204	0.240	0.035*	0.109	0.646	0.137	0.226	0.208	0.335
SupFront.R	0.385	0.001*	0.262	0.061	0.229	0.041*	0.082	0.670	0.067	0.566	0.172	0.360
SupParietal.R	0.419	0.000*	0.195	0.181	-0.173	0.122	-0.143	0.512	0.215	0.068	-0.061	0.805

Appendix table 2.21: Correlation coefficients and p-values for the relationship between cognitive components and graph theory metrics of a given node within the reasoning network constructed using a 4.0 SD thresholding approach. R=Pearson's r, p(FDR)=p-value with FDR correction applied across nodes.

4.5 SD Units

GT Metrics	Degree				Local Eff				Clustering Coeff			
Node	Reasoning		Working mem.		Reasoning		Working mem.		Reasoning		Working mem.	
	R.	p(FDR)	R.	p(FDR)	R.	p(FDR)	R.	p(FDR)	R.	p(FDR)	R.	p(FDR)
CaudMidFront.L	0.273	0.012*	0.092	0.495	0.219	0.047*	0.075	0.669	0.274	0.018*	0.010	0.962
Cuneus.L	0.312	0.004*	0.072	0.538	-0.334	0.003*	-0.069	0.669	-0.348	0.005*	-0.051	0.854
Fusiform.L	0.342	0.002*	0.142	0.308	-0.378	0.003*	-0.206	0.364	-0.325	0.006*	-0.228	0.344
InfParietal.L	0.311	0.004*	0.076	0.532	-0.270	0.015*	-0.093	0.669	-0.255	0.026*	-0.171	0.344
InfTemporal.L	0.265	0.014*	0.094	0.495	-0.340	0.003*	-0.180	0.364	-0.352	0.005*	-0.236	0.344
LatOcc.L	0.319	0.004*	0.089	0.496	-0.333	0.003*	-0.095	0.669	-0.368	0.005*	-0.074	0.789
LatOrbFront.L	0.228	0.033*	0.282	0.050	0.030	0.808	-0.167	0.364	0.191	0.093	-0.020	0.958
ParsOperc.L	0.258	0.016*	0.157	0.271	0.002	0.987	-0.207	0.364	-0.174	0.114	-0.153	0.344
Pericalcarine.L	0.330	0.003*	0.120	0.413	-0.348	0.003*	-0.072	0.669	-0.341	0.005*	-0.037	0.902
Precentral.L	0.110	0.295	0.085	0.496	0.038	0.776	-0.106	0.669	0.102	0.349	-0.136	0.425
RosMidFront.L	0.290	0.007*	0.201	0.145	0.096	0.412	-0.020	0.847	0.077	0.468	0.047	0.854
SupFront.L	0.181	0.087	0.202	0.145	0.400	0.002*	0.133	0.540	0.328	0.006*	0.158	0.344
SupParietal.L	0.345	0.002*	0.151	0.280	-0.367	0.003*	-0.175	0.364	-0.308	0.009*	-0.201	0.344

CaudMidFront.R	0.214	0.044*	0.319	0.050	0.242	0.028*	0.077	0.669	0.241	0.034*	0.183	0.344
Cuneus.R	0.379	0.001*	0.109	0.439	-0.319	0.005*	-0.051	0.720	-0.211	0.064	-0.001	0.993
Fusiform.R	0.418	0.000*	0.227	0.128	-0.336	0.003*	-0.173	0.364	-0.241	0.034*	-0.116	0.539
InfParietal.R	0.380	0.001*	0.159	0.271	-0.241	0.028*	-0.133	0.540	0.109	0.328	-0.029	0.923
InfTemporal.R	0.339	0.002*	0.165	0.271	-0.314	0.005*	-0.242	0.364	-0.174	0.114	-0.157	0.344
LateralOcc.R	0.327	0.003*	0.026	0.806	-0.334	0.003*	-0.041	0.738	-0.305	0.009*	-0.065	0.827
Lingual.R	0.383	0.001*	0.108	0.439	-0.351	0.003*	-0.114	0.660	-0.262	0.023*	-0.096	0.632
ParsOperc.R	0.343	0.002*	0.259	0.066	0.297	0.008*	0.039	0.738	0.300	0.009*	0.101	0.628
Paricalcarine.R	0.307	0.005*	0.057	0.615	-0.296	0.008*	-0.050	0.720	-0.281	0.016*	-0.052	0.854
Precentral.R	0.230	0.033*	0.276	0.050	0.149	0.184	0.090	0.669	0.343	0.005*	0.157	0.344
RosMidFront.R	0.302	0.005*	0.200	0.145	0.287	0.010*	0.052	0.720	0.185	0.102	0.158	0.344
SupFront.R	0.360	0.002*	0.298	0.050	0.260	0.019*	0.081	0.669	0.171	0.117	0.205	0.344
SupParietal.R	0.428	0.000*	0.219	0.132	-0.193	0.081	-0.181	0.364	0.223	0.049*	-0.013	0.962

Appendix table 2.22: Correlation coefficients and p-values for the relationship between cognitive components and graph theory metrics of a given node within the reasoning network constructed using a 4.5 SD thresholding approach. R=Pearson's r, p(FDR)=p-value with FDR correction applied across nodes.

5.0 SD Units

GT Metrics	Degree				Local Eff				Clustering Coeff			
Node	Reasoning		Working mem.		Reasoning		Working mem.		Reasoning		Working mem.	
	R.	p(FDR)	R.	p(FDR)	R.	p(FDR)	R.	p(FDR)	R.	p(FDR)	R.	p(FDR)
CaudMidFront.L	0.212	0.048*	0.066	0.606	0.230	0.040*	0.064	0.656	0.243	0.032*	-0.037	0.859
Cuneus.L	0.304	0.005*	0.062	0.606	-0.318	0.005*	-0.070	0.656	-0.335	0.007*	-0.063	0.731
Fusiform.L	0.350	0.003*	0.144	0.344	-0.377	0.003*	-0.203	0.395	-0.318	0.007*	-0.207	0.435
InfParietal.L	0.309	0.005*	0.065	0.606	-0.272	0.013*	-0.112	0.632	-0.240	0.033*	-0.194	0.435
InfTemporal.L	0.262	0.015*	0.076	0.587	-0.356	0.003*	-0.186	0.395	-0.331	0.007*	-0.230	0.435
LatOcc.L	0.303	0.005*	0.083	0.564	-0.326	0.004*	-0.084	0.656	-0.357	0.007*	-0.071	0.726
LatOrbFront.L	0.231	0.033*	0.303	0.048*	0.055	0.655	-0.211	0.395	0.285	0.014*	-0.071	0.726
ParsOperc.L	0.280	0.010*	0.171	0.222	0.035	0.740	-0.150	0.503	-0.171	0.116	-0.125	0.515
Pericalcarine.L	0.342	0.003*	0.115	0.420	-0.344	0.003*	-0.070	0.656	-0.324	0.007*	-0.022	0.938
Precentral.L	0.125	0.235	0.109	0.436	0.051	0.655	-0.106	0.632	0.151	0.162	-0.110	0.515
RosMidFront.L	0.307	0.005*	0.232	0.078	0.167	0.146	-0.018	0.863	0.231	0.036*	0.123	0.515
SupFront.L	0.184	0.082	0.194	0.152	0.388	0.003*	0.131	0.553	0.316	0.007*	0.127	0.515
SupParietal.L	0.324	0.004*	0.135	0.346	-0.352	0.003*	-0.161	0.468	-0.316	0.007*	-0.181	0.435
CaudMidFront.R	0.187	0.080	0.256	0.078	0.219	0.049*	0.079	0.656	0.214	0.049*	0.127	0.515
Cuneus.R	0.362	0.002*	0.105	0.436	-0.299	0.008*	-0.049	0.730	-0.213	0.049*	-0.018	0.938
Fusiform.R	0.406	0.001*	0.226	0.078	-0.337	0.003*	-0.172	0.435	-0.244	0.032*	-0.113	0.515
InfParietal.R	0.359	0.002*	0.136	0.346	-0.160	0.157	-0.074	0.656	0.103	0.329	0.002	0.988
InfTemporal.R	0.364	0.002*	0.231	0.078	-0.275	0.013*	-0.236	0.395	-0.132	0.217	-0.139	0.515
LateralOcc.R	0.332	0.004*	0.016	0.877	-0.341	0.003*	-0.035	0.773	-0.300	0.010*	-0.057	0.731
Lingual.R	0.319	0.004*	0.115	0.420	-0.342	0.003*	-0.109	0.632	-0.277	0.015*	-0.077	0.726
ParsOperc.R	0.293	0.007*	0.287	0.048*	0.311	0.006*	0.065	0.656	0.297	0.010*	0.119	0.515
Paricalcarine.R	0.303	0.005*	0.057	0.615	-0.306	0.007*	-0.062	0.656	-0.281	0.015*	-0.060	0.731

Precentral.R	0.212	0.048*	0.229	0.078	0.101	0.381	0.134	0.553	0.323	0.007*	0.170	0.455
RosMidFront.R	0.321	0.004*	0.232	0.078	0.293	0.008*	0.042	0.746	0.224	0.042*	0.156	0.512
SupFront.R	0.347	0.003*	0.297	0.048*	0.297	0.008*	0.078	0.656	0.254	0.027*	0.186	0.435
SupParietal.R	0.404	0.001*	0.243	0.078	-0.137	0.230	-0.194	0.395	0.234	0.036*	-0.009	0.966

Appendix table 2.23: Correlation coefficients and p-values for the relationship between cognitive components and graph theory metrics of a given node within the reasoning network constructed using a 5.0 SD thresholding approach. R=Pearson's r, p(FDR)=p-value with FDR correction applied across nodes.

Chapter 5

Node	Thresh 1	Thresh 2	Thresh 3	Thresh 4	Thresh 5	Thresh 6	Thresh 7	Thresh 8	Thresh 9	Thresh 10
Caudate.L	0.44	0.07	0.00	0.00	0.01	0.00	0.00	0.00	0.01	0.05
Pallidum.L	0.44	0.76	0.44	0.05	0.04	0.23	0.00	0.00	0.01	0.06
Hippocampus.L	0.73	0.59	0.98	0.88	0.23	0.24	0.09	0.52	0.51	0.65
Caudate.R	0.05	0.01	0.00	0.00	0.00	0.00	0.00	0.00	0.00	0.01
Pallidum.R	0.72	0.95	0.88	0.40	0.05	0.12	0.23	0.07	0.06	0.06
Hippocampus.R	0.44	0.77	0.82	0.62	0.47	0.49	0.05	0.07	0.06	NaN
CaudAntCing.L	0.44	0.01	0.01	0.00	0.00	0.03	0.01	0.03	0.01	0.01
LatOrbitoFront.L	0.92	0.01	0.00	0.00	0.00	0.01	0.00	0.00	0.00	0.00
Paracentral.L	0.65	0.28	0.05	0.05	0.08	0.62	0.86	0.64	0.67	0.65
PostCentral.L	0.65	0.61	0.24	0.12	0.34	0.47	0.99	0.64	0.65	0.65
PostCingulate.L	0.44	0.44	0.03	0.11	0.23	0.17	0.15	0.16	0.05	0.65
Precentral.L	0.44	0.41	0.32	0.40	0.56	0.92	0.54	0.69	0.64	0.65
Precuneus.L	0.44	0.90	0.65	0.63	0.55	0.41	0.23	0.17	0.65	NaN
RosAntCing.L	0.92	0.07	0.00	0.00	0.00	0.00	0.00	0.01	0.06	0.06
RosMidFront.L	0.44	0.03	0.00	0.00	0.00	0.01	0.00	0.00	0.00	0.01
SupFront.L	0.69	0.44	0.01	0.04	0.01	0.01	0.00	0.01	0.01	0.01
Insula.L	0.16	0.42	0.98	0.07	0.01	0.02	0.00	0.00	0.00	0.06
CaudaAntCing.R	0.44	0.01	0.03	0.05	0.02	0.00	0.00	0.03	0.06	0.02
CaudMidFront.R	0.71	0.89	0.60	0.12	0.39	0.27	0.02	0.07	NaN	NaN
LatOrbitoFront.R	0.92	0.41	0.05	0.02	0.01	0.00	0.00	0.03	0.01	0.06
Paracentral.R	0.85	0.77	0.95	0.19	0.12	0.07	0.00	0.34	0.06	0.06

PostCentral.R	0.92	0.41	0.24	0.07	0.01	0.11	0.08	0.18	0.06	0.65
PostCingulate.R	0.44	0.77	0.46	0.12	0.28	0.79	0.54	0.73	0.73	0.84
Precentral.R	0.73	0.64	0.69	0.63	0.85	0.90	0.54	0.69	NaN	NaN
Precuneus.R	0.92	0.88	0.60	0.55	0.32	0.49	0.86	0.57	0.79	0.65
RosAntCing.R	0.44	0.54	0.02	0.00	0.00	0.00	0.00	0.00	0.01	0.01
RosMidFront.R	0.47	0.01	0.00	0.00	0.00	0.00	0.00	0.00	0.00	0.01
SupFront.R	0.44	0.09	0.05	0.02	0.01	0.01	0.01	0.03	0.01	0.06
SupParietal.R	0.73	0.87	0.85	0.56	0.32	0.80	0.86	0.79	0.67	NaN
SupraMarg.R	0.83	0.23	0.01	0.05	0.19	0.02	0.12	0.05	0.06	0.06
Insula.R	0.65	0.76	0.83	0.06	0.23	0.11	0.26	0.07	0.06	0.01

Appendix table 2.24: P values (FDR corrected) of comparison of nodal degree centrality measures between TBI patients in subacute phase of injury and healthy controls across the 10 connectome threshold iterations. Thresh1=0.5 SD, Thresh10=5.0SD

Node	Thresh 1	Thresh 2	Thresh 3	Thresh 4	Thresh 5	Thresh 6	Thresh 7	Thresh 8	Thresh 9	Thresh 10
'Caudate.L'	0.85	0.48	0.12	0.06	0.01	0.01	0.01	0.01	0.04	0.04
'Pallidum.L'	0.85	0.48	0.23	0.09	0.00	0.00	0.00	0.00	0.00	0.00
'Hippocampus.L'	0.01	0.10	0.32	0.33	0.20	0.03	0.11	0.03	0.00	0.00
'Caudate.R'	0.85	0.78	0.76	0.26	0.07	0.02	0.04	0.03	0.09	0.18
'Pallidum.R'	0.85	0.84	0.77	0.21	0.31	0.13	0.14	0.12	0.13	0.13
'Hippocampus.R'	0.87	0.78	0.72	0.79	0.20	0.64	0.28	0.15	0.19	0.22
'CaudAntCing.L'	0.87	0.48	0.81	0.72	0.07	0.02	0.10	0.12	0.19	0.35
'LatOrbitoFront.L'	0.57	0.78	0.79	0.72	0.66	0.68	0.41	0.57	0.51	0.81
'Paracentral.L'	0.99	0.88	0.59	0.95	0.83	0.64	0.51	0.43	0.19	0.20
'PostCentral.L'	0.85	0.48	0.32	0.15	0.01	0.04	0.05	0.07	0.07	0.13
'PostCingulate.L'	0.85	1.00	0.76	0.50	0.06	0.04	0.00	0.10	0.11	0.23
'Precentral.L'	0.98	0.84	0.81	0.72	0.20	0.04	0.04	0.05	0.02	0.01
'Precuneus.L'	0.87	0.88	0.80	0.47	0.17	0.07	0.04	0.05	0.03	0.06
'RosAntCing.L'	0.00	0.00	0.00	0.00	0.01	0.02	0.01	0.02	0.11	0.23
'RosMidFront.L'	0.41	0.19	0.01	0.00	0.00	0.00	0.01	0.05	0.13	0.56
'SupFront.L'	0.85	0.48	0.46	0.00	0.00	0.00	0.00	0.00	0.00	0.00
'Insula.L'	0.41	0.04	0.01	0.00	0.00	0.00	0.00	0.00	0.00	0.00
'CaudaAntCing.R'	0.85	0.48	0.37	0.00	0.00	0.02	0.34	0.78	0.99	0.88

'CaudMidFront.R'	0.88	0.84	0.76	0.72	0.04	0.03	0.01	0.01	0.02	0.02
'LatOrbitoFront.R'	0.02	0.00	0.01	0.00	0.00	0.00	0.00	0.00	0.00	0.00
'Paracentral.R'	0.52	0.42	0.97	0.57	0.92	0.76	0.80	0.89	0.95	0.88
'PostCentral.R'	0.87	0.20	0.32	0.02	0.02	0.10	0.24	0.36	0.42	0.85
'PostCingulate.R'	0.56	0.10	0.01	0.45	0.83	0.89	0.91	0.59	0.95	0.88
'Precentral.R'	0.85	1.00	0.97	0.72	0.33	0.06	0.07	0.13	0.13	0.20
'Precuneus.R'	0.98	0.48	0.63	0.72	0.92	0.87	0.85	0.84	0.95	0.88
'RosAntCing.R'	0.85	0.04	0.01	0.01	0.00	0.04	0.07	0.13	0.18	0.23
'RosMidFront.R'	0.87	0.52	0.63	0.72	0.79	0.97	0.86	0.42	0.90	0.80
'SupFront.R'	0.85	0.52	0.63	0.44	0.02	0.01	0.05	0.07	0.10	0.11
'SupParietal.R'	0.85	0.48	0.30	0.39	0.54	0.64	0.89	0.99	0.95	0.88
'SupraMarg.R'	0.88	0.48	0.46	0.06	0.36	0.43	0.36	0.42	0.54	0.80
'Insula.R'	0.87	1.00	0.63	0.44	0.33	0.61	0.17	0.12	0.18	0.23

Appendix table 2.25: P values (FDR corrected) of comparison of nodal local efficiency measures between TBI patients in subacute phase of injury and healthy controls across the 10 connectome threshold iterations. Thresh1=0.5 SD, Thresh10=5.0SD

Node	Thresh 1	Thresh 2	Thresh 3	Thresh 4	Thresh 5	Thresh 6	Thresh 7	Thresh 8	Thresh 9	Thresh 10
'Caudate.L'	0.81	0.36	0.96	0.99	0.89	0.84	0.38	0.15	0.12	0.05
'Pallidum.L'	0.75	0.92	0.74	0.71	0.37	0.11	0.03	0.00	0.01	0.01
'Hippocampus.L'	0.19	0.22	0.21	0.05	0.07	0.15	0.38	0.50	0.05	0.01
'Caudate.R'	0.84	0.98	0.96	0.87	0.90	0.77	0.35	0.27	0.12	0.14
'Pallidum.R'	0.49	0.29	0.59	0.62	0.79	0.84	0.49	0.35	0.34	0.19
'Hippocampus.R'	0.58	0.98	0.96	0.94	0.90	0.80	0.21	0.13	0.09	0.07
'CaudAntCing.L'	0.18	0.17	0.37	0.16	0.30	0.11	0.31	0.30	0.87	0.91
'LatOrbitoFront.L'	0.37	0.17	0.37	0.54	0.85	0.25	0.21	0.44	0.30	0.37
'Paracentral.L'	0.58	0.29	0.05	0.38	0.48	0.95	0.77	0.50	0.30	0.23
'PostCentral.L'	0.47	0.49	0.96	0.94	0.85	0.51	0.24	0.27	0.30	0.32
'PostCingulate.L'	0.09	0.66	0.56	0.44	0.25	0.63	0.38	0.15	0.29	0.14
'Precentral.L'	0.25	0.17	0.21	0.27	0.78	0.97	0.88	0.27	0.10	0.07
'Precuneus.L'	0.58	0.50	0.54	0.54	0.79	0.77	0.24	0.15	0.09	0.06
'RosAntCing.L'	0.58	0.17	0.04	0.03	0.01	0.11	0.21	0.35	0.10	0.19

'RosMidFront.L'	0.00	0.00	0.00	0.00	0.00	0.03	0.21	0.27	0.34	0.37
'SupFront.L'	0.92	0.93	0.59	0.70	0.90	0.80	0.47	0.89	0.18	0.07
'Insula.L'	0.06	0.04	0.05	0.32	0.35	0.11	0.18	0.01	0.00	0.00
'CaudaAntCing.R'	0.09	0.06	0.18	0.00	0.01	0.09	0.24	0.15	0.10	0.31
'CaudMidFront.R'	0.25	0.17	0.12	0.38	0.90	0.90	0.90	0.27	0.10	0.07
'LatOrbitoFront.R'	0.58	0.57	0.74	0.94	0.90	0.63	0.21	0.50	0.32	0.19
'Paracentral.R'	0.40	0.62	0.96	0.38	0.35	0.25	0.29	0.50	0.58	0.70
'PostCentral.R'	NaN	0.93	0.96	0.54	0.79	0.51	0.47	0.50	0.73	0.91
'PostCingulate.R'	0.58	0.29	0.02	0.16	0.35	0.25	0.24	0.28	0.30	0.20
'Precentral.R'	0.47	0.29	0.54	0.54	0.90	0.90	0.97	0.59	0.34	0.32
'Precuneus.R'	0.58	0.49	0.37	0.99	0.85	0.84	0.59	0.59	0.63	0.62
'RosAntCing.R'	0.63	0.86	0.78	0.54	0.35	0.37	0.27	0.10	0.10	0.14
'RosMidFront.R'	0.02	0.06	0.18	0.16	0.07	0.84	0.88	0.68	0.99	0.91
'SupFront.R'	0.47	0.29	0.78	0.94	0.90	0.77	0.43	0.61	0.87	0.63
'SupParietal.R'	0.40	0.38	0.37	0.99	0.99	0.63	0.90	0.89	0.98	0.92
'SupraMarg.R'	0.73	0.84	0.59	0.71	0.78	0.84	0.88	0.85	0.87	0.91
'Insula.R'	0.76	0.64	0.74	0.38	0.74	0.80	0.90	0.29	0.29	0.14

Appendix table 2.26: P values (FDR corrected) of comparison of nodal clustering coefficient measures between TBI patients in subacute phase of injury and healthy controls across the 10 connectome threshold iterations. Thresh1=0.5 SD, Thresh10=5.0SD

Node	Thresh 1	Thresh 2	Thresh 3	Thresh 4	Thresh 5	Thresh 6	Thresh 7	Thresh 8	Thresh 9	Thresh 10
'Caudate.L'	0.57	0.10	0.01	0.00	0.00	0.00	0.00	0.00	0.01	0.00
'Pallidum.L'	0.76	0.46	0.13	0.05	0.02	0.01	0.00	0.00	0.00	0.01
'Hippocampus.L'	0.60	0.10	0.10	0.04	0.05	0.04	0.08	0.14	0.79	0.32
'Caudate.R'	0.01	0.00	0.00	0.00	0.00	0.00	0.00	0.00	0.00	0.00
'Pallidum.R'	0.83	0.61	0.13	0.01	0.02	0.02	0.07	0.06	0.06	0.06
'Hippocampus.R'	0.24	0.62	0.29	0.14	0.74	0.67	0.82	0.29	NaN	NaN
'CaudAntCing.L'	0.62	0.01	0.01	0.00	0.00	0.05	0.04	0.01	0.00	0.01
'LatOrbitoFront.L'	0.78	0.00	0.00	0.00	0.00	0.00	0.00	0.00	0.00	0.00
'Paracentral.L'	0.62	0.34	0.02	0.01	0.08	0.15	0.31	0.24	0.32	0.62

'PostCentral.L'	0.78	0.33	0.24	0.09	0.05	0.10	0.09	0.03	0.15	0.32
'PostCingulate.L'	0.62	0.33	0.12	0.01	0.03	0.01	0.00	0.03	0.04	0.32
'Precentral.L'	0.38	0.23	0.13	0.15	0.15	0.04	0.22	0.10	0.09	0.15
'Precuneus.L'	0.57	0.63	0.80	0.76	0.74	0.37	0.09	0.09	0.06	NaN
'RosAntCing.L'	0.60	0.00	0.00	0.00	0.00	0.00	0.00	0.00	0.06	0.06
'RosMidFront.L'	0.38	0.01	0.00	0.00	0.00	0.00	0.00	0.00	0.00	0.00
'SupFront.L'	0.78	0.31	0.01	0.01	0.01	0.00	0.00	0.00	0.00	0.00
'Insula.L'	0.08	0.59	0.22	0.02	0.01	0.02	0.00	0.00	0.01	0.62
'CaudaAntCing.R'	0.24	0.02	0.02	0.02	0.01	0.00	0.03	0.06	0.09	0.02
'CaudMidFront.R'	0.83	0.76	0.56	0.10	0.16	0.11	0.02	0.01	0.01	0.06
'LatOrbitoFront.R'	0.76	0.24	0.08	0.00	0.00	0.00	0.00	0.00	0.02	0.06
'Paracentral.R'	0.78	0.48	0.15	0.14	0.07	0.10	0.11	0.07	0.04	0.04
'PostCentral.R'	0.76	0.10	0.01	0.00	0.00	0.00	0.04	0.01	0.02	0.01
'PostCingulate.R'	0.57	0.03	0.10	0.05	0.03	0.04	0.04	0.02	0.06	0.04
'Precentral.R'	0.78	0.42	0.13	0.13	0.23	0.04	0.03	0.01	0.06	0.06
'Precuneus.R'	0.62	0.62	0.62	0.94	0.92	0.86	0.59	0.46	0.79	0.52
'RosAntCing.R'	0.78	0.10	0.00	0.00	0.00	0.00	0.00	0.01	0.01	0.01
'RosMidFront.R'	0.29	0.00	0.00	0.00	0.00	0.00	0.00	0.00	0.00	0.00
'SupFront.R'	0.57	0.16	0.01	0.01	0.00	0.00	0.00	0.00	0.02	0.02
'SupParietal.R'	0.61	0.71	0.97	0.62	0.40	0.77	0.92	0.27	0.66	NaN
'SupraMarg.R'	0.57	0.00	0.00	0.01	0.20	0.02	0.04	0.06	0.32	NaN
'Insula.R'	0.57	0.71	0.75	0.13	0.07	0.00	0.06	0.01	0.06	NaN

Appendix table 2.27: P values (FDR corrected) of comparison of nodal degree centrality. measures between TBI patients in chronic phase of injury and healthy controls across the 10 connectome threshold iterations. Thresh1=0.5 SD, Thresh10=5.0SD

Node	Thresh 1	Thresh 2	Thresh 3	Thresh 4	Thresh 5	Thresh 6	Thresh 7	Thresh 8	Thresh 9	Thresh 10
'Caudate.L'	0.85	0.48	0.12	0.06	0.01	0.01	0.01	0.01	0.04	0.04
'Pallidum.L'	0.85	0.48	0.23	0.09	0.00	0.00	0.00	0.00	0.00	0.00
'Hippocampus.L'	0.01	0.10	0.32	0.33	0.20	0.03	0.11	0.03	0.00	0.00
'Caudate.R'	0.85	0.78	0.76	0.26	0.07	0.02	0.04	0.03	0.09	0.18

'Pallidum.R'	0.85	0.84	0.77	0.21	0.31	0.13	0.14	0.12	0.13	0.13
'Hippocampus.R'	0.87	0.78	0.72	0.79	0.20	0.64	0.28	0.15	0.19	0.22
'CaudAntCing.L'	0.87	0.48	0.81	0.72	0.07	0.02	0.10	0.12	0.19	0.35
'LatOrbitoFront.L'	0.57	0.78	0.79	0.72	0.66	0.68	0.41	0.57	0.51	0.81
'Paracentral.L'	0.99	0.88	0.59	0.95	0.83	0.64	0.51	0.43	0.19	0.20
'PostCentral.L'	0.85	0.48	0.32	0.15	0.01	0.04	0.05	0.07	0.07	0.13
'PostCingulate.L'	0.85	1.00	0.76	0.50	0.06	0.04	0.00	0.10	0.11	0.23
'Precentral.L'	0.98	0.84	0.81	0.72	0.20	0.04	0.04	0.05	0.02	0.01
'Precuneus.L'	0.87	0.88	0.80	0.47	0.17	0.07	0.04	0.05	0.03	0.06
'RosAntCing.L'	0.00	0.00	0.00	0.00	0.01	0.02	0.01	0.02	0.11	0.23
'RosMidFront.L'	0.41	0.19	0.01	0.00	0.00	0.00	0.01	0.05	0.13	0.56
'SupFront.L'	0.85	0.48	0.46	0.00	0.00	0.00	0.00	0.00	0.00	0.00
'Insula.L'	0.41	0.04	0.01	0.00	0.00	0.00	0.00	0.00	0.00	0.00
'CaudaAntCing.R'	0.85	0.48	0.37	0.00	0.00	0.02	0.34	0.78	0.99	0.88
'CaudMidFront.R'	0.88	0.84	0.76	0.72	0.04	0.03	0.01	0.01	0.02	0.02
'LatOrbitoFront.R'	0.02	0.00	0.01	0.00	0.00	0.00	0.00	0.00	0.00	0.00
'Paracentral.R'	0.52	0.42	0.97	0.57	0.92	0.76	0.80	0.89	0.95	0.88
'PostCentral.R'	0.87	0.20	0.32	0.02	0.02	0.10	0.24	0.36	0.42	0.85
'PostCingulate.R'	0.56	0.10	0.01	0.45	0.83	0.89	0.91	0.59	0.95	0.88
'Precentral.R'	0.85	1.00	0.97	0.72	0.33	0.06	0.07	0.13	0.13	0.20
'Precuneus.R'	0.98	0.48	0.63	0.72	0.92	0.87	0.85	0.84	0.95	0.88
'RosAntCing.R'	0.85	0.04	0.01	0.01	0.00	0.04	0.07	0.13	0.18	0.23
'RosMidFront.R'	0.87	0.52	0.63	0.72	0.79	0.97	0.86	0.42	0.90	0.80
'SupFront.R'	0.85	0.52	0.63	0.44	0.02	0.01	0.05	0.07	0.10	0.11
'SupParietal.R'	0.85	0.48	0.30	0.39	0.54	0.64	0.89	0.99	0.95	0.88
'SupraMarg.R'	0.88	0.48	0.46	0.06	0.36	0.43	0.36	0.42	0.54	0.80
'Insula.R'	0.87	1.00	0.63	0.44	0.33	0.61	0.17	0.12	0.18	0.23

Appendix table 2.27: P values (FDR corrected) of comparison of nodal local efficiency measures between TBI patients in chronic phase of injury and healthy controls across the 10 connectome threshold iterations. Thresh1=0.5 SD, Thresh10=5.0SD

Node	Thresh 1	Thresh 2	Thresh 3	Thresh 4	Thresh 5	Thresh 6	Thresh 7	Thresh 8	Thresh 9	Thresh 10
'Caudate.L'	0.74	0.84	0.77	0.41	0.24	0.72	0.57	0.15	0.24	0.13
'Pallidum.L'	0.74	0.67	0.87	0.77	0.19	0.03	0.01	0.01	0.00	0.00
'Hippocampus.L'	0.10	0.49	0.35	0.14	0.16	0.02	0.02	0.00	0.00	0.00
'Caudate.R'	0.74	0.65	0.87	0.53	0.72	0.04	0.06	0.04	0.01	0.02
'Pallidum.R'	0.74	0.66	0.55	0.87	0.78	0.72	0.51	0.28	0.20	0.07
'Hippocampus.R'	0.74	0.77	0.97	0.90	0.72	0.93	0.51	0.16	0.16	0.07
'CaudAntCing.L'	0.10	0.31	0.34	0.42	0.19	0.00	0.07	0.16	0.35	0.52
'LatOrbitoFront.L'	0.29	0.31	0.18	0.11	0.16	0.12	0.01	0.04	0.29	0.46
'Paracentral.L'	0.74	0.53	0.12	0.38	0.72	0.93	0.52	0.40	0.51	0.23
'PostCentral.L'	0.74	0.53	0.16	0.17	0.24	0.33	0.57	0.30	0.20	0.23
'PostCingulate.L'	0.30	0.40	0.12	0.11	0.05	0.08	0.04	0.04	0.11	0.07
'Precentral.L'	0.37	0.44	0.19	0.38	0.72	0.93	0.60	0.48	0.23	0.07
'Precuneus.L'	0.58	0.39	0.24	0.35	0.72	0.93	0.66	0.58	0.37	0.09
'RosAntCing.L'	0.30	0.49	0.12	0.01	0.05	0.12	0.10	0.33	0.69	0.98
'RosMidFront.L'	NaN	0.00	0.00	0.00	0.00	0.00	0.01	0.03	0.16	0.66
'SupFront.L'	NaN	0.68	0.97	0.18	0.13	0.72	0.52	0.40	0.32	0.23
'Insula.L'	0.10	0.05	0.18	0.35	0.18	0.15	0.03	0.00	0.00	0.00
'CaudaAntCing.R'	0.29	0.41	0.05	0.00	0.00	0.00	0.11	0.45	0.72	0.98
'CaudMidFront.R'	0.29	0.31	0.12	0.17	0.72	0.58	0.11	0.04	0.10	0.04
'LatOrbitoFront.R'	0.74	0.65	0.97	0.35	0.72	0.72	0.15	0.45	0.56	0.31
'Paracentral.R'	0.74	0.72	0.76	0.90	0.72	0.93	0.52	0.58	0.73	0.98
'PostCentral.R'	NaN	0.49	0.58	0.77	0.49	0.58	0.11	0.33	0.37	0.96
'PostCingulate.R'	0.39	0.19	0.04	0.36	0.74	0.83	0.73	0.40	0.72	0.69
'Precentral.R'	0.74	0.63	0.41	0.41	0.72	0.91	0.35	0.45	0.32	0.36
'Precuneus.R'	0.66	0.48	0.48	0.90	0.78	0.91	1.00	0.94	0.85	0.80
'RosAntCing.R'	0.74	0.49	0.97	0.44	0.13	0.87	0.40	0.58	0.72	0.75
'RosMidFront.R'	0.37	0.49	0.58	0.41	0.72	0.93	0.57	0.79	0.59	0.71
'SupFront.R'	0.37	0.41	0.35	0.65	0.89	0.72	0.73	0.65	0.56	0.38
'SupParietal.R'	0.66	0.41	0.45	0.88	0.72	0.93	0.73	0.65	0.99	0.98
'SupraMarg.R'	0.83	0.65	0.34	0.90	0.72	0.93	0.57	0.48	0.56	0.71
'Insula.R'	0.74	0.65	0.48	0.79	0.72	0.82	0.73	0.48	0.56	0.23

Appendix table 2.28: P values (FDR corrected) of comparison of nodal clustering coefficient measures between TBI patients in chronic phase of injury and healthy controls across the 10 connectome threshold iterations. Thresh1=0.5 SD, Thresh10=5.0SD